STRUCTURE AND ELECTRONIC PROPERTIES OF POROUS MANGANESE OXIDES.

Donna Claire Arnold

University College London and The Royal Institution of
Great Britain

Submitted for the Degree of Doctor of Philosophy.

September 2003

Abstract.

Manganese oxides with varying pore sizes from ~2Å to ~7Å have been prepared by standard solid-state techniques and by low temperature hydrothermal methods. These materials have an open framework composed exclusively of manganese oxide, which in simple tunnel and layered structures is built up exclusively of edge and corner shared MnO_6 octahedra. In more complex structures, such as that exhibited by $Na_{0.44}MnO_2$, this framework is built up of MnO_6 octahedra and MnO_5 square pyramids, where Mn^{3+} and Mn^{4+} are ordered on crystallographically distinct sites. The size of the tunnels or layer gap is dependent on the size of the cation used as a template.

This thesis shows that it is possible to remove the 'template' ion from within many framework materials without destroying the structural integrity, this is due primarily to the ready conversion between the various manganese oxidation states to maintain charge balance. This makes it possible to tune the properties by incorporating varying amounts of foreign cations and/or small molecules into the vacant pore sites. These intercalation reactions result in small changes in the average manganese oxidation state, which in turn leads to differences in the thermal stability, observed magnetic and transport properties.

We have also shown that it is possible to intercalate conducting polymers into the framework of some layered materials. Whilst the mechanism is not known, it can be seen that the oxidation state of the framework plays an important part in the ordering of the monomer/polymer units within the layers. Incorporation of these polymers leads to large changes in the magnitude of the observed magnetic moment as well as in the magnetic ordering.

This work shows that these materials have a versatile framework, which leads to the real possibility of tuning the properties of a material to achieve desired effects leading to many possible uses for these types of materials.

Acknowledgements.

I would like to thank my supervisor Dr Mark Green for all his support, guidance and insights. I would also like to thank Dr Alexandros Lappas for his help and facilitating my visits to Crete

I am thankful to Kevin Knight, Kevin Reeves and Marianne Odlyha for their help with various experiments both in their application and interpretation.

I am grateful to all at The Royal Institution of Great Britain, especially those of the Green group, Katie, Tom Will and Dinah, and also to Naseem and Ilona for providing discussion and helpful insights into chemistry, computing and life.

I am indebted to those especially my family and friends who have supported me throughout the last three years and throughout my academic career.

Table of Contents.

CHAPTER 1: Introduction.

CHAPTER 3: Hollandite '$K_{0.125}MnO_2$' system. 65

Table of Figure Captions.

Table of Table Captions.

CHAPTER 1. Introduction.

1.1. Introduction to Porous Manganese Oxides.

The structural and physical properties of some porous manganese oxides are reviewed in this chapter with an emphasis placed on those reported within this thesis. More specific chemical features are introduced on individual systems at the beginning of the relevant chapter.

Over many years there has been extensive work on porous materials, including aluminosilicates, zeolites, clay minerals and mesoporous silicates, often built on well defined three dimensional frameworks of aluminium, silicon and oxygen. Zeolites are extensively used in industry for their catalytic and porous activity such as the use of Chabazite and Clinoptilolite in the removal of ammonia from wastewater.[1-3] There has been a recent expansion of the known mesoporous and microporous metal oxides with similar cage like structures in terms of size and accessibility, to those exhibited by zeolites.[4] For example, materials based on ZrO_2 and Nb_2O_5 with pore sizes of 20-40Å and 8.5-20Å respectively have been reported.[5-7] More specifically there are a number of reported transition metal oxides showing one dimensional tunnels and layered structures, whereby the structural diversity of these materials is dependent upon the route of synthesis and template ion used.[8-17]

One family of interest, and the main focus of this thesis, are porous manganese oxides. These materials have a framework composed solely of manganese and oxygen. The frameworks are composed of vacant channels or layers, which have the ability to intercalate or absorb various molecules making them of interest. Pore sizes range from 3Å up to about 12Å.[18] As with zeolites many of these materials can be found naturally as part of mineral deposits but growing interest in potential applications has lead to the development of synthetic analogues and the preparation of novel materials.[19,20] The tunnel and layered structures of MnO_2 phases are mostly built up exclusively of edge and corner shared MnO_6 octahedra. More complex structures also exist, such as that exhibited by $Na_{0.44}MnO_2$, which contains MnO_6 octahedra and MnO_5 square pyramids.[21] The tunnels or inter layer spacing formed within the frameworks are usually occupied by alkali metals and alkaline earth metals such as Na^+, K^+ or Mg^{2+} and/or water molecules, which are thought to act as a template in their synthesis.

Extraction or insertion of template ions within the framework can be done topotatically by two different mechanisms, as listed below.[18,22,23]

I) Redox-type mechanisms.

$$AMn^{III}O_2 - xe^- \rightarrow A_{1-x}Mn_{1-x}{}^{III}Mn_x{}^{IV}O_2 + xA^+ \qquad (1.1)$$

II) Ion exchange mechanisms.

$$AMn^{III}O_2 + xH^+ \rightarrow A_{1-x}H_xMn^{III}O_2 + xA^+ \qquad (1.2)$$

where A is a cation such as Na^+, Li^+ or K^+.

A large structural diversity of porous manganese oxides exists since many metals or organic ions can be used as templates to control the dimensions of the tunnel, these templates can be readily removed by chemical and electrochemical reactions facilitated through the ready conversion between Mn^{4+} and Mn^{3+}. However it is difficult to obtain large single crystals of these materials due to the formation of defects.[18]

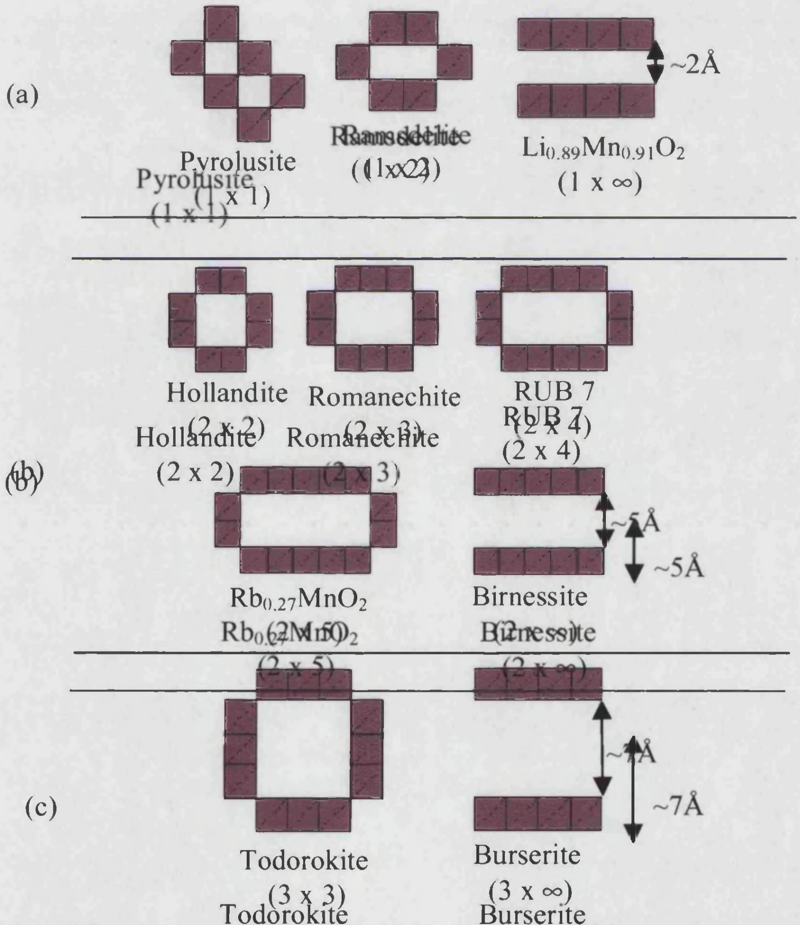

Figure 1.1. Schematic representation of some tunnel and layered structures where the pink squares represent the MnO_6 octahedral units.[3]

(a) *One dimensional Structures belonging to the Pyrolusite-Ramsdellite family,*[24]

(b) *One dimensional structures belonging to the Hollandite-Romanechite family,*[25]

(c) *One dimensional structures belonging to the Todorokite family.*

Turner and Buseck[26] proposed that simple tunnel and layered manganese oxide minerals could be classified into various groups based on the number of edge-sharing MnO_6 octahedra, whereby the Pyrolusite-Ramsdellite family consists of structures built up by one MnO_6 octahedra corner shared with a chain of n octahedra to form a (1 x n) tunnel. Pyrolusite has the (1 x 1) configuration involving one MnO_6 octahedron that is corner shared with another MnO_6 octahedron to form a tunnel of (1 x 1) dimensions. When $n = \infty$ this corresponds to an infinite unit width and therefore a layered structure. Also based on this classification are the Hollandite-Romanechite family with (2 x n) framwork structures and the Todorokite family with a (3 x n) network. Diagrammatic representations of some tunnel and layered structures are given in figure 1.1. In addition, there are a number of more complex structures often formed through the intergrowths of two or more of these family members. For example $Ba_6Mn_{24}O_{48}$ (Figure 1.2(a)) can be thought of as a combination of pyrolusite and hollandite building blocks, as well as an additional tunnel formed by 10 MnO_6 octahedra.[27]

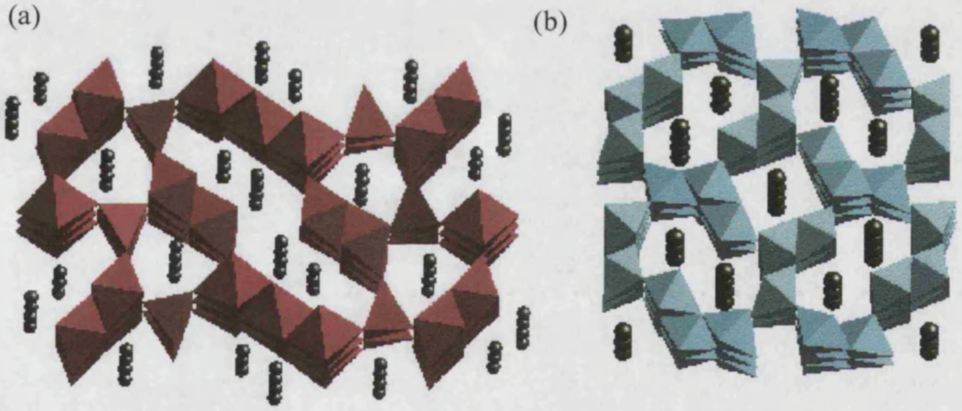

Figure 1.2. Complex tunnel structures of (a) $Na_{0.44}MnO_2$ viewed down the c axis, where the pink squares and triangles represent the MnO_6 octahedra and the MnO_5 square pyramids respectively and the green spheres are the sodium cations and (b) $Ba_6Mn_{24}O_{48}$ structure composed of a combination of pyrolusite and hollandite as well as an additional tunnel formed by 10 MnO_6 octahedra, where the blue squares are the MnO_6 octahedra and the green spheres are the barium cations.

1.2. Potential Applications of Porous Manganese Oxides.

Much of the interest in these materials stems from their many potential applications, such as excellent cation-exchange and molecular absorptive properties that could lead to possible uses as;[18]

- Ion sieves.
- Molecular sieves.
- Catalyst properties, such as the catalytic decomposition of pollutants. (similar to those of the aluminosilicates)
- Chemical absorption.

1.2.1. Ion/Molecular Sieve Applications.

Ion and molecular sieve applications of zeolite and silicate framework structures are well known and widely used in industry.[2] The size of the pore or tunnel is determined by the template used during synthesis thus allowing the opportunity of producing a size selective ion/molecular sieve.[18] The application of porous manganese oxides such as hollandite, todorokite and birnessite, which have effective pore radii of 0.14, 0.27 and 0.15nm respectively, as ion sieves materials have recently been investigated.[18] These structures have lead to the development of advanced separation and sensing technology with the application of these ion sieve properties. For example magnesium todorokite which has a pore size of 0.69nm shows attractive properties for C_6H_{12} and CCl_4 absorption, whose dimensions are 0.61nm and 0.69nm respectively.[28] To activate the manganese oxide ion or molecular sieves, the template ion must be removed from the framework by topotatic extraction reaction with acid. After extraction, metal ions can enter into the tunnels and the inter layer spaces again by topotatic reaction.

Ooi *et al* suggested that the absorption sites within the framework could be classified into non specific and specific sites, where crystal surface sites are non-specific ion exchange sites and the bulk crystal includes both specific ion exchange and specific redox sites.[29,30] It is worth noting that ion exchange sites show a higher acidity and stability than redox sites. The ion sieve properties were characterised by pH titration and distribution coefficient measurement studies. The selectivities of manganese oxide ion sieves for the absorption of metal ions have been reported by many authors and are strongly dependent on their structures. Some selectivity sequences are given below;

$Li^+ < Cs^+, Na^+ << Rb^+ < K^+$ - Hollandite.[30-32]

$Li^+ < Na^+ < Cs^+, K^+ < Rb^+$ - Birnessite.[33]

$Li^+ < Na^+ < K^+ < Rb^+ < Cs^+$ - Todorokite.[34]

It is important to note that selectivity is a consequence of the mismatch between each tunnel and its ideal sized cation.[35]

1.2.2. Catalysis.

Manganese oxides, in combination with other transition metal elements, serve as highly active and thermally stable catalysts for the oxidation of a variety of volatile organic materials.[18] Suib *et al* have carried out an extensive study of the possible catalytic potential of hollandite, todorokite and birnessite.[36] It has been shown that the catalytic oxidation of cyclohexane and n-hexane in aqueous solution in a batch reactor shows conversions of 10 and 8% respectively for Hollandite.[37] It has been suggested that whilst the reaction mechanisms are complicated they clearly point to both a shape selective effect and to selective oxidations. The rate of reactions is controlled by the average manganese oxidation state and therefore the primary focus of catalytic reactions has been in oxidation reactions. The oxidation of CO by hollandite at low temperatures is very efficient and in general small tunnel materials are usually more active and selective than those with larger tunnels.[36] The degradation of dye molecules, such as pinacyanol chloride dye, was investigated over a pH range of 6-11 at room temperature.[36] Doping of the framework with other transition metals affects the catalytic activity, with Fe, Cr and Co showing increased activities of 67.7%, 58.6% and 51.4% for hollandite (OMS-2) and 17.6%, 16.5% and 18.1% for todorokite (OMS-1) whilst Ni and Cu exhibited a decrease in the activity to 39.5% and 31.9% for OL-1 and 10.4% and 9.4% for OMS-1 relative to the pure Mn framework which shows activities of 45.9% and 13.3% for OMS-2 and OMS-1 respectively.[36,38] It has been reported that manganese oxides can be used as photo catalysts for the oxidation of Propan-2-ol to acetone and for the decomposition of phosphine and phosphine oxide.[39] However a poisoning of the catalyst has posed a real problem.[36]

1.2.3. Lithium Battery Technology.

The search for high energy rechargeable batteries have lead to significant development of materials for the different battery components; anodes, cathodes and electrolytes. Attention has been paid in particular to advanced lithium batteries with layered materials as cathodes. Generally the chemical reactions that take place within the cell consist of intercalation of Li ions into the host structure during discharge, followed by deintercalation from the host lattice during charging (oxidation) without significant modification of the host structure.[25] This is demonstrated in figure 1.3.

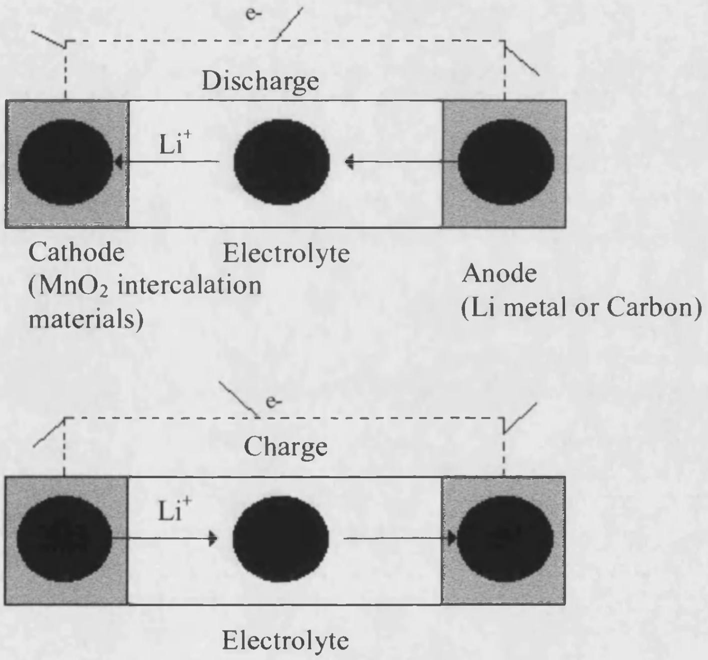

Figure 1.3. Schematic representation of charge and discharge mechanisms for lithium batteries.[22]

Manganese oxides having good electrochemical performances are attractive as cathode materials in lithium cells because manganese has economic and environmental advantages over compounds based on Co or Ni which are currently used.[40-42] $Li_{0.44}MnO_2$ has been investigated as an intercalation electrode.[43] The lithium content of the host was varied by chemical and electrochemical intercalation/de intercalation over the range Li_xMnO_2; $0.25 < x < 0.63$. The associated change in the Li site occupancies was determined by a combination of powder neutron diffraction and electrochemical measurements. It was reported that the structure demonstrates a remarkable ability to cycle Li with no perceptive loss of capacity when cycled over the 2.8 - 3.6V range corresponding to a capacity of 85 - 90mAh/g.[21,44] A concise review of the potential of lithium manganese oxide materials as insertion electrodes is available in reference 45, which highlights the structural versatility of these materials, their structural stability and limitations.[45] Doping of these materials with other transition metal ions, such as Fe or Co, to stabilise the framework structure have also been reported.[46,47]

1.2.4. Magnetic Applications.

Whilst extensive studies have been conducted into the magnetic properties and the structure of non porous perovskite and pyrochlore structures,[48-53] little work has been done on porous manganese oxides. Magnetism in Na_xMnO_2 phases was briefly mentioned by Parent *et al.*[54,55] The magnetic ordering in hollandite and todorokite materials has also been discussed, with these materials reported as spin glasses.[56] Many of these systems contain manganese in non integral formal oxidation states, thereby offering interesting correlations between the structure and electronic interactions. These studies have heightened importance since the discovery of colossal magnetoresistance (CMR), in manganese perovskites and pyrochlores. Magnetoresistance (MR) is the relative change in electrical resistance of a material on the application of a magnetic field defined by equation 1.3.

$$MR = \rho(H) - \rho(0)/\rho(0) \qquad \text{-(1.3)}$$

Where MR is the magnetoresistance, ρ(0) is the resistivity in zero field and ρ(H) is the resistivity in an applied field.

Materials showing such properties have aroused great interest recently due to their possible application in magnetic storage and sensing devices.[57-61] Much of this work has been related to the perovskite system, of general formula, $AMnO_3$ (where A = alkali earth metal and/or lanthanide ion).

The mechanism for CMR in perovskite type materials involves the double exchange interaction between the mixed valence manganese ions Mn^{3+} and Mn^{4+} leading to simultaneous ferromagnetic ordering and metal-insulator transition.[49,61]

Colossal magnetoresistance is also observed in the pyrochlore structure, $Tl_2Mn_2O_7$, which is comprised entirely of Mn^{4+} ions and therefore excludes the double exchange interaction. It is suggested that the CMR effect is derived from the interactions between low carrier electrons originating from the Tl-O overlap and localised ferromagnetic electrons caused by superexchange between the Mn ions.[61]

1.3. Preparation of Porous Manganese Oxides.

Both the tunnel and layered manganese oxides can be prepared synthetically by a number of different processes, but since the oxides are metastable in comparison to condensed phases, the majority of the preparations fall into the 'chimie-douce' regime, particularly those with larger tunnel sites such as todorokite. These processes can be split into three main groups;[22]

I) Dry Processes - solid state reactions/melting salt reflux processes.

II) Wet Processes - redox precipitation processes/hydrothermal processes/soft chemical processes.

III) Wet and Dry Processes - sol-gel processes.

The specific route used in the synthesis of many of these materials has a direct effect on their observed ion sieve, electrochemical or catalytic properties despite displaying similar structures. These differences can mainly be attributed to variations in particle size and the type/amount of defects in the structure. This means that small changes in synthetic parameters can often greatly alter their properties and this also accounts for differences observed between naturally occurring minerals and their synthetic counterparts. Phases with large tunnels or hydrated layered structures, such as todorokite and buserite, can only be prepared by wet processes.[22]

I)Dry Processes.

High Temperature Solid State Routes.

In solid state reactions, metal ions are used as templates with the resulting tunnel size/inter-layer width being dependent upon the size and quantity of the template used, which are usually an alkali or alkaline earth metal. The preparation of $Ba_6Mn_{24}O_{48}$, see figure 1.2b, by solid state techniques, yielded highly ordered samples when compared to those prepared by 'chimie-douce' methods due to the high temperatures used,[27] though this preparation did not yield a single phase product and small amounts of minor phases were present. Parent *et al*, prepared a number of manganese oxides with tunnel and layered structures based on the general formula $Na_{1-x}MnO_2$, where x has values of 0 to 1.[54,55] These phases were prepared under oxygen pressures of 1 and 4 bar at varying temperatures. Additionally $Na_{0.44}MnO_2$ has also been prepared by various authors in air at 800°C.[21,44]

The related composite tunnel structure of $LnMn_2O_5$ (where Ln is a rare earth) is also prepared at high temperatures.[62,63] $LnMn_2O_5$ can be thought of as a complex one dimensional tunnel structure, consisting of manganese with octahedral (MnO_6) and square pyramidal (MnO_5) co-ordination, though in this case the lanthanide ions cannot be removed. These rare earth oxides were prepared by solid state techniques from citrate gel precursors. After removal of the organics from the precursor materials, the samples were reacted at 1000°C under flowing oxygen.[13,14] Single crystals of $NdMn_2O_5$ were made by reacting MnO_2 and $NdCl_3$ (equation 1.4) at 1123K in an evacuated sealed silica tube for a week.[64]

$$5MnO_2 + 2NdCl_3 \rightarrow 2NdMn_2O_5 + MnCl_2 + 2Cl_2 \qquad \text{-(1.4)}$$

$Bi_2Mn_4O_{10}$ which is isostructural with $LnMn_2O_5$ was prepared by heating Bi_2O_3 and MnO_2 at 850°C in air for 24 hours and then slowly cooled to room temperature.[65]

Melting Salt Flux Processes.

It is usually difficult to obtain large crystalline samples of porous manganese oxides by the molten salt flux process, though, it has been reported for $Ba_6Mn_{24}O_{48}$.[27] Furthermore, crystalline samples of the orthorhombic layered oxide, $LiMnO_2$, have been prepared by Tang et al using a (LiCl and LiOH) flux.[23]

I) Wet Processes.

Redox Precipitation/Ion Exchange.

The reduction and precipitation of permanganate salts in solution is a common route to the production of synthetic manganese oxides. Birnessites and hollandites are frequently prepared by this method, however, whilst birnessite can be obtained in either alkaline or weakly acidic solutions, an acidic solution is required to obtain compounds with the hollandite structure.[18] Layered birnessite materials are prepared typically with alkali earth ions between layers and small amounts of hydrated water.[22] Birnessites as with other porous structures can undergo ion exchange reactions with the template cation being replaced. Luo *et al* performed a detailed investigation on the contribution of various synthetic parameters to the crystallinity and ion exchange properties of birnessite.[20]

Thin films of porous manganese oxides have been prepared from a solution obtained by redox precipitation of $KMnO_4$ and sucrose. The thin films are then prepared via immersion, spray coating, spin coating or spatula coating.[66] Extensive ion exchange reactions have been employed in the preparation of $Li_{0.44}MnO_2$. $Na_{0.44}MnO_2$ is prepared by conventional solid state techniques as a precursor usually from Na_2CO_3 and Mn_2O_3 and ion exchange reactions are performed to exchange the Na for Li. Alternatively, ion exchange can be performed as described in the preparation of layered $LiMnO_2$, the manganese oxide is refluxed with n-Hexanol and an excess of LiBr[20,43,67] though, this leads to an incomplete exchange. A new method was proposed using a eutectic mixture of $LiNO_3$/LiCl (88/12 mol%), the precursor was mixed with an appropriate amount of ion exchange medium (5-10 fold Li excess) and fired at 260-275°C. On cooling the solidified melt is dissolved in ethanol and the product filtered, washed and dried. A concise literature review of extraction/ion exchange is given elsewhere.[18]

Hydrothermal Methods.

Hydrothermal methods rely on the action of water at temperatures near its critical temperature in a closed bomb and therefore under high pressures.[68] This is a useful and unique method for the preparation of tunnel and layered manganese oxides, and comprises of two steps;

1) Preparation of a framework with a layered or analogous structure with template ions or molecules occupying the inter-layer space.
2) Transformation of the layered structure into a tunnel one by hydrothermal treatment. The dimensions of the resulting tunnel can be designed and predicted easily from the dimensions of the template used

This process has been used recently in the synthesis of ion and molecular sieves from layered birnessite or burserite precursors, to produce, for example, todorokite.[18] A systematic study has been carried out on the effect of the template on tunnel size under low temperature hydrothermal conditions.[33,69] Spinels and birnessite can be prepared by hydrothermally treating γ-MnO_2 in LiOH, NaOH or KOH solution.[33,39] Birnessites are also obtained by hydrothermally treating β-MnO_2 or α-MnO_2 in a NaOH solution.[70-72] A summary of the favourable transformations is given in Figure 1.4. These transformation reactions are carried out at low temperature to prevent destruction of the metastable tunnel structure. The template ion or molecule can be incorporated into the precursor from the solution phase during the transformation reaction.[25,69,71-77]

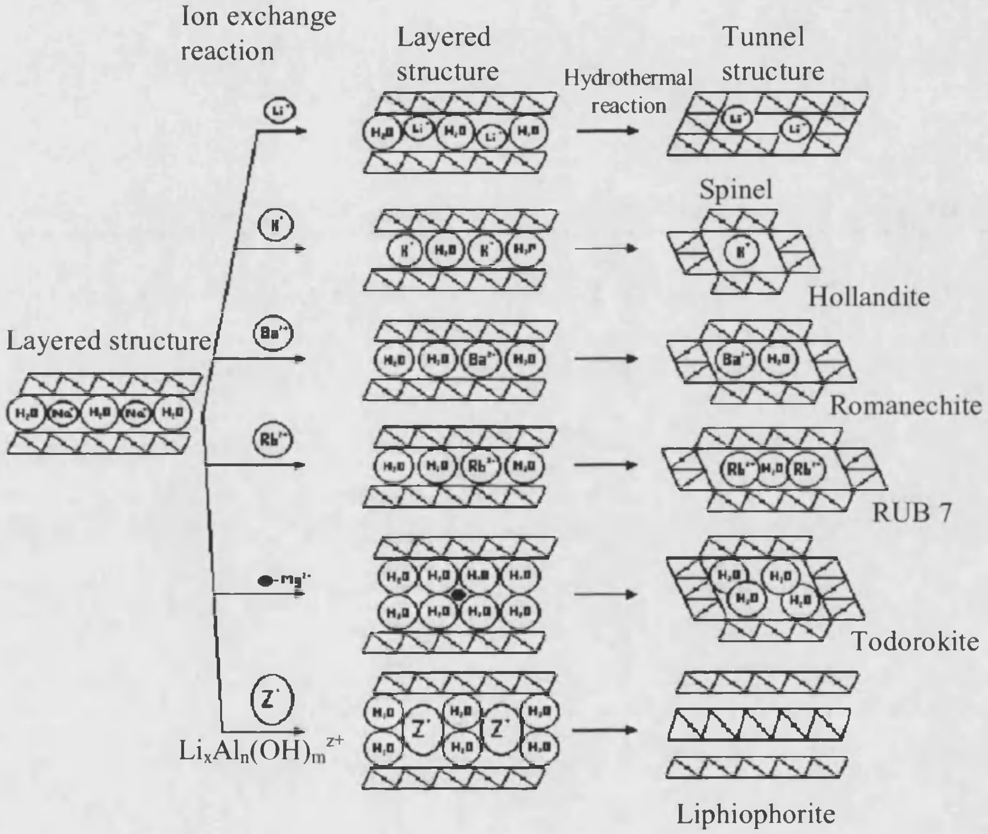

Figure 1.4. Transformation reactions from birnessite to tunnel and layered manganese oxides under hydrothermal conditions, where the squares represent the MnO_6 octahedra.[18]

III) Wet and Dry Processes.

Sol-Gel Processing.

Sol-Gel processing offers new approaches to the synthesis of transition metal oxides based on inorganic polymerisation from molecular precursors and many tunnel and layered manganese oxides can be prepared by this method.[78,79] These reactions occur in solution and the term ‘sol-gel processing’ is often used broadly to describe the synthesis of inorganic oxides by wet chemistry methods. In this process the gel is heated to remove trace amounts of organic materials and then heated at an optimal temperature to yield the desired product. Hollandite, birnessites and spinel type manganese oxides have been synthesised in this way.[18,31,35,80-86]

1.4. Overview of the Na_xMnO_2 System.

A summary of the structural motifs and phase diagram for $Na_{1-x}MnO_2$, where $0 \geq x \geq 1$, is given in table 1.1 and figure 1.5 respectively. These tunnel and layered manganese oxide structures were first reported by Parent et al in 1971.[54] All phases were prepared in oxygen at various temperatures and pressures to maintain the Mn oxidation state above 3. $Na_{0.40}MnO_2$, $Na_{0.44}MnO_2$ and both α and β $Na_{0.70}MnO_2$ are semiconductors. It is evident that the sodium composition plays an important role in the structure of the phase, as it is possible to obtain different structures by varying the temperature, pressure and sodium content.

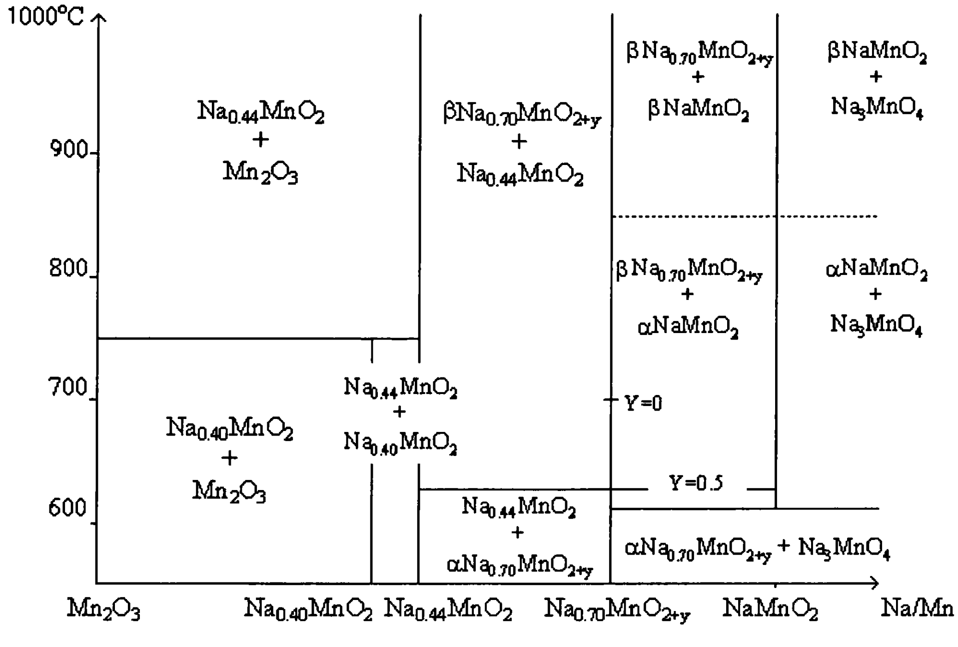

Figure 1.5. Phase diagram for the Na_xMnO_2 system depicting the phases obtained as a function of sodium content (x) and temperature, under oxygen pressure of 1 Bar.[9]

Table 1.1. Summary of phases, synthesis and properties of the Na_xMnO_2 family as reported by Parant et al.[54]

Phase	Structure Type	System	Preparation	Properties
$Na_{0.2}MnO_2$	Hollandite (figure 1.1(a))	Tetragonal	4 Bar oxygen pressure.	Not measured
$Na_{0.4}MnO_2$	Romanechite (figure 1.1(b))	Monoclinic	1 Bar oxygen Pressure.	Antiferromagnetic $T_N \sim 25K$
$Na_{0.44}MnO_2$	1D structure (figure 1.2(a))	Orthorhombic	1 Bar oxygen pressure.	No order of magnetism between 20 and 300K.
$\beta Na_{0.7}MnO_2$	Layered	Orthorhombic	1 Bar oxygen pressure	Spontaneous magnetism under 60K.
$\alpha Na_{0.7}MnO_2$	Layered	Hexagonal		
$\beta NaMnO_2$	Layered (figure 1.6(a))	Orthorhombic	1 Bar oxygen pressure	Meta-magnetic similar to $\alpha NaNiO_2$.
$\alpha NaMnO_2$	Layered (figure 1.6(b))	Monoclinic		

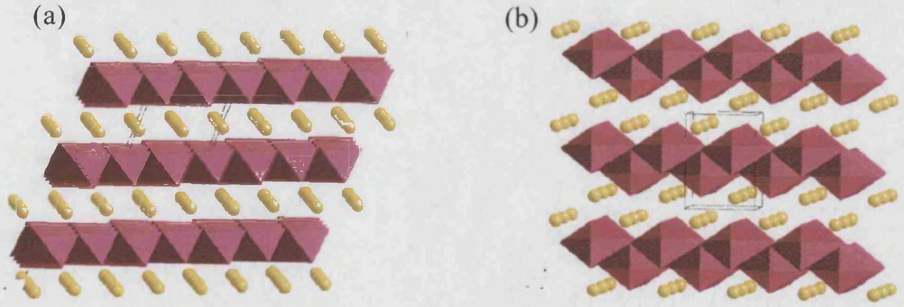

Figure 1.6. Schematic representation of (a) α-$NaMnO_2$ and (b) β-$NaMnO_2$, where the pink squares represent the MnO_6 octahedra and the yellow spheres are the sodium cations.

1.5. References.

(1) S. K. Ouki, M. Kavannagh, *Waste Management and Research*, **1997**, *15(4)*, 383.

(2) S. H. Park, J. B. Parise, H. Lui, C. P. Grey, B. H. Toby, H. Gies, *Microporous and Mesoporous Materials*, **2000**, *37*, 129.

(3) M. Takahashi, M. Fuji, *KONA*, **2002**, *20*, 84.

(4) Y. Ma, W. Tong, H. Zhou, S. L. Suib, *Microporous and Mesoporous Materials*, **2000**, *37*, 243.

(5) G. Pacheco, E. Zhou, A. Garcia, A. Sklyarov, J. J. Fripiat, *Chemical Communications*, **1997**, *5*, 491.

(6) R. Abe, K. Shinohara, A. Tanaka, M. Hara, J. N. Kondo, K. Domen, *Chemistry of Materials*, **1997**, *9(10)*, 2179.

(7) T. Sun, J. Y. Ying, *Nature*, **1997**, *389*, 704.

(8) J. Akimoto, H. Takei, *Journal of Solid State Chemistry*, **1990**, *85*, 8.

(9) H. Wang, Y. I. Jang, B. Huang, D. R. Sadoway, Y. M. Chiang, *Journal of the Electrochemical Society*, **1999**, *146*, 473.

(10) M. Takano, R. Kanno, T. Takeda, *Materials Science and Engineering B Solid State Materials and Advanced Technology*, **1999**, *63*, 6.

(11) M. Y. Avdeev, V. B. Nalbandyan, B. S. Medvedev, *Inorganic Materials*, **1997**, *33(5)*, 500.

(12) J. Akimoto, H. Takei, *Journal of Solid State Chemistry*, **1989**, *83*, 132.

(13) L. D. Noailles, C. S. Johnson, J. T. Vaughey, M. M. Thackeray, *Journal of Power Sources*, **1999**, *81*, 259.

(14) P. H. M. van Loosdrecht, C. N. Presura, M. Popinciuc, D. van der Marel, G. Maris, T. T. M. Palstra, P. J. M. van Bentum, H. Yamada, T. Yamauchi, Y. Ueda, *Journal of Superconductivity: Incorporating Novel Magnetism*, **2002**, *15*, 587.

(15) A. Kuhn, N. Menendez, F. Garcia-Alvarado, E. Moran, J. D. Tornero, M. A. Alario-Franco, *Journal of Solid State Chemistry*, **1997**, *130*, 184.

(16) S. Andersson, A. D. Wadsley, *Acta Crystallographica*, **1962**, *15*, 194.

(17) A. Kuhn, F. Garcia-Alvarado, E. Moran, M. A. Alario-Franco, U. Amador, *Solid State Ionics*, **1996**, *86-88*, 811.

(18) Q. Feng, H. Kanoh, K. Ooi, *Journal of Materials Chemistry*, **1999**, *9(2)*, 319.

(19) D. L. Bish, J. E. Post, *American Mineralogist*, **1989**, *74*, 177.

(20) J. Luo, S. L. Suib, *Journal of Physical Chemistry B*, **1997**, *101(49)*, 10403.

(21) M. M. Doeff, T. J. Richardson, L. Kepley, *Journal of the Electrochemical Society*, **1996**, *143(8)*, 2507.

(22) S. L. Brock, N. Duan, Z. R. Tian, O. Giraldo, H. Zhou, S. L. Suib, *Chemistry of Materials*, **1998**, *10(10)*, 2619.

(23) W. Tang, H. Kanoh, K. Ooi, *Journal of Solid State Chemistry*, **1999**, *142*, 19.

(24) M. H. Rossouw, D. C. Liles, M. M. Thackeray, *Journal of Solid State Chemistry*, **1993**, *104(2)*, 464.

(25) T. Rziha, H. Gies, J. Ruis, *European Journal of Mineralogy*, **1996**, *8(4)*, 675.

(26) S. Turner, P. R. Buseck, *Science*, **1981**, *212*, 1024.

(27) P. Boullay, M. Hervieu, B. Raveau, *Journal of Solid State Chemistry*, **1997**, *132*, 239.

(28) Y. F. Shen, R. P. Zerger, R. N. Deguzman, S. L. Suib, L. McCurdy, D. I.. Potter, C. L. O'Young, *Science*, **1993**, *260*, 511.

(29) K. Ooi, Y. Miyai, S. Katoh, *Separation Science and Technology*, **1987**, *22(7)*, 1779.

(30) K. Ooi, Y. Miyai, S. Katoh, *Solvent Extraction and Ion Exchange*, **1987**, *5(3)*, 561.

(31) P. Barboux, J. M. Tarascon, F. K. Shokoohi, *Journal of Solid State Chemistry*, **1991**, *94(1)*, 185.

(32) M. Tsuji, M. Abe, *Bulletin of the Chemical Society of Japan*, **1985**, *58(4)*, 1109.

(33) Q. Feng, K. Yanagisawa, N. Yamasaki, *Journal of Porous Materials*, **1998**, *5(1)*, 153.

(34) M. Tsuji, S. Komarneni, *Journal of Materials Research*, **1993**, *8(3)*, 611.

(35) N. Duan, S. L. Suib, C. L. O'Young, Journal of the *Chemical Society. Chemical Communications*, **1995**, *13*, 1367.

(36) S. L. Suib, *Chemical Innovation-Sorption, Catalysis, Separation Design*, **2000**, *30(3)*, 27.

(37) H. Cao, S. L. Suib, *Journal of the American Chemical Society*, **1994**, *116(12)*, 5334.

(38) S. R. Segal, S. L. Suib, L. Foland, *Chemistry of Materials*, **1997**, *9(11)*, 2526.

(39) Q. Feng, H. Kanoh, Y. Miyai, K. Ooi, *Chemistry of Materials*, **1997**, *7(1)*, 148.

(40) Z. R. Tian, W. Tong, Y. Y. Wang, N. G. Duan, V. V. Krishnan, S. L. Suib, *Science*, **1997**, *276*, 926.

(41) S. Turner, P. R. Buseck, *Science*, **1979**, *203*, 456.

(42) F. Leroux, L. F. Nazar, *Solid State Ionics*, **1997**, *100*, 103.

(43) A. R. Armstrong, P. G. Bruce, *Nature*, **1996**, *381*, 499.

(44) M. M. Doeff, M. Y. Peng, Y. P. Ma, L. C. De Jonghe, *Journal of the Electrochemical Society*, **1994**, *141(11)*, L145.

(45) M. M. Thackeray, *Progress in Solid State Chemistry*, **1997**, *25*, 1.

(46) M. S. Whittingham, P. Y. Zavalij, *Solid State Ionics*, **2000**, *131*, 109.

(47) M. S. Whittingham, *Solid State Ionics*, **2000**, *134*, 169.

(48) C. N. R. Rao, A. K. Cheetham, R. Mahesh, *Chemistry of Materials*, **1996**, *8(10)*, 2421.

(49) Y. Moritomo, A. Asamitsu, H. Kuwahara, Y. Tokura, *Nature*, **1996**, *380*, 141.

(50) Y. Shimakawa, Y. Kubo, Y. Manako, *Nature*, **1996**, *379*, 53.

(51) S. Mori, C. H. Chen, S. W. Cheong, *Nature*, **1998**, *392*, 473.

(52) R. Von Helmolt, J. Wecker, B. Holzaofel, L. Schultz, K. Samwer, *Physical Review Letters*, **1993**, *71(4)*, 2331.

(53) M. McCormack, S. Jin, T. H. Tiefel, R. M. Flemming, J. M. Phillips, R. Ramesh, *Applied Physics Letters*, **1994**, *64(22)*, 3045.

(54) J. P. Parant, R. Olazcuaga, M. Devalette, C. Fouassier, P. Hagenmuller, *Journal of Solid State Chemistry*, **1971**, *3*, 1.

(55) A. Mendiboure, C. Delmas, P. Hagenmuller, *Journal of Solid State Chemistry*, **1985**, *57*, 323.

(56) S. L. Suib, L. E. Iton, *Chemistry of Materials*, **1994**, *6(4)*, 429.

(57) R. Mahesh, R. Mahendiran, A. K. Raychaudhuri, C. N. R. Rao, *Materials Research Bulletin*, **1991**, *31(8)*, 897.

(58) H. L. Ju, J. Gopalakrishnan, J. L. Peng, Q. Li, G. C. Xiong, T. Venkatesan, R. L. Greene, *Physical Review B*, **1995**, *51(9)*, 6143.

(59) J. R. Sun, G. H. Rao, Y. Z. Zhang, *Applied Physics Letters*, **1998**, *72(24)*, 3208.

(60) Y. Ng-Lee, F. Sapina, E. Martinez-Tomayo, J. V. Folgado, R. Ibenez, D. Beltran, F. Lloret, A. Segura, *Journal of Materials Chemistry*, **1997**, *7(9)*, 1905.

(61) A. D. Ramirez, *Journal of Physics. Condensed Matter*, **1997**, *9*, 8171.

(62) J. A. Alonso, M. T. Casais, M. J. Martinez-Lope, I Rasines, *Journal of Solid State Chemistry*, **1997**, *129*, 105.

(63) J. A. Alonso, M. T. Casais, M. J. Martinez-Lope, J. L. Martinez, M. T. Fernandez-Diaz, *Journal of Physics. Condensed Matter*, **1997**, *9(40)*, 8515.

(64) P. Euzen, P. Leone, C. Gueho, P. Palvadeau, *Acta Crystallographica C Crystal Structure Communications*, **1993**, *49*, 1875.

(65) N. Nguyen, M. Legrain, A. Ducouret, B. Raveau, *Journal of Materials Chemistry*, **1999**, *9(3)*, 731.

(66) S. R. Segal, S. H. Park, S. L. Suib, *Chemistry of Materials*, **1997**, *9(1)*, 98.

(67) A. R. Armstrong, H. Huang, R. A. Jennings, P. G. Bruce, *Journal of Materials Chemistry*, **1998**, *8(1)*, 255.

(68) K. Byrappa, M. Yoshimura, *Handbook, of Hydrothermal Technology*, William Andrew Publishing, Norwich, **1999**.

(69) Q. Feng, K. Yanagisawa, N. Yamasaki, *Chemical Communications*, **1996**, *14*, 607.

(70) Q. Feng, K. Yanagisawa, N. Yamasaki, K. Ooi, *Journal of Materials Science Letters*, **1996**, *15(11)*, 963.

(71) S. Hirano, R. Narita, S. Naka, *Materials Research Bulletin*, **1984**, *19(9)*, 1229.

(72) T. Endo, S. Kume, M. Shimada, M. Koizumi, *Mineral Magazine*, **1974**, *39*, 559.

(73) M. H. Rossouw, D. C. Liles, M. M. Thackeray, W. I. F. David, S. Hull, *Materials Research Bulletin*, **1992**, *27(2)*, 22.

(74) D. Tamada, N. Yamamoto, *Mineral d*, **1986**, *13*, 130.

(75) Q. Feng, H. Kanoh, Y. Miyai, K. Ooi, *Chemistry of Materials Chemistry*, **1995**, *7(9)*, 1722.

(76) J. Luo, S. L. Suib, *Chemical Communications*, **1997**, *11*, 1031.

(77) E. Silvester, A. Manceau, V. A. Dritts, *American Mineralogist*, **1997**, *82(9-10)*, 962.

(78) J. Livage, *Journal of Solid State Chemistry*, **1986**, *64*, 322.

(79) R. Koksbang, J. Barker, H. Shi, M. Y. Saidi, *Solid State Ionics*, **1996**, *84(3)*, 1.

(80) S. Ching, J. A. Landrigan, M. L. Jorgensen, N. G. Duan, S. L. Suib, C. L. O'Young, *Chemistry of Materials*, **1995**, *7(9)*, 1604.

(81) S. Ching, J. L. Roark, N. Duan, S. L. Suib, *Chemistry of Materials*, **1997**, *9(3)*, 750.

(82) S. Bach, J. P. Pariera-Ramos, N. Baffier, R. Messina, *Acta Crystallographica*, **1991**, *36(10)*, 1595.

(83) S. Bach, M. Henry, N. Baffier, J. Livage, *Journal of Solid State Chemistry*, **1990**, *88(2)*, 325.

(84) S. Ching, D. J. Petrovay, M. L. Jorgensen, *Inorganic Chemistry*, **1997**, *36(5)*, 883.

(85) T. Takada, H. Hayakawa, E. Akiba, *Journal of Solid State Chemistry*, **1997**, *115(2)*, 420.

(86) T. Takada, H. Hayakawa, T. Kumagai, E. Akiba, *Journal of Solid State Chemistry*, **1996**, *121 (1)*, 79.

CHAPTER 2: Theory and Experiment

2.1. Introduction.

This chapter gives an overview of the experimental techniques used in the structural and property characterisation of the porous manganese oxide materials reported in this thesis. The individual mechanisms for the synthesis of these materials are discussed later as part of the experimental sections in the relevant chapters.

2.2 Diffraction Techniques.

The unit cell is the smallest unit that repeats infinitely to form a crystal. The diffraction condition can be expressed in reciprocal space where the relationship between the reciprocal lattice and the crystal structure is given by equation 2.1.

$$a^* = \frac{\vec{b}x\vec{c}}{Vc} \quad b^* = \frac{\vec{c}x\vec{a}}{Vc} \quad c^* = \frac{\vec{a}x\vec{b}}{Vc} \qquad \text{-(2.1)}$$

Where V_C is the volume of the unit cell and hence;

$$V_C = \vec{a} \cdot \left(\vec{b} \times \vec{c}\right) \qquad \text{-(2.2)}$$

The reciprocal lattice vector $d^* = ha^* + kb^* + cl^*$ is perpendicular to the direct lattice planes with Miller indices [hkl], with magnitude being the reciprocal of the shortest distance between these [hkl] planes.

$$\left|d^*\right| = \frac{1}{d_{hkl}} \qquad \text{-(2.3)}$$

A useful representation of the diffraction process is given by a set of lattice planes. Bragg regarded each of these planes as a semi transparent mirror such that when a crystal is bombarded with x-rays some of the beams are reflected by a plane, whilst the remainder are transmitted to be reflected by subsequent planes. (Figure 2.1.) If we consider a crystal to be comprised of planes A and B, for the reflected beams 1' and 2' to be in phase, then the additional distance that beam 11' has to travel compared to 22', which is a distance of xyz, has to be an exact multiple of the wavelength. The distance, d, between the planes and the angle of incidence, θ, (Bragg angle) is related to the distance xy by equation 2.4, Bragg's law is thus given by equation 2.5.

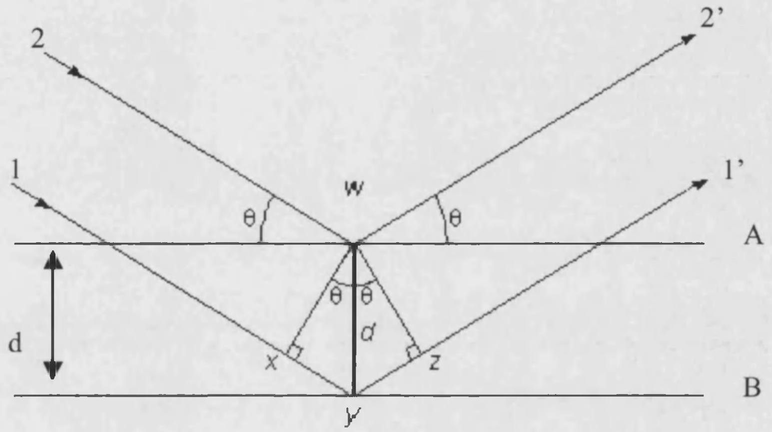

Figure 2.1. Graphical representation of Bragg's Law for X-ray Diffraction.

$$xy = yz = d\sin\theta \qquad \text{-(2.4)}$$

$$n\lambda = 2d\sin\theta \qquad \text{-(2.5)}$$

Where n is an integer, λ is the wavelength, d is the interplanar spacing and θ is the Bragg angle.

The requirement for the reflected beams to be in phase is due to the necessity for the radiation to interfere constructively. Reflected beams, which are out of phase, even by a small amount, interfere destructively resulting in their complete cancellation. A simple geometric construction in reciprocal space, developed by Ewald, helps in understanding when a Bragg reflection is or is not observed. The origin, O, is defined as the point where the incident beam, k_0, terminates and C as the centre of a sphere of radius 1/λ. The diffraction condition is met if one or more reciprocal lattice points, such as the point P, lie on the surface of the sphere, making the Bragg angle, θ, such that the angle OCP is equal to 2θ.

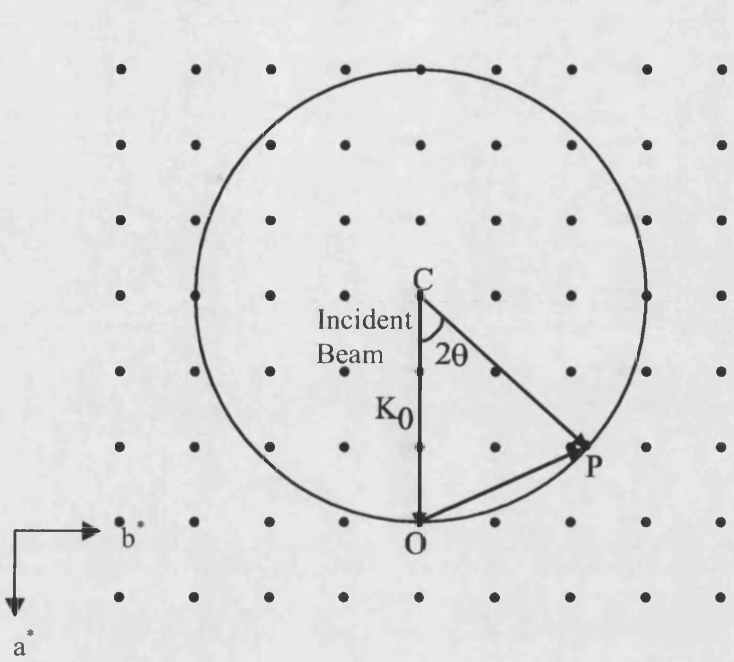

Figure 2.2. Schematic representation of the scattering triangle for elastic scattering in a reciprocal lattice plane described by Ewald.

The position of diffracted radiation is determined by the distance between the Miller planes and therefore, the lattice parameters of the crystal. The relative intensities of the Bragg reflections, I_{hkl}, are dependent on a number of factors but most importantly on the position of the atoms within the unit cell. The scattering power for a reflection [hkl] is defined by the structure factor, F_{hkl}, where I_{hkl} is the square of the amplitude of the structure factor as shown by equation 2.6. In the case of X-ray scattering it is the atomic electrons that scatter radiation while the nucleus is responsible for diffraction in neutron scattering.

$$I_{hkl} = \left|F_{hkl}\right|^2 \qquad \text{-(2.6)}$$

The structure factor is given in equation 2.7 for X-rays and 2.8 for neutron diffraction.

$$F_{hkl} = \sum_i f_i \exp[-2\pi i(hx_i + ky_i + lz_i)]\exp(-W_i) \qquad \text{-(2.7)}$$

$$F_{hkl} = \sum_i b_i \exp[-2\pi i(hx_i + ky_i + lz_i)]\exp(-W_i) \qquad \text{-(2.8)}$$

The fractional co-ordinates of the ith atom are x_i, y_i and z_i, f_i is the scattering amplitude for the X-rays, b_i the neutron scattering length and W_i is the Debye-waller isotropic temperature factor and takes into account the thermal vibration of the atoms as defined by equation 2.9.

$$W_i = \frac{8\pi^2 \sin^2 \theta \langle u_i^2 \rangle}{\lambda^2} \qquad \text{-(2.9)}$$

Where $\langle u_i^2 \rangle$ is the mean square displacement of the ith atom.

2.2.1. Powder X-ray Diffraction.

Laboratory X-ray diffractometers are composed of three main components: a monochromator, which diffracts X-rays giving single wavelength radiation, a source, and a radiation detector. The X-ray source is a highly evacuated tube consisting of a metal target, which is typically copper, and a filament. The filament is heated emitting an electron beam, which is accelerated towards the copper target. The electron beam ionises core electrons from the K-shell (1s) of the copper, which results in the transition of electrons from higher, filled, shells to drop into the vacant (1s) orbitals emitting electromagnetic radiation. The difference between the high shells and the (1s), is in the X-ray range which therefore produces X-ray radiation. This relaxation of electrons into the vacant (1s) orbital is governed by the transition selection rule, which requires a change in orbital angular momentum of one ($\Delta l = +/-1$) thus the relaxing electron must come from the L (2p) or M (3p) orbitals, resulting in two intense lines in the emission spectrum.

X-ray data for the materials discussed in this thesis were collected using the Siemens D500 X-ray diffractometer, using a copper source. For the purpose of these experiments the diffractometer was fitted only with a secondary graphite monochromator to minimize manganese fluorescence. Samples were finely ground and laid into an amorphous ceramic X-ray plate to minimize preferred orientation effects. The materials were initially studied over a two-theta range of 5 to 70°, stepwise in steps of 0.04° at 1 second per step to verify phase purity. Longer scans were then collected over a two-theta range of 5 to 100° in smaller steps of 0.02° at 12 seconds per step. Collected data were then refined in most cases using the Rietveld method discussed in 2.2.4.

2.2.2. Powder Neutron Diffraction.

There are two standard techniques for the production of neutrons: spallation and reactor sources. The Rutherford Appleton Laboratories (RAL) in Didcot, Oxon, UK is a spallation source, which generates pulses of neutrons analysed through the time of flight (TOF) technique. Constant wavelength diffraction is performed using a reactor source such as that employed by the National Institute of Standards and Technology (NIST) in Gaithersburg, MD, USA.

2.2.2.1. Constant Wavelength Experiments.

Powder neutron diffraction is widely performed using constant wavelength beams from steady-state nuclear reactor sources. In a typical experimental arrangement, thermal neutrons from a nuclear reactor are guided through a collimator to a large single crystal monochromator, which directs single wavelength radiation onto the sample. The sample then scatters the radiation, which is then picked up by the detector. (Figure 2.3)

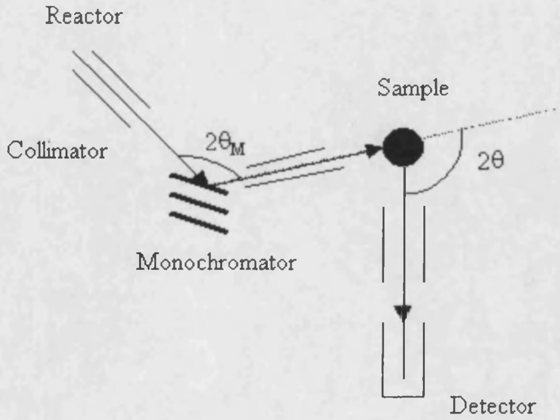

Figure 2.3. Schematic diagram of a powder neutron diffractometer operating at constant wavelength.

BT1 Diffractometer at NIST, USA.

Powder neutron diffraction data for some of the phases described in this thesis were collected using the BT1 diffractometer at the National Institute of Standards and Technology. Experiments using the BT1 Diffractometer are at constant wavelength, with the reactor producing a thermal flux of 4×10^4 neutrons/cm^{2}s^1 using uranium fuel cells. A choice of 3 monochromators, of different mosaic spread, namely Ge[311], Cu[311] and Si[531], utilising different take off angles as shown in table 2.1. Two different incident Soller collimators allow the instrument response to be tailored to the needs of the experiment. The diffractometer is a 32 detector instrument allowing data to be collected over a two theta range of 0 to 167°.[1]

Table 2.1. Monochromator information for BT1 at NIST.

Monochromator	in-pile Collimation (arcmin)	2Theta	Relative Bragg Intensities	Flux (ns^{-1}cm^{-2})	Wavelength (Å)
Ge[311]	15'	75°	3.34	700,000	2.0784
Ge[311]	7'	75°	1.84	400,000	2.0795
Cu[311]	15'	90°	1.00	400,000	1.5401
Cu[311]	7'	90°	0.59	200,000	1.5405
Si[531]	15'	120°	0.47	200,000	1.5903
Si[531]	7'	120°	0.33	100,000	1.5904

Neutron diffraction measurements were performed on the $Ln_{1-x}Ca_{1+x}MnO_4$ series discussed in chapter 7 using a Cu [311] monochromator (λ = 1.5401Å) and 15' final collimation. Scans were taken from 3° to 165° with a step size of 0.05°. Additionally data were collected at room temperature for the $Na_{0.40}MnO_2$ material.

2.2.2.2. Pulsed Experiments.

A second possible experimental arrangement makes use of an accelerator based source, which produces a pulsed neutron beam. In the case of a spallation source, neutrons are produced by bombarding a heavy metal, for example U or Ta, with highly energetic protons (~800 MeV) at a certain frequency. A high flux, white neutron pulse (typically about 30 neutrons per proton) emerges from the target. These highly energetic neutrons need to be moderated in order to increase the proportion of the useful thermal ones with wavelengths appropriate for diffraction from crystals. However, the moderation of the white neutron beam also creates a significant amount of epithermal neutrons. As a result, the neutron flux extends down to a very short wavelength (λ ~0.6Å) compared with reactor sources. In a conventional experiment, the detector is placed at a fixed scattering angle 2θ, and the time that neutrons with different wavelengths take to reach the detector can be measured through the time of flight method and the scattered intensity is determined as a function of the wavelength. (Figure 2.4)

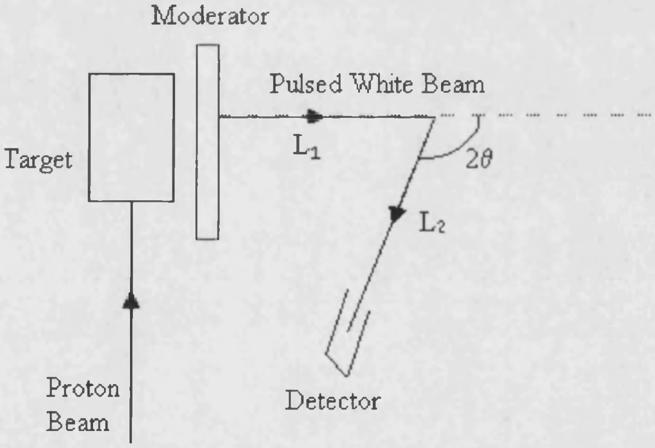

Figure 2.4. Schematic diagram of a neutron powder diffractometer operating at fixed scattering 2θ

The time-of-flight, t_{hkl}, is related to the d-spacing through de Broglie's relation, by substituting the wavelength (λ_{hkl}) from Bragg's law:

$$t_{hkl} = \left(\frac{2m_n L \sin\theta_0}{h} \right) d_{hkl} \qquad \text{-(2.10)}$$

Where m_n is the neutron mass, h is Plancks constant, $L=L_1+L_2$ is the total flight path and $2\theta_0$ is the fixed scattering angle. The spectral distribution of the incident beam is modelled by measuring the isotropic scattering from a standard vanadium sample, which also accounts for corrections in the detector efficiency as a function of wavelength variation.[2]

High Resolution Powder Diffractometer (HRPD) at RAL, UK.

Neutron diffraction data for the many of the tunnel structures in this thesis were collected using HRPD. Operating on the time-of-flight principle, HRPD offers the advantage of variable incident wavelength with fixed detector, namely the backscattering detector and 90° detector geometry. A summary of both the detectors' characteristics are given in table 2.2. The diffractometer is situated almost 100m from the target at the end of a neutron guide, which maintains a usable flux level and results in a resolution in the main backscattering detector bank of $\Delta d/d \sim 4 \times 10^{-4}$, which is effectively constant over the *d*-spacing range.[3]

Table 2.2. Summary of detectors used at HRPD

	Detectors		
Position	Backscattering	90 degrees	Low angle
Detector type	ZnS scintillator	ZnS scintillator	10 atm. ^{3}He gas tube (½")
2θ range	160° - 176°	80° - 100°	28° - 32°
Ω (ster)	0.41 ster	0.70 ster	0.01 ster
Resolution($\Delta d/d$)	$\sim 4 \times 10^{-4}$	$\sim 2 \times 10^{-3}$	$\sim 2 \times 10^{-2}$

Data were collected using HRPD at a range of temperatures for different materials depending on their magnetic properties at a current of approximately 200μA.

2.2.3. The Rietveld Method.

The random orientation of crystallites in the beam results in the superposition of the crystallographic axes onto the same axis of the diffraction pattern, this results in similar distances between some Miller planes causing overlap of the peaks preventing accurate measurement of the observed intensities and hence the structure. In 1969 Rietveld proposed a refinement method to overcome these problems based on linear least squares minimization of a function, S_y, composed of the observed and calculated intensities for each individual point, i, in the profile where;[4]

$$S_i = \sum_i w_i (y_i - y_{ci})^2 \qquad \text{-(2.11)}$$

where y_i is the observed intensity for the ith point and y_{ci} is the calculated intensty at the ith point, w_i is the weighting of the observables and is defined by;

$$w_i = \frac{1}{y_i} \qquad \text{-(2.12)}$$

Since observed intensity is not associated directly with a Bragg reflection, for an accurate profile to be achieved a reasonable starting model is required. The calculated intensity is therefore dependent on the structure factor $|F_{hkl}|^2$ values taken from the model, which are calculated as follows.

$$y_i = s \sum_{hkl} m_{hkl} L_{hkl} |F_{hkl}|^2 A_i G(2\theta_i - 2\theta_{hkl}) P_{hkl} T + y_{ib} \qquad \text{-(2.13)}$$

Where s is the scale factor, L_{hkl} is the lorentz-polarisation factor for the reflection (hkl), m_{hkl} is the multiplicity factor, A_i is the symmetry parameter, $G(\theta)$ is the reflection profile function, $2\theta_{hkl}$ is the calculated position of the Bragg peak, corrected for the zero point shift, P_{hkl} is the preferred orientation function, T is the absorption correction and y_{ib} is the background intensity at the ith step.

The agreement between the observed and calculated structures is measured by the goodness of fit factors. The factors are defined as;

(a) 'weighted profile' – R_{wp}

$$R_{wp} = \sqrt{\left[\frac{\sum_i w_i |y_i - y_{ci}|^2}{\sum_i w_i y_i^2}\right]} \qquad \text{-(2.14)}$$

This compares how well the structural model under refinement, accounts for relatively small and large Bragg peaks across the diffraction profile. The weighting factor is given by w_i

(b)'Profile R-factor' - R_p

$$R_p = \frac{\sum_i |y_i(obs) - y_i(calc)|}{\sum_i y_i(obs)} \qquad \text{-(2.15)}$$

(d) 'Expected' – R_{exp}

$$R_{exp} = \sqrt{\left[\frac{(N-P+C)}{\sum_i w_i y_i^2}\right]} \qquad \text{-(2.16)}$$

Which accounts for the statistical quality of the data and the number of variables used in the refinements where N is the number of profile points, P is the number of refinable parameters, C is the number of constraints used.

During the course of a structural refinement, the goodness of fit factor, χ^2, can be used to compare the quality of the data.

$$\chi^2 = \left(\frac{R_{wp}}{R_{exp}}\right)^2 \qquad \text{-(2.17)}$$

When a very accurate fit to the observed profile is achieved, a value of χ^2 close to one is achieved.

2.3. Magnetism.

An important part of materials characterisation is the observed magnetic behaviour of a material with the application of a field. When a material is placed into a magnetic field, H, it induces a magnetic moment per unit volume as given by;

$$M = \chi H \qquad \text{-(2.18)}$$

where χ is the magnetic susceptibility and M is the magnetization of the material. The density of the lines of force or magnetic flux, B, in the sample can be defined by equation 2.19.

$$B = H + 4\pi M \qquad \text{-(2.19)}$$

2.3.1. Magnetism in Bulk Materials.

Lenz's law states that the induced voltage is in a direction, which opposes the flux change producing it.[5] In an applied field electrons produce a tiny magnetic field as they orbit atoms. This magnetic field obeys Lenz's law in that this magnetic field opposes the applied field. This is known as diamagnetism and is observed in all materials with core electrons. Diamagnetism is normally the dominant observed property in materials that exhibit only electron pairs or closed shells. These materials characteristically show small negative values of magnetic susceptibility, χ. (Figure 2.4a)

The presence of unpaired electrons in a material leads to paramgnetism, where both the electron spin and the orbital angular momentum contribute to the observed magnetisation leading to a positive magnetic susceptibility and a tendency of these materials to attract magnetic field. (Figure 2.5(b))

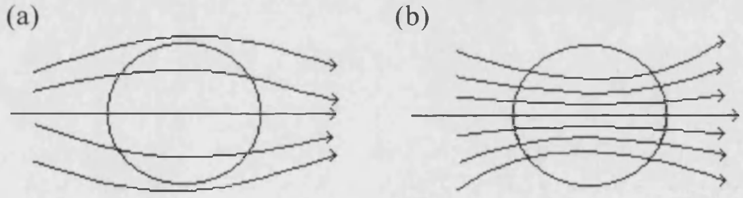

Figure 2.5. Schematic representation of magnetic field behaviour with a) Diamagnetic materials and b) Paramagnetic materials.

Magnetic susceptibility of an ideal paramagnet can be described by the Curie law, which is given by equation 2.20. Materials, which obey this law, yield a straight line for a plot of $1/\chi$ against temperature with an intercept of 0K.

$$\chi = \frac{C}{T} \qquad \text{-(2.20)}$$

Where C is the Curie constant.

However, Curie observed that some materials deviate from this law; this is due to the magnetic interactions. In systems with strong magnetic interactions at some critical temperature, the spins order in a long-range fashion. The types of magnetic order are summarised below.

Ferromagnetism.

Ferromagnetic ordering is observed in materials below the Curie temperature, T_C; the magnetic moments within domains are aligned in a parallel fashion giving rise to a net magnetic moment in that direction.

Antiferromagnetism.

Below the Néel temperature, T_N, the magnetic spins of neighbouring atoms order in an anti-parallel way.

Ferrimagnetism.

Ferrimagnetism usually occurs when two or more magnetic species are present in a lattice. The magnetic spins order in an antiferromagnetic way but since the magnitudes of the moments of the neighbouring atoms are different a resultant magnetisation is observed.

Materials which show order below a critical temperature have a temperature dependence of χ in the paramagnetic region that is given by the Curie-Weiss law.

$$\chi = \frac{C}{T + \theta} \qquad \text{-(2.21)}$$

where θ is the Weiss constant, and is the temperature at the intercept of the straight line plotted as $1/\chi$ against temperature. When the Weiss constant has a negative value it indicates antiferromagnetic interaction whereas a positive Weiss constant is indicative of ferromagnetic coupling. Susceptibility only fits the Curie-Weiss law in the paramagnetic region above the ordering temperature. Once a material becomes ordered the susceptibility behaves in a very complicated way and no longer has a unique value for a given field strength.[5]

The relationship between magnetic moment, μ, of a material and its magnetic susceptibility, χ, is given by;

$$\chi = \frac{N\mu_B{}^2\mu^2}{3kT} \qquad \text{-(2.22)}$$

where N is Avogadro's number, μ_B is the Bohr magneton, defined by equation 2.23, and k is the Boltzmann constant.

$$1BM = \frac{eh}{4\pi mc} \qquad -(2.23)$$

where e is the electron charge, h is Planck's constant, m is the electron mass and c is the velocity of light.

The magnetic properties of unpaired electrons are regarded as arising from two causes, electron spin and electron orbital motion. These can be related to the magnetic moment by equation 2.24.[6] However, for first row transition metal ions, it is more common to calculate effective magnetic moments using the spin only formula (Equation 2.25).

$$\mu_{S+L} = \sqrt{4S(S+1)+L(L+1)} \qquad -(2.24)$$

where L is the orbital angular momentum quantum number for the ion and S is the sum of the spin quantum numbers of the individual unpaired electrons.

$$\mu_s = g\sqrt{S(S+1)} \qquad -(2.25)$$

where g is the gyromagnetic ratio and usually has a value of about 2.00.

2.3.2. Mechanisms for magnetic exchange.

Superexchange is the mechanism which describes the interaction of magnetic moments through a nonmagnetic intermediary ion, such as O^{2-}. The simplest process by which coupling of spins occurs is illustrated in figure 2.6, where the localised electrons on two transition metal (TM) ions occupy orbitals which are directed at each other and are overlapping with the same p orbital of the intermediate ligand.[7] Antiferromagnetic coupling arises as a result of the electron occupying the d orbital on the TM pairs with the electron occupying the overlapping p orbital of the oxygen, since the Pauli exclusion principle states that for two electrons to occupy one orbital their spins must be paired.[6] This is demonstrated in NiO where the Ni^{2+} ion has 8d electrons with two of these electrons singly occupying the d_{z^2} and $d_{x^2-y^2}$ orbitals respectively. These orbitals are orientated so as to be parallel to the axes of the unit cell and therefore point directly at adjacent oxide ions. The unpaired electrons in the e_g orbitals of Ni^{2+} ions are able to couple magnetically with electrons in the p orbitals of the O^{2-} ions. The p-orbitals of the O^{2-} ion contain two electrons each, which are also coupled anti-parallel. This is known as 180° exchange.

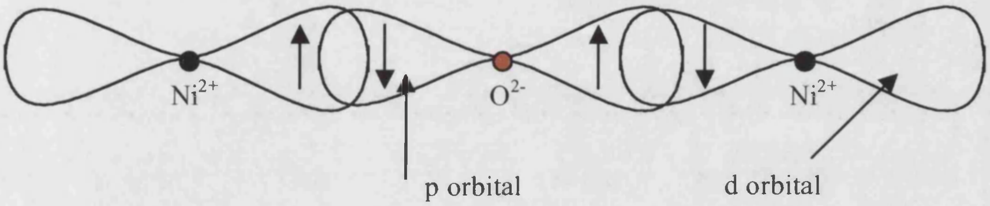

Figure 2.6. Antiferromagnetic coupling of spins of d electrons on Ni^{2+} ions through p electrons of oxide ions.

Ferromagnetic ordering comes about by a 90° exchange path as shown in figure 2.7(a). As with the 180° exchange mechanism the transfer occurs between the d-orbitals of the transition metal and the p-orbitals of the oxygen resulting in the overlap of two different p-orbitals, p_x and p_y with the corresponding d-orbitals of the two TM sites. This results in two electrons or p-holes present on the oxygen in the excited intermediate state (figure 2.7(b)). Depending on the two TM ions, the remaining p-electrons will either have spins which are parallel or antiparallel since Hund's rules suggest that the two electrons would have the lowest energy when they are parallel this means that the spins on the two TM ions must also be parallel and therefore ferromagnetic.

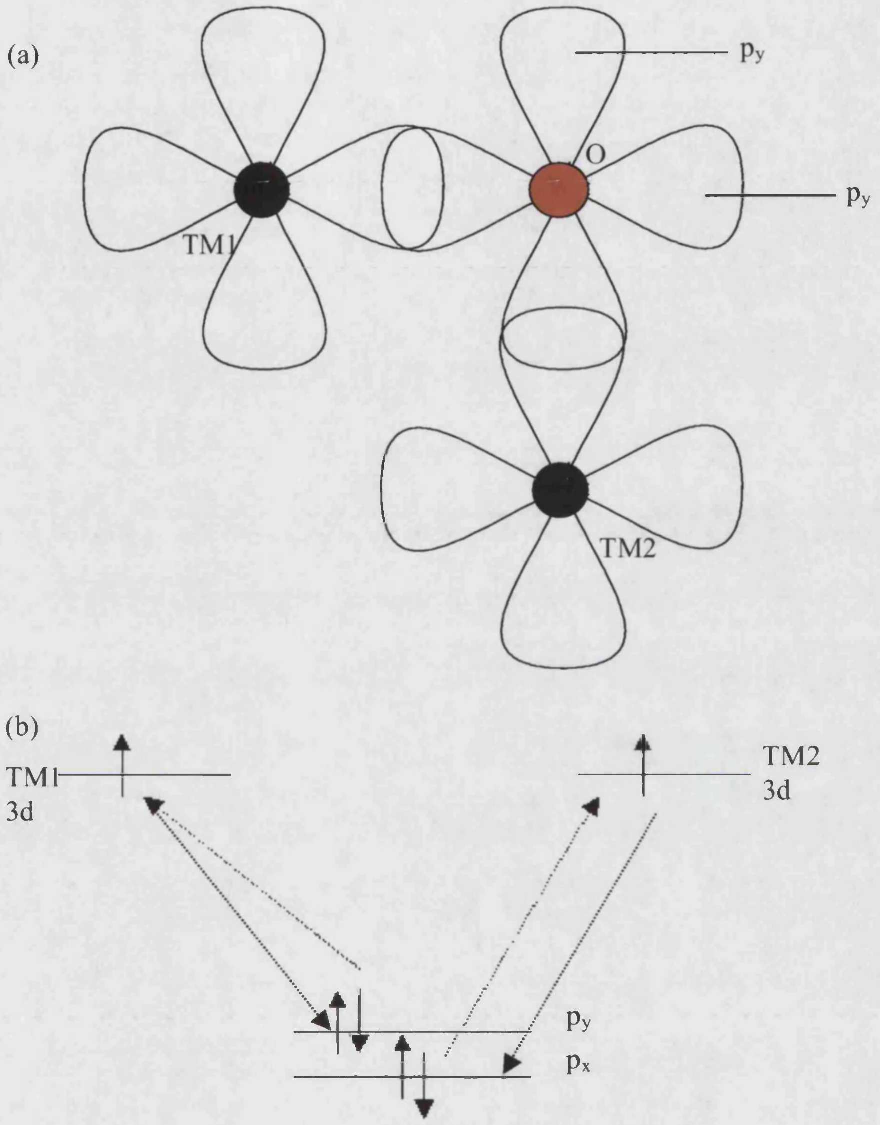

Figure 2.8. Schematic representation of 90° exchange resulting in ferromagnetic ordering (a) showing orbital overlap (b) showing electron interaction.

Double exchange is a mechanism for spin coupling arising from electron delocalization. The term double exchange was originally introduced in 1951 by Clarence Zener to explain the magneto-conductive properties of mixed-valence solid, notably doped Mn Perovskites.[8] Zener proposed a mechanism for translocation of an electron from one Mn to another through an intervening O^{2-}. As the oxygen p-orbitals are doubly occupied, the translocation had to proceed in two steps: the movement of an electron from oxygen to the "left" Mn followed by a transfer of a second electron from the "right" Mn into the (just) vacated oxygen orbital; hence the term double exchange. According to Hund's rules the metallic conduction, via hopping of e_g electrons, can only occur if the electrons of the t_{2g} orbitals for both the Mn^{3+} and Mn^{4+} ions are ferromagnetically aligned.

2.3.3. Measurement of Magnetic Properties.

DC magnetic susceptibility measurements were collected using a quantum design MPMS-7 SQUID instrument. Measurements were made in zero field cooled (ZFC) and field cooled (FC) environment over a temperature range of 1.8 to 300K. Measurements were typically collected in applied magnetic fields of either 100 or 1000G.

2.3.4. SQUID Magnetometer

SQUID (Superconducting QUantum Interference Device) instruments are capable of sensitive magnetisation measurements including the study of single magnetic particles.[9] A SQUID consists of two superconductors separated by thin insulating layers to form two parallel Josephson Junctions. The current in the SQUID device oscillates with the changes in phase at the two junctions, which depends upon the change in the magnetic flux. Counting the oscillations allows you to evaluate the flux change, which has occurred. The two Josephson Junctions are superconductors separated by a thin insulating layer small enough to allow the tunneling of Cooper pairs of electrons through the junction. In a SQUID device the magnetic field produced by the sample is measured by means of a bridge circuit consisting of a primary coil and two secondary coils wound in opposition and connected in series. If the two secondary coils were perfectly balanced the induced voltage would exactly cancel out. Introducing a sample into one of the coils unbalances the bridge, and results in a net current. This current is used to induce a field across the SQUID, causing the critical current to fluctuate. A constant biasing current is being passed through the ring, so the voltage across the ring will fluctuate and this is the quantity which is measured, whilst moving the sample through the pickup coil. The field inducing the current in the pickup loop is proportional to the magnetic moment of the sample divided by the cube of the distance between the sample and the loop. The relationship of the voltage across the SQUID and this distance allows the calculation of the dipole moment of the sample and hence, the magnetization and susceptibility of the sample to be determined.

2.4. Conductivity Measurements.

Conductivity measurements were collected using the electronic properties probe on an Oxford Instruments MagLab^{2000} system. The standard four probe technique was employed. A constant current was passed across a sintered pellet of the sample, of approximate dimension 1cm x 0.5cm x 0.5cm, by means of copper wire attached to the pellet using gold paint. The potential difference was measured between the two inner wires and hence the measurement of the resistance of the sample thus allowing the calculation of resistivity and conductivity from equations 2.26 and 2.27

$$\rho = \frac{RA}{l} \qquad \text{-(2.26)}$$

where ρ is the resistivity, R is the resistance, A is the area of the pellet and l is the length.

$$\sigma = \frac{1}{\rho} \qquad \text{-(2.27)}$$

where conductivity is given by σ.

Since the materials in this thesis are semiconducting the band gap can be calculated from the Arrhenius relationship give by;

$$\sigma = A\exp\left(\frac{-E}{RT}\right) \qquad \text{-(2.28)}$$

Where E is the activation energy, R is the gas constant and T is the absolute temperature.

2.5. Thermal Analysis.

Compositional information was collected for the materials reported here using the Shimadzu TGA 50 analyser over a temperature range of room temperature to 950°C at a heating rate of 10°C per minute in an inert atmosphere of N_2. DSC data were also collected from room temperature to a maximum temperature of 600°C.

Thermal analysis may be defined as the measurement of changes in the physical and chemical properties of a substance as a function of either temperature or time, whilst the substance is subjected to a controlled temperature regime.[10] However, in reality the term 'Thermal Analysis' is used to describe changes in enthalpy (DSC), heat capacity (DTA), mass (TG) and coefficient of thermal expansion as a function of temperature. All these techniques may be used separately or combined using a simultaneous thermal analysis instrument. A generalized thermal analysis instrument is shown in figure 2.9.

The two most widely recognized techniques are Thermogravimetry (TG) and Differential Thermal Analysis (DTA). All experiments can be undertaken in various atmospheres such as a reducing atmosphere of N_2,

Thermogravimetry (TG) measures the change in sample weight as a function of either temperature or time. The simplest example is that of a single stage decomposition route as illustrated in figure 2.8. The sample is heated at a pre-selected constant rate. Prior to the onset of decomposition the weight of the sample is constant and can be denoted as W_i. As the temperature begins to increase the sample begins to decompose between T_i and T_f. Above T_f the sample returns to a constant weight, W_f. The total weight loss, Δw is equivalent to the difference between W_i and W_f, The weights W_i, W_f and ΔW can be used to derive quantitative information on the compositional changes during the experiments.[6] It is worth noting that both temperatures T_i and T_f are dependent on variables such as heating rate, particle size and the atmosphere of the sample chamber. Changes in these variables can have a dramatic effect often shifting the decomposition temperatures by hundreds of degrees.

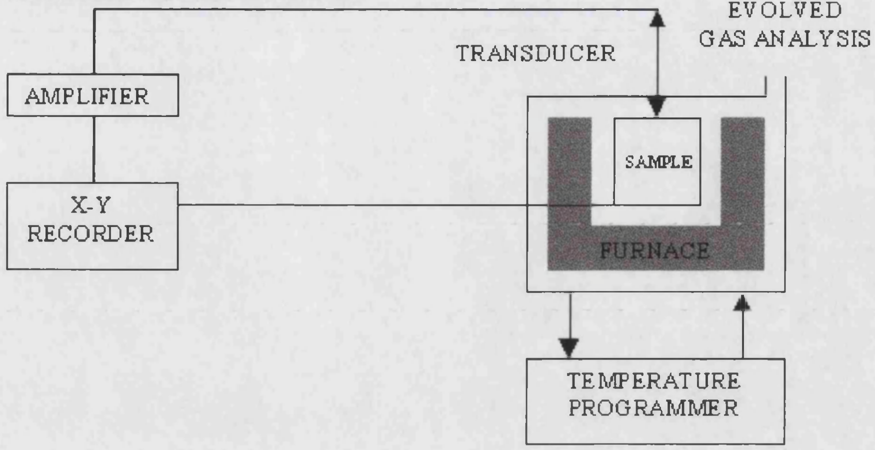

Figure 2.8. Generalized Thermal Analysis Instrument.[10]

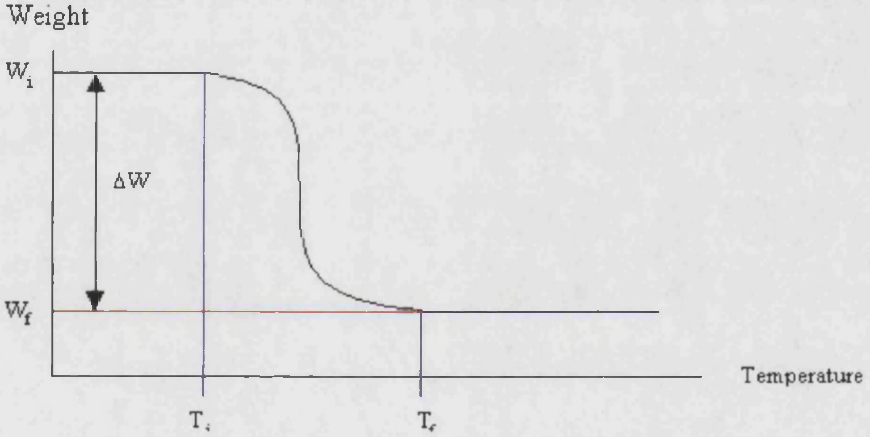

Figure 2.9. Schematic Representation of a Typical Single Step Decomposition Reaction.[6]

Differential Thermal Analysis (DTA) records the difference in temperature between an inert reference material and the sample as a function of temperature. The temperature of both the reference and the sample are the same until a thermal event such as melting occurs, in which case the temperature of the sample will either lag that of the reference in endothermic reactions or lead it, as is the case for exothermic events. In a DTA experiment the sample and the reference are placed side by side in a heating block. Identical thermocouples are attached to the sample and the reference and connected back to back. When the sample and the reference are at the same temperature the net output from the pair of thermo couples is zero. When the sample undergoes a thermal event a temperature difference, ΔT, exists between the sample and the reference, which is detected by a net voltage across the thermocouples. A third thermocouple is used to monitor the temperature of the heating block and the results are presented as a plot of ΔT vs T. The temperature of the peak is taken at either the point at which deviation from the baseline begins, T_1, or as the temperature at the tip of the peak, T_2.

2.6. EDX.

Additional compositional information was collected using the JEOL CF35 Scanning Electron Microscope fitted with a 120KV EDX detector. Whilst oxygen content could not be accurately determined by EDX, a Mn:Cation ratio could be determined and hence the composition.

2.7. References.

(1) www.ncnr.nist.gov.

(2) *Introduction to neutron scattering*, Neutron Summer School, Rutherford Appleton Laboratories, UK, **2001**.

(3)R. M. Ibberson, W. I. F. David, K. S. Knight. *The High Resolution Powder Diffractometer (HRPD) at ISIS - A User Guide*, Rutherford Appleton Laboratories, **1992**.

(4) H. M. Rietveld, *Journal of Applied Crystallography*, **1969**, *2*, 665.

(5) D. Jiles, *Introduction to Magnetism and Magnetic Materials*; Chapman and Hall: London, **1994**.

(6) A. R. West, *Basic Solid State Chemistry*; John Wiley and Sons: Chichester, **1997**.

(7) D. Khomskii, *Electronic Structure, Exchange and Magnetism in Oxides*, Groningen University, **1999**.

(8) C. Zener, *Physical Review*, **1951**, *82*, 403.

CHAPTER 2: Theory and Experiment

(9) M. Hanson, Z. G. I., C. Johansson, Y. Kislinski, P. Larsson, *Journal of Magnetism and Magnetic Materials*, **1998**, *177-181*, 519.

(10) G.Lombadi, *For Better Thermal Analysis*; ICTA, **1980**.

3.1. Introduction.

Hollandite in particular has received extensive attention due its possible applications in, for example, molecular sieves, catalytic activity and as a cathode active material.[1] Hollandite was first described by Fermor in 1909 and early studies concentrated on the naturally occurring forms of the mineral, $Ba_xMn_8O_{16}$. These are found as needle-like crystals in deep-sea nodules and in the soil of certain regions.[2-5] A comprehensive structural study of the naturally occurring hollandite, corondite, cryptomelane and related systems was conducted by Byström and Byström in 1950 and continued by Mukherjee in 1960.[3,4] Nistor *et al* investigated defects within these natural materials using electron diffraction and high resolution electron microscopy.[5] The main defects observed were uniformly arranged crystallographic shear planes, often leading to incommensurate diffraction patterns. They also observed a phase change in hollandite materials at 330°C, contrary to other work, which claimed that these materials are relatively insensitive to heat up to 400°C, before further heating causes a reduction of Mn^{4+} with loss of oxygen.[2]

Hollandite or cryptomelane-type manganese oxides have a one-dimensional structure consisting of 4.6Å x 4.6Å tunnels as a result of (2 x 2) MnO_6 edge shared octahedral arrangement (§1). Synthesis is enabled by using large metal cations such as K^+, Rb^{2+}, Cs^+ and Ba^{2+} as a template, which reside in the tunnel along with small amounts of water to stabilise the structure,[6,7] see figure 3.1. In a typical hollandite structure, such as that of potassium, the A cation is surrounded by eight oxygen ions at a distance of 2.74Å, forming a cube and at a greater distance (3.31Å) by four oxygen ions forming a square at the same z level as the A ion. The B ion is surrounded by six oxygen ions forming an octahedron, and with a mean oxygen distance of 1.98Å.[3] Traditionally, the names of hollandite-type materials refers to the cation present in the tunnel sites, therefore hollandite contains Ba^{2+} cations, cryptomelane is K^+, corondite is Pb^{2+} and marjorite is Na^+. Whilst some authors still refer to the original nomenclature most just use the mineral name hollandite to refer to any compounds with the (2 x 2) transition metal oxide structural motif, irrespective of the tunnel/template cation.

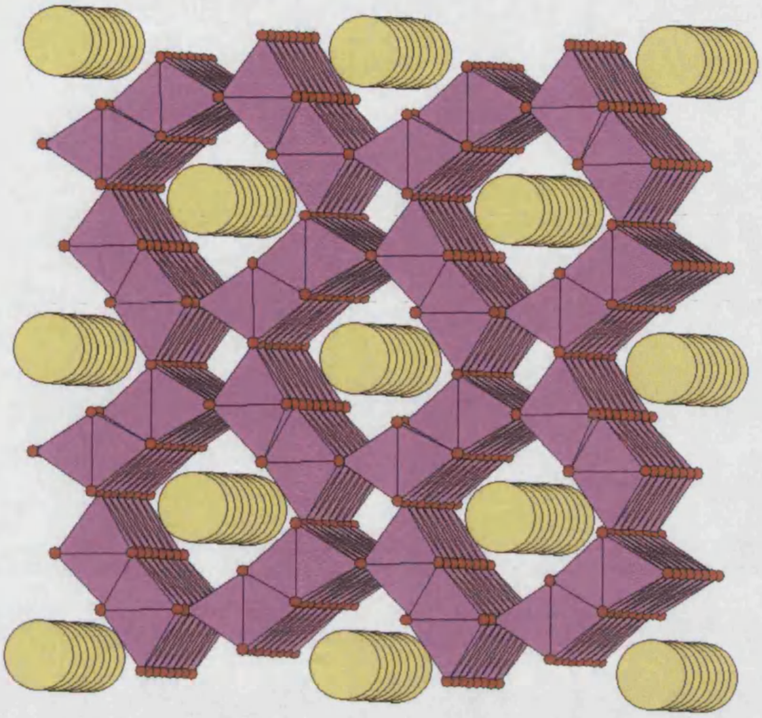

Figure 3.1. Schematic representation of the (2 x 2) hollandite structure, where pink squares represent the MnO_6 octahedron, yellow spheres are the potassium cation and red spheres are the oxygen atoms.

Potassium hollandite (cryptomelane) is most readily synthesised reflecting the effectiveness of the K^+ ion in stabilising the structure. It is prepared by sol-gel methods and has the approximate stoichiometry of $K_{0.125}MnO_2$ (KMn_8O_{16}). The average manganese oxidation state of 3.88 reflects mixed valency of Mn (IV) with minor amounts of Mn(III).[7] Duan *et al* prepared octahedral molecular sieve materials (OMS-2), whereby the 2 denote hollandite and OMS-1 is todorokite, of composition KMn_8O_{16} by sol-gel methods. These materials are highly crystalline with pronounced thermal stability in relation to materials produced by reflux or hydrothermal alleration methods.[8] The possibility of using these materials as cathodes in lithium battery technology has led to many authors studying the electrolytic cyclability of lithium intercalation and deintercalation.[1,6,9-12] Since it has been suggested that the presence of a large counter ion limits these applications, research into the possibility of synthesising this material without the need of large template ions or with subsequent removal of the tunnel ion is therefore important. Bach *et al* and other authors have looked at Li cyclability on a potassium deficient form of hollandite, with a formula of $K_{0.062}MnO_2$ after acid leaching but complete removal does not seem to be favourable.[9,10] Li ion insertion occurs in one electrochemical step and has a specific capacity 280 $AhKg^{-1}$over a charge range of 4.1-2.3V. Preparation of H^+ hollandite was achieved by H_2SO_4 treatment of Li_2MnO_3 at 90°C and shows good electrochemical cycling properties.[6] The hollandite structure has also been obtained by reacting $LiMnO_4$ with $Mn(NO_3)_2$ solution, which contains only a small amount of foreign cations (Li^+).[9] Electrochemical studies showed this material to have a reversible discharge capacity of 230mAh/g from 3.8 to 2.0V. This capacity initially drops slightly upon cycling then stabilizes, with no damage to the structural integrity of the material. It has been suggested that not only does the lithium insert into the larger (2 x 2) tunnels but also into the smaller (1 x 1) pyrolusite channels.[13] Hollandite with hydronium as the tunnel counter ion has also been synthesised by oxidation of $MnSO_4$ with ozone in a concentrated sulphuric acid solution.[1] The hydronium ion can be replaced with hydrated lithium and then dehydrated at 300°C.

Small organic ions such as $(NH_4)^+$ can also act as the template cation. Feng *et al* prepared NH_4 hollandite by first preparing NH_4 birnessite by the ion exchange reaction of sodium birnessite with 1M NH_4Cl. The resulting layered material was then hydrothermally treated with $(NH_4)_2SO_4$-H_2SO_4 solution under autogenous pressure to transform the layered material to the NH_4 hollandite form. The $(NH_4)^+$ ions can be easily removed from the tunnel site and Li^+ ion insertion is achieved by heating with LiOH.[6] Ohzuku *et al* also reported a synthetic NH_4^+ Hollandite with the formulae of $(NH_4)_{0.17}MnO_2$, $(NH_4)_{1.41}Mn_8O_{16}$.[14] Discharge curves in the voltage range 2-3.4V were investigated giving discharge capacities of 170-220mAh/g.

Magnetic and electronic studies of hollandite and the related todorokite material (3 x 3) have been conducted. Suib *et al* measured AC + DC magnetic susceptibilities of octahedral molecular sieves with a mixed manganese oxidation state, namely for todorokite (OMS-1), prepared from birnessite (OL-1) and for potassium hollandite (OMS-2) both materials contain manganese in a mixed 3+/ 4+-enviroment.[15] Comparison of field cooled (FC) and zero field cooled (ZFC) data collected showed diverging data below the transition temperature of 35K indicating a clear irreversibility in magnetic character. Data collected over a range of frequencies showed a decrease with increasing frequency of the real or in-phase component of the magnetic susceptibility (χ') suggesting spin glass behaviour. Four probe DC resistivity measurements performed by De Guzman *et al* showed hollandite to follow conventional

Arrhenius behaviour in contrast to both birnessite and todorokite materials which show deviations from this at low temperature.[16]

It has been reported that hollandite (without a tunnel ion) is a good microwave absorber due to its effective coupling with the MnO_2. Microwave induced oxygen evolution is fast and uniform and leads to oxygen deficient products. This is reversible and the material shows a strong tendency to recombine with oxygen and water.[17,18] However, this product forms Mn_2O_3 above 425°C compared to 600°C with conventional heating. Duan *et al* suggested that the insertion of 2+ ions into the Hollandite structure is not possible due to relative thermal stabilities,[8] however, the possibility of intercalating Cu^{2+} with relative concentrations of 0.0171%, 0.0245% and 0.0334% was achieved by adding $CuSO_4 \cdot 5H_2O$ or $Cu(NO_3)_2$ to one of the initial solutions prior to sol-gel synthesis.[19] It was reported that resistivity increases as the concentration of Cu with a commensurate decrease in the thermal stability. In the synthesis of Cu-OMS-2, the sol –gel method was not advantageous compared to the reflux method in incorporating Cu^{2+} ions. Paramelaconite, a copper oxide, is readily formed in the sol-gel process based on XRD analysis of the product. $Ba_x(M^{3+}Ti^{4+})_8O_{16}$, also known as SYNROC, was evaluated for the immobilisation of radioactive waste.[20,21] Powder neutron diffraction established how various trivalent ions such as Fe, Al and Ga alter the crystal structure and predispose it to radwaste substitution. Some other materials of interest with the hollandite structure are $K_4Cu_2Fe_7V_7O_{32}$, $KNi_{0.5}Fe_{3.5}V_{3.5}O_{16}$, $KCo_{0.5}Fe_{3.5}V_{3.5}O_{16}$ and $K_{0.54}Mg_{0.77}Ti_{7.28}O_{16}$, some with ferromagnetic ordering above room temperature.[22-24]

The work in this chapter reports the synthesis of potassium hollandite by two different methods resulting in slight difference in composition and observed properties. The removal of the K^+ counter ion has been achieved by acid leaching and an intercalation study has been carried out. The effects of intercalation on the structural, magnetic and electronic properties are discussed.

3.2. Synthesis.

Two preparations of Potassium hollandite, with an intended composition of $K_{0.125}MnO_2$ were prepared by two different methods described by Ching *et al* (K1) and Duan *et al* (K2):[7,8]

Preparation of K1: Approximately 6.7mmol of solid Fumaric acid was added to a stirring solution containing 20mmol of $KMnO_4$. The reaction proceeded with mild effervescence followed by the appearance of a brown sol within a few minutes. After 30 minutes the sol evolved into a floculant brown gel. The gel was allowed to settle and after 1 hour was isolated by filtration and washed 4 times with 100mL of water. A black xerogel was formed after drying overnight at 110°C. Calcinations of the xerogel at 450°C for 2 hours yields potassium hollandite as a hard black solid.

Preparation of K2: 0.38g of Maleic acid was added to a 10mmol $KMnO_4$ solution and the mixture stirred for 30 minutes at room temperature. As with the K1 preparation a dark brown sol is formed which starts to gel after approximately 5 minutes. The water was decanted off and the resultant gel was washed with 4 alliquots of distilled/deionised water and then left to filter under vacuum for 20 minutes before being heated for 10 hours at 100°C and subsequently calcined at 450°C for 4 hours.

Products were characterised by x-ray diffraction using the Siemens D500 x-ray diffractometer. The potassium was removed from within the tunnel by stirring the prepared hollandite (sample K1) with a 1 molar solution of HNO_3 overnight at room temperature.[9] In the insertion study the treated hollandite was reacted with LiI, NH_4I, CsI and CuI_2 based on the equation given in 3.1. All reactions were done with an excess of metal iodide and iodine was liberated instantaneously in the reaction.

$$xLiI + K_{0.125-y}MnO_2 \rightarrow \tfrac{1}{2}\, xI_2 + Li_xK_{0.125-y}MnO_2 \qquad -(3.1)$$

3.3. Results and Discussion.

3.3.1. Elemental Analysis/EDX.

Elemental Analysis and EDX results for these samples are given in table 3.1. Complete removal of the potassium involves the complete oxidation of all the Mn^{3+} to Mn^{4+}. It is clear from these results that this does not occur and only small amounts of K are deintercalated from the framework, which reflects the strong K-framework interactions and the poor mobility of the K ions.[9,14] Intercalation is consistent with reported data that the levels of alkali metal insertion is inversely related to increasing radii as proposed by Ching *et al.*[7]

This gives the following selectivity's order with increasing radii as shown in figures 3.2 (a) and (b).

$Li_{0.18} > Cu_{0.08} > K_{0.125} = NH_4 > Cs_{0.04}$

Increasing ionic radii →

Table 3.1. Results obtained by EDX and Elemental Analysis for the composition of K containing hollandite structures.

Sample	Elemental Analysis	EDAX Analysis	K Wt %
$K_{0.125}MnO_2$ (K1)	-	$K_{0.120(1)}MnO_2$	5.0
(K2)	-	$K_{0.0800(1)}MnO_2$	3.4
$K_{0.125-y}MnO_2$	-	$K_{0.0900(1)}MnO_2$	3.8
$Li_xK_{0.125-y}MnO_2$	$Li_{0.180(2)}K_{0.07}MnO_2$	$Li_xK_{0.0800(1)}MnO_2^*$	4.0
$(NH_4)_xK_{0.125-y}MnO_2$	-	$(NH_4)_xK_{0.0700(1)}MnO_2^*$	2.9
$Cu_xK_{0.125-y}MnO_2$	-	$Cu_{0.0800(1)}K_{0.0900(1)}MnO_2$	3.5
$Cs_xK_{0.125-y}MnO_2$	-	$Cs_{0.0400(1)}K_{0.100(1)}MnO_2$	3.9

* Li and NH_4 content could not be analysed using the EDX method. TGA data suggests a NH_4 content of approximately 0.07 and is consistent with previous data reported for NH_4^+ hollandite.[12]

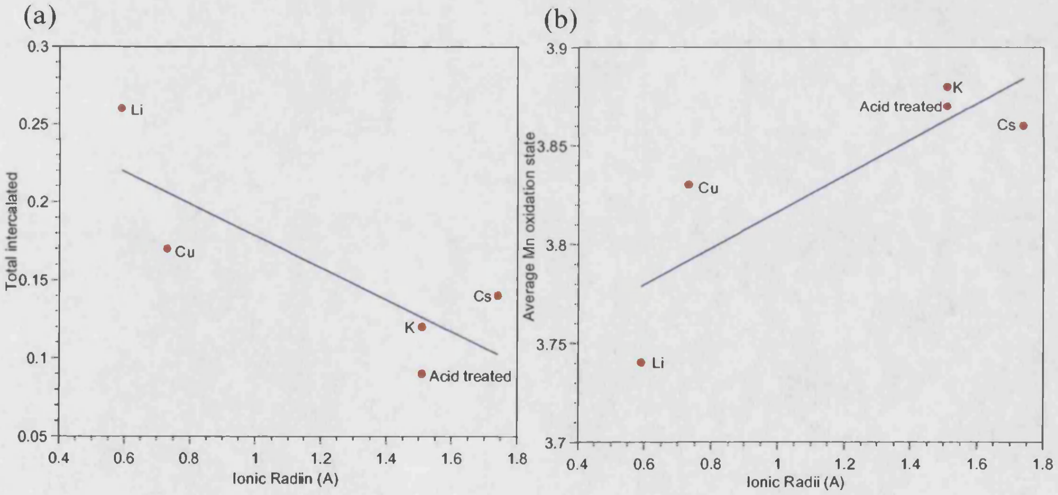

Figure 3.2. Plots showing (a) decreasing total amount intercalated and (b) increasing average manganese oxidation state as a function of ionic radii.

3.3.2. Thermal Analysis.

All calculations of the TGA data were based on the compositions determined from EDX analysis. Table 3.2 summarises the decomposition routes for potassium hollandite and its treated analogues. Samples K1 and K2 undergo a three-step decomposition route as illustrated by equations 3.2 to 3.4 (Figures 3.3-3.4). The onset and endset temperatures for both are similar, though the potassium deficient sample, K2, shows additional water content, as shown by the larger weight loss of 3.301% in the first step compared to that of the $K_{0.12}MnO_2$, K1 sample, of 1.409%. DSC data collected shows that a broad endothermic trough followed by a slight exothermic hump accompanies this loss of water.

X-ray analysis of the material obtained after the second step can be identified as hollandite. However a weight loss of approximately 3% is observed, has been suggested that this is equivalent of loss of oxygen, as some of the Mn^{4+} are reduced to Mn^{3+} to give an average manganese oxidation state of approximately 3.5.[7] This loss is marked in all 3 samples with a sharp endothermic peak. Step 3 occurs above 700°C and is due to loss of oxygen as the potassium Hollandite decomposes to form the more stable $K_2Mn_4O_8$ phase and Mn_2O_3. These results demonstrate an extremely high thermal stability of >700°C.

$$K_{0.12}MnO_2 \bullet xH_2O \rightarrow K_{0.12}MnO_2 + xH_2O \qquad -(3.2)$$

$$K_{0.12}MnO_2 \rightarrow K_{0.12}MnO_{2-x} + {}^{x}/_{2}O_2\uparrow \qquad -(3.3)$$

$$K_{0.12}MnO_{2-x} \rightarrow 0.06K_2Mn_4O_8 + 0.38Mn_2O_3 + 0.108O_2\uparrow \qquad -(3.4)$$

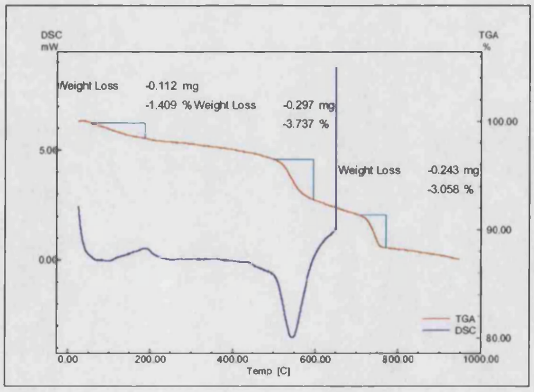

Figure 3.3. TGA/DSC Trace showing the three step decomposition route and percentage weight losses for $K_{0.12}MnO_2$ (K1) in an inert atmosphere of nitrogen.

Table 3.2. Decomposition routes and percentage weight losses for $K_{0.125}MnO_2$ *and intercalated species in an inert atmosphere of nitrogen.*

	Sample	K1	K2	Acid Treated	
1st Step	Onset (°C)	53.91	43.90	43.47	
	Endset (°C)	186.34	193.10	192.22	
	% Wt loss	1.41	3.30	3.52	
2nd Step	Onset (°C)			369.82	
	Endset (°C)			432.56	
	% Wt loss			0.84	
3rd Step	Onset (°C)	500.22	460.04	456.34	
	Endset (°C)	596.26	562.55	567.15	
	% Wt loss	3.74	3.31	4.32	
4th Step	Onset (°C)	703.42	692.97	717.42	
	Endset (°C)	772.16	799.04	777.12	
	% Wt loss	3.06	3.39	3.03	
		Li	NH_4	Cu	Cs
1st Step	Onset (°C)	42.23	49.02	44.34	43.36
	Endset (°C)	202.61	151.99	199.53	165.21
	% Wt loss	4.44	1.68	4.16	2.45
2nd Step	Onset (°C)				335.80
	Endset (°C)				409.93
	% Wt loss				1.25
3rd Step	Onset (°C)	371.84	421.81	464.92	491.67
	Endset (°C)	567.15	582.09	581.69	617.08
	% Wt loss	5.72	7.07	4.20	2.99
4th Step	Onset (°C)	673.62	693.16	685.82	697.29
	Endset (°C)	779.69	645.91	750.02	790.71
	% Wt loss	2.10	2.14	2.08	3.40

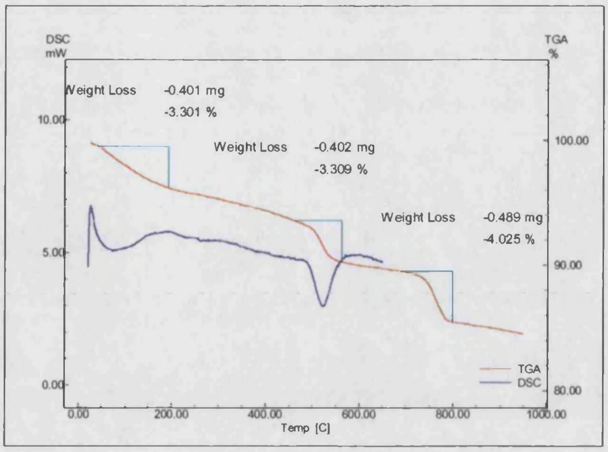

Figure 3.4. TGA/DSC Trace showing the three step decomposition route and percentage weight losses for $K_{0.08}MnO_2$ (K2) in an inert atmosphere of nitrogen.

The acid treated sample, $K_{0.09}MnO_2$, decomposes in a similar way to the parent sample. However, an additional decomposition begins at 369°C this is assigned to the breakdown of H_3O^+, ion exchanged into the sample during the acid leaching procedure. A weight loss of 0.839% is observed consistent with the deintercalation of 0.04 K^+ ions and the intercalation of 0.04 H_3O^+ ions. Decomposition then proceeds as observed for the $K_{0.12}MnO_2$ sample.

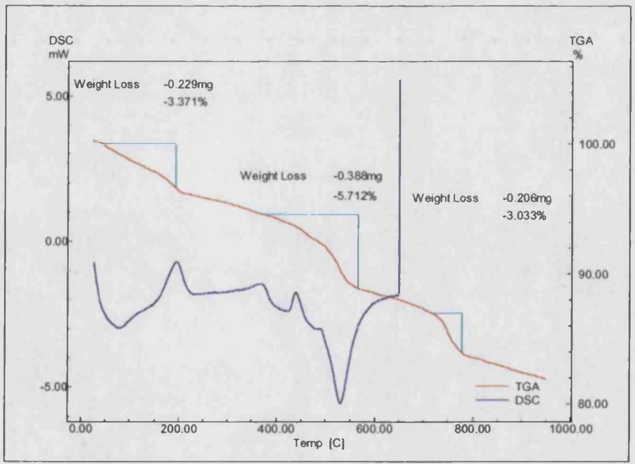

Figure 3.5. TGA/DSC Trace showing the three step decomposition route and percentage weight losses for the acid leached sample, $K_{0.09}MnO_2$, in an inert atmosphere of nitrogen.

$Li_{0.18}K_{0.08}MnO_2$ shows a three-step decomposition route as exhibited by $K_{0.12}MnO_2$. Step 1 is marked by a broad endothermic peak and is due to loss of water from within the tunnel sites (figure 3.6). Step 2 is marked by a sharp exothermic peak followed by a large endothermic trough in the DSC with a percentage weight loss of 5.721% this may be due to loss of a small amount of H_3O^+ from the tunnel sites and loss of oxygen due to the reduction of Mn^{4+} to Mn^{3+} and the breakdown of the hollandite to Li_2MnO_3, $K_2Mn_4O_8$ and Mn_2O_3. Decomposition of $Li_{0.18}K_{0.08}MnO_2$ occurs at a lower temperature and is hence less stable than the potassium hollandite due to the presence of the intercalated Li, which results in more than one cation site in the tunnel.

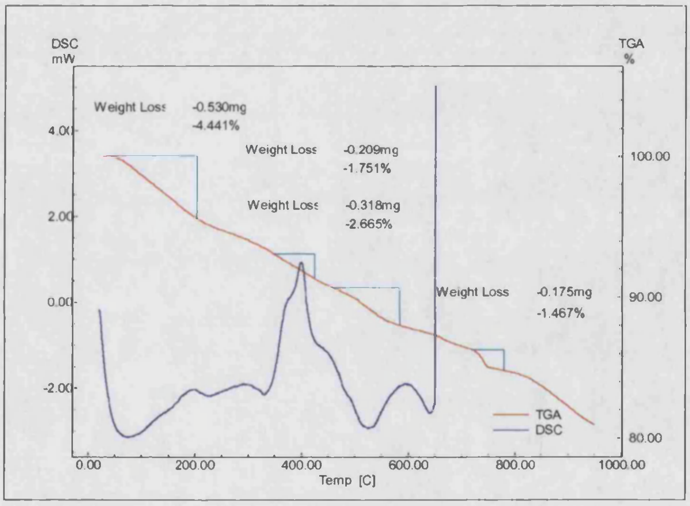

Figure 3.6. TGA/DSC Trace showing the three step decomposition route and percentage weight losses for $Li_{0.18}K_{0.08}MnO_2$in an inert atmosphere of nitrogen.

The characteristic three-step decomposition is again observed for $(NH_4)_xK_{0.07}MnO_2$, shown in figure 3.7, which is again attributable to loss of water from the tunnels, followed by loss of the NH_4 and O_2 and finally loss of O_2 as the hollandite breaks down to form $K_2Mn_4O_8$. This is shown by equations 3.5-3.7. The presence of nitrogen was confirmed by elemental analysis, however a quantitative amount could not be determined. The value of 0.078 is consistent with what you would expect to intercalate based on the ionic radii of NH_4 and is similar to that reported by Feng *et al.*[7] The observed thermal stability of this material fits the observed pattern shown in figure 3.10.

$$(NH_4)_{0.078}K_{0.07}MnO_2{\bullet}0.087H_2O \rightarrow (NH_4)_{0.078}K_{0.07}MnO_2 + 0.087H_2O\uparrow \qquad \text{-(3.5)}$$

$$(NH_4)_{0.078}K_{0.07}MnO_2 \rightarrow K_{0.07}MnO_2 + 0.078NH_4\uparrow + 0.1575O_2\uparrow \qquad \text{-(3.6)}$$

$$K_{0.07}MnO_2 \rightarrow 0.035K_2Mn_4O_8 + 0.43Mn_2O_3 + 0.0575O_2\uparrow \qquad \text{-(3.7)}$$

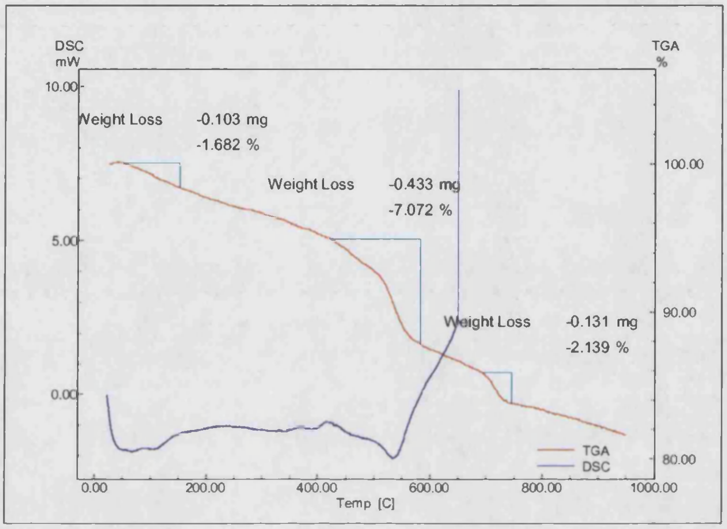

Figure 3.7. TGA/DSC Trace showing the three step decomposition route and percentage weight losses for $(NH_4)_{0.078}K_{0.07}MnO_2$ *in an inert atmosphere of nitrogen.*

This three step decomposition profile is repeated for $Cu_{0.08}K_{0.09}MnO_2$ (figure 3.8) with the Final decomposition products being $K_2Mn_4O_8$, Mn_2O_3 and Cu_2O. The presence of Cu_2O and the average manganese oxidation state after decomposition in step 2 suggests that copper is in the +1 oxidation state. This is consistent with the data reported by Duan *et al* which suggested that the insertion of 2+ ions into sol-gel synthesised hollandite was not possible due to relative thermal stabilities.[9] It is likely that the reported[19] successful intercalation of Cu^{2+} into the tunnel structure may actual be facilitated by initial reduction of Cu^{2+} to Cu^{+}.

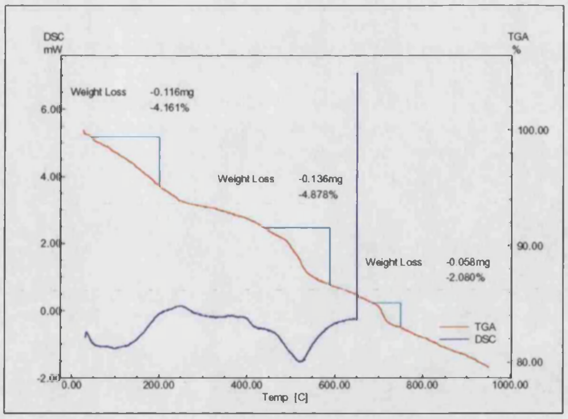

Figure 3.8. TGA/DSC Trace showing the three step decomposition route and percentage weight losses for $Cu_{0.08}K_{0.09}MnO_2$ in an inert atmosphere of nitrogen.

As with the acid treated sample, the decomposition route for $Cs_{0.04}K_{0.1}MnO_2$ proceeds in four steps (figure 3.9). The second step is attributable to the loss of H_3O^+, which suggests that the intercalation of Cs is negligible. This would be expected since the ionic radii of Cs is just slightly too large to fit comfortably into the tunnel site. The relatively small amount observed by EDX suggests that some Cs ions are bound to the surfaces.

Complete formulae for all samples including waters of crystallization are given in table 3.3. A plot of thermal stability against total cation content is plotted in figure 3.10 and quite clearly shows a decrease in thermal stability with increasing amount of intercalated cation and hence with decreasing ionic radii of the intercalated species.

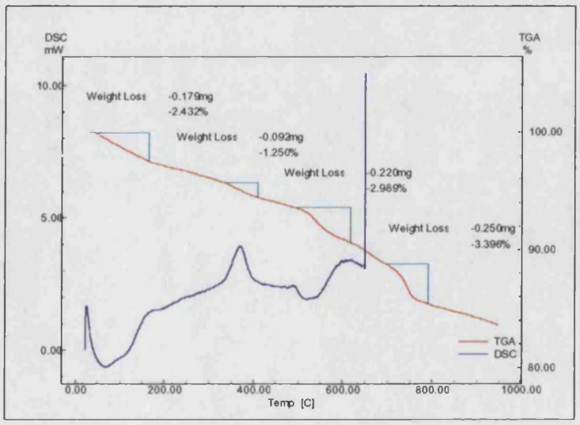

Figure 3.9. TGA/DSC Trace showing the three step decomposition route and percentage weight losses for $Cs_{0.04}K_{0.1}MnO_2$ in an inert atmosphere of nitrogen.

Table 3.3. Complete formula and corresponding molecular weights for all samples.

Sample	Formulae	Molecular Weight
$K_{0.12}MnO_2$ (K1)	$K_{0.12}MnO_2 \bullet 0.0725H_2O$	92.936
$K_{0.09}MnO_2$ (K2)	$K_{0.08}MnO_2 \bullet 0.171H_2O$	93.146
$K_{0.08}MnO_2$ (acid leached)	$K_{0.09}(H_3O)_{0.04}MnO_2 \bullet 0.221H_2O$	94.514
$Li_{0.18}K_{0.08}MnO_2$	$Li_{0.18}K_{0.08}O_2 \bullet 0.388H_2O$	98.345
$(NH_4)_{0.078}K_{0.07}MnO_2$	$(NH_4)_{0.078}K_{0.07}MnO_2 \bullet 0.087H_2O$	94.273
$Cu_{0.08}K_{0.09}MnO_2$	$Cu_{0.08}K_{0.09}MnO_2 \bullet 0.231H_2O$	99.702
$Cs_{0.04}K_{0.10}MnO_2$	$Cs_{0.04}K_{0.10}MnO_2 \bullet 0.205H_2O$	99.857

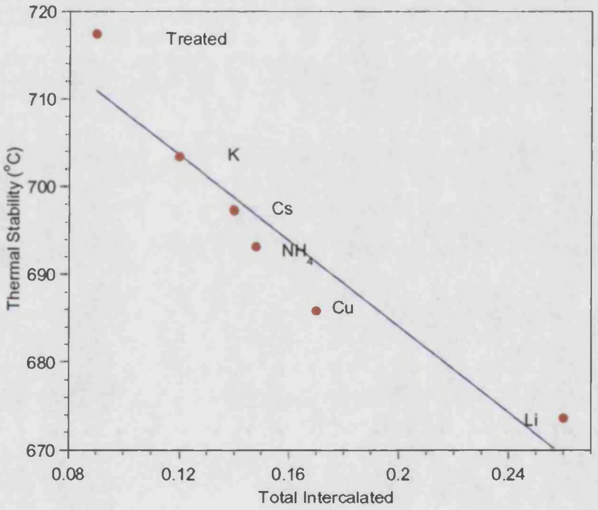

Figure 3.10. Increasing thermal stability as a function of the total amount intercalated.

3.3.3. Diffraction.

3.3.1. Neutron diffraction.

Neutron data were collected using HRPD for $K_{0.12}MnO_2$ (K1) at temperatures of 4K and 80K, which were chosen as they are above and below the magnetic transition and the difference could show the magnetic scattering. However, no perceivable differences can be observed between the data collected from the 90° detector bank at these two temperatures, suggesting a spin glass state and no long range order consistent with measurements on other systems. The GSAS refined structure at 80K and 4K are given in figure 3.11 and 3.12 respectively. The refined lattice parameters, goodness of fit factors and atom positions are given in table 3.4 and 3.5 respectively for both refinements. The observed potassium fractional occupancies of 0.49 giving the formula as $K_{0.125(2)}MnO_2$ suggests that it should be possible to further intercalate the tunnels with K, a fractional occupancy of 1 would result in a formula of $K_2Mn_8O_{16}$ or $K_{0.25}MnO_2$. However whilst an average manganese oxidation state of +3.75 is realistic this would result in two potassium ions per formula unit cell. This would produce very large coloumbic repulsion between the K^+ ions, and is not energetically favourable (figure 3.13).

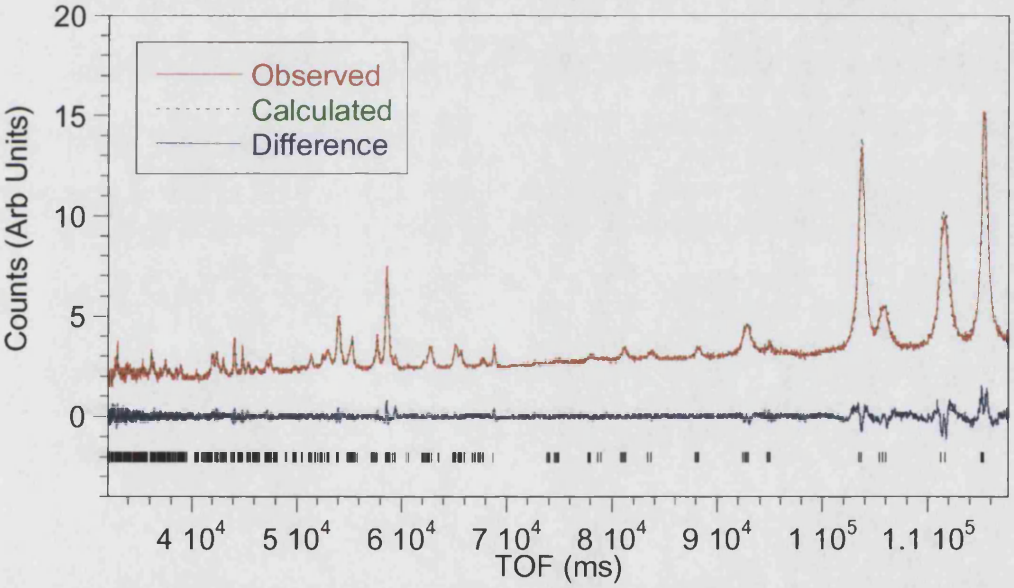

Figure 3.11. Observed, calculated and difference for the Rietveld refinement of neutron diffraction measurements for $K_{0.125}MnO_2$ (K1) at a temperature of 80K in the I 2/m space group.

Table 3.4. Final lattice parameters derived from the Rietveld profile refinements of $K_{0.125}MnO_4$ *at temperatures of 4K and 80K (space group I 2/m)*

	Temperature (K)	
	4K	80K
a (Å)	9.8262(5)	9.8270(5)
b (Å)	2.85041(7)	2.85099(7)
c (Å)	9.7840(5)	9.7837(5)
β	90.205(3)	90.212(3)
Cell Volume (Å^3)	274.03(2)	274.11(2)
χ^2	2.276	2.152
wRp (%)	3.53	3.46
Rp (%)	3.18	3.08

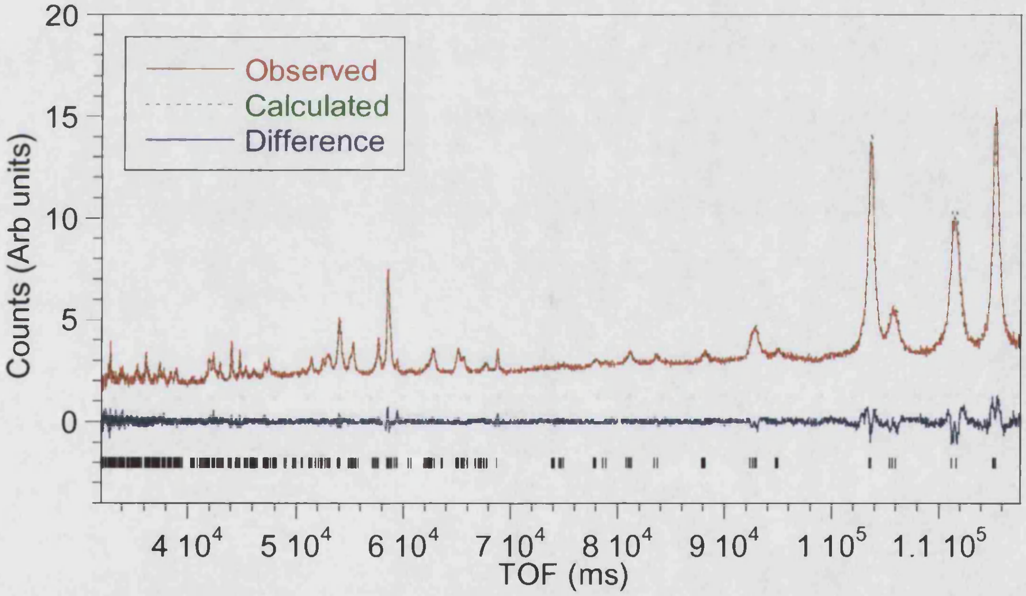

Figure 3.12. Observed, calculated and difference for the Rietveld refinement of neutron diffraction measurements for $K_{0.125}MnO_2$ *(K1) at a temperature of 4K in the I 2/m space group.*

Table 3.5. Final atom positions from the Rietveld profile refinements of neutron diffraction data of $K_{0.125}MnO_4$ (K1) at 4K and 80K. (space group I 2/m)

Temperature					
	4K	80K		4K	80K
K (0,0.5,0)			O2 (x,0,z)		
F	0.49(7)	0.49(8)	x	0.1572(8)	0.1571(8)
Mn1 (x,0,y)			z	0.7972(8)	0.7979(9)
x	0.1593(11)	0.1588(10)	U_{11}(x100)	1.71(4)	1.59(34)
z	0.3433(9)	0.3436(9)	U_{22}(x100)	0.10(4)	0.4(4)
U_{iso} (x100)	0.52(20)	0.42(18)	U_{33}(x100)	2.18(47)	2.93(52)
Mn2 (x,0,y)			U_{13}(x100)	0.71(25)	0.65(38)
x	0.3546(9)	0.3542(9)	O3 (x,0,z)		
z	0.8307(10)	0.8312(11)	x	0.1653(8)	0.1656(8)
U_{iso} (x100)	-0.56(16)	0.00	z	0.5404(7)	0.5403(7)
O1 (x,0,z)			U_{11}(x100)	0.86(4)	1.04(41)
x	0.2067(9)	0.2063(9)	U_{22}(x100)	-0.16(4)	0.2(4)
z	0.1548(10)	0.1541(10)	U_{33}(x100)	0.44(34)	0.67(35)
U_{11}(x100)	4.08(5)	3.61(46)	U_{13}(x100)	-1.54(25)	-1.33(26)
U_{22}(x100)	-0.22(5)	-0.3(4)	O4 (x,0,z)		
U_{33}(x100)	2.42(44)	2.85(45)	x	0.5413(8)	0.5412(8)
U_{13}(x100)	1.75(43)	2.07(42)	z	0.8339(8)	0.8350(8)
			U_{11}(x100)	1.88(4)	1.89(37)
			U_{22}(x100)	-1.46(4)	-1.4(4)
			U_{33}(x100)	0.11(33)	0.63(36)
			U_{13}(x100)	0.41(32)	1.12(32)

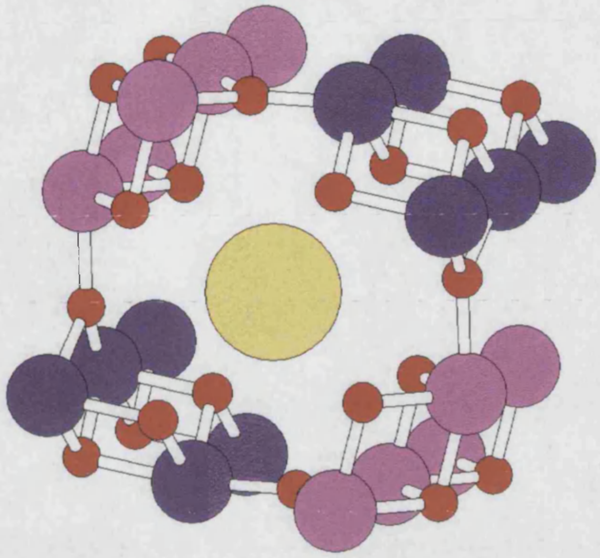

Figure 3.13. Schematic representation illustrating oxygen:cation arrangement for the refined neutron data for $K_{0.12}MnO_2$ at 80K. Where yellow is the potassium ion, blue is the manganese on site 1, pink is the manganese on site 2 and red is oxygen.

The eight fold coordinate potassium site, see figure 3.13, gives mean K-O distances of 2.889(7) and 3.311(8). The average Mn-O bond length observed for both manganese sites is approximately 1.90Å in a relatively isotropic environment expected for a Mn^{4+} system with little influence of the Mn^{3+} Jahn-Teller distortion. Both manganese sites exhibit similar environments in their 3 + 2 + 1 Mn-O bond environments. A summary of the bond angles and lengths is given in table 3.6. As expected the results show minimal differences between the data collected at 4K and that at 80K. The validity of all bond lengths and individual valences obtained from Rietveld refinement have been calculated using the bond valence sum program.[25] The program works based on Pauling's principle of electrostatic bond strength (EBS), where, the cation charge is divided by the coordination number. These EBS ideas have been developed in a more general way to study the factors that control bond lengths in solids. In modern usage the electrostatic bond strength is replaced by the bond valence given by equation 3.8.[26-27]

$$s = \exp[(r - r_0)/B] \qquad \text{-(3.8)}$$

or as

$$s = (r/r_0)^{-N} \qquad -(3.9)$$

Table 3.6. Final bond lengths derived from the Rietveld refinement of neutron diffractometer data for $K_{0.125}MnO_4$ (K1) at 4K and 80K (space group I 2/m).

	4K		80K	
	Length	Valence	Length	Valence
M1-O1 (Å)	1.90358(9)	0.661	1.914(11)	0.642
M1-O1 (Å)	1.94022(5)	0.599	1.946(10)	0.589
M1-O1 (Å)	1.94022(5)	0.599	1.946(10)	0.589
M1-O3 (Å)	1.92940(9)	0.616	1.925(11)	0.624
M1-O4 (Å)	1.83910(4)	0.787	1.837(8)	0.791
M1-O4 (Å)	1.83910(4)	0.787	1.837(8)	0.791
Total		4.049		4.026
M2-O2(Å)	1.9918(9)	0.558	1.963(12)	0.563
M2-O2 (Å)	1.89997(5)	0.667	1.908(9)	0.653
M2-O2 (Å)	1.89997(5)	0.667	1.908(9)	0.653
M2-O3 (Å)	1.91367(5)	0.643	1.911(9)	0.648
M2-O3 (Å)	1.91367(5)	0.643	1.911(9)	0.648
M2-O4 (Å)	1.83479(9)	0.796	1.838(13)	0.789
Total		3.974		3.954

These results confirm the isotropic nature of the Mn-O bond environment and dominance of the Mn^{4+} in the crystal chemistry. Many of these porous manganese oxides show distinct charge ordering where Mn^{3+} and Mn^{4+} sites are unique. However, there is no evidence in the measurements of any ordering of the Mn^{3+}/Mn^{4+} between the two sites. This is a possible consequence of the high Mn oxidation state and may well be more visible in systems with an average manganese oxidation state nearer to +3.5.

3.3.3.2. X-ray diffraction.

X-ray data have been collected using the Siemens D500 X-ray diffractometer. Figure 3.12 gives the powder XRD patterns arranged in order of increasing oxidation state as a result of intercalation, and show a systematic change in the unit cell parameters as a result of reductive intercalation.[28]

The refinement was performed in the I 2/m space group based on the model proposed by Miura in 1986.[25] The refined data for $K_{0.125}MnO_2$, treated $K_{0.07}MnO_2$ and the intercalated species is given in tables 3.7, 3.8 and 3.9. The cell volume dependence on average manganese oxidation state increases. This is shown graphically in figure 3.14. The observed cell volume for the copper intercalated species fits with the trend if we assume Cu^+, this fits better with the observed data as shown in figure 3.15 compared to Cu^{2+} and confirms the observations made in the TGA analysis. All refinement plots are given in figures 3.16 through 3.22.

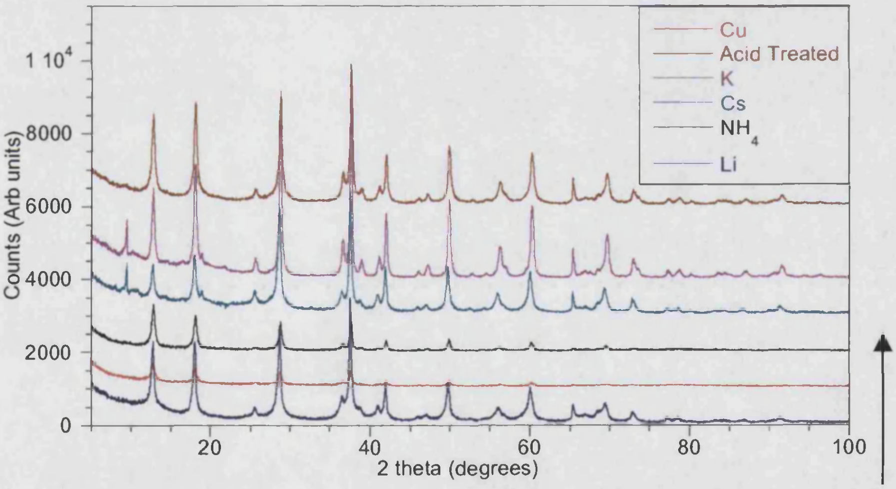

Increaing average
Mn oxidation state

Figure 3.14. X-Ray Diffraction patterns plotted as a function of increasing average manganese oxidation state showing the effects of intercalation on lattice parameters.

Table 3.7. Lattice parameters and goodness of fit parameters derived from the Rietveld profile refinements of the room temperature x-ray data for $K_{0.125}MnO_4$, $K_{0.07}MnO_2$ and intercalated species.

	Sample			
	K1	K2	NoK	Li
a (Å)	9.8323(6)	9.8030(7)	9.830(1)	9.871(2)
b (Å)	2.8543(1)	2.8533(1)	2.8542(2)	2.8569(3)
c (Å)	9.7926(6)	9.8166(8)	9.8075(8)	9.873(2)
β	90.163(7)	89.96(1)	89.94(1)	89.85(2)
CellVol ($Å^3$)	274.82(2)	274.58(3)	275.15(4)	278.45(6)
χ^2	3.511	3.765	2.612	3.301
wRp (%)	10.50	11.21	9.17	10.11
Rp (%)	8.23	8.52	6.92	7.31
	NH_4	Cu	Cs	
a (Å)	9.8709(2)	9.851(4)	9.8503(9)	
b (Å)	2.8595(1)	2.8631(4)	2.8531(2)	
c (Å)	9.8615(2)	9.847(4)	9.874(2)	
β	90.044(2)	90.126(35)	89.94(2)	
CellVol ($Å^3$)	278.35(7)	277.72(17)	277.49(5)	
χ^2	4.310	1.448	2.954	
wRp (%)	12.06	10.30	9.52	
Rp (%)	8.89	7.82	7.35	

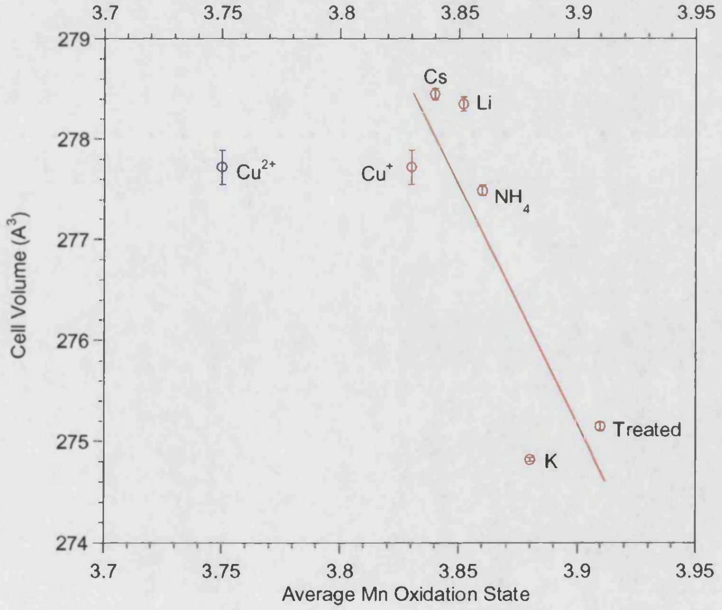

Figure 3.15. Decreasing cell volume with increasing average manganese oxidation state showing that the Cu^{2+} position is inconsistent with emerging models.

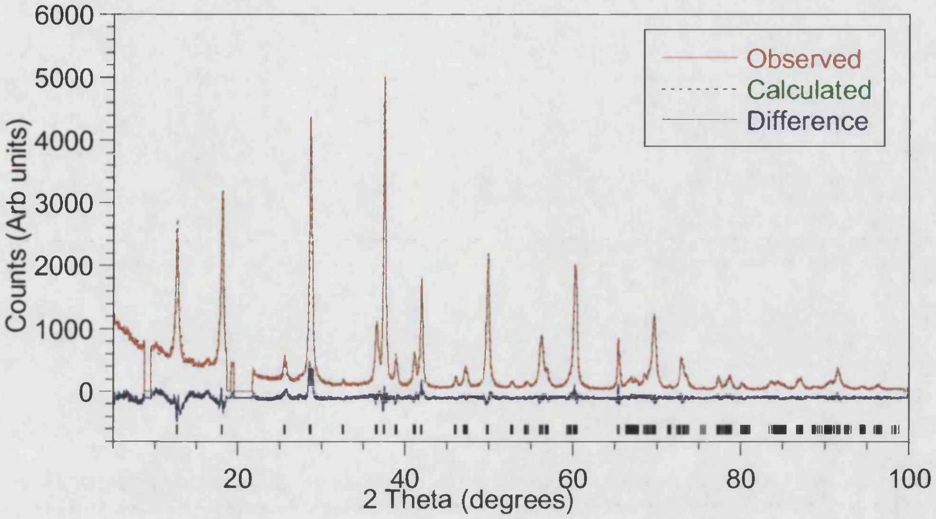

Figure 3.16. Observed, calculated and difference for the Rietveld profile refinement of the room temperature x-ray data for $K_{0.12}MnO_2$. *(space group I 2/m)*

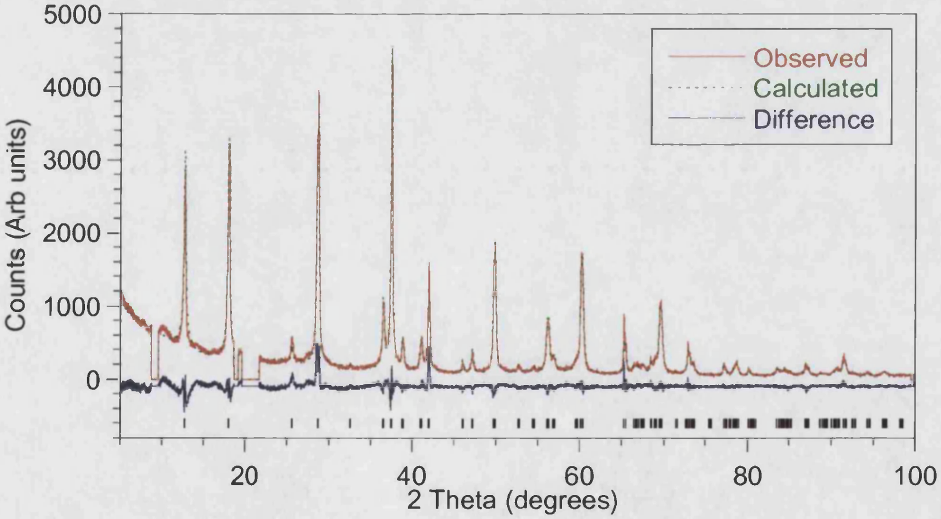

Figure 3.17. Observed, calculated and difference for the Rietveld profile refinement of the room temperature x-ray data for $K_{0.08}MnO_2$. *(space group I 2/m)*

Table 3.8. Final structural parameters derived from the Rietveld profile refinements of the room temperature x-ray data for $K_{0.125}MnO_4$ and $K_{0.07}MnO_2$. (space group I 2/m)

	K1	K2	NoK
K (0,0.5,0)			
F	0.48	0.32	0.36
AM(0,0.5,0)	-	-	-
F	-	-	-
Mn1(x,0,z)			
X	0.1693(4)	0.1695(5)	0.1647(5)
Z	0.3492(4)	0.3545(6)	0.3422(5)
Mn2(x,0,z)			
X	0.3505(4)	0.3452(6)	0.3567(4)
Z	0.8329(4)	0.8345(6)	0.8320(4)
O1 (x,0,z)			
X	0.189(2)	0.215(1)	0.190(2)
Z	0.156(2)	0.152(2)	0.153(1)
O2 (x,0,z)			
X	0.146(2)	0.145(2)	0.151(2)
Z	0.789(1)	0.831(2)	0.787(1)
O3 (x,0,z)			
X	0.171(2)	0.176(2)	0.165(2)
Z	0.547(2)	0.538(2)	0.5571(9)
O4 (x,0,z)			
X	0.546(2)	0.548(2)	0.533(1)
Z	0.826(2)	0.827(2)	0.831(2)

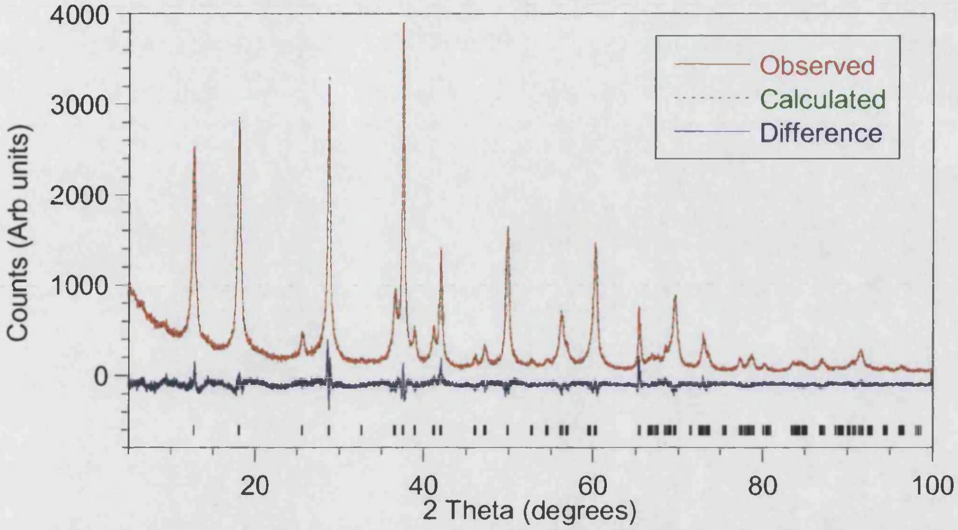

Figure 3.18. Observed, calculated and difference for the Rietveld profile refinement of the room temperature x-ray data for $K_{0.09}MnO_2$. (space group I 2/m)

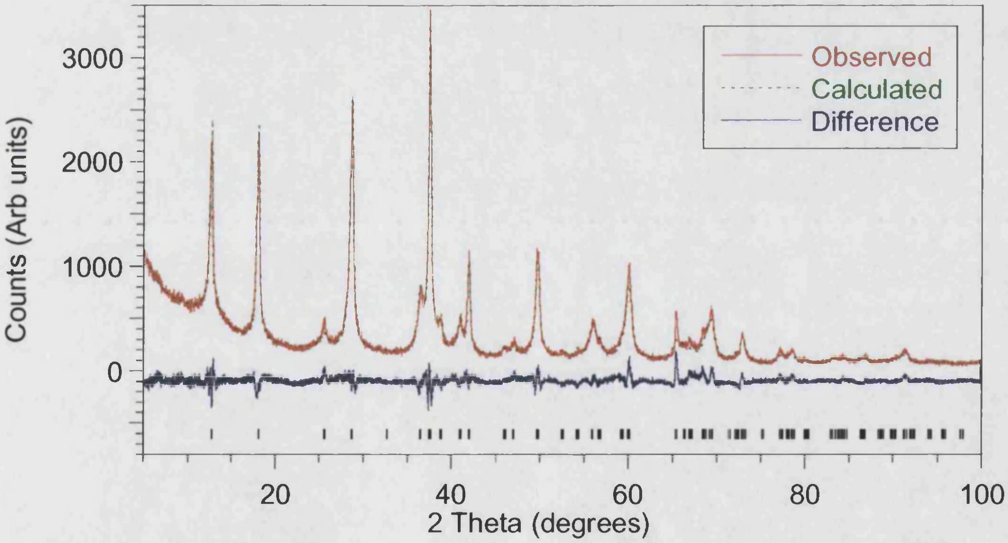

Figure 3.19. Observed, calculated and difference for the Rietveld profile refinement of the room temperature x-ray data for $Li_{0.18}K_{0.09}MnO_2$. (space group I 2/m)

Table 3.9. Final structural parameters derived from the Rietveld profile refinements of the room temperature x-ray data for Li, NH_4 and Cs intercalated species. (space group I 2/m)

	Li	NH_4	Cs
K (0,0.5,0)			
F	0.36	0.28	0.40
AM(0,0.5,0)			
F	0.72	0.31	0.16
Mn1(x,0,z)			
X	0.1562(5)	0.1523(6)	0.1684(5)
Z	0.3427(6)	0.3463(7)	0.3530(5)
Mn2(x,0,z)			
X	0.3283(5)	0.3517(6)	0.3450(5)
Z	0.8536(5)	0.8302(5)	0.8359(8)
O1 (x,0,z)			
X	0.231(1)	0.1892(17)	0.214482
Z	0.177(2)	0.1342(15)	0.141519
O2 (x,0,z)			
X	0.122(1)	0.1584(18)	0.1676(14)
Z	0.849(2)	0.7935(19)	0.8263(15)
O3 (x,0,z)			
X	0.178(2)	0.1420(24)	0.1484(14)
Z	0.534(2)	0.5454(17)	0.5433(15)
O4 (x,0,z)			
X	0.540(1)	0.5536(18)	0.5614(13)
Z	0.851(1)	0.8472(24)	0.8357(18)

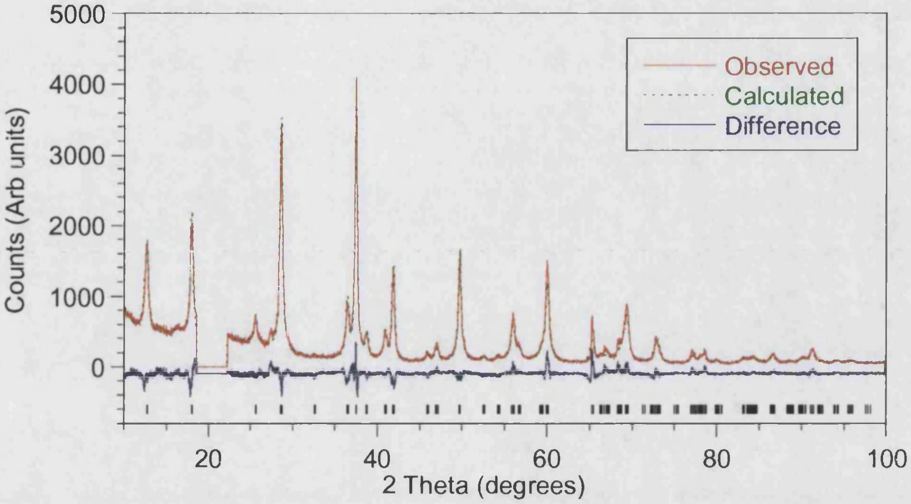

Figure 3.20. Observed, calculated and difference for Rietveld profile refinement of the room temperature x-ray data for $(NH_4)_{0.078}K_{0.07}MnO_2$. *(space group I 2/m)*

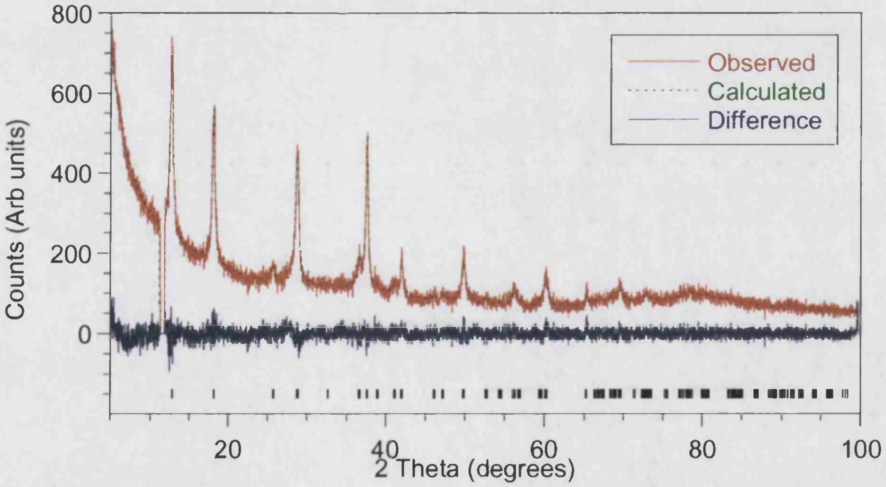

Figure 3.21. Observed, calculated and difference for the Rietveld profile refinement of the room temperature x-ray data for $Cu_{0.08}K_{0.07}MnO_2$. *(space group I 2/m)*

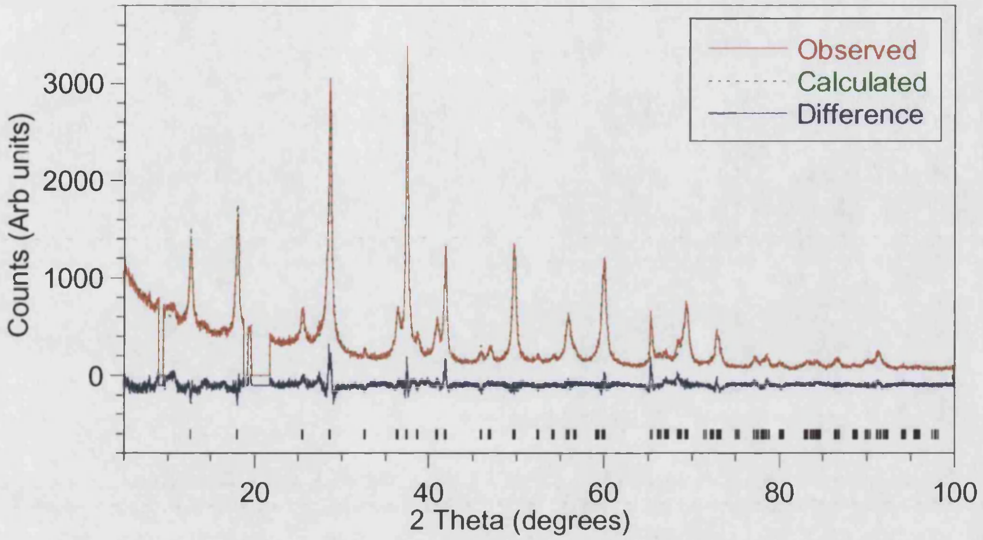

Figure 3.22. Observed, calculated and difference for the Rietveld profile refinement of the room temperature x-ray data for $Cs_{0.04}K_{0.1}MnO_2$. (space group I 2/m)

3.3.4. Magnetic properties.

$K_{0.12}MnO_2$ (K1) develops a ferromagnetic component on cooling below 50K, however, a negative Weiss constant is observed which is characteristic of antiferromagnetic interactions. Given the lack of magnetic scattering in the low temperature neutron pattern, the deviation from the field cooled and zero field cooled susceptibilities are indicative of spin glass behaviour (figure 3.23). The origins of the increase in magnetisation at 50K is probably due to short range ferromagnetic coupling resulting from the complicated Mn-O-Mn framework and presence of Mn^{3+} impurities giving local Mn^{3+}/Mn^{4+} double exchange coupling. Above 55K the material shows paramagnetic behaviour and can be fitted to the Curie-Weiss law (figure 3.23). Hysteresis data are given in figure 3.24, with all magnetic data summarised in table 3.10.

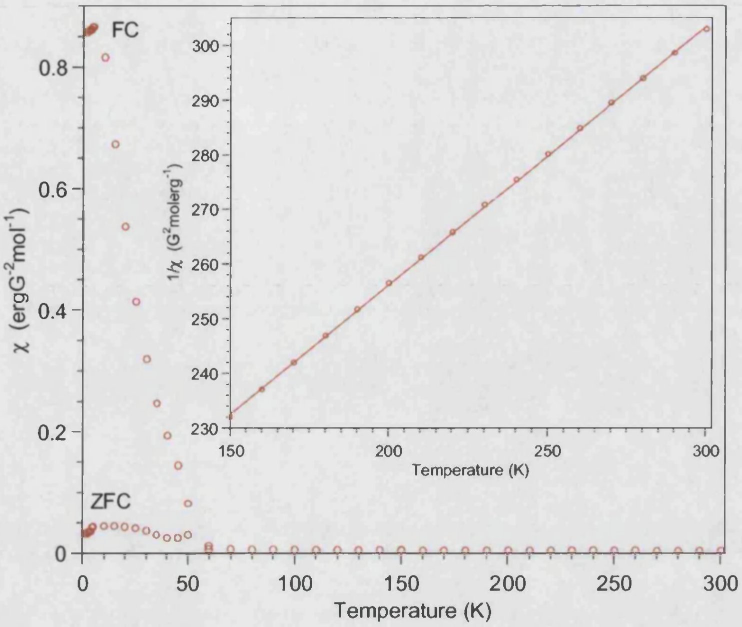

Figure 3.23. Magnetic susceptibility of $K_{0.12}MnO_2$ (K1), showing deviation between zero field cooled (ZFC) and field cooled (FC) measurement indicative of a spin glass transition; insert shows Curie-Weiss behaviour.

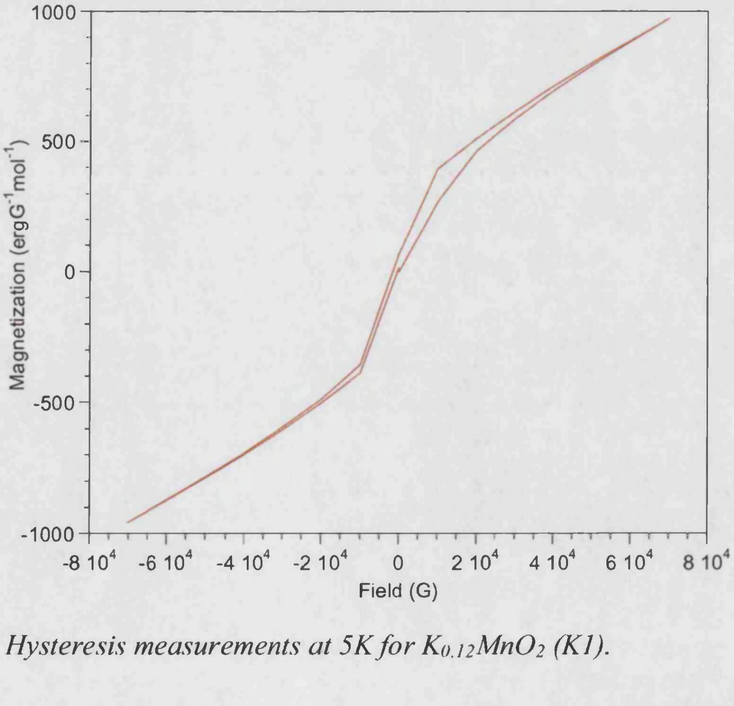

Figure 3.24. Hysteresis measurements at 5K for $K_{0.12}MnO_2$ (K1).

With the exception of Li all intercalated species behave in a similar way to $K_{0.12}MnO_2$. Figures 3.25 to 3.29 show the magnetic behaviour of these materials. Figure 3.30 shows the trend of increasing magnitude of the magnetic susceptibility with increasing average manganese oxidation state for the FC data. The Curie-Weiss fit of the paramagnetic region of $Cu_{0.08}K_{0.09}MnO_2$ gives an observed magnetic moment of 3.81, this suggests that the average manganese oxidation state is close to 4+ this supports the suggestion that Cu is in fact intercalated in the Cu^+ oxidation state and not as previously suggested in the Cu^{2+} state. Suib *et al* also suggested that changes in the average manganese oxidation state do not affect the observed magnetic properties. It is clear from these measurements that small changes in the average manganese oxidation state on intercalation controls the magnetic properties and in particular the magnitude of the magnetisation.[15]

Table 3.10. Curie constant, Weiss constant, observed and calculated magnetic moments for $K_{0.12}MnO_2$ and the intercalated analogues.

Sample	Av Mn ox state	T_f (K)	C (Kerg/G^2mol)	θ (K)	μ_{eff} (μ_B)	μ_{calc} (μ_B)
$K_{0.12}MnO_2$ (K1)	+3.88	55	2.106(7)	-340(2)	4.10	3.99
$K_{0.08}MnO_2$ (K2)	+3.92	55	2.27(1)	-289(3)	4.26	3.95
$K_{0.09}MnO_2$	+3.91	55	1.821(9)	-301(3)	3.82	3.96
$Li_{0.18}K_{0.09}MnO_2$	+3.74	50	1.75(1)	-225(4)	3.74	4.14
$(NH_4)_{0.078}K_{0.07}MnO_2$	+3.852	50	0.854(6)	-338(4)	2.61	4.02
$Cu_{0.08}K_{0.09}MnO_2$	+3.83	55	1.81(2)	-263(6)	3.81	4.04
$Cs_{0.04}K_{0.1}MnO_2$	+3.86	50	0.734(5)	-305(4)	2.42	4.01

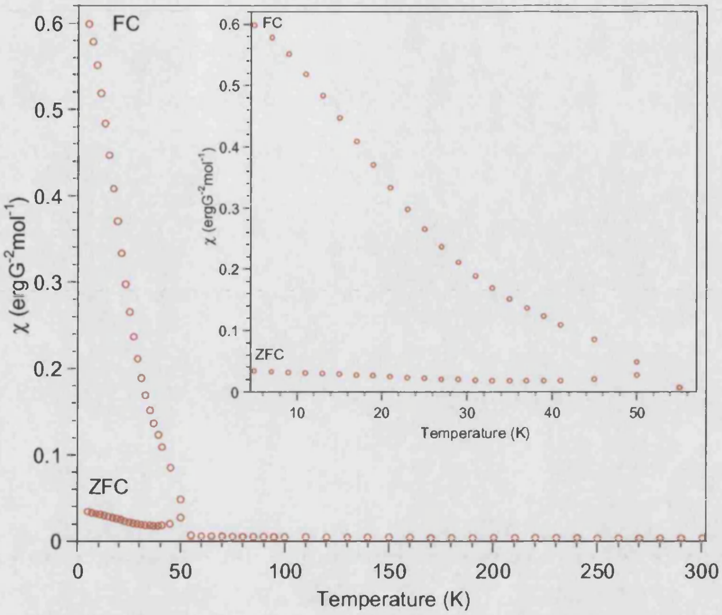

Figure 3.25. Magnetic susceptibility of $K_{0.09}MnO$, showing deviation between zero field cooled (ZFC) and field cooled (FC) measurements indicative of a spin glass transition; inset shows the region below T_F.

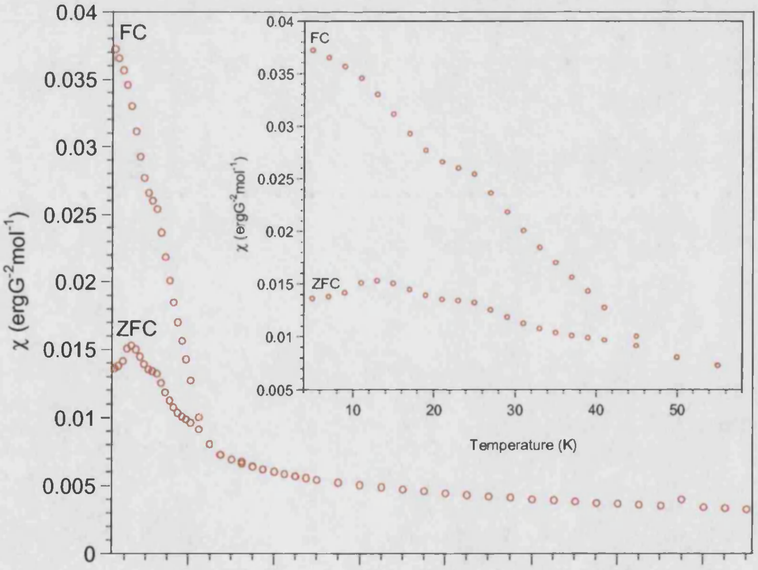

Figure 3.26. Magnetic susceptibility of $Li_{018}K_{0.09}MnO_2$, showing deviation between zero field cooled (ZFC) and field cooled (FC) measurements indicative of a spin glass transition; inset shows the region below T_F.

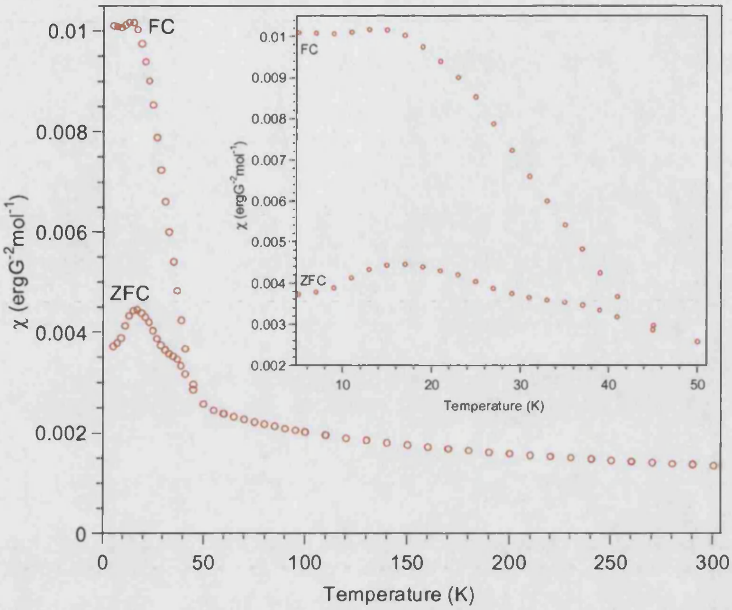

Figure 3.27. *Magnetic susceptibility of* $(NH_4)_{0.078}K_{0.07}MnO_2$, *showing deviation between zero field cooled (ZFC) and field cooled (FC) measurements indicative of a spin glass transition; inset shows the region below* T_F.

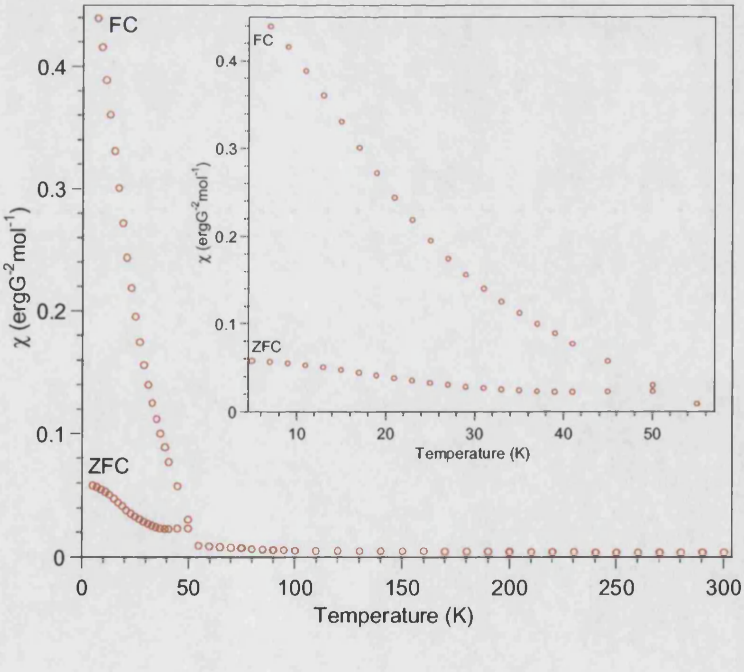

Figure 3.28. *Magnetic susceptibility of* $Cu_{0.08}K_{0.09}MnO_2$, *showing deviation between zero field cooled (ZFC) and field cooled (FC) measurements indicative of a spin glass transition; inset shows the region below* T_F.

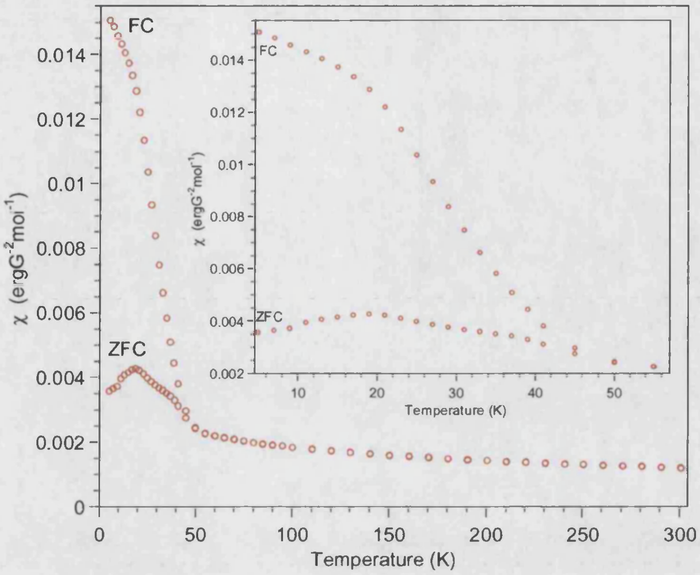

Figure 3.29. Magnetic susceptibility of Cs$_{0.04}$K$_{0.1}$MnO$_2$, showing deviation between zero field cooled (ZFC) and field cooled (FC) measurements indicative of a spin glass transition; inset shows the region below T$_F$.

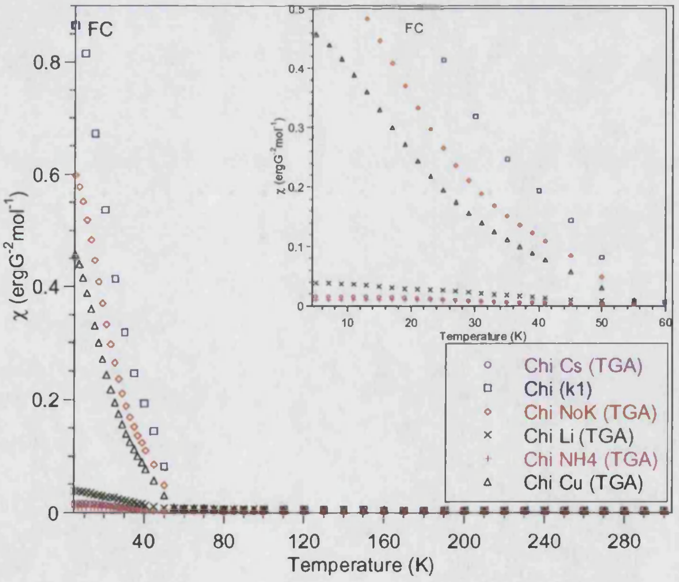

Figure 3.30. Field Cooled (FC) magnetic susceptibilities for all hollandite samples, showing the change in magnetisation with changing average manganese oxidation state; inset shows the region below T$_F$.

3.3.5 Transport Properties.

Information of the electrical resistance of some of these samples was collected using an Oxford instruments MagLab^{2000} system. The sample resistance was measured over a temperature range of approximately 150 – 350K in a zero applied field. All samples measured showed an exponential drop of resistance with increasing temperature; the signature of semiconducting properties. Figure 3.31 to 3.33 show the results for $K_{0.125}MnO_2$, $K_{0.09}MnO_2$ and $Li_{0.18}K_{0.09}MnO_2$. The band gaps were calculated from Arrhenius plots of ln conductivity against reciprocal temperature and are shown as inserts in figures 3.31 to 3.33. The band gaps calculated as 0.170(2) eV, 0.160(1) eV and 0.200(1) eV for the Hollandite, treated hollandite and Li hollandite respectively. It can be seen that with decreasing average manganese oxidation state that the band gap increases.

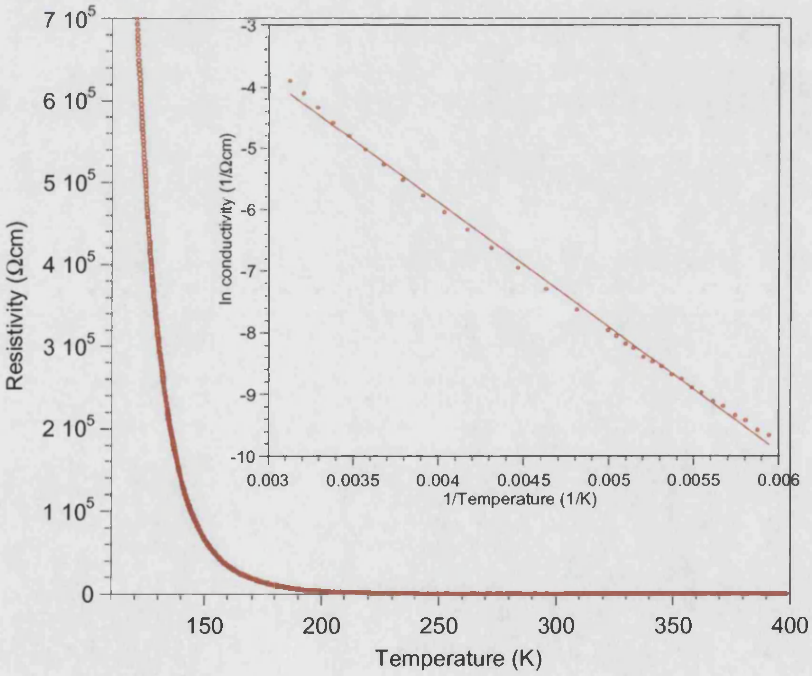

Figure 3.31. Resistivity as a function of temperature for $K_{0.125}MnO_2$; insert shows Arrhenius relationship.

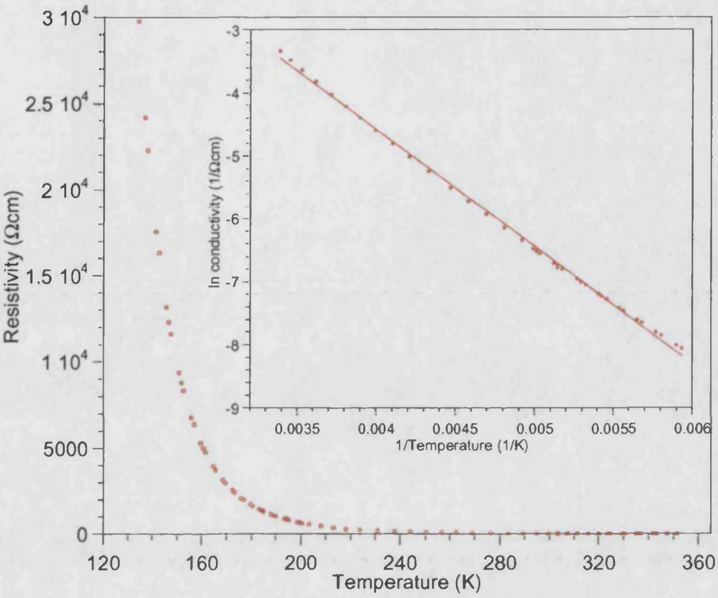

Figure 3.32. Resistivity as a function of temperature for $K_{0.09}MnO_2$*; insert shows Arrhenius relationship.*

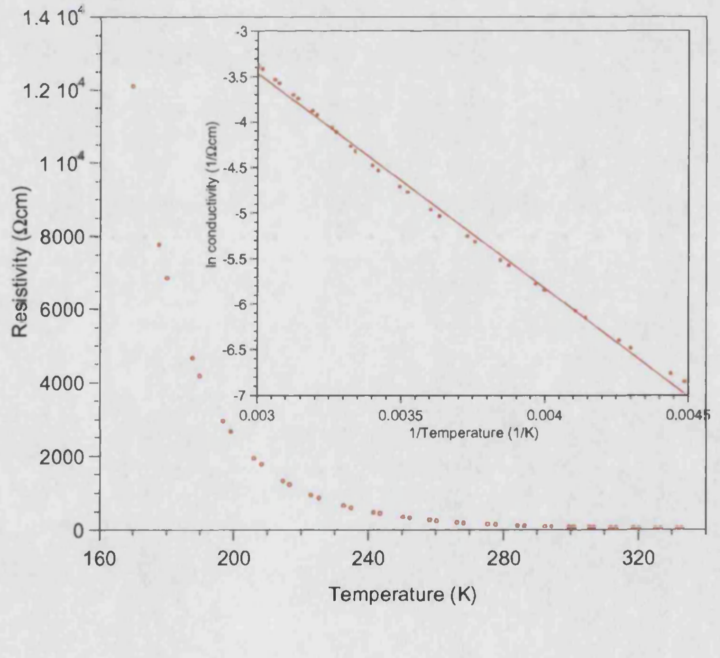

Figure 3.33. Resistivity as a function of temperature for $Li_{0.18}K_{0.09}MnO_2$*; insert shows Arrhenius relationship.*

3.4. Conclusions.

The framework structure of hollandite can be easily refined to existing models and it can be seen from the results presented here that slight difference in the preparation method can result in large changes in the sample, for example the composition of the two potassium hollandite materials K(1) and K(2). We have shown that it is possible to remove some of the potassium template ion from the framework and to intercalate different species and that selectivity decreases as a function of increasing ionic radii of the intercalated species.

It can be seen that whilst intercalation does not destroy the framework structure it does affects the thermal stability of the phase, with stability decreasing with decreasing average manganese oxidation state. Changes in the average manganese oxidation state also have a large effect on the observed magnetism and electronic properties with the band gap increasing with decreasing average manganese oxidation state, which would further change the observed magnetism and electronic structure.

It is obvious from these results that the properties of these materials are controlled by the average manganese oxidation state and the ready conversion between Mn^{3+} and Mn^{4+} makes the 'tuning' of these materials to achieve a desired set of properties a real possibility.

3.5. References.

(1) J. Dai, S. F. Y. Li, K. S. Siow, Z. Gao, *Electrochimica Acta*, **2000**, *45(14)*, 2211.

(2) D. L. Bish, J. E. Post, *American Mineralogist*, **1989**, *74*, 177.

(3) A. Byström, A. M. Byström, *Acta Crystallographica*, **1950**, *3*, 146.

(4) B. Mukherjee, *Acta Crystallographica*, **1960**, *13*, 164.

(5) L. C. Nistor, G. Van Tendeloo, S. Amelinckx, *Journal of Solid State Chemistry*, **1994**, *109*, 152.

(6) Q. Feng, T. Horiuchi, T. Mitsusio, K. Yanagisawa, N. Yamasaki, *Journal of Materials Science Letters*, **1999**, *18(17)*, 1375.

(7) S. Ching, J. L. Roark, N. Duan, S. L. Suib, *Chemistry of Materials*, **1997**, *9(3)*, 750.

(8) N. Duan, S. L. Suib, C. L. O'Young. *Journal of the Chemical Society. Chemical Communications*, **1995**, *13* 1367.

(9) Q. Feng, H. Kanoh, K. Ooi, M. Tani, Y. Nakacho, *Journal of the Electrochemical Society*, **1994**, *141*, L135.

(10) S. Bach, J. P. Pereira-Ramos, N. Baffier, *Solid State Ionics*, **1995**, *80*, 151.

(11) Q. Feng, H. Kanoh, Y Miyai, K. Ooi, *Chemistry of Materials*, **1995**, *7(1)*, 148.

(12) R. N. De Guzman, Y. F. Shen, B. R. Shaw, S. L. Suib, C. L. O'Young, *Chemistry of Materials*, **1993**, *5(10)*, 1395.

(13) T. Ohzuku, M. Kitagaw, K. Sawai, T. Hirai. *Journal of the Electrochemical Society* **1991**, *138(2)*, 360.

(14) S. L. Suib, L. E. Iton, *Chemistry of Materials*, **1994**, *6(4)*, 429.

(15) R. N. De Guzman, A. Awaluddin, Y. F. Shen, Z. R. Tian, S.L. Suib, S. Ching, C. L. O'Young, *Chemistry of Materials,* **1995**, *7(7)*, 1286.

(16) Q. Zhang, S. L. Suib, *Chemistry of Materials*, **1999**, *11(5)*, 1306.

(17) Q. Zhang, J. Luo, E. Vileno, S. L. Suib, *Chemistry of Materials*, **1997**, *9(10)*, 2090.

(18) E. Nicolas-Tolentino, Z. R. Tian, H. Zhou, G. Xia, S. L. Suib, *Chemistry of Materials*, **1999**, *11(7)*, 1733.

(19) R. W. Cheary, *Acta Crystallographica B*, **1986**, *42*, 229.

(20) R. W. Cheary, *Acta Crystallographica* B, **1990**, *46*, 599.

(21) H. U. Beyeler, *Physical Review Letters*, **1976**, *37*, 1557.

(22) I. Jacyna-Onyszkeiwicz, T. Mydlarz, *Journal of Magnetism and Magnetic Materials*, **1996**, *160*, 379.

(23) I. Jacyna-Onyszkeiwicz, M. A. Obolensky, *Journal of Physics IV. France*, **1997**, *7*, C1371.

(24) H. Miura, *Mineralogical Journal (Japan)*, **1986**, *13*, 119.

4.1. Introduction.

Romanechite, $(Ba,H_2O)_2Mn_5O_{10}$, is a naturally occurring manganese oxide mineral and is common as minor phases in massive deposits and in fracture linings. The structure was first reported by Wadsley in 1953.[1,2] Wadsley showed that the structure consisted of double and triple edge sharing chains of MnO_6 octahedra, which are corner shared to form tunnels measuring (2 x 3) octahedral units shown in Figure 4.1. Wadsley also proposed a superstructure for this material with a tripling of the b parameter as a result of cation ordering within the tunnels, this was later confirmed by Turner et al using electron diffraction,[3] who went on to suggest that Mn^{3+} ions are preferably located at the corner shared edges of the longer chains, which is also consistent with other porous manganese structures such as todorokite and RUB 7.[4,5]

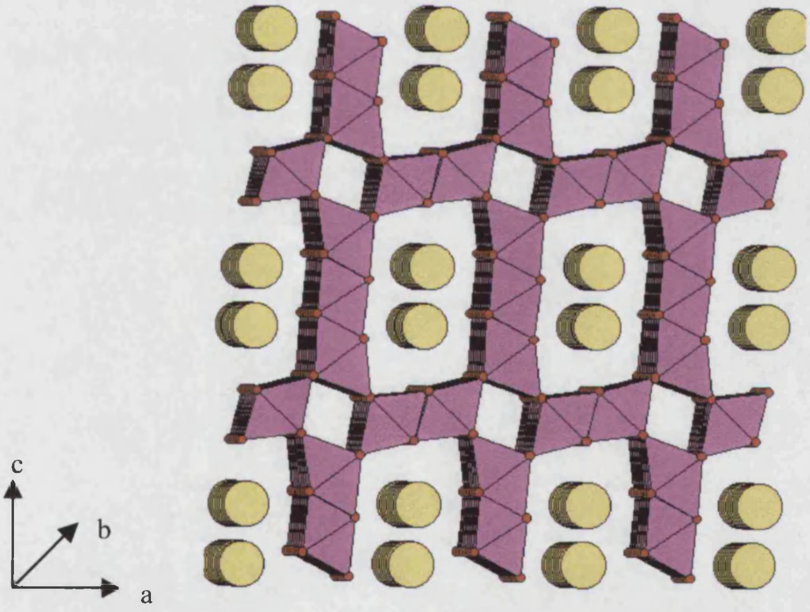

Figure 4.1. Schematic Representation of $(Ba,H_2O)_2Mn_5O_{10}$, romanechite, where the pink squares represent the MnO_6 octahedra and the yellow spheres represent the Barium and H_2O sites.

Sodium romanechite, $Na_{0.40}MnO_2$, was first reported in 1971, with a monoclinic, C 2/m space group.[6] Though the X-ray pattern showed peaks forbidden in this space group, such that $h + k = 2n + 1$, which was attributed to a supercell caused by the ordering of the template ions within the tunnels as well as Mn^{3+} and Mn^{4+} ions within the framework.

Mendiboure *et al* commented that the large tunnels in $Na_{0.40}MnO_2$ would allow the intercalation and deintercalation of sodium ions.[7] The exact site of sodium within the channels is not well known, though electrochemical experiments were performed to determine the amount of Na ions possible to intercalate. Subsequent X-ray diffraction data showed the existence of a solid solution in the range of $0.30 \leq x \leq 0.58$, where x is the sodium content of the tunnels, the deintercalation could not be performed at below $x = 0.30$ due to electrolyte instability at high cell voltages. The electrochemical potentials of both Li and Ba analogues has been investigated by Tsuda *et al*; in both cases the compounds showed a decrease in capacity on cycling and poor reversibility.[8,9] The removal of the Ba from the tunnel sites proves difficult and is in fact impossible by acid leaching methods resulting in the breakdown of the material to γ-MnO_2.[9,10] The material shows a reasonable thermal stability decomposing to hollandite at temperatures above 500°C.[1]

4.2. Synthesis.

$Na_{0.40}MnO_2$ was prepared as reported by Parant et al.[6] Stoichiometric ratios of Na_2CO_3 and Mn_2O_3 were ground together and the material heated at 550°C in flowing O_2 for 2-3 days. As reported for the preparation of the phase $Na_{0.44}MnO_2$ slight excess of Na_2CO_3 was employed to minimize the possible formation of a manganese oxide second phase due to the loss of sodium during the reaction.[11] After the reaction the material was allowed to cool slowly to room temperature whilst in an atmosphere of flowing oxygen.

Removal of the Na from the tunnels was achieved by stirring the prepared $Na_{0.40}MnO_2$ material with a solution of approximately 1M HCl at room temperature overnight.[12] The possibility of intercalating other alkali metals such as Li, K, and Cs as well as the rare earths Y, Ho and Yb was investigated by reacting the acid leached $Na_{0.40}MnO_2$ with an excess of metal iodide and in the case of potassium the hydroxide based on the equations 4.1 and 4.2. All reactions were rapid and can be monitored by the liberation of iodine.

$$xLiI + Na_{0.40-y}MnO_2 \rightarrow \tfrac{1}{2}xI_2 + Li_xNa_{0.40-y}MnO_2 \qquad -(4.1.)$$

$$xKOH + Na_{0.40-y}MnO_2 \rightarrow xOH^- + K_xNa_{0.40-y}MnO_2 \qquad -(4.2.)$$

All products were characterised using the Siemens D500 X-ray diffractometer fitted with a secondary monochromator to minimize background intensity due to fluorescence of Mn. Additional diffraction data were collected for $Na_{0.40}MnO_2$ using the High Resolution Powder Neutron Diffractometer (HRPD) at the Rutherford Appleton Laboratories in Didcot, Oxon, UK and the powder diffractometer at the National Institute of Standards and Technology (NIST), Gaithersburg, Maryland, USA. Diffraction data collected were subsequently refined using the GSAS suite of programs. Magnetic and resistivity measurements were performed using the Quantum Design MPMS7 SQUID magnetometer and the Oxford Instruments Maglab respectively. Additional compositional information was collected using elemental analysis, EDX, EPMA and thermal methods.

4.3. Results and Discussion.

4.3.1. Structure.

The X-ray diffraction pattern of the as made product was identical to that previously reported[6] (JCPDS file No 27-749). Rietveld refinement was performed using the model proposed for the $(Ba,H_2O)_2Mn_5O_{10}$ structure[2] as well as the romanechite supercell as a model proposed by Turner *et al*,[3] the latter exhibiting the larger lattice parameters of a = 13.929, b = 8.5377, c = 9.678 and β = 92.39° compared to those reported by Parant et al of a = 13.81, b = 2.863, c = 9.74 and β = 95.2°.[6] Both of these models gave a poor fit to the observed data, with marked differences in peak intensities as well as the absence of some peaks whilst others appear to be either extra or the result of peak splitting. These observed deviancies could be a result of intergrowths of the structure as illustrated by the intergrowth of hollandite in figure 4.2.[13,14] These types of defects are common in these porous systems. For example, the mixture of tunnels formed by (1 x 2) octahedra and (1 x 1) octahedra gives the excellent electrochemical properties of electrolytic manganese dioxides (EMD).

The possibility that the structure of $Na_{0.40}MnO_2$ was not that of romanechite was considered, since Na is widely reported to be too small to act as a template ion for hollandite, it is probable that this is also true for the larger pore observed in the romanechite structure.[15] Additionally preparation of porous manganese oxides vary, but traditionally preparation of these materials with larger pore dimensions are restricted to wet chemical or hydrothermal techniques. For example, hollandite is in fact prepared by wet chemical methods and can not be prepared by conventional solid state methods as is $(Ba, H_2O)_2Mn_5O_{10}$.[9,16] A loss in crystallinity in X-ray data with increasing pore size is a general trend in these materials, such as in todorokite and birnessite, which show poor crystallinity. Considering the relatively large size of the romanechite tunnels and the high temperature preparation route it is considered possible that the structure may differ from that reported.

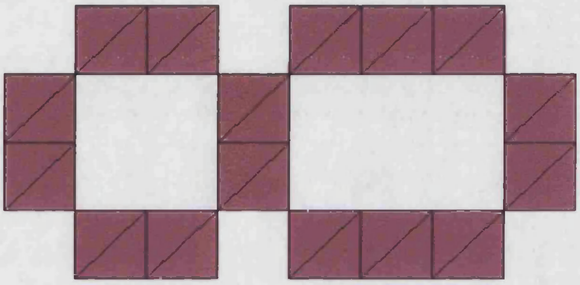

Figure 4.2. Schematic representation showing the intergrowth between hollandite with romanechite, where the pink squares represent the MnO_6 octahedra.

Comparisons of the data with that of $Na_{0.44}MnO_2$ showed some similarities but were obviously not identical phases. The peaks of both the neutron data collected at NIST and the X-ray diffraction data were indexed by the Crysfire program.[17] Two monoclinic cell suggestions gave good figures of merit and looked good in comparison to other unit cells reported for porous manganese oxides. That is they showed similar b values of approximately 2.8 or multiples there of, these are given below.[15] This value of 2.8 (or 5.6) represents the distance down the tunnel and is independent of the tunnel size.

1. $a = 14.82$ $b = 5.907$ $c = 11.31$ and $\beta = 105.166^{\circ}$
2. $a = 16.17$ $b = 5.680$ $c = 12.28$ and $\beta = 92.3460^{\circ}$

Lebail fits using the GSAS suite of programs on these cells were attempted using firstly the data collected at NIST. Both cells gave superior fits compared to Lebail fits using the romanechite model with $\chi^2 = 1.31$ and $\chi^2 = 1.899$ for cell 1 and cell 2 and shown in figures 4.3 and 4.4 respectively. Attempts were made to solve the structure by direct methods using the EXPO and SIRPOW programs.[18] Due to the quality of the data no usable solutions were achieved, however results indicated that the material is porous in nature.

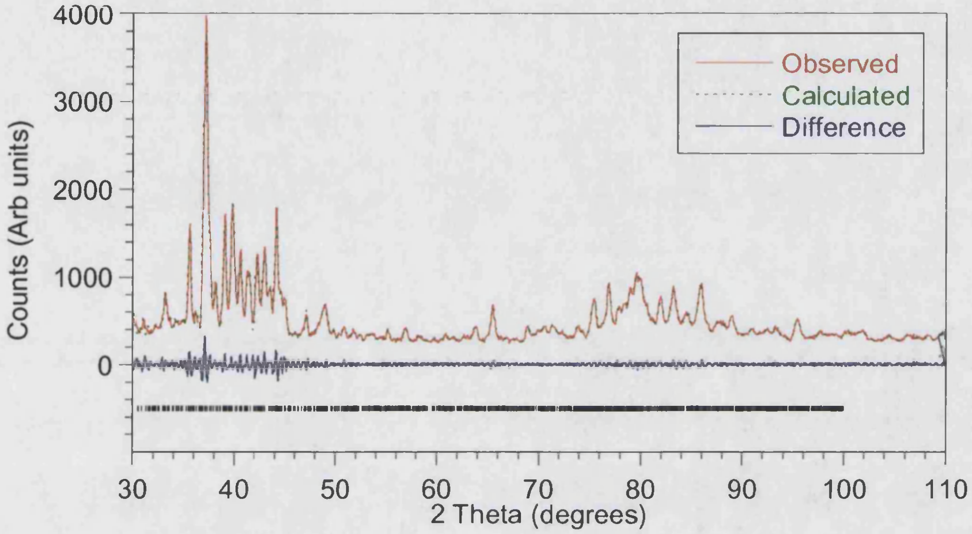

Figure 4.3. Observed, calculated and difference for the Lebail refinement of neutron powder diffractometer data for $Na_{0.40}MnO_2$ *using model 1:* $a = 14.82$ $b = 5.907$ $c = 11.31$ *and* $\beta = 105.166^o$.

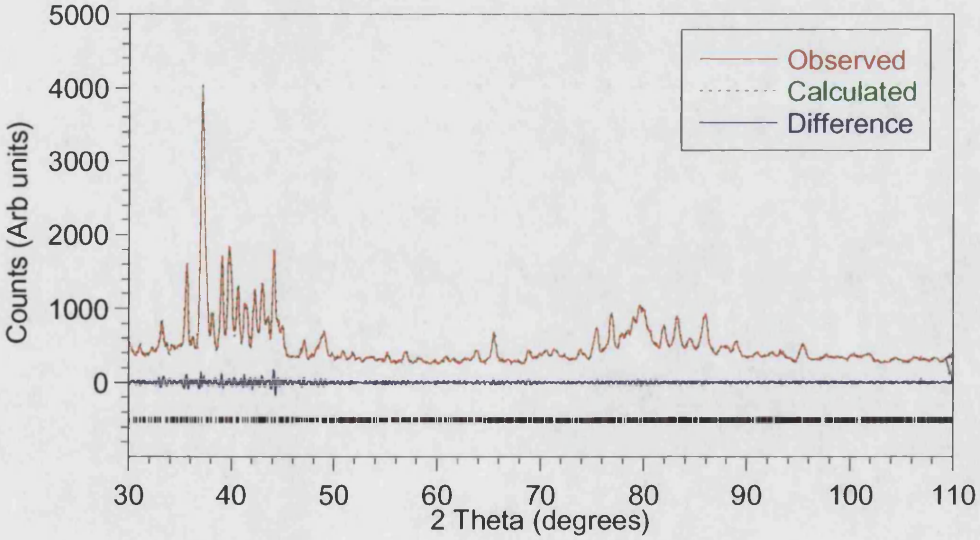

Figure 4.4. Observed, calculated and difference for the Lebail refinement of neutron powder diffractometer data for $Na_{0.40}mnO_2$ *using model 2:* $a = 16.17$ $b = 5.680$ $c = 12.28$ *and* $\beta = 92.3460^o$.

EDX and elemental analysis data confirm the composition as being that intended, namely $Na_{0.39(3)}MnO_2$. Removal of the sodium template by acid leaching appears also to be possible with approximately half of the sodium being removed this is consistent with other data reported in this thesis and confirms the porous nature of this material. It is evident from the results that acid leaching of the framework is a more effective method for the removal of the template ion from within the tunnel site than the electrolytic deintercalation, giving a value of $x = 0.17$ as apposed to $x = 0.30$ observed.[7] The intercalation of other alkali metals and lanthanides within the tunnel occurred with a great deal of ion selectivity as can be seen from the EDX, elemental analysis and EPMA results in tables 4.1 and 4.2.

Table 4.1. Results obtained by elemental analysis and EDX for the chemical composition of $Na_{0.40}MnO_2$ and intercalated species.

Sample	Elemental Analysis	EDX Analysis
$Na_{0.40}MnO_2$	$Na_{0.390(3)}MnO_2$	$Na_{0.390(3)}MnO_2$
$Na_{0.40-y}MnO_2$	$Na_{0.170(2)}MnO_2$	$Na_{0.150(2)}MnO_2$
$Li_{0.5}Na_{0.40-y}MnO_2$	$Li_{0.260(3)}Na_{0.150(2)}MnO_2$	$Li_xNa_{0.160(2)}MnO_2{}^*$
$K_xNa_{0.40-y}MnO_2$	$K_{0.0400(4)}Na_{0.170(2)}MnO_2$	$K_{0.0500(5)}Na_{0.160(2)}MnO_2$
$Cu_xNa_{0.40-y}MnO_2$	-	$Cu_{0.0300(3)}Na_{0.090(1)}MnO_2$

* Li content cannot be analysed by the EDX method.

Table 4.2. EPMA results for lanthanide intercalated $Na_{0.40}MnO_2$ species calculated from the average of 20 analysed points.

Sample	EPMA Analysis
$Y_xNa_{0.40-y}MnO_2$	$Y_{0.260(3)}Na_{0.070(1)}MnO_2{}^*$
$Yb_xNa_{0.40-y}MnO_2$	$Yb_{0.450(5)}Na_{0.050(1)}MnO_2{}^*$
$Ho_xNa_{0.40-y}MnO_2$	$Ho_{0.040(4)}Na_{0.070(1)}MnO_2$

* Both Y and Yb treated samples are not homogenous suggesting the possible presence of a second phase or the possibility of lanthanide intercalation at surface sites only.

Intercalation is consistent with increasing radii as proposed for the hollandite system with the exception of Cu, K and Ho, which show negligible intercalation.[19] Since the intercalation of Cs into the tunnel sites proved impossible this suggests that the pore in $Na_{0.39}MnO_2$ is only large enough to accommodate Na ions. Hollandite has the capacity to intercalate both K and Cs suggesting that the pores in $Na_{0.39}MnO_2$ are in fact smaller than those of hollandite. It appears as though it is possible to intercalate greater amounts of rare earth metals than alkali earth metals, this may be in part due to the removal of more sodium during the reaction, in other words there is an ion exchange mechanism at play as well as a direct intercalation experiment. This gives the following selectivity's order with increasing radii.[20]

$$Li > Cu > Yb > Y = Ho > Na > K$$

X-ray diffraction data showed slight shifts in peak position for all new compounds when compared with $Na_{0.39}MnO_2$, corresponding to the slight change in lattice parameters, which is shown in figure 4.5.[11] All the X-ray data were fitted to both the proposed cell using the Lebail refinement in the GSAS suite of programs in an attempt to elucidate a trend in the cell parameters as a function of intercalation. The refinement patterns are given in figures 4.6 to 4.11 and the refinement fit data and cell data are given in tables 4.3 and 4.4 respectively. Some regions were excluded due to the presence of slight amounts of a $Na_{0.44}MnO_2$ phase, which also appears to grow with time this is unsurprising as it is known to be the most thermodynamically stable member of the series. Refinements were difficult due to intergrowths, stacking faults and preferred orientation of these materials. The refinement of both Y and Yb materials was not possible due to the quality of the data collected as a result of small amount of sample material. Lebail refinements for both models result in very similar lattice parameters, with the difference between the two models being the angle beta. In both cases there is a drop in cell volume as the sodium is removed from the tunnel sites. Upon intercalation there is an increase in cell volume as would expected for porous materials.

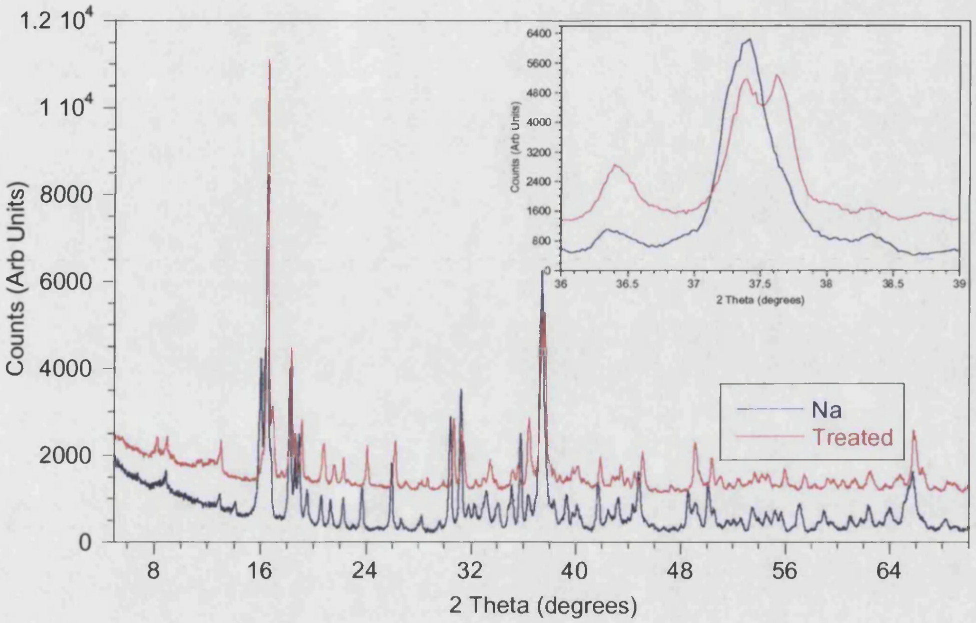

Figure 4.5. X-ray diffraction data for $Na_{0.36}MnO_2$ and $Na_{0.16}MnO_2$ showing peak splitting as a result of increasing average manganese oxidation state and hence changes in lattice parameters.

Table 4.3. Final lattice parameters derived from the Lebail extraction of $Na_{0.40}MnO_2$, acid treated $Na_{0.40}MnO_2$ and lithium intercalated $Na_{0.40}MnO_2$ using models 1 and 2.

Sample		a (Å)	b (Å)	c (Å)	β	Cell Vol (Å^3)
Na	1	14.9246(10)	5.86710(30)	11.2261(8)	106.792(6)	941.09(11)
	2	15.9723(13)	5.60264(34)	12.0089(11)	93.172(5)	1072.99(15)
Treated	1	14.4129(20)	5.7089(5)	10.9781(15)	105.904(9)	868.72(19)
	2	15.7938(12)	5.58483(31)	11.8938(9)	93.147(7)	1047.52(12)
Li	1	14.7282(13)	5.8654(4)	11.3214(11)	106.199(4)	939.18(14)
	2	16.1540(22)	5.6587(5)	12.2440(14)	93.179(8)	1117.52(23)

Table 4.4. Goodness of fit factors for Lebail extraction of $Na_{0.40}MnO_2$, *acid treated* $Na_{0.40}MnO_2$ *and lithium intercalated* $Na_{0.40}MnO_2$ *using models 1 and 2.*

Sample		χ^2	WRp (%)	Rp (%)
Na	1	19.41	16.86	12.39
	2	10.68	12.36	8.24
Treated	1	13.46	15.06	11.74
	2	12.63	15.35	10.84
Li	1	5.000	9.50	6.80
	2	8.467	12.56	8.87

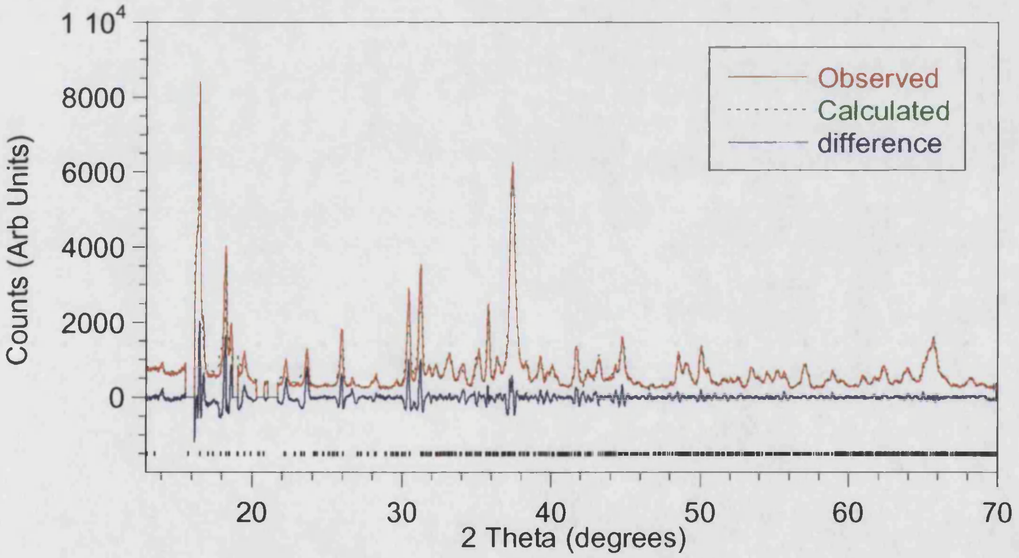

Figure 4.6. Observed, calculated and difference for the room temperature X-ray diffraction data for the Lebail extraction pattern of $Na_{0.40}MnO_2$ *using model 1:* $a = 14.82$ $b = 5.907$ $c = 11.31$ *and* $\beta = 105.166^o$.

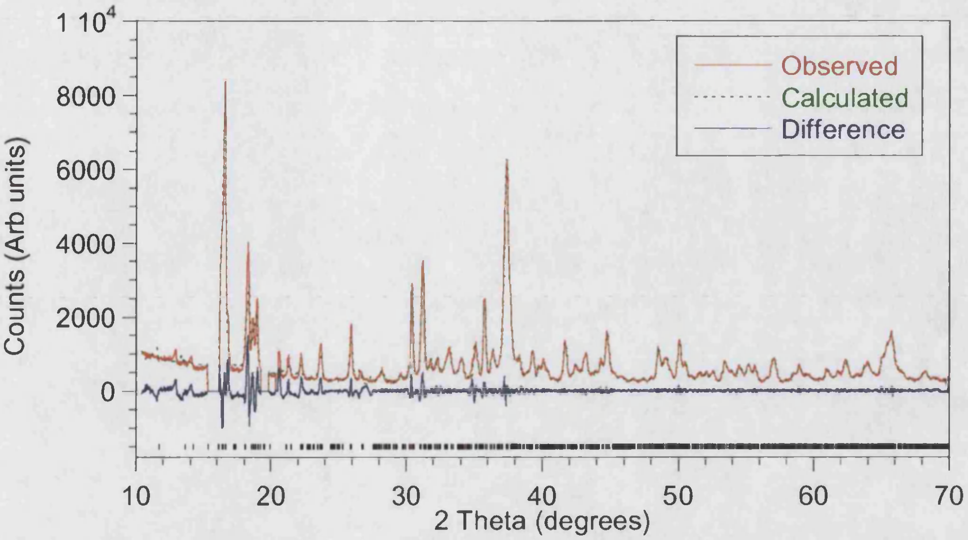

Figure 4.7. Calculated, observed and difference for the Lebail extraction of room temperature X-ray diffraction data of $Na_{0.40}MnO_2$ *using model 2: a = 16.17 b = 5.680 c = 12.28 and* $\beta = 92.3460^o$.

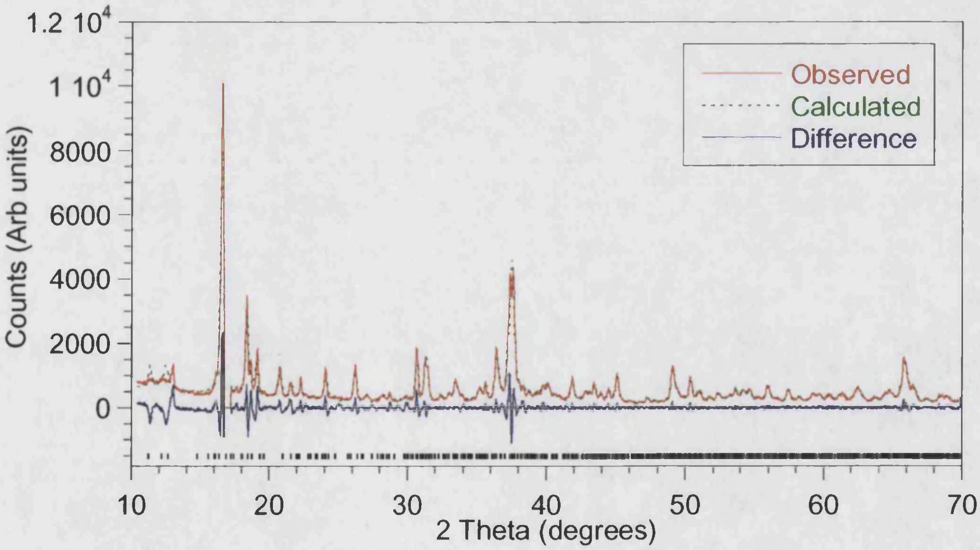

Figure 4.8. Observed, calculated and difference for the Lebail extraction of X-ray diffraction data of $Na_{0.17}MnO_2$ *using model 1: a = 14.82 b = 5.907 c = 11.31 and* $\beta = 105.166^o$.

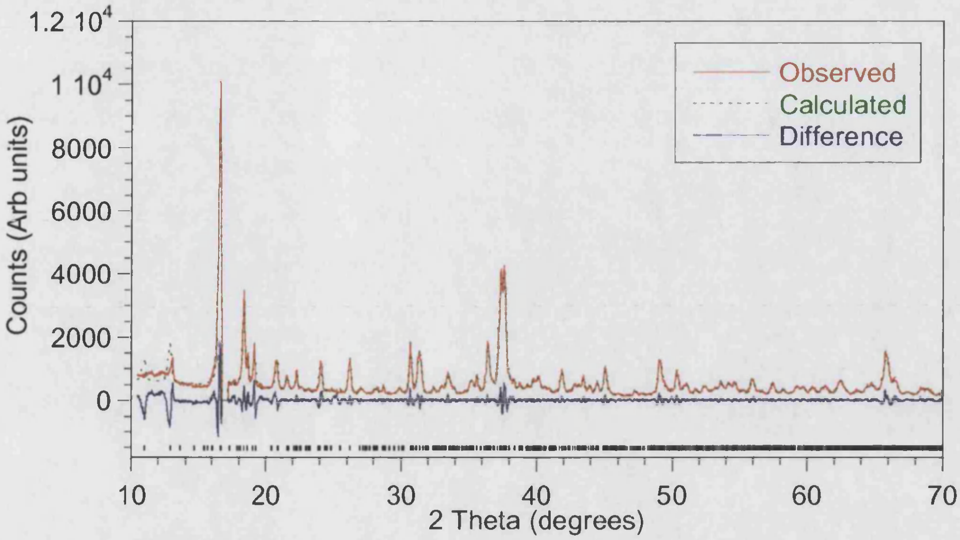

Figure 4.9. Observed, calculated and difference for the Lebail extraction of X-ray diffraction data of Na$_{0.17}$MnO$_2$ using model 2: $a = 16.17$ $b = 5.680$ $c = 12.28$ *and* $\beta = 92.3460^o$

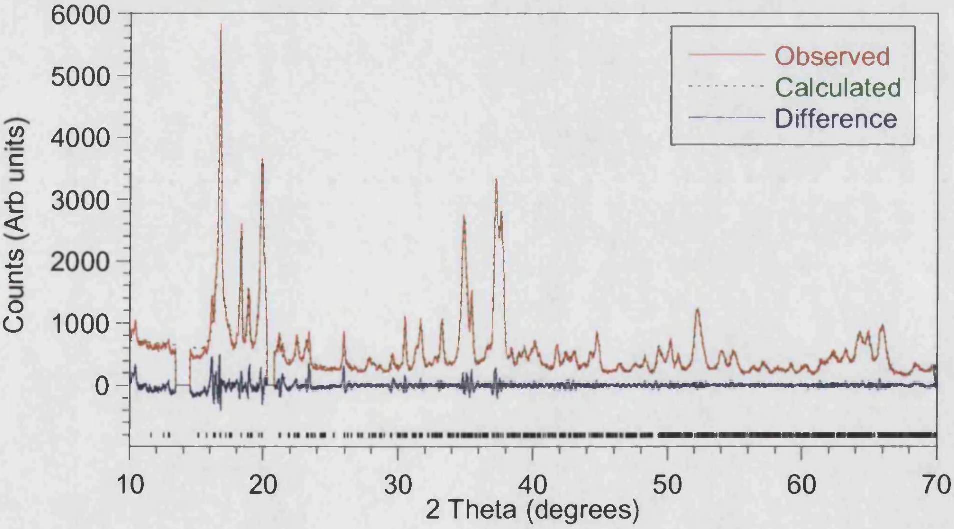

Figure 4.10. Observed, calculated and difference for the Lebail extraction of X-ray diffraction data of Li$_{0.26}$Na$_{0.16}$MnO$_2$ *using model 1:* $a = 14.82$ $b = 5.907$ $c = 11.31$ *and* $\beta = 105.166^o$.

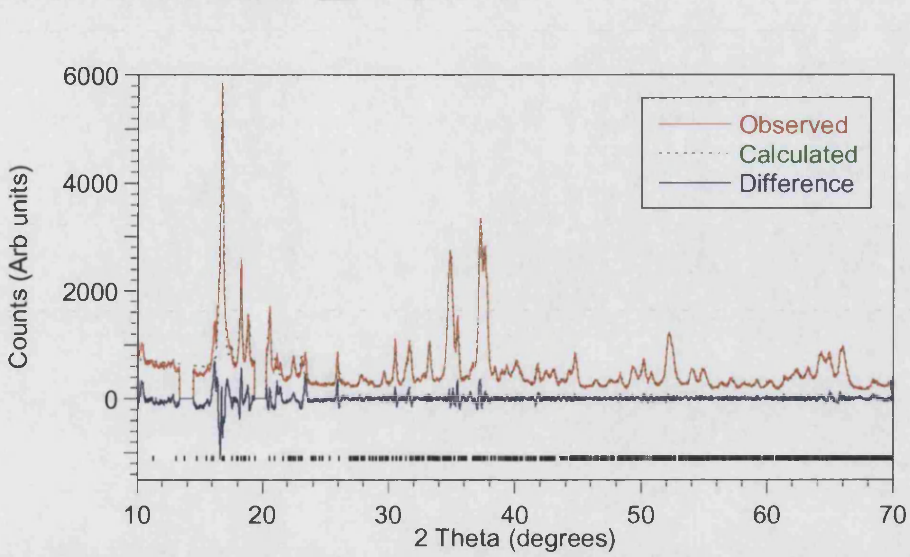

Figure 4.11. Observed, calculated and difference for the Lebail extraction of X-ray diffraction data of $Li_{0.26}Na_{0.16}MnO_2$ using model 2: *a = 16.17 b = 5.680 c = 12.28 and* $\beta = 92.3460^{o}$.

4.3.2. Thermal Analysis.

Thermal data have been collected using the Shimadzu TGA 50 analyser over a programmed temperature range of room temperature to 950°C at a heating rate of 10°C/min in an inert atmosphere of nitrogen for $Na_{0.39}MnO_2$, $Na_{0.17}MnO_2$ and $Li_{0.26}Na_{0.16}MnO_2$. The subsequent residues were identified using the Siemens D500 powder X-ray Diffractometer. No thermal data have been collected for the K, Y or the Yb doped materials but it would be expected that they would decompose in a similar fashion to the Li intercalated material. Table 4.5 summarises the decomposition routes for the materials studied.

Figure 4.12 shows the three step decomposition route in the TGA data for $Na_{0.39}MnO_2$. X-ray analysis of the final residue can be readily identified as $Na_{0.44}MnO_2$, which is more thermally stable, with trace amounts of Mn_2O_3 present as a secondary phase. The final decomposition temperature is consistent with that reported for the barium romanechite, however the final product in the decomposition of $(Ba,H_2O)_2Mn_5O_{10}$ is hollandite.[1] The first weight loss is most likely due to loss of small amounts of water absorbed from post reaction of the starting materials in air. This is followed by loss of oxygen as $Na_{0.44}MnO_2$ is formed.

Table 4.5. Decomposition routes and percentage weight loss for $Na_{0.40}MnO_2$, $Na_{0.16}MnO_2$ and $Li_{0.26}Na_{0.155}MnO_2$ in an inert atmosphere of nitrogen.

	1st decomposition			2nd decomposition			3rd decomposition		
Sample	Onset (°C)	Endset (°C)	% Wt loss	Onset (°C)	Endset (°C)	% Wt loss	Onset (°C)	Endset (°C)	% Wt loss
Na	235.79	333.65	0.300	450.77	518.21	0.327	653.09	778.33	2.695
Treated	291.26	436.27	2.031	474.94	522.76	1.741	713.05	806.67	3.002
Li	148.96	233.66	0.220	390.51	438.61	0.190	526.45	910.21	5.653

After treatment with acid the TGA (figure 4.13.) trace shows again a three-step decomposition as before. Most notably step 1 shows a larger percentage weight loss than the parent $Na_{0.40}MnO_2$ compound, which can be suggested as the loss of a greater amount of water as the result of the Na removal process performed in dilute acid solution. The final decomposition temperature observed for the acid treated material is higher, suggesting an increased thermal stability as a result of sodium removal, this is contrary to results observed for similar materials which show a decrease in thermal stability with the removal of the template cation.

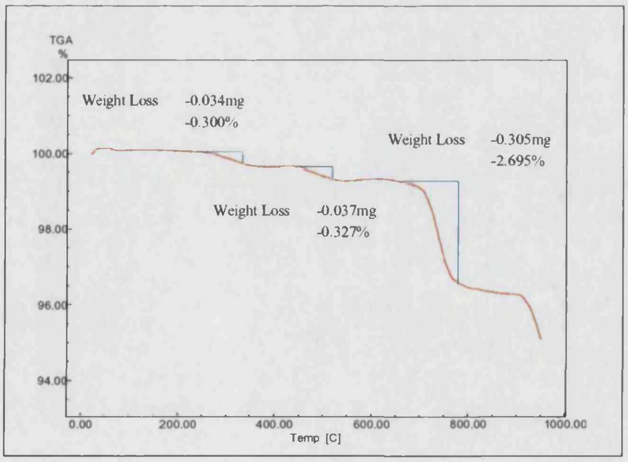

Figure 4.12. TGA trace showing three step decomposition route and percentage weight losses for $Na_{0.39}MnO_2$ in an inert atmosphere of nitrogen.

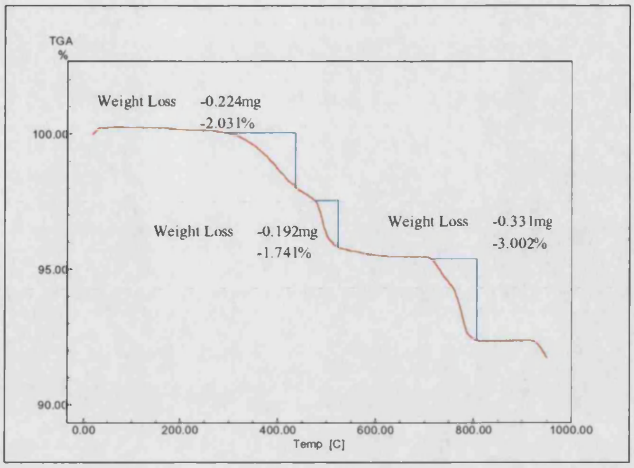

Figure 4.13. TGA trace showing three step decomposition route and percentage weight losses for Na$_{0.16}$MnO$_2$ *in an inert atmosphere of nitrogen.*

As expected the decomposition observed for the Li intercalated material proceeded in three steps. (figure 4.14.) As with the previous materials this first step can be attributed to loss of water from the tunnels, however this loss is small suggesting the replacement of the water with Li during the intercalation process. The final decomposition of the material to Na$_{0.44}$MnO$_2$ and Li spinel occurs at a much lower temperature suggesting loss in thermal stability as a result of intercalation. This suggests that this material is thermally more stable when the average manganese oxidation state tends towards +4.

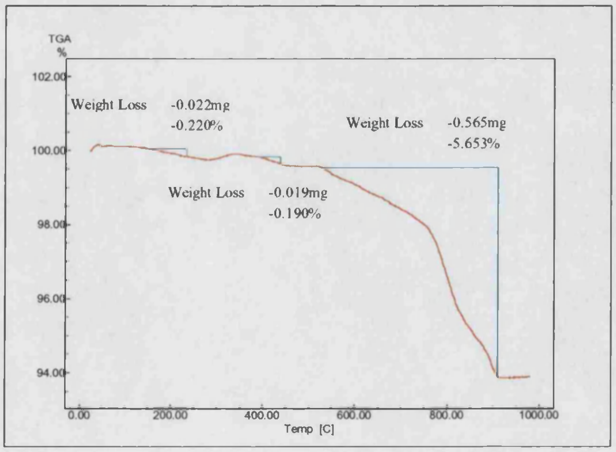

Figure 4.14. TGA trace showing here step decomposition route and percentage weight losses for Li$_{0.26}$Na$_{0.16}$MnO$_2$ *in an inert atmosphere of nitrogen.*

4.3.3. Magnetic properties.

The zero field cooled (ZFC) and field cooled (FC) magnetic susceptibility of $Na_{0.40}MnO_2$ in 1000G shows an anomaly around 5K on top of a paramagnetic signal, shown in figure 4.15. The insert shows the straight-line fit in the paramagnetic region (150 – 300K) to the Curie-Weiss law, yielding a negative Weiss constant indicative of antiferromagnetic exchange. The overlap of ZFC and FC suggests a long range antiferromagnetic state but the absence of a maximum shows most of the sample remains paramagnetic. The calculated and observed magnetic moments are in good agreement with each other and are given in table 4.6.

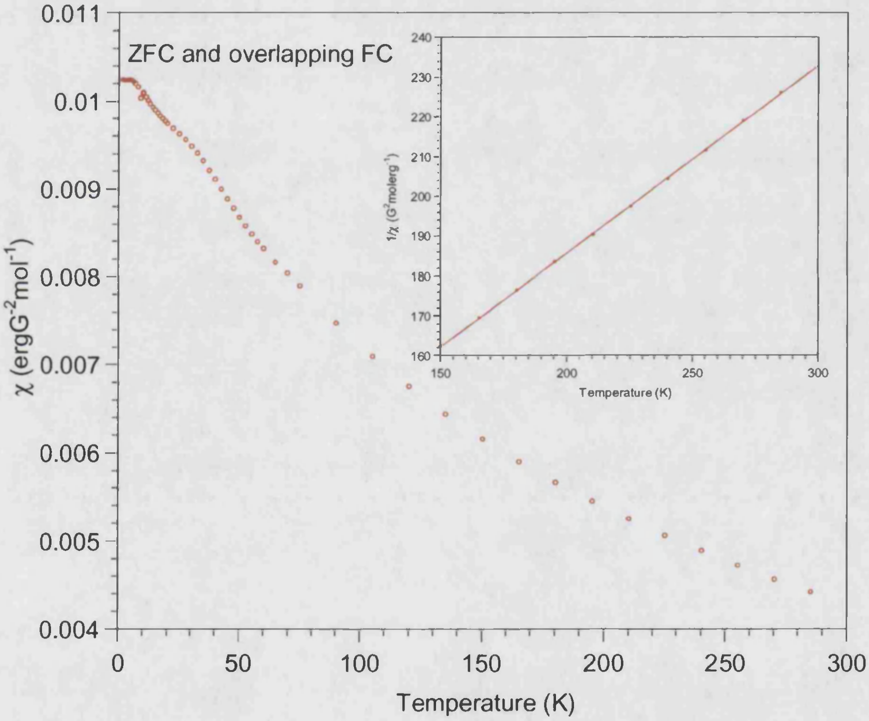

Figure 4.15. Zero field cooled (ZFC) and field cooled (FC) magnetic susceptibilities of $Na_{0.39}MnO_2$, showing paramagnetic character; inset shows Curie-Weiss behaviour.

Removal of the sodium from the tunnel site, $Na_{0.16}MnO_2$, significantly affects the observed magnetism. The susceptibility now shows a maximum at 22K and deviation from ZFC/FC susceptibility at 30K (figure 4.16). This deviation is consistent for a spin glass system. The magnetic susceptibility of the intercalated system, shown in figure 4.17 and 4.18 and compared to the other samples in figure 4.19 retains the same spin glass character. This is expected in such a system that has the disorder induced from the different moments on the Mn^{3+} and Mn^{4+} ions as well as the positional disorder associated with the disordered cations.

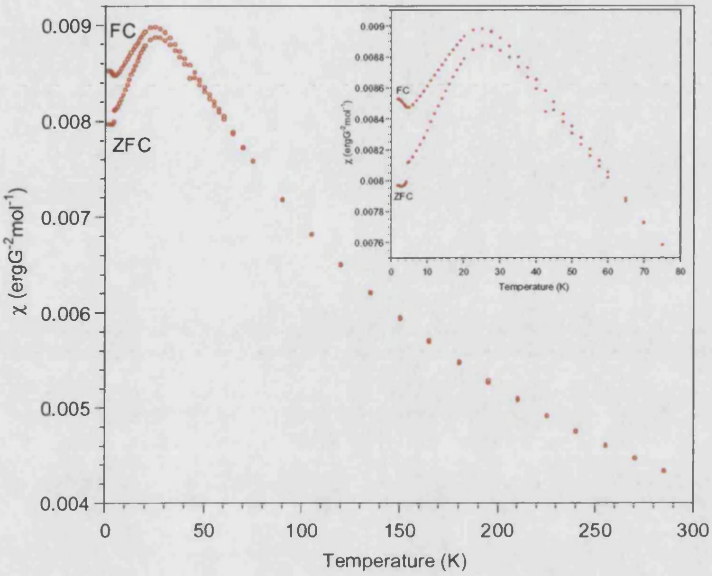

Figure 4.16. Magnetic susceptibility of $Na_{0.16}MnO_2$ *showing a maximum at around 22K with deviation from ZFC/FC susceptibility at 30K, typical of a transition to a spin glass state; inset shows the region below* T_F.

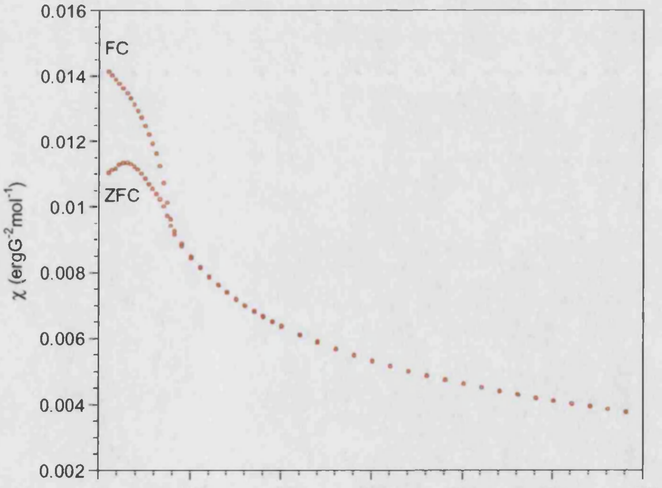

Figure 4.17. Magnetic susceptibility of $Li_{0.26}Na_{0.15}MnO_2$ *showing a maximum at around 15K with deviation from ZFC/FC susceptibility at 45K, typical of a transition to a spin glass state.*

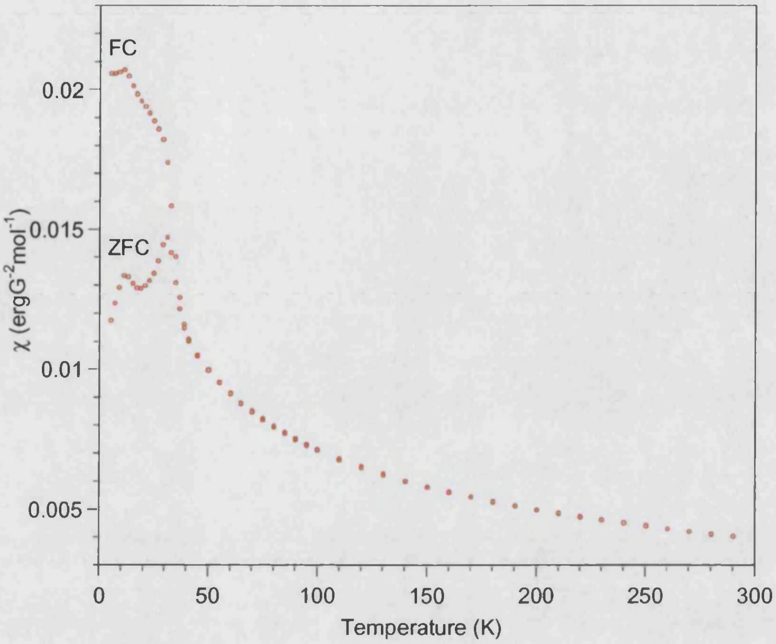

Figure 4.18. Magnetic susceptibility of $K_{0.05}Na_{0.15}MnO_2$ showing a maximum at around 22K with deviation from ZFC/FC susceptibility at 30K, typical of a transition to a spin glass state.

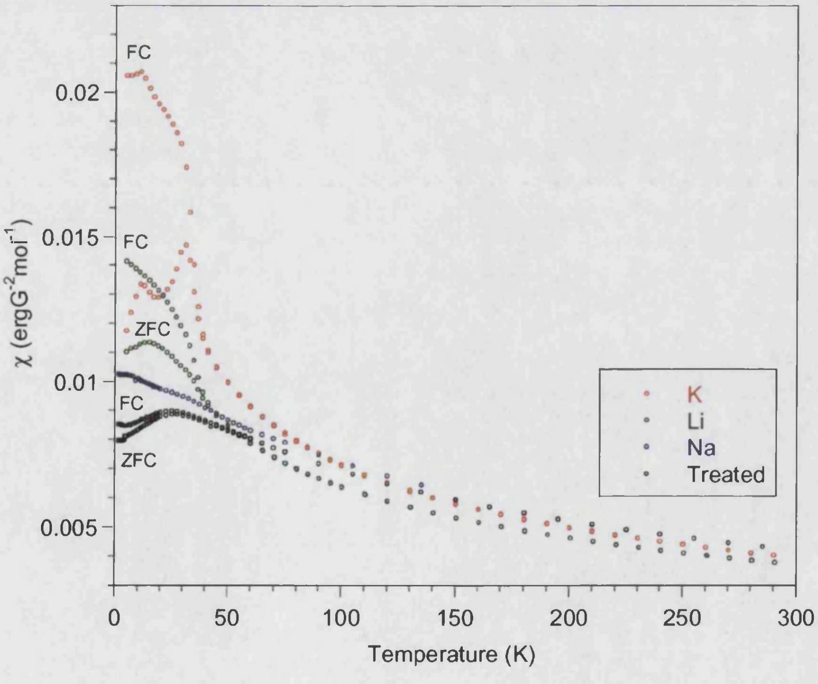

Figure 4.19. Magnetic susceptibilities of $Na_{0.39}MnO_2$ and intercalated species showing the transition from paramagnetic behaviour to a spin glass state.

The magnetic susceptibilities of the lanthanide samples are grossly different to that observed for those containing alkali earth metals (figures 4.20 and 4.21). All susceptibilities follow the dependence of a paramagnetic. The anomaly at 45K in $Yb_{0.26}Na_{0.05}MnO_2$ is assigned to an impurity. Figure 4.23 shows the magnetic susceptibilities of the lanthanide samples in comparison with $Na_{0.39}MnO_2$. Calculation of the observed magnetic moment from the Curie constant, C, gives a value of $3.85\mu_B$ suggesting an average manganese oxidation state of approximately 3+. If Yb^{3+} is intercalated into the structure this would result in an average manganese oxidation state of +2.60 with a calculated magnetic moment of $5.05\mu_B$, however it is more likely that Yb is intercalated into the framework as Yb^{2+} resulting in an average manganese oxidation state of +3.05 and calculated magnetic moment of $4.83\mu_B$ which is closer to that observed. This observation may offer an explanation as to why Yb can be intercalated into the framework but Ho, which, exists, as Ho^{3+} cannot.

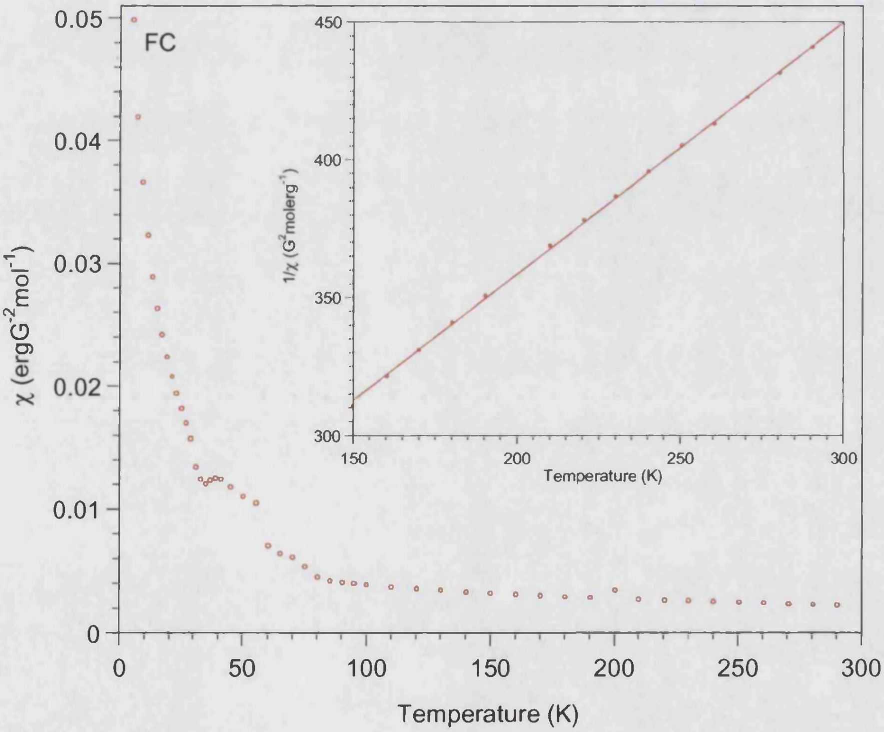

Figure 4.20. Field cooled (FC) magnetic susceptibility of $Y_{0.26}Na_{0.05}MnO_2$, showing paramagnetic character; inset shows Curie-Weiss behaviour.

Table 4.6. Curie constant, Weiss constant, observed and calculated magnetic moments for $Na_{0.40}MnO_2$ and intercalated species.

Sample	C (Kerg/G^2mol)	θ (K)	$T_N/T_F/T_C$ (K)	μ_{eff} (μ_B)	μ_{calc} (μ_B)
$Na_{0.39}MnO_2$	2.124(5)	-194.5(9)	5	4.12	4.36
$Na_{0.17}MnO_2$	2.166(5)	-214(1)	60	4.16	4.71
$Li_{0.26}Na_{0.15}MnO_2$	1.82(9)	-193(2)	45	3.81	4.45
$K_{0.05}Na_{0.15}MnO_2$	1.851(8)	-169(1)	45	3.84	4.08
$Y_{0.26}Na_{0.07}MnO_2$	1.355(6)	-189(1)	75	3.29	4.74
$Yb_{0.45}Na_{0.05}MnO_2$	1.86(1)	-149(2)	120	3.85	4.83

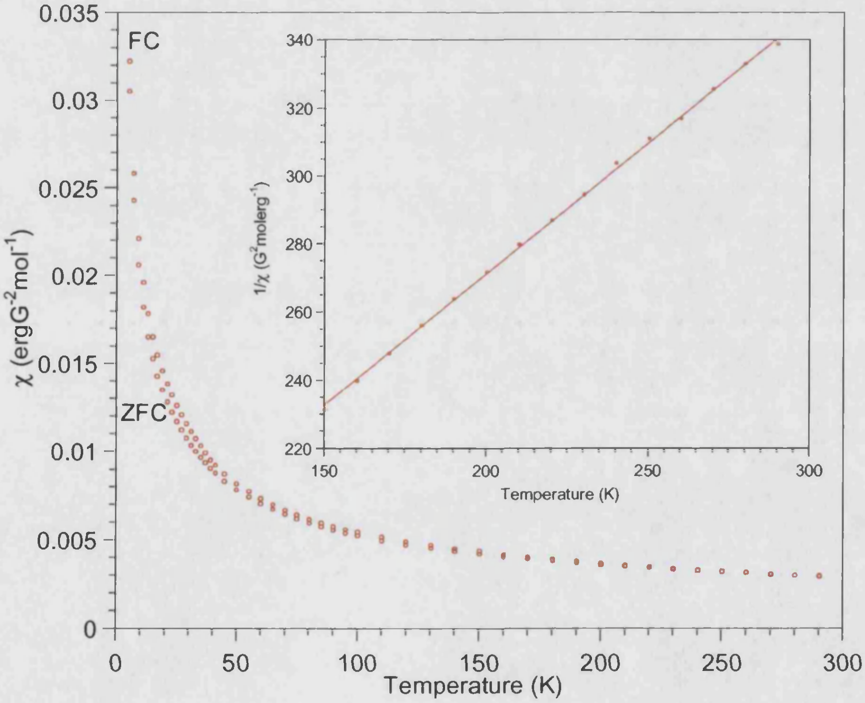

Figure 4.21. Zero field cooled (ZFC) and field cooled (FC) magnetic susceptibilities of $Yb_{0.45}Na_{0.05}MnO_2$, showing paramagnetic character; inset shows Curie-Weiss behaviour.

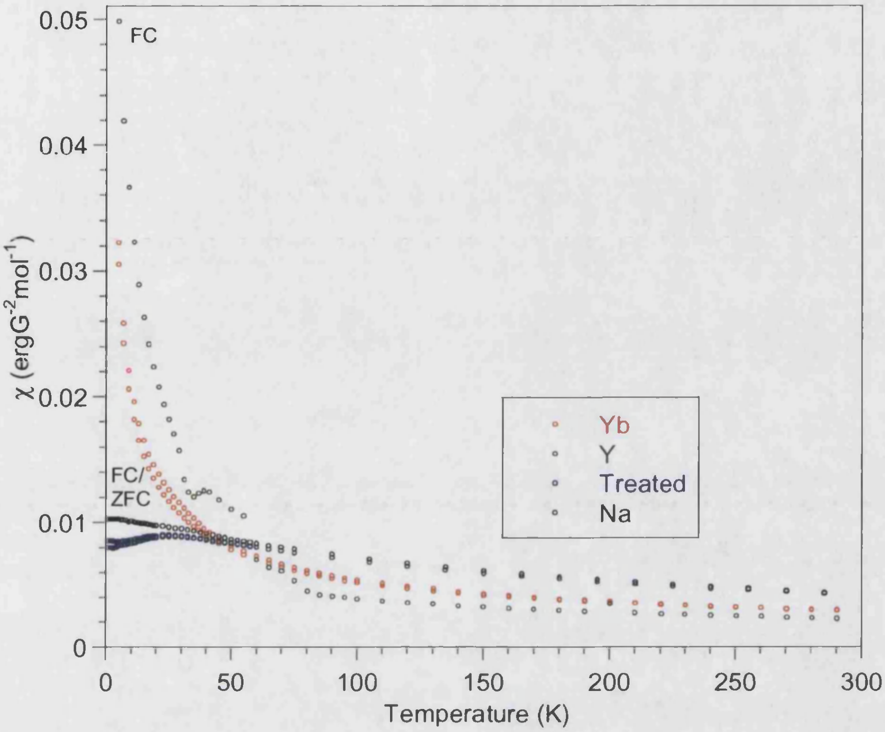

Figure 4.22. Magnetic susceptibilities of $Na_{0.39}MnO_2$ and lanthanide intercalated species showing paramagnetic behaviour.

4.3.4. Transport Properties.

Electrical resistivity of $Na_{0.40}MnO_2$ and $Li_{0.26}Na_{0.16}MnO_2$ has been collected using the 4-point DC method available on an Oxford Instruments Maglab over a temperature range of 150-350K using a current of 0.001mA. An exponential decrease of resistance with increasing temperature was observed for both materials, indicative of semi-conducting properties. (Figures 4.23 And 4.24) This is consistent with data published previously for these materials which are semiconducting over a temperature range of 150-650K.[6] The band gap was calculated from the slope of the Arrhenius plots given in figures 4.25 and 4.26, the plots showed the $Na_{0.40}MnO_2$ and $Li_{0.26}Na_{0.16}MnO_2$ to have band gaps well within the semiconductor range. The effect of doping Li into the material increases the band gap from 0.240(2) eV to 0.320(1) eV.

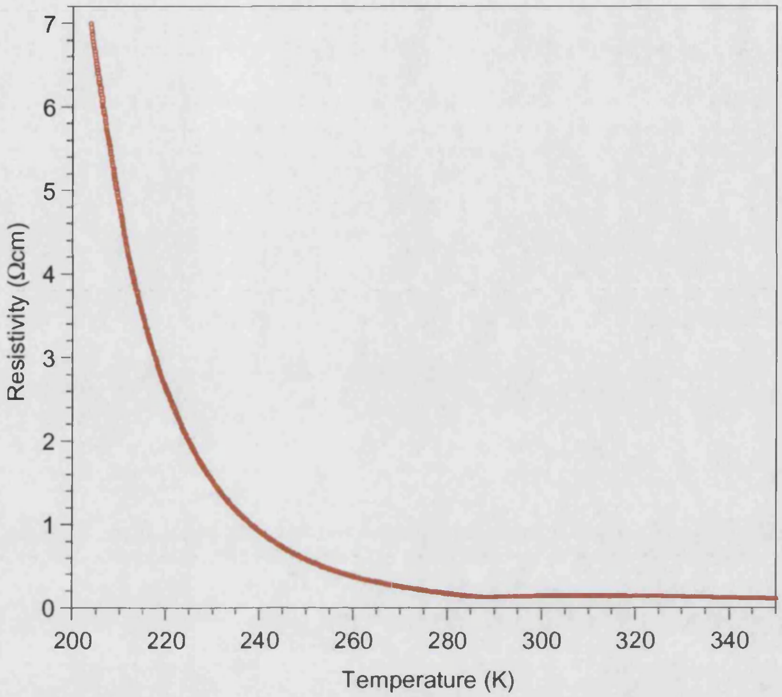

Figure 4.23. Resistivity of $Na_{0.39}MnO_2$ *as a function of temperature in zero field.*

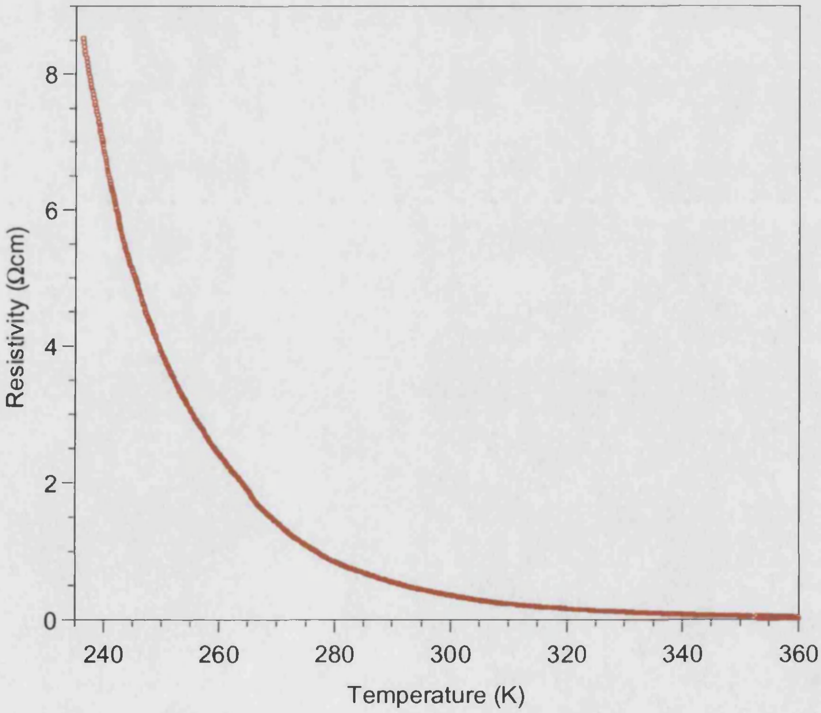

Figure 4.24. Resistivity of $Li_{0.26}Na_{0.16}MnO_2$ *as a function of temperature in zero field.*

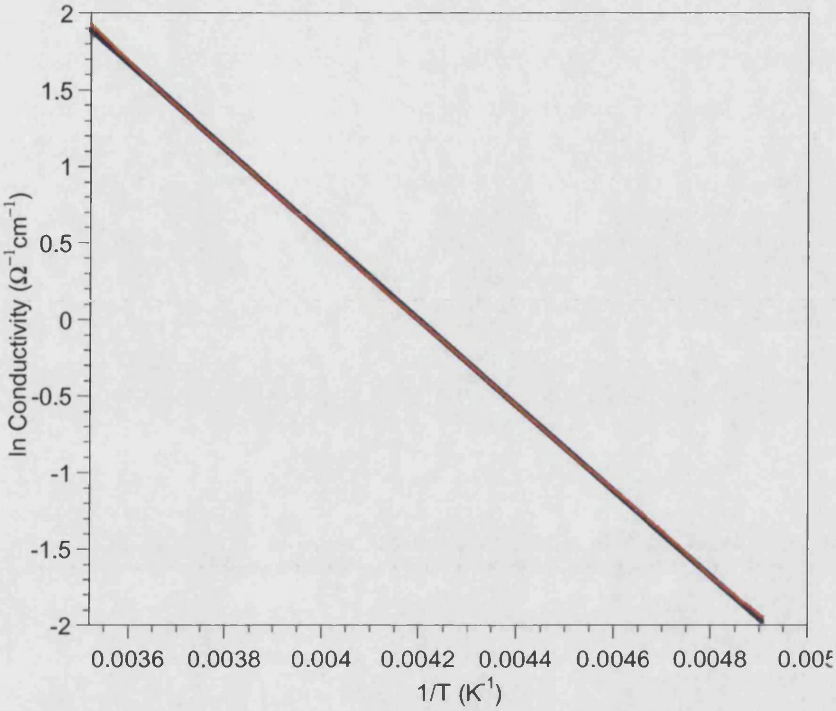

Figure 4.25. Arrhenius plot of ln conductivity Vs 1/temperature for $Na_{0.44}MnO_2$.

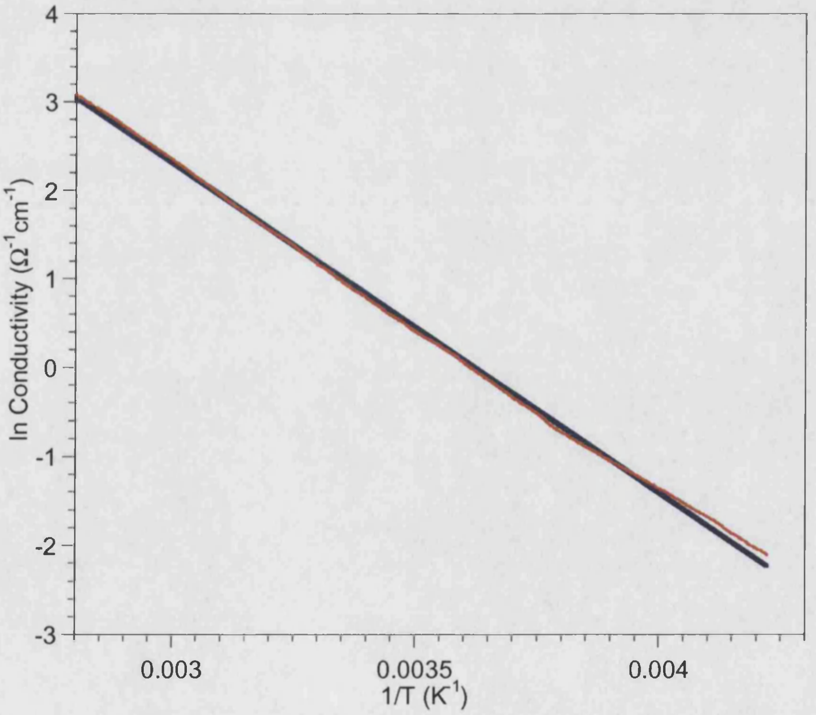

Figure 4.26. Arrhenius plot of ln conductivity Vs 1/temperature for $Li_{0.26}Na_{0.16}MnO_2$.

4.4. Conclusions.

A porous material with the formulae, $Na_{0.39}MnO_2$, can be prepared by solid state methods and identified as the phase first prepared by Parant *et al.*[6] Little literature exists for the Na romanechite, especially with respect to magnetic properties and is limited mostly to lithium cyclability for battery technology. Refinement of data collected proved difficult and gave poor fits to both full and Lebail refinements using the GSAS suite of programs. It is suggested that whilst this material is similar to $(Ba,H_2O)_2Mn_5O_{10}$ romanechite they are not identical either due to presence of large amounts of intergrowths affecting the peak positions and intensities or because of a slightly different framework structure. Evidence reported here confirms that the material is indeed porous with intercalation and deintercalation possible. Size limitations on the intercalation of cations is limited to potassium ions, attempts to intercalate Cs were not successful, this is not consistent with what you would expect for (2 x 3) pores and suggests that the tunnel is smaller and the structure is incorrect. Data collected shows the material to behave in a similar fashion to the $Na_{0.44}MnO_2$ material as opposed to the hollandite material. On thermal treatment the barium romanechite breaks down giving rise to the hollandite material, whilst the sodium analogue breaks down to $Na_{0.44}MnO_2$. Attempts to solve either the structure by direct methods or to model the many possible intergrowths were not successful and other avenues will need to be pursued to fully elucidate the structure, possibly through computational techniques.

4.5. References.

(1) D. L. Bish, J. E. Post, *American Mineralogist*, **1989**, *74*, 177.

(2) A. D. Wadsley, *Acta Crystallographica*, **1953**, *6*, 433.

(3) S. Turner, J. E. Post, *American Mineralogist*, **1988**, *73*, 1155.

(4) J. E. Post, D. L. Bish, *American Mineralogist*, **1988**, *73*, 861.

(5) O. Tamada, N. Yamamoto, *Mineralogical Journal*, **1986**, *13*, 130.

(6) J. P. Parant, R. Olazcuaga, M. Devalette, C. Fouassier, P. Hagenmuller, *Journal of Solid State Chemistry*, **1971**, *3*, 1.

(7) A. Mendiboure, C. Delmas, P. Hagenmuller, *Journal of Solid State Chemistry*, **1985**, *57*, 323.

(8) M. Tsuda, H. Arai, Y. Nemoto, Y. Sakurai, *Journal of the Electrochemical Society*, **2003**, *150(6)*, A659.

(9) M. Tsuda, H. Arai, Y. Nemoto, Y. Sakurai, *Journal of Power Sources*, **2001**, *102*, 135.

(10) R. Giovanoli, B. Balmer, *Chimica*, **1983**, 37*(11)*, 424.

(11) M. M. Doeff, T. J. Richardson., L. Kepley, *Journal of the Electrochemical Society*, **1996**, *143(8)*, 2507.

(12) M. M. Doeff, M. Y. Peng, Y. P. Ma, L. C. De Jonghe, *Journal of the Electrochemical Society*, **1994**, *141(11)*, L145.

(13) S. Turner, P. R. Buseck, *Science*, **1979**, *203*, 456.

(14) L. C. Nistor, G. Van Tendeloo, S. Amelinckx, *Journal of Solid State Chemistry*, **1994**, *109*, 152.

(15) Q. Feng, H. Kanoh, K. Ooi, *Journal of Materials Chemistry*, **1999**, *9(2)*, 319.

(16) S. L. Brock, N. G. Duan, Z. R. Tian, O. Giraldo, H. Zhou, S. L. Suib, *Chemistry of Materials*, **1998**, *10(10)*, 2619.

(17) R. Shirley, *The CRYSFIRE System for Automatic Powder Indexing*. **2000**, *v3.25*.

(18) A. Alltomore, M. C. Burla, M. Carnalli, B. Corrozzini, G. Cascarano, G. Giacovozzo, A. Guagliardi, A. G. G. Moliterni, G. Polidorri, R. Rizzi. *Sirware*; 1.01 ed.

(19) Q. Feng, H. Kanoh, Y. Miyai, K. Ooi, *Chemistry of Materials*, **1995**, *7(1)*, 148.

(20) D. R. Lide, *CRC Handbook of Chemistry and Physics*; 76 ed.; CRC Press: New York, **1995**; section 12.

5.1. Introduction.

The sodium manganese oxide, $Na_{0.44}MnO_2$ or $Na_4Mn_4^{III}Mn_5^{IV}O_{18}$ was synthesised in 1971 and found to be isostructural with the known compound, $Na_4Mn_4Ti_5O_{18}$.[1,2] The structure is orthorhombic with the Pbam space group and contains two separate manganese sites with MnO_6 octahedra and MnO_5 square pyramid units shown in figure 5.1. These units are linked together by corner and edge sharing forming two distinct tunnel sites parallel to c; the smaller tunnel (n1) is defined by four MnO_6 octahedra and two MnO_5 square pyramids, whereas the larger 's' shaped tunnels containing two different cation sites parallel to c (n2 and n3) are defined by ten MnO_6 octahedra and two MnO_5 square pyramids. Three crystallographically distinct cation sites within the framework have been suggested.[3] It has been suggested that whilst the smaller n1 site is approximately full, the 's' shaped tunnel sites are ⅔ and ⅓ full for the n2 and n3 sites respectively.[4]

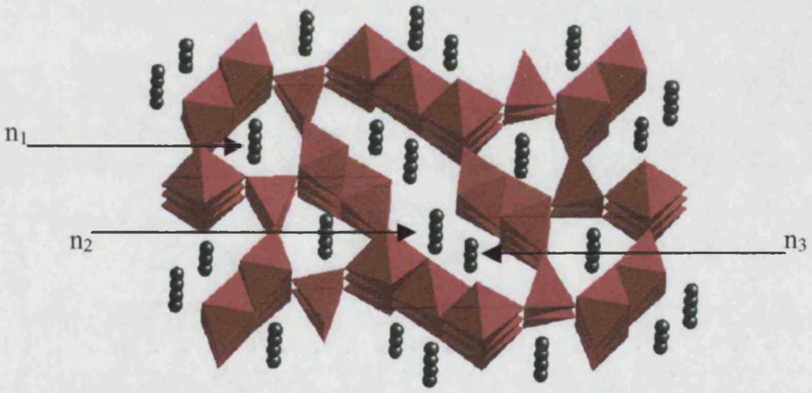

Figure 5.1. Structure of $Na_{0.44}MnO_2$ shown along the c-axis, where the pink squares represent the MnO_6 octahedra, the pink triangles represent the MnO_5 square pyramids and the green spheres are the sodium cations.

It was initially suggested that due to the occurrence of two different manganese sites (octahedral and pyramidal) that a hopping mechanism could be difficult, therefore making intercalation and de-intercalation of this compound impossible.[5] However, since then extensive studies have been conducted replacing the sodium with lithium for use in Lithium Batteries.[3,4,6] The main advantage of this material is that it does not transform to spinel-like phases during the electrochemical charge and discharge of the cell unlike some of the other manganese oxides and complete recovery of the capacity is obtained if cells are charged at a slow rate.[6,7] During these studies it has been shown that $Na_{0.44}MnO_2$ has an exceptional capacity for retention upon cycling and can intercalate 0.55-0.6 Li^+ or Na^+ ions with a retention capacity of 160-180mAh/g.[8]

Whilst it is commonly thought that this structure has a formula of $Na_{0.44}MnO_2$, consistent with that reported for the isostructural titanate, it has been shown to be prepared with small amounts of Mn_2O_3 present as a second phase.[8] The preparation of a pure phase was reported to be possible by the pH controlled reduction of sodium permanganate with sodium iodide and subsequent firing in an atmosphere of air at temperatures greater than 600°C.[7,9] Rietveld analysis of this product gave a formula of $Na_{0.50}MnO_2$, and the authors suggest that previous preparations where, $x \neq 0.50$, contains impurities. This compound can also be prepared by hydrothermal treatment of MnO_2 with NaOH at temperatures above 500°C.[10]

Original work on $Na_{0.44}MnO_2$ suggests paramagnetic behaviour down to 20K.[2] However, more recent work on the $Na_{0.50}MnO_2$ phase shows antiferromagnetic order at T_N φ 30K, with an observed magnetic moment of 4.027 in good agreement with that expected.[7]

An isostructural compound with the formula $Na_{1.1}Ca_{1.8}Mn_9O_{18}$ has been reported,[11] with the positions of the mixed cations differing to that seen for the pure Na case. The insertion of Ca into the tunnel sites was achieved by solid-state reaction of CaO, MnO_2 and $NaMnO_2$ directly. This material exhibits a high resistivity ($2.5 \times 10^4 \Omega$cm) at room temperature, which increases rapidly as the temperature decreases. The resisitivity becomes too high to be measured below 220K. The magnetic susceptibility was measured at 3000G over the temperature range of 130-400K and showed the material to be paramagnetic. However, the presence of the perovskite, $CaMnO_3$, prevents any interpretation of the magnetic susceptibility below 122K.

More recently the possibility of doping the manganese framework sites with other transition metal elements has been explored by Doeff *et al.* The substitution of Cu^{2+} on to the Mn^{4+} sites within the framework was achieved, with a maximum intercalation of 11%. The electrochemical characteristics of the lithium intercalated species showed a reduction in capacity from that of the copper intercalated sodium species.[12]

Work in this chapter reports the synthesis of $Na_{0.44}MnO_2$, the subsequent removal of the Na^+ counter ion and the intercalation of foreign species into the tunnel site. The effects of intercalation on the structural, magnetic and electrical properties are discussed. The possibility of doping the framework site with Fe has also been considered and is reported here.

5.2. Intercalation of the tunnel Site.

5.2.1. Synthesis.

$Na_{0.44}MnO_2$ was prepared as reported by Doeff *et al*, stoichiometric ratios of $NaCO_3$ and Mn_2O_3 were ground together using an agate pestle and mortar to thoroughly mix the starting materials before being transferred to a furnace at 700°C in air for 2-3 days.[4] A slight excess of $NaCO_3$ was employed to minimize the possible formation of a manganese oxide second phase due to the loss of sodium during the reaction.[3] Powder neutron diffraction was collected using the High Resolution Powder Neutron Diffractometer (HRPD) at the Rutherford Appleton Laboratories in Didcot, Oxon, UK.

The sodium was removed from within the tunnel by stirring the prepared $Na_{0.44}MnO_2$ with a solution of approximately 1M, HCl overnight at room temperature.[8] In the insertion study the treated $Na_{0.44}MnO_2$ was reacted with an excess of LiI, with iodine being liberated instantaneously (equation 5.1) and KOH. (Equation 5.2.)

$$xLiI + Na_{0.44-y}MnO_2 \rightarrow \tfrac{1}{2}xI_2 + Li_xNa_{0.44-y}MnO_2 \qquad \text{-(5.1.)}$$

$$xKOH + Na_{0.44-y}MnO_2 \rightarrow xOH^- + K_xNa_{0.44-y}MnO_2 \qquad \text{-(5.2.)}$$

It was attempted to remove the intercalated potassium from the tunnels by the same method employed for sodium removal. This however, proved impossible, with only a negligible change in potassium content. Prolonged stirring in acid results in the dissolution of some of the product rather than further deintercalation. This is consistent with results observed for Hollandite, which suggests that the level of alkali metal insertion is inversely related to ionic radii, however, cation retention upon acid treatment shows the opposite relationship and is more favourable for larger cations. [13] The removal of lithium from the tunnels was not tried due to restraints on the amount of sample and dissolution of the material during the reaction but it is expected that removal could be achieved in this manner.

5.2.2. Results and Discussion.

5.2.2.1. Elemental Analysis/EDX.

Elemental Analysis and EDX results are summarised in table 5.1. Complete removal of the sodium should theoretically be possible by the reduction of the Mn^{4+} sites to Mn^{3+} sites within the framework. However, realistically complete removal of the template ion from within the framework results in decreased thermal stability and the subsequent 'collapse' of the framework. The removal of sodium appears to be only possible from the large 's' shape tunnel sites giving a minimum Na content of $x = 0.20$.[8] The Na in the smaller channels may be too tightly bound with strong Na-O interactions to allow deintercalation. Since, the EDX results show a lower than expected sodium content, with a minimum content of $x = 0.17$ and an original sodium content of 0.36 it can be suggested that a smaller proportion of the (n1) tunnels are filled than in previously reported materials. A maximum intercalation of $x = 0.60$ was observed by Doeff *et al*, which cannot be achieved with the intercalation of foreign species into the tunnel sites. A maximum fill corresponding to Na + M, where M is the foreign cation, of $x = 0.42$ is observed for Li without the use of a galvanic cell and decreases with increasing ionic radii of the intercalated cation. This suggests that it is not energetically favourable to fill all three tunnel sites within this material. Figures 5.2 a and b show increasing ionic radii with increasing average manganese oxidation state and decreasing intercalation amount with increasing ionic radii respectively. It is worth considering that differences in selectivities may be due to the differences in co-ordination of the different cations within the tunnel sites and hence differences in interstitial sites as this affects the ionic radii, as seen for Ca intercalation.[11,14]

Table 5.1. Results obtained by elemental analysis and EDX results for the chemical composition of $Na_{0.44}MnO_2$ *and intercalated analogues.*

Sample	Elemental Analysis	EDX Analysis
$Na_{0.44}MnO_2$	Not Collected	$Na_{0.360(4)}MnO_2$
$Na_{0.44-y}MnO_2$ (acid treated sample)	Not Collected	$Na_{0.170(2)}MnO_2$
$Li_xNa_{0.44-y}MnO_2$	$Li_{0.260(3)}Na_{0.170(2)}MnO_2$	$Li_xNa_{0.170(2)}MnO_2^*$
$K_xNa_{0.44-y}MnO_2$	Not Collected	$K_{0.0800(8)}Na_{0.140(1)}MnO_2$

* Li content cannot be analysed by the EDX method.

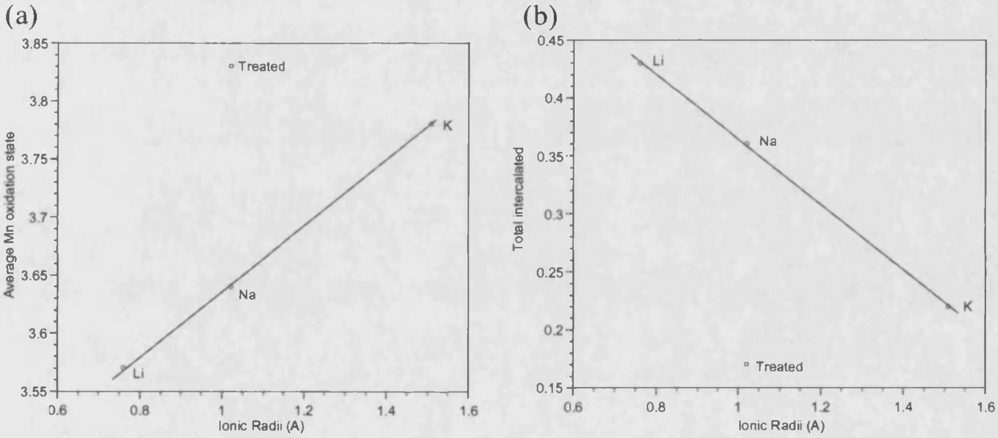

Figure 5.2. (a) Increasing average manganese oxidation state and (b) decreasing intercalation amounts as a function of ionic radii.

5.2.2.2. Thermal Analysis.

Thermal data have been collected over a programmed temperature range of room temperature to 950°C at a heating rate of 10°C/min in an inert atmosphere of nitrogen. DSC measurements were collected over a temperature range of room temperature to 600°C by measuring the amount of heat required to maintain the temperature of the sample and that of the reference equal. The subsequent residues were identified by X-ray diffraction. All calculations were made assuming the compositions observed by

EDX analysis to be true. Table 5.2 gives the decomposition routes for $Na_{0.44}MnO_2$ and its treated analogues.

Table 5.2. Decomposition routes and percentage weight loss for $Na_{0.44}MnO_2$ and its treated analogues in an inert atmosphere of nitrogen.

Sample	1st Decomposition			2nd Decomposition			3rd Decomposition		
	onset (°C)	endset (°C)	%Wt loss	onset (°C)	endset (°C)	%Wt loss	onset (°C)	endset (°C)	%Wt loss
$Na_{0.36}$	300.29	438.93	0.774	668.82	809.47	1.522			
$Na_{0.17}$	146.05	297.79	0.715	398.41	579.61	2.958			
$Li_{0.26}Na_{0.17}$	45.02	387.60	2.385	531.80	897.11	5.198			
$K_{0.14}Na_{0.14}$	30.32	350.86	0.811	386.09	648.88	2.991	672.75	937.12	4.944

Sample $Na_{0.36}MnO_2$ undergoes a two-step decomposition as illustrated in figure 5.3. The first step is marked by a small weight loss of 0.774%, followed by a second weight loss of 1.522%. X-ray analysis of the residue remaining after TGA analysis is readily identifiable as the starting material, $Na_{0.44}MnO_2$, with trace amounts of Mn_2O_3 second phase. Since this phase is usually stable at these temperatures, it would be expected to see no evidence of thermal decomposition, however, due to a slightly low sodium content from the ideal of 0.44, observed in the EDX analysis, this phase is not stable at these elevated temperatures and therefore decomposes to form the more sodium rich $Na_{0.44}MnO_2$ with loss of oxygen and corresponding to a lower Mn oxidation state consistent with the reducing environment.

A two-step decomposition route is also evident in $Na_{0.16}MnO_2$ where the Na content is low as a result of the acid leaching (Figure 5.4). These two weight losses can be contributed firstly to loss of water from the tunnel sites acquired during the sodium removal process and secondly to decomposition of $Na_{0.16}MnO_2$ to $Na_{0.44}MnO_2$ and are in good agreement with those previously published by Doeff *et al.*[4] It is evident that there is a reduction in stability as a result of sodium removal, with the decomposition beginning at a lower temperature in $Na_{0.16}MnO_2$ than in $Na_{0.36}MnO_2$. During decomposition small amounts of the oxide Mn_2O_3 are also formed.

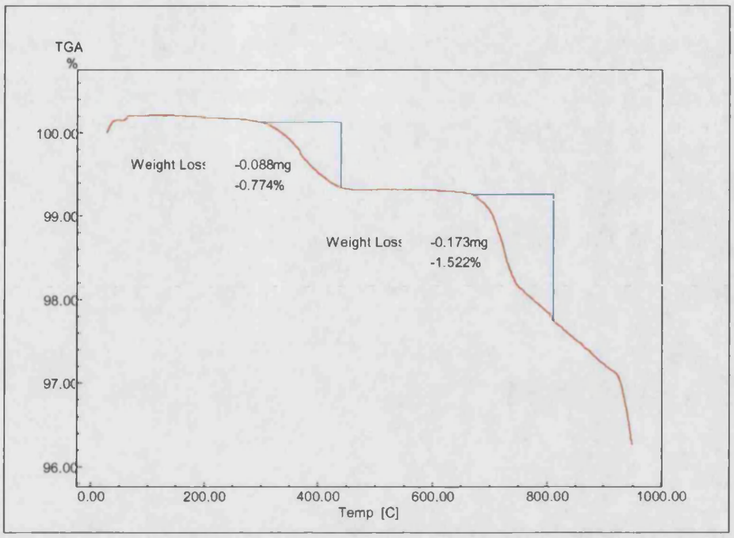

Figure 5.3. TGA trace showing the two step decomposition route and percentage weight loss for $Na_{0.44}MnO_2$ in an inert atmosphere of nitrogen.

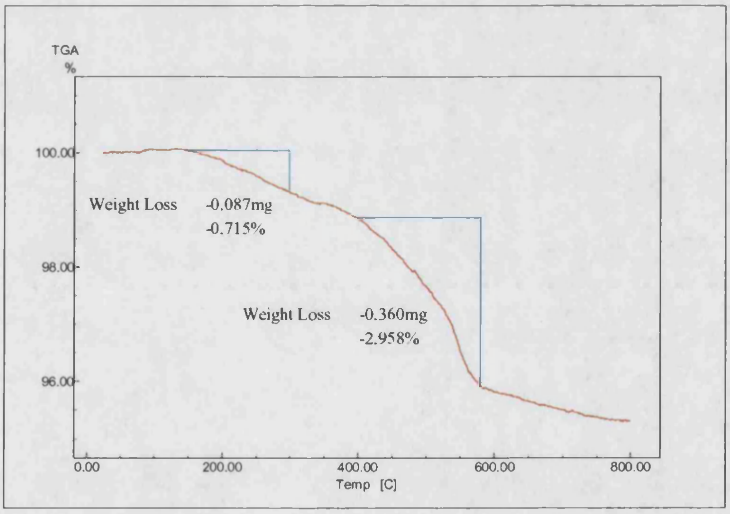

Figure 5.4. TGA trace showing the two step decomposition route and percentage weight loss for $Na_{0.16}MnO_2$ in an inert atmosphere of nitrogen.

As expected $Li_{0.26}Na_{0.17}MnO_2$ also shows a two-step decomposition, with the first step again being attributable to loss of water, a broad endothermic peak in the DSC marks this (Figure 5.5). The most notable difference as a result of lithium intercalation is the complete decomposition of the $Na_{0.44}MnO_2$ type phase to a mixture of more stable Li spinel-type materials and sodium oxides as given by equation 5.3. At the beginning of this decomposition is a large exothermic peak indicating a phase change. An increase in thermal stability is observed, upon the insertion of Li into the tunnel sites. The $NaMn_2O_4$ is not known and not therefore a path of decomposition for the previous compounds.

$$Li_{0.26}Na_{0.155}MnO_2 \rightarrow 0.081Li_2MnO_4 + 0.098LiMnO_2 + 0.27Mn_3O_4 + 0.085Na_2O + 0.15O_2\uparrow \qquad \text{-(5.3)}$$

Unexpectedly $K_{0.08}Na_{0.14}MnO_2$ undergoes a three-step decomposition route as illustrated by equations 5.4-5.6. (Figure 5.6) As with all these materials a broad endothermic peak is observed in the DSC at this first step, yielding a weight loss of 0.811% equivalent to loss of water from the surface and from the tunnel sites. Step two shows a weight loss of 2.991% and is accompanied by a broad endothermic shoulder to a very pronounced endothermic peak; this is equivalent to loss of oxygen as the metastable potassium-sodium manganate breaks down to form the more stable $Na_{0.44}MnO_2$, Mn_2O_3 and $KMnO_2$ as identified by X-ray analysis of the DSC residues. The third weight loss (4.944%) can be attributed to loss of oxygen as the remaining $Na_{0.44}MnO_2$ reacts with the other oxides to form a mixture of manganese oxides, Na_4MnO_4, K_2MnO_4, $K_2Mn_4O_8$ and some residual $KMnO_2$. Had DSC data been collected at this temperature we would expect to see an exothermic peak due to the phase change observed.

$$K_{0.08}Na_{0.14}MnO_2 \bullet 0.046H_2O \rightarrow K_{0.08}Na_{0.14}MnO_2 + 0.046H_2O \qquad \text{-(5.4)}$$

$$K_{0.08}Na_{0.14}MnO_2 \rightarrow Na_{0.44}MnO_2 + 0.34Mn_2O_3 + 0.08KMnO_2 + 0.09O_2\uparrow \qquad \text{-(5.5)}$$

$$Na_{0.44}MnO_2 + 0.34Mn_2O_3 + 0.08KMnO_2 \rightarrow 0.035Na_4MnO_4 + 0.03KMnO_2 + 0.02K_2MnO_4 + 0.005K_2Mn_4O_8 + 0.2575Mn_2O_3 + 0.01Mn_3O_4 + 0.35MnO_{1.88} + 0.14O_2\uparrow \qquad \text{-(5.6)}$$

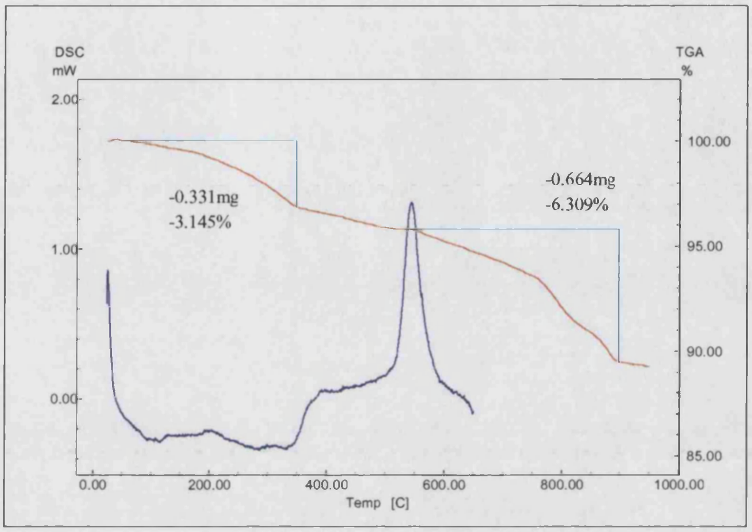

Figure 5.5. TGA trace showing the two step decomposition route and percentage weight loss for $Li_{0.26}Na_{0.155}MnO_2$ in an inert atmosphere of nitrogen.

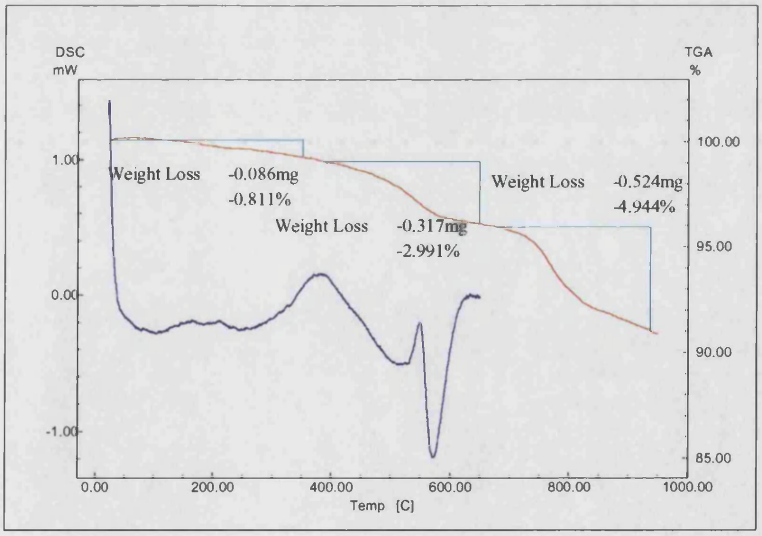

Figure 5.6. TGA trace showing the three step decomposition route and percentage weight loss for $K_{0.08}Na_{0.14}MnO_2$ in an inert atmosphere of nitrogen.

Removal of the sodium from the tunnel sites results in decrease in the thermal stability of the phase. However, whilst the intercalation of different cations into the now vacant tunnel sites initially results in an increase in thermal stability relative to the acid leached phase these samples eventually degrade to more stable phases. Complete formulae for all samples including waters of crystallization are given in table 5.3.

Table 5.3. Complete formulae and corresponding molecular weights for $Na_{0.44}MnO_2$ *and intercalated species.*

Sample	Formulae	Molecular Weight
$Na_{0.44}MnO_2$	$Na_{0.36}MnO_2$	95.1964
$Na_{0.44-y}MnO_2$	$Na_{0.17}MnO_2 \bullet 0.036H_2O$	91.2649
$Li_xNa_{0.44-y}MnO_2$	$Li_{0.26}Na_{0.17}MnO_2 \bullet 0.123H_2O$	94.8668
$K_xNa_{0.44-y}MnO_2$	$K_{0.08}Na_{0.14}MnO_2 \bullet 0.046H_2O$	94.1133

5.2.2.3. Diffraction.

Rietveld refinement of HRPD data at room temperature gave an Rwp value of 11.90% compared with 25.23% using laboratory X-ray data. The refined patterns, showing the observed and calculated diffraction data, as well as the difference curve are given in figure 5.7 (a) and (b) with the final parameters given in tables 5.4 and 5.5. Refinement of the sodium occupancies support the EDX results with a lower than full occupancy being observed for the n_1 site. However, the refined fractional occupancy of the second site in the 's' shaped tunnels namely the n_3 site is slightly fuller than expected giving rise to an artificially high sodium content of 0.47. The crystals of $Na_{0.44}MnO_2$ show a tendency for preferred orientation lying along the h01 axis, and led to poor agreement in the X-ray fits. Additional inconsistencies in the observed intensities of the peaks in both the neutron and X-ray data are due to the presence of intergrowths in this material. All atom positions, bond lengths and angles are in good correlation with those reported for $Li_{0.44}MnO_2$.[3] A slight amount of second phase is observed in this material and can be identified as Mn_2O_3 Bixbyite, for the purpose of refinement these peaks were excluded from the X-ray data.

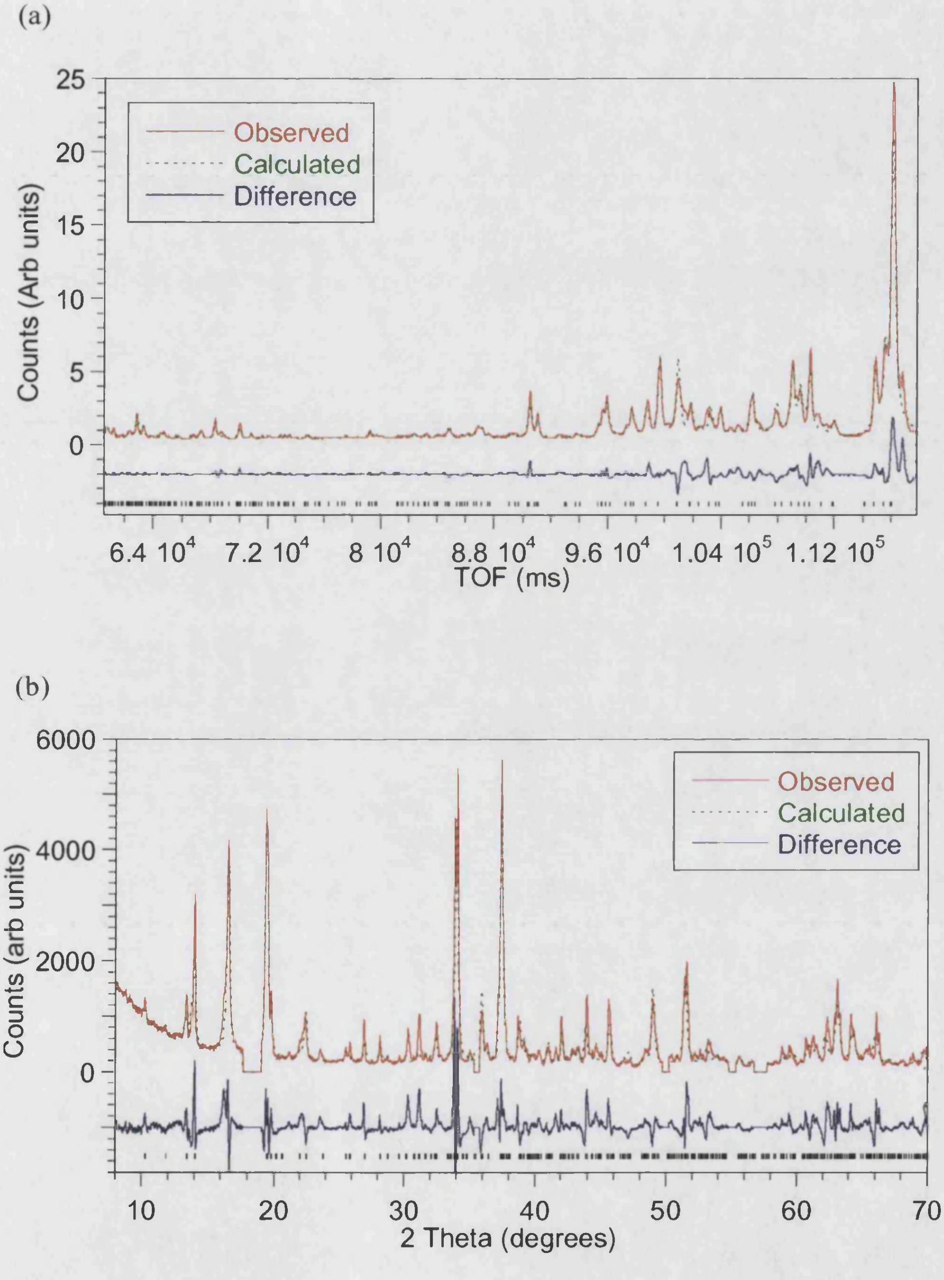

Figure 5.7. Observed, calculated and difference for the joint Rietveld refinement of (a) powder neutron data and (b) X-ray data for $Na_{0.44}MnO_2$ refined in the orthorhombic Pbam space group.

Table 5.4. Final lattice parameters and goodness of fit parameters derived from the joint Rietveld refinement of neutron and powder X-ray diffraction of $Na_{0.44}MnO_2$ *refined in space group Pbam.*

a (Å)	b (Å)	c (Å)	Cell volume ($Å^3$)	χ^2	WRp (%)	Rp (%)
9.11595(23)	26.4125(6)	2.83048(6)	681.510(28)	43.35	13.71	18.02

Table 5.5. Refined atom positions, thermal parameters and fractional occupancies from the joint Rietveld profile refinements for neutron and powder X-ray diffraction of $Na_{0.44}MnO_2$ *refined in space group Pbam.*

Atom	x	y	z	Ui/Ue x 100	Fractional occupancy
Mn1	0	0.5	0	0.79(24)	1.00
Mn2	0.3739(13)	0.3047(4)	0.5	2.18(38)	1.00
Mn3	0.0234(11)	0.1121(4)	0	0.69(33)	1.00
Mn4	0.0346(11)	0.1121(4)	0	0.85(34)	1.00
Mn5	0.3566(14)	0.0872(5)	0.5	3.80(42)	1.00
O6	0.3570(8)	-0.00071(34)	0.5	1.35(30)	1.00
O7	0.2260(10)	0.09253(36)	0	3.05(32)	1.00
O8	0.0435(11)	0.15659(36)	0.5	4.55(35)	1.00
O9	0.4359(9)	0.17009(34)	0.5	2.02(27)	1.00
O10	0.1730(9)	0.28060(28)	0.5	0.28(25)	1.00
O11	0.4257(9)	0.26518(28)	0	1.23(28)	1.00
O12	0.3177(11)	0.35478(38)	0	2.78(30)	1.00
O13	0.5081(9)	0.07219(36)	0	1.29(29)	1.00
O14	0.4772(9)	0.43375(32)	0.5	3.60(35)	1.00
Na	0.2100(22)	0.1957(7)	0	5.1(13)	0.85(6)
Na	0.2237(58)	0.4075(19)	0.5	14.5(31)	0.56(8)
Na	0.1150(37)	-0.0066(11)	0	9.6(18)	0.72(6)

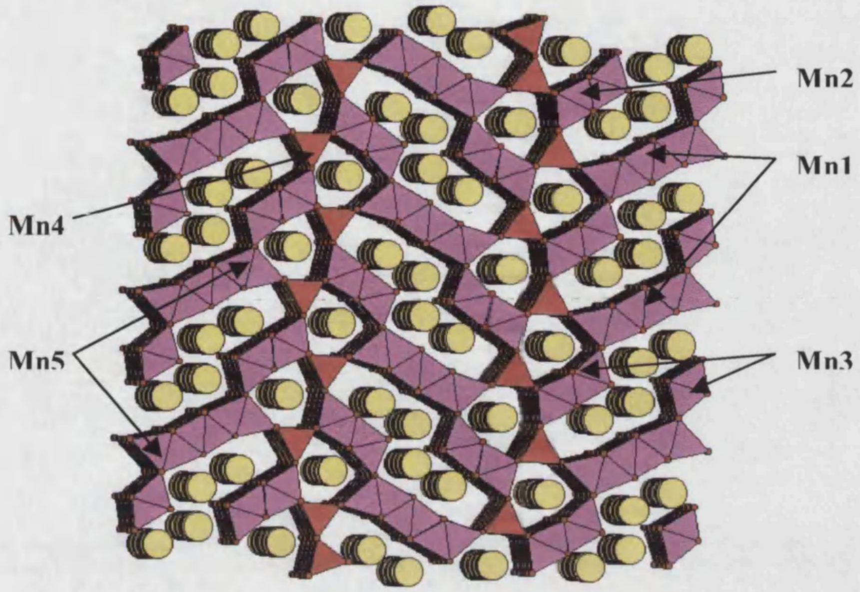

Figure 5.8. Representation of $Na_{0.44}MnO_2$ illustrating manganese ion sites plotted from the Rietveld refined atom positions given in table 5.5, where the pink squares represent the MnO_6 octahedra, the pink triangles the MnO_5 square pyramids and the yellow spheres the sodium cations.

Table 5.6. Bond lengths from the joint refinements for the neutron and X-ray refinement of $Na_{0.44}MnO_2$ in the Pbam space group.

	Mn1 (Å)	Mn2 (Å)	Mn3 (Å)	Mn4 (Å)	Mn5 (Å)
O	1.924(5)	1.854(15)	1.918(12)	1.782(8)	2.322(14)
O	1.924(5)	1.939(13)	1.848(8)	1.782(8)	1.855(10)
O	1.924(5)	1.821(8)	1.848(8)	2.021(8)	1.855(10)
O	1.924(5)	1.821(8)	2.069(13)	2.021(8)	2.306(13)
O	1.908(9)	2.004(10)	1.910(8)	2.153(12)	2.017(10)
O	1.908(9)	2.004(10)	1.910(8)		2.017(10)
Total valence	+3.806	+4.017	+3.893	+3.135	+2.916

Bond lengths indicate that the Mn^{3+} and Mn^{4+} order on crystallographically distinct sites with the Mn^{3+} occupying the 5 coordinate Mn4 site and the 6 coordinate

Mn5 site as shown in figure 5.8. The X-ray diffraction patterns of the intercalated systems are shown as a function of increasing average manganese oxidation state in figure 5.9. There is some shift in peaks observed consistent with changes in the unit cell parameters as a result of the intercalation process. It has been reported previously that very small changes in lattice parameters can shift many of the peak positions and can make it appear as though they either overlap or split as observed here.[4] The observed disappearance of some peaks between the treated analogues and the parent material, $Na_{0.44}MnO_2$, is due to the removal of some of the Mn_2O_3 second phase during acid leaching of the sodium site.

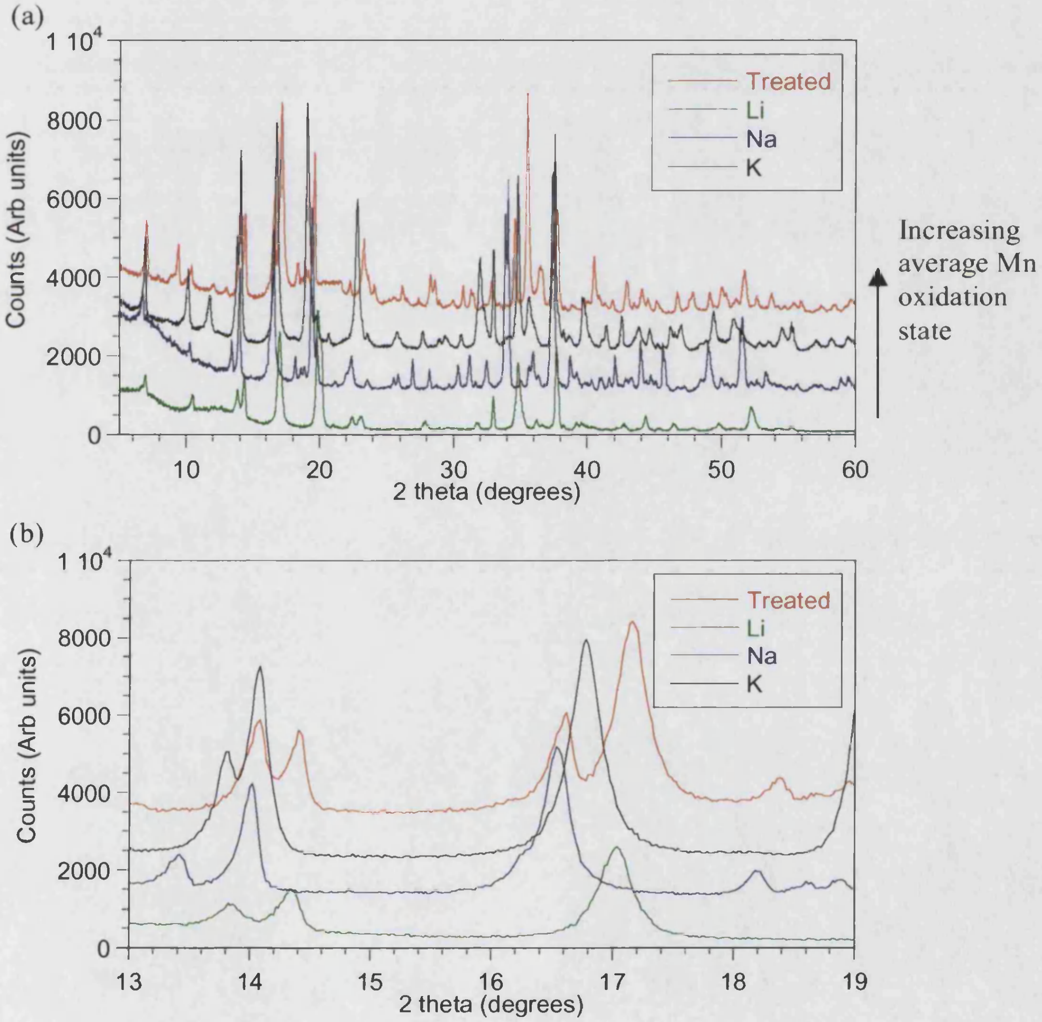

Figure 5.9. X-ray diffraction patterns for $Na_{0.44}MnO_2$, $Na_{0.17}MnO_2$, $Li_{0.5}Na_{0.17}MnO_2$ and $K_{0.04}Na_{0.16}MnO_2$ showing peak splitting as a result of increasing average manganese oxidation state and hence changes in lattice parameters.

The data for $Na_{0.16}MnO_2$ was difficult to refine due to excessive broadening of some of the peaks due to disorder induced on Na deintercalation, which is recovered on intercalation with other alkali metals. The removal of sodium from the 's' shape tunnels appears to result in a distortion of the lattice, Lebail refinements were attempted both in the orthorhombic Pbam and monoclinic P2 space groups however, due to the poor quality of the data neither yielded a particularly good fit. The X-ray data for $Na_{0.16}MnO_2$ showed a likeness to that reported by Doeff *et al*, however, refinement of the material was not undertaken.[4] Lattice parameters for $Na_{0.16}MnO_2$ were determined for comparison using the refinement process in the Cellref program and as expected showed a decrease in all directions and hence the cell volume. Refinement of the potassium and lithium intercalated samples showed preferred orientation problems with changes in the apparent intensities of some peaks. The quality of the data was insufficient to refine either the fractional occupancies or the thermal parameters, for refinement purposes the thermal parameters were set to 0.01 Ui/Ue x 100 and the fractional occupancies were set from the EDX results. The refinement data and patterns for $K_{0.08}Na_{0.14}MnO_2$ and $Li_{0.26}Na_{0.16}MnO_2$ are given in tables 5.7 and 5.8 and figures 5.10 and 5.11 respectively.

Table 5.7. Final lattice parameters and goodness of fit parameters derived from the Rietveld refinement of X-ray diffraction of $Na_{0.44}MnO_2$ and intercalated species refined in space group Pbam.

Sample	a (Å)	b (Å)	c (Å)	Cell volume ($Å^3$)	χ^2	WRp (%)	Rp (%)
Na	9.11595(23)	26.4125(6)	2.83048(6)	681.510(28)	-	-	-
Treated	8.8888	25.8500	2.7390	629.298	-	-	-
Li	8.9562(10)	25.647(4)	2.82620(23)	649.18(12)	4.526	13.36	9.92
K	9.3323(11)	25.8225(25)	2.82869(23)	681.67(12)	15.76	17.68	13.10

The removal of sodium from the tunnel sites results in a large drop in cell volume. This cell volume increases again with intercalation, and as expected is dependent upon increasing ionic radii of the tunnel species, shown in Figure 5.12. Only a small change is observed on Li intercalation corresponding to small Li ions having a limited effect on the Mn-O framework in contrast to that seen for Na and K. Only a small difference is observed in the n_1 cation site between the Li and K refinements. However, a larger difference is observed in the n_2 and n_3 sites supporting the idea that intercalation occurs in the larger 's' shaped tunnels. Bond lengths for $Li_{0.26}Na_{0.16}MnO_2$ and $K_{0.08}Na_{0.14}MnO_2$ refinements are given in table 5.9, the bond lengths observed for the Mn1 and Mn2 sites are a little short resulting in a high valence for the manganese. This is due to difficulties in refining accurately the atom positions in these materials as a result of distortions occurring during intercalation and possible intergrowths in the parent material.

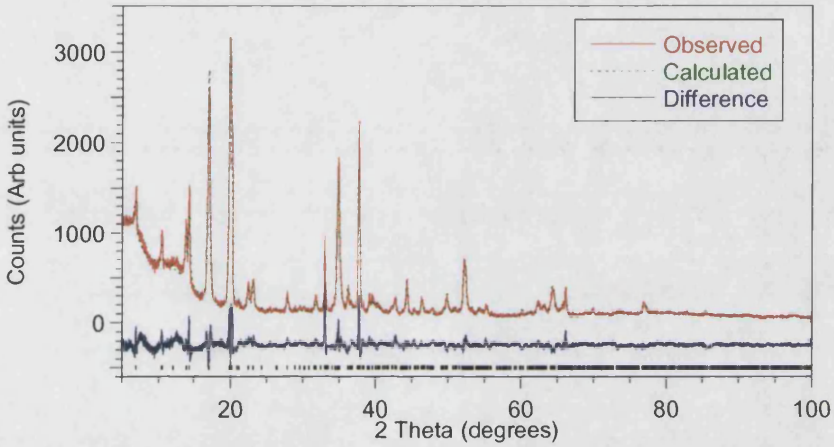

Figure 5.10. Observed, calculated and difference of the Rietveld refinement of X-ray diffraction data of $Li_{0.26}Na_{0.155}MnO_2$ in the Pbam space group.

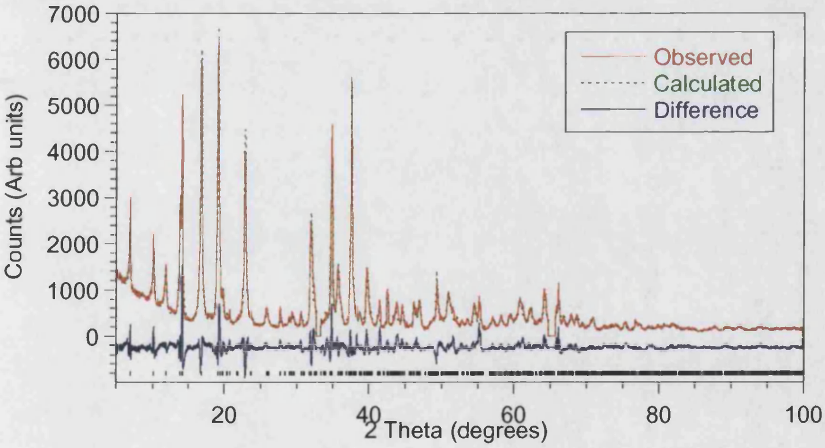

Figure 5.11. Observed, calculated and difference of the Rietveld refinement of X-ray diffraction data for $K_{0.08}Na_{0.16}MnO_2$ in the Pbam space group.

Table 5.8. Refined atom positions for Li and K intercalated $Na_{0.44}MnO_2$ *from X-ray diffraction at room temperature. Refined in space group Pbam.*

	Li			K		
Atom	x	y	z	x	y	z
Mn	0	0.5	0	0	0.5	0
Mn	0.3409(12)	0.30366(38)	0.5	0.4099(11)	0.29969(34)	0.5
Mn	-0.0053(11)	0.10646(40)	0	0.0660(10)	0.11036(35)	0
Mn	0.0251(9)	0.31190(37)	0	0.0783(8)	0.30668(35)	0
Mn	0.3415(11)	0.08803(33)	0.5	0.4035(11)	0.09343(28)	0.5
O	0.3599(33)	0.0041(12)	0.5	0.4139(29)	0.0198(10)	0.5
O	0.1773(32)	0.1005(12)	0	0.3253(35)	0.0967(11)	0
O	-0.0246(37)	0.1561(13)	0.5	0.0096(33)	0.1844(12)	0.5
O	0.4491(34)	0.1668(11)	0.5	0.4581(29)	0.1772(10)	0.5
O	0.1647(35)	0.2972(13)	0.5	0.2239(31)	0.2985(13)	0.5
O	0.4404(39)	0.2579(11)	0	0.4562(33)	0.2660(12)	0
O	0.3211(37)	0.3555(10)	0	0.4227(34)	0.3364(14)	0
O	0.4512(33)	0.0599(12)	0	0.5030(37)	0.0768(11)	0
O	0.4751(36)	0.4166(11)	0.5	0.6321(31)	0.4049(10)	0.5
Na	0.2347(25)	0.1794(10)	0	0.2302(24)	0.1420(8)	0
Li/K	0.318(16)	0.419(6)	0.5	0.3285(35)	0.3807(11)	0.5
Li/K	0.12(17)	0.008(6)	0	0.1420(15)	-0.0183(5)	0

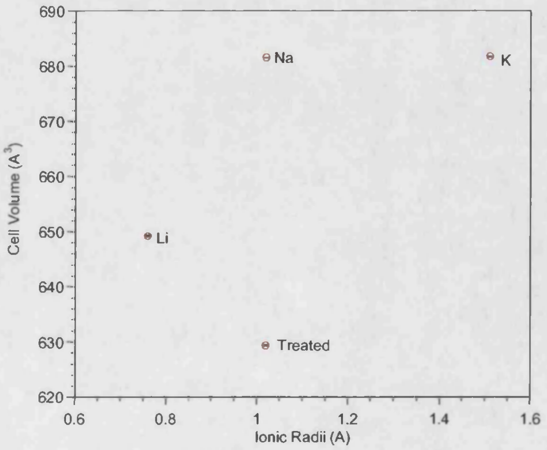

Figure 5.12. Plot of cell volume Vs ionic radii of tunnel cation.

Table 5.9. Bond lengths for $Li_{0.26}Na_{0.16}MnO_2$ *and* $K_{0.08}Na_{0.14}MnO_2$ *from the Rietveld refinement of room temperature X-ray diffraction data refined in the Pbam space group.*

Li	Mn1 (Å)	Mn2 (Å)	Mn3 (Å)	Mn4 (Å)	Mn5 (Å)
O	1.891(19)	1.580(34)	1.714(27)	1.674(17)	2.163(30)
O	1.891(19)	1.599(29)	1.905(22)	1.674(17)	2.004(22)
O	1.891(19)	2.056(22)	1.905(22)	1.925(22)	2.004(22)
O	1.891(19)	2.056(22)	1.834(29)	1.925(22)	2.212(28)
O	1.574(31)	1.956(18)	1.552(13)	1.916(29)	1.886(20)
O	1.574(31)	1.956(18)	1.552(13)		1.886(20)

K	Mn1 (Å)	Mn2 (Å)	Mn3 (Å)	Mn4 (Å)	Mn5 (Å)
O	1.706(14)	1.716(19)	2.445(33)	1.852(18)	1.594(17)
O	1.706(14)	1.716(19)	2.437(27)	1.852(18)	1.594(17)
O	1.706(14)	1.716(19)	2.437(27)	1.972(20)	2.223(24)
O	1.706(14)	1.737(27)	1.917(33)	1.972(20)	1.746(21)
O	1.983(30)	1.707(22)	1.592(15)	2.196(20)	1.746(21)
O	1.983(30)	1.707(22)	1.592(15)		2.533(30)

5.2.2.4. Magnetic properties.

Magnetic data were collected between 5 and 300K for all samples in both field cooled and zero field cooled measurements. $Na_{0.44}MnO_2$ shows a broad low dimensional antiferromagnetic peak with a T_N of approximately 16K. This is contrary to the data published by Parant et al who reported no order of magnetism, however, the transition temperature is below the range studied by these authors.[2] Jeong et al reported the $Na_{0.50}MnO_2$ phase to have a T_N of approximately 30K.[7] This difference in the observed Neel temperature can be explained by changes in the average manganese oxidation state as a result of differing amounts of cation present in the tunnels and demonstrates the sensitivity of the magnetic system with Mn oxidation state. This observation confirms the lower than expected sodium content observed in the EDX analysis. A Curie-Weiss plot of the paramagnetic region (150-300K) yields a straight line. The Weiss constant, Curie constant, calculated and observed magnetic moments are given in table 5.10 and are in good agreement with those previously published. Figure 5.13 shows the antiferromagnetic transition and the Curie-Weiss fit to the paramagnetic region (150-300K).

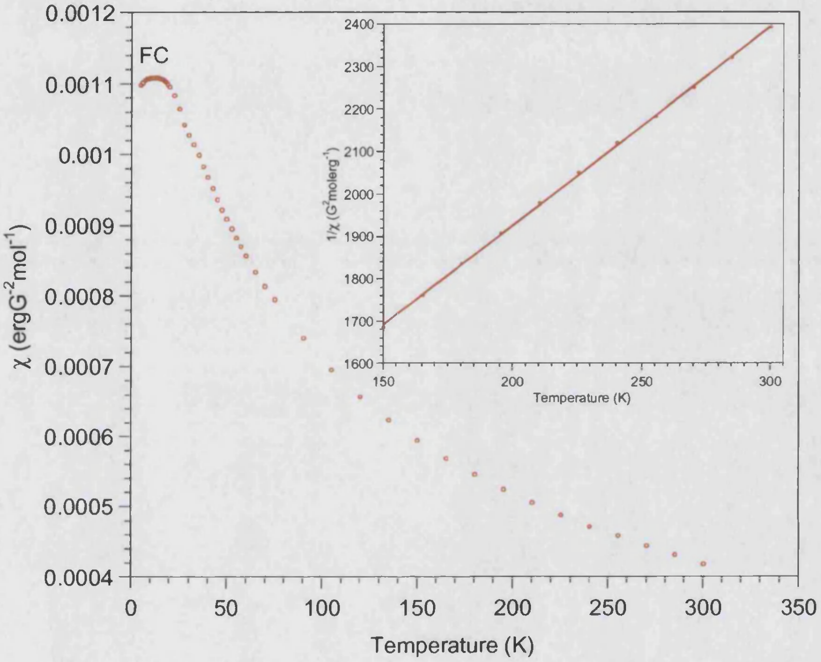

Figure 5.13. Field cooled (FC) magnetic susceptibility for $Na_{0.44}MnO_2$ showing a maxima at 16K indicative of antiferromagnetic ordering; inset shows the Curie-Weiss behaviour.

$Na_{0.16}MnO_2$ exhibits a sharper antiferromagnetic peak with a T_N of approximately 45K, with the appearance of a Curie tail below the transition temperature. This confirms the structural disorder in the framework as a result of removing the sodium from the tunnels; this is possibly due to the non uniform removal of the sodium and the consequent change in average manganese oxidation state resulting in changes in the Mn^{3+} and Mn^{4+}distribution around the framework and hence affecting the antiferromagnetic exchange.

The effect of intercalation of both Li and K into the tunnel sites increases the amount of disorder resulting in increasing paramagnetic character with increasing ionic radii, showing many of the spins are not involved with the magnetic transition. All samples exhibit a negative Weiss constant typical of antiferromagnetic materials. However, in the case of potassium only a slight shoulder can be observed at a T_N of approximately 40K. The calculated, observed magnetic moments, the Weiss constant and the Curie constant, are given in table 5.10. Whilst, this increasing paramagnetic character is illustrated in figure 5.14.

Table 5.10. Curie constant, Weiss constant, observed and calculated magnetic moments for $Na_{0.44}MnO_2$ and all intercalated species.

Sample	Molecular Weight	C (Kerg/G^{2}mol)	θ (K)	T_N/T_C (K)	μ_{eff} (μ_B)	μ_{calc} (μ_B)
$Na_{0.36}MnO_2$	95.7368	2.122(1)	-208(2)	16	4.11	4.23
$Na_{0.17}MnO_2$	91.2649	1.59(1)	-154(3)	45	3.57	4.04
$Li_{0.26}Na_{0.16}MnO_2$	94.8668	2.292(4)	-164(1)	20	4.28	4.30
$K_{0.08}Na_{0.14}MnO_2$	94.1133	13.3(1)	-495(3)	40	10.43	4.09

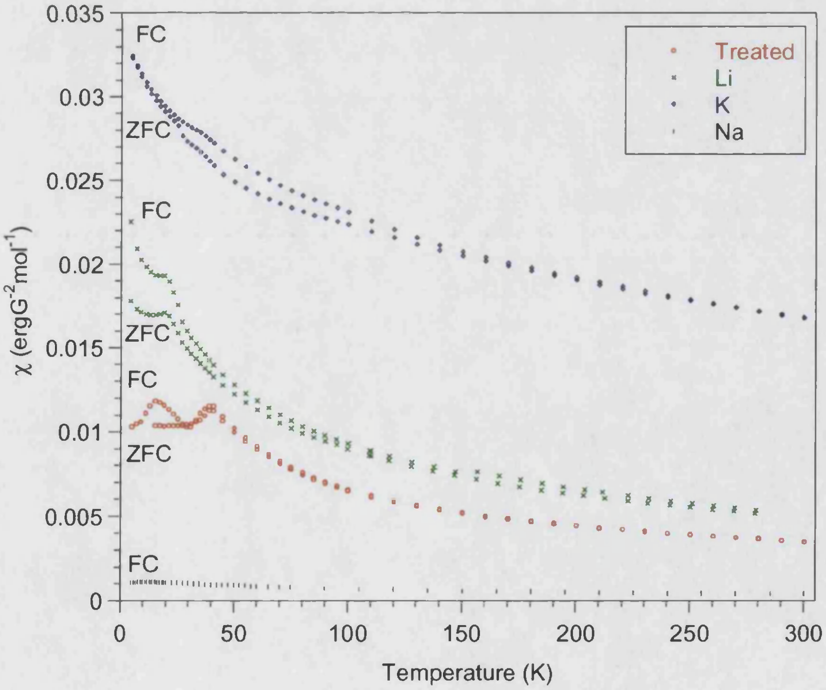

Figure 5.14. Magnetic susceptibilities observed as a result of intercalation of $Na_{0.44}MnO_2$ showing the increasing paramagnetic character.

5.2.2.5. Transport Properties.

Resistivity information for $Na_{0.44}MnO_2$ was collected using the 4-point DC method down to 150K using a 0.001mA current. Below this temperature the resistivity was higher than is possible to measure with the equipment used. An exponential decrease of resistance with increasing temperature was observed, indicative of thermally activated conduction and semiconducting properties (figure 5.15). The band gap was calculated to be 0.18eV.

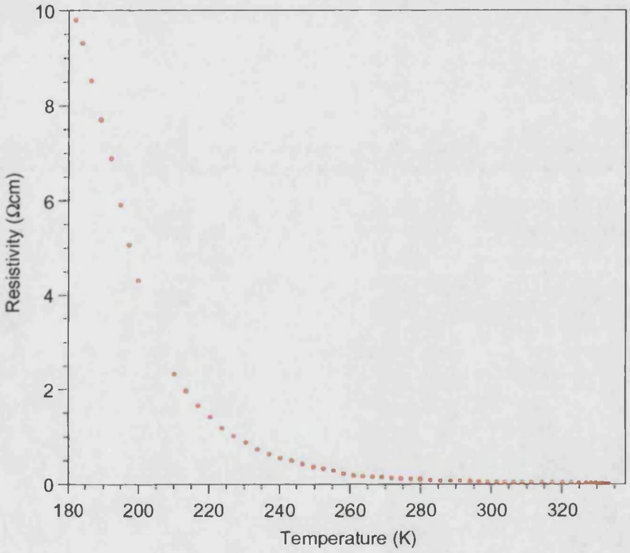

Figure 5.15. Resistivity as a function of temperature for $Na_{0.44}MnO_2$.

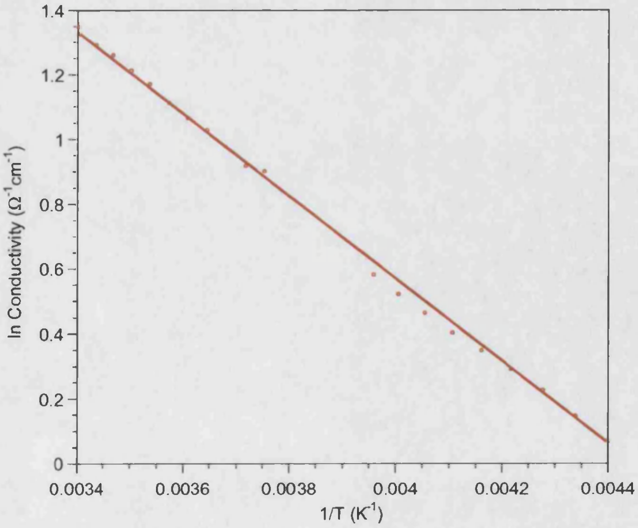

Figure 5.16. Arrhenius plot of ln conductivity Vs 1/temperature for $Na_{0.44}MnO_2$.

5.2.2.6. Removal of the Intercalated Tunnel Species.

The removal of the intercalated potassium from within the tunnels by acid leaching of the material was attempted. This appeared to result in no removal of either the Na or K from these sites, as seen in the X-ray analysis of the two materials, which showed no significant difference in the lattice parameters (Figure 5.17). EDX results confirmed that a negligible amount of cations was removed giving an overall composition of $K_{0.07}Na_{0.13}MnO_2$ compared to that of the parent material, $K_{0.08}Na_{0.14}MnO_2$. Though it can be seen from the reflections at high angle that there is a certain loss of long range structural order, this implies that the intercalation of K is irreversible in contrast with the smaller alkali metals

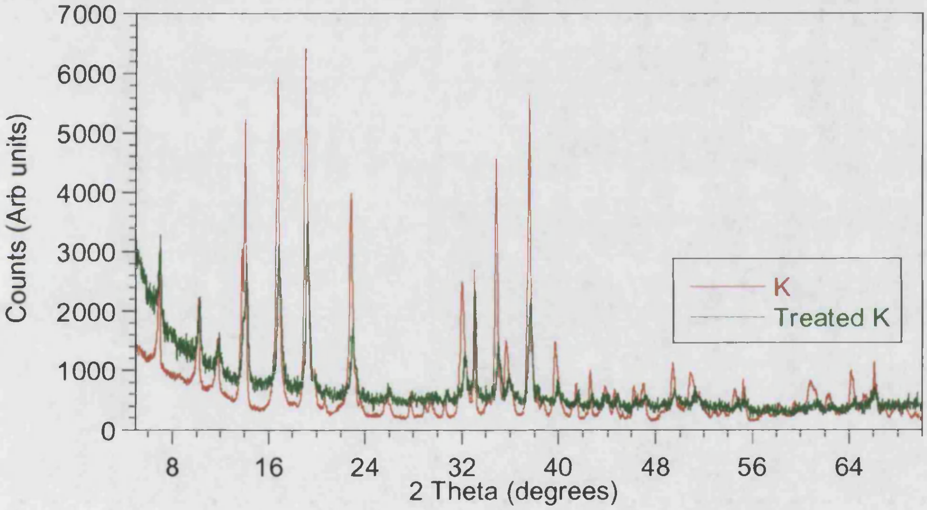

Figure 5.17. X-ray diffraction patterns for $K_{0.08}Na_{0.14}MnO_2$ and the acid leached material showing negligible changes in lattice parameters and loss of long range structural order.

5.3. Doping of the Mn Framework Sites with Fe.

5.3.1. Synthesis

A new series with the formula $Na_{0.44}Mn_{1-x}Fe_xO_2$, where x = 0.11, 0.13 and 0.15, was prepared in a similar procedure to the parent system. Stoichiometric ratios of $NaCO_3$, Fe_2O_3 and Mn_2O_3 were ground together using an agate pestle and mortar to thoroughly mix the starting materials before being transferred to a furnace at 700°C in air for 2-3 days. A slight excess of Na_2CO_3 was employed to minimize the possible formation of a manganese oxide second phase due to the loss of sodium during the reaction. The X-ray analysis showed an increasing amount of a second phase with increasing Fe content. This second phase was readily identifiable as Fe_2O_3 hematite. Whilst this is negligible in the 11% iron material this grows steadily in the other materials suggesting that the maximum level of doping is around 11%, consistent with the data observed for the doping of the framework sites with Cu.[12] The sodium was removed from the tunnel site in $Na_{0.44}Mn_{0.89}Fe_{0.11}O_2$ by stirring the material with a solution of approximately 1M, HCl overnight at room temperature as done for $Na_{0.44}MnO_2$.[8]

5.3.2. Results and Discussion.

5.3.2.1. EDX.

EDX analysis confirmed the presence of iron in these materials with an increasing Fe content observed, consistent with the increasing amount of iron oxide second phase shown by x-ray analysis. EDX results for the 11% Fe sample gives a composition of $Na_{0.440(4)}Mn_{0.89(1)}Fe_{0.160(2(}O_2$. It is worth noting that unlike the 100% manganese material the sodium content is not low. Upon treatment with acid it is possible to remove some of the sodium from within the larger ‘s’ shaped tunnel. A composition of $Na_{0.200(2)}Mn_{0.89(1)}Fe_{0.130(1)}O_2$ is observed, commensurate with our previous studies. A loss of iron is also observed; X-ray analysis shows the removal of some of the Fe_2O_3 second phase due to dissolution in the acid.

5.3.2.2. Thermal Analysis.

Table 5.11 gives the decomposition routes for $Na_{0.44}MnO_2$ and $Na_{0.44}Mn_{0.89}Fe_{0.11}O_2$. Sample $Na_{0.44}Mn_{0.89}Fe_{0.11}O_2$ undergoes a three step decomposition compared to the two step decomposition observed for $Na_{0.44}MnO_2$ this is illustrated by Figure 5.18. Unlike $Na_{0.44}MnO_2$, the first step can be attributed to loss of water from the surface of the materials and is marked by a weight loss of 1.717%. This is followed by weight losses of 1.781% and 2.006%, X-ray analysis of the residue remaining after TGA analysis is readily identifiable as $Na_{0.44}MnO_2$, Mn_2O_3 and Fe_2O_3 suggesting that the material decomposes to form more stable oxides. This material also shows a decrease in thermal stability relative to $Na_{0.44}MnO_2$ and is more similar to those obtained by intercalation of the tunnel site. This is due primarily to the change in the average manganese oxidation state from a relatively stable +3.56 to +3.23 due to the presence of Fe^{3+}.

Table 5.11. Decomposition routes and percentage weight loss for $Na_{0.44}MnO_2$ *and its* $Na_{0.44}Mn_{0.89}Fe_{0.11}O_2$ *in an inert atmosphere of nitrogen.*

Sample	1st Decomposition			2nd Decomposition			3rd Decomposition		
	onset (°C)	endset (°C)	%Wt loss	onset (°C)	endset (°C)	%Wt loss	onset (°C)	endset (°C)	% Wt loss
Mn				305.33	422.79	0.545	682.43	867.45	1.522
Mn/Fe	65.75	112.30	1.717	357.16	520.57	1.781	637.44	843.85	2.006

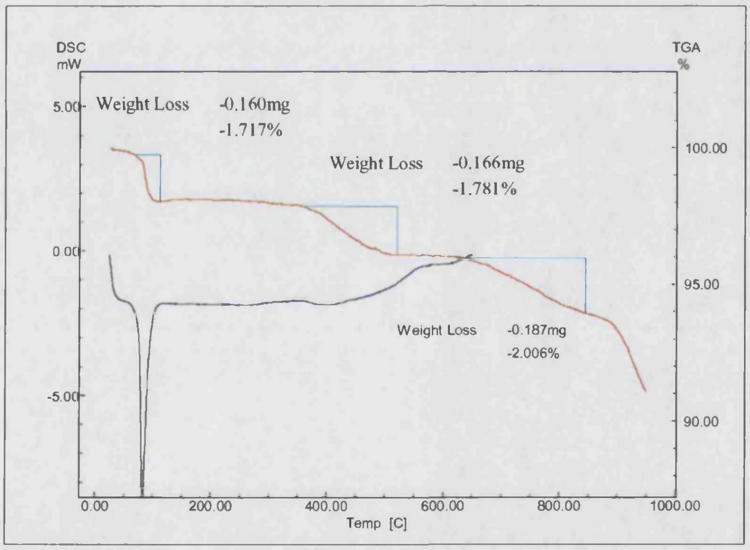

Figure 5.18. TGA/DSC traces showing the three step decomposition route and percentage weight losses for $Na_{0.44}Mn_{0.89}Fe_{0.11}O_2$ *in an inert atmosphere of nitrogen.*

5.3.2.3. Diffraction.

The X-ray diffraction patterns of $Na_{0.44}MnO_2$ and the 11% Fe sample show a clear shift in peaks due to significant change in lattice parameters. Table 5.12 gives the lattice parameters for both $Na_{0.44}MnO_2$ and $Na_{0.44}Mn_{0.89}Fe_{0.11}O_2$ for ease of comparison. A small reduction in cell volume is observed due to the slightly smaller ionic radii of Fe. The refinement data and patterns are given in table 5.13 and figure 5.19 respectively and show good correlation to those reported previously and those discussed here.

Table 5.12. Final lattice parameters and goodness of fit parameters for $Na_{0.44}MnO_2$, $Na_{0.44}Fe_{0.11}Mn_{0.89}O_2$ and acid treated $Na_{0.44}Fe_{0.11}Mn_{0.89}O_2$ refined in space group Pbam.

Sample	a (Å)	b (Å)	c (Å)	Cell volume (Å^3)
$Na_{0.44}MnO_2$	9.11595(23)	26.4125(6)	2.83048(6)	679.19(6)
$Na_{0.44}Mn_{0.89}Fe_{0.11}O_2$	9.1016(9)	26.2634(24)	2.82793(19)	675.98(10)
$Na_{0.20}Mn_{0.89}Fe_{0.11}O_2$	9.0834(11)	25.310(4)	2.83186(31)	651.04(14)

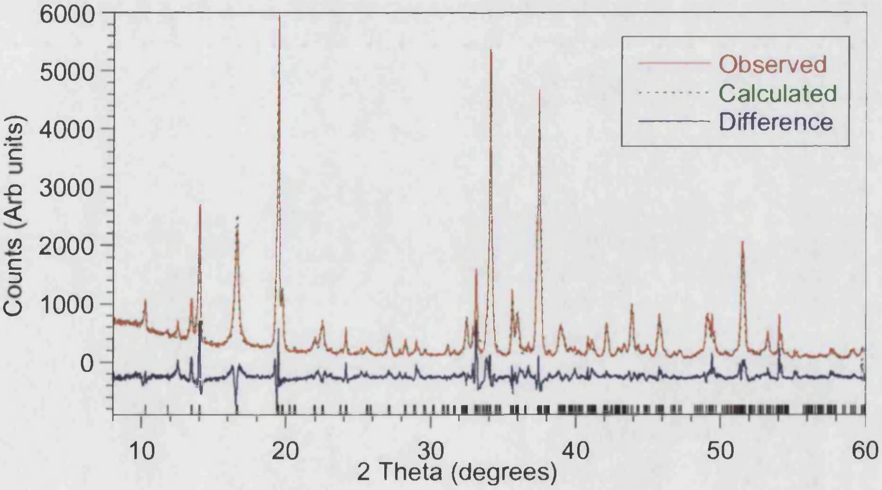

Figure5.19. Observed, calculated and difference for the Rietveld refinement of room temperature X-ray diffraction data for $Na_{0.44}Mn_{0.89}Fe_{0.11}O_2$ in the space group, Pbam.

Table 5.13. Refined atom positions, thermal parameters and fractional occupancies from X-ray diffraction data for $Na_{0.44}Fe_{0.11}Mn_{0.89}O_2$ refined in space group Pbam. Goodness of fit factors, $\chi^2 = 11.19$, wRp = 17.11% and Rp = 12.48%.

Atom	x	y	z	Fractional occupancy
Mn1	0	0.5	0	1.00
Mn2	0.3784(13)	0.3091(5)	0.5	1.00
Mn3	0.0162(13)	0.1111(4)	0	1.00
Mn4	0.0287(9)	0.3058(4)	0	1.00
Mn5	0.3573(11)	0.0918(4)	0.5	1.00
O1	0.3596(36)	-0.0011(16)	0.5	1.00
O2	0.2142(32)	0.0891(13)	0	1.00
O3	0.1079(40)	0.1648(13)	0.5	1.00
O4	0.4037(35)	0.1790(16)	0.5	1.00
O5	0.1509(36)	0.2895(15)	0.5	1.00
O6	0.4577(33)	0.2721(12)	0	1.00
O7	0.3199(42)	0.3497(13)	0	1.00
O8	0.5209(34)	0.0808(13)	0	1.00
O9	0.4964(43)	0.4424(14)	0.5	1.00
Na1	0.1912(32)	0.2189(16)	0	0.64
Na2	0.2201(25)	0.4120(11)	0.5	0.84
Na3	0.1343(50)	-0.0046(21)	0	0.50

Due to the similarities in scattering power, Fe and Mn could not be distinguished from X-ray diffraction data. Lattice constants are given in table 5.12, the removal of the sodium from within the tunnels again results in a marked decrease in cell volume consistent with that observed for $Na_{0.44}MnO_2$. The refinement data and plot is given in table 5.15 and figure 5.20 respectively.

Table 5.14. Bond lengths from the Rietveld refinement of X-ray diffraction data for $Na_{0.44}Mn_{0.89}Fe_{0.11}O_2$ *refined in the Pbam space group.*

	Mn1 (Å)	Mn2 (Å)	Mn3 (Å)	Mn4 (Å)	Mn5 (Å)
O	1.906(22)	2.2(4)	1.892(27)	1.858(21)	2.44(4)
O	1.906(22)	2.133(30)	2.164(22)	1.858(21)	1.924(19)
O	1.906(22)	1.861(21)	2.164(22)	1.849(20)	1.924(19)
O	1.906(22)	1.861(21)	2.061(32)	1.849(20)	2.33(4)
O	2.132(35)	1.850(25)	2.003(25)	2.145(32)	2.074(23)
O	2.132(35)	1.850(25)	2.003(25)		2.074(23)

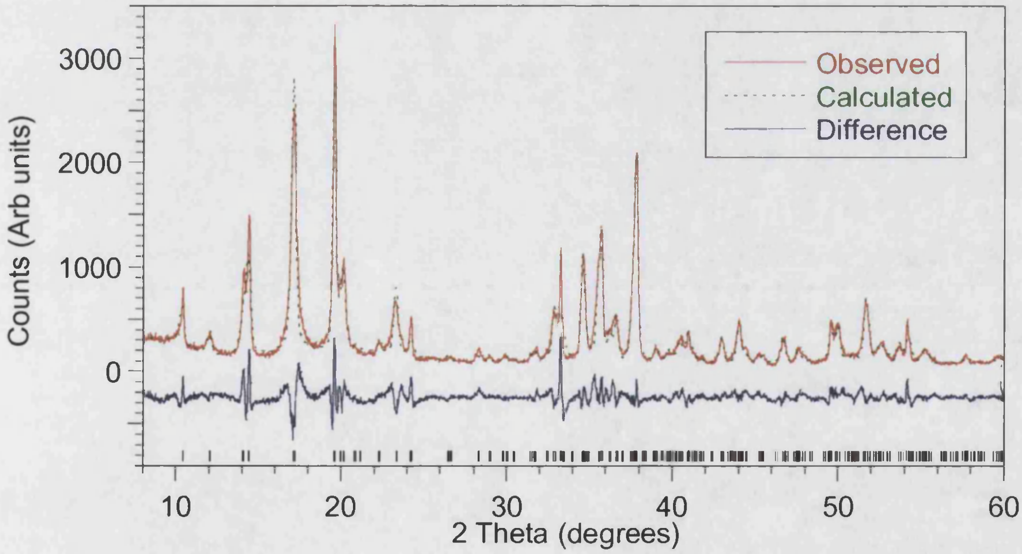

Figure 5.20. Observed, calculated and difference for Rietveld refinement of room temperature X-ray diffraction data for acid treated $Na_{0.20}Fe_{0.11}Mn_{0.89}O_2$ *refined in the Pbam space group.*

Table 5.15. Refined atom positions, thermal parameters and fractional occupancies from the Rietveld refinement of X-ray diffraction data for acid treated $Na_{0.44}Mn_{0.89}Fe_{0.11}O_2$ *refined in space group Pbam. Goodness of fit factors,* $\chi^2 = 8.618$, *wRp = 17.21% and Rp = 12.95%.*

Atom	x	y	z	Fractional occupancy
Mn1	0	0.5	0	1.00
Mn2	0.4099(23)	0.3090(8)	0.5	1.00
Mn3	0.0358(16)	0.1085(7)	0	1.00
Mn4	0.0272(18)	0.3099(9)	0	1.00
Mn5	0.3753(14)	0.0926(9)	0.5	1.00
O1	0.427(4)	-0.0148(22)	0.5	1.00
O2	0.241(4)	0.1081(24)	0	1.00
O3	0.058(7)	0.1524(23)	0.5	1.00
O4	0.279(5)	0.0844(30)	0.5	1.00
O5	0.124(6)	0.3036(32)	0.5	1.00
O6	0.366(5)	0.2719(19)	0	1.00
O7	0.403(5)	0.3892(2)	0	1.00
O8	0.510(5)	0.0782(17)	0	1.00
O9	0.526(5)	0.4190(20)	0.5	1.00
Na1	0.090(7)	0.2948(42)	0	0.49(5)
Na2	0.243(4)	0.3169(20)	0.5	0.83(5)
Na3	0.243(4)	0.0099(24)	0	0.50(5)

5.3.2.4. Magnetic properties.

The ZFC/FC magnetic susceptibility measurements of $Na_{0.44}Fe_{0.11}Mn_{0.89}O_2$ and $Na_{0.20}Fe_{0.11}Mn_{0.89}O_2$ are shown in figure 5.21 and figure 5.22. Both measurements show a slight hump at high temperature (~250K), which is due to the Fe_2O_3 impurity. The Curie-Weiss plot of the paramagnetic region is given in the insert of figure 5.21, and the Curie constants and observed magnetic moments are given in table 5.17 and are in good agreement with those calculated.

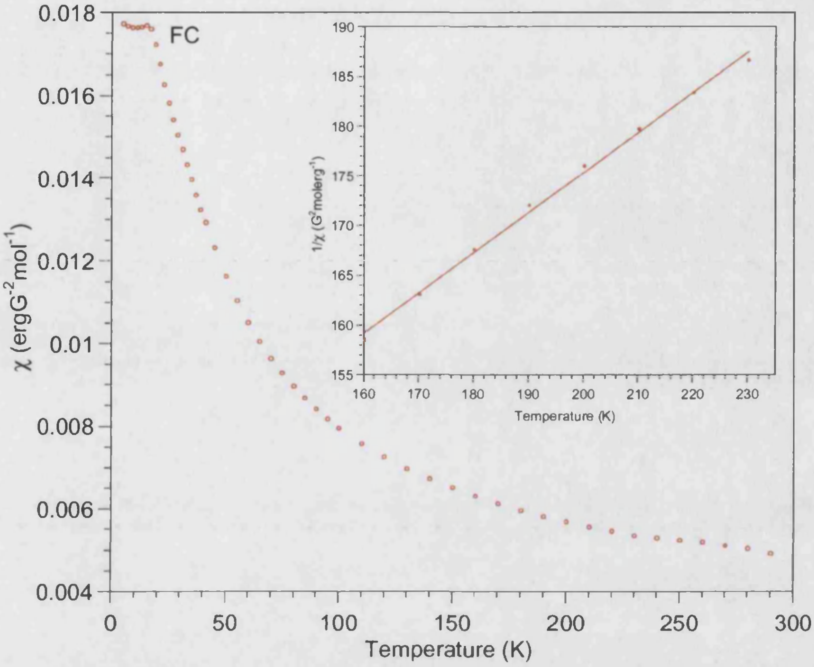

Figure 5.21. Field cooled (FC) magnetic susceptibility showing maxima at low temperature of $Na_{0.44}Fe_{0.11}Mn_{0.89}O_2$; inset shows Curie-Weiss behaviour .

Table 5.16. Curie constants, Weiss constant, observed and calculated magnetic moments for $Na_{0.44}MnO_2$, $Na_{0.44}Fe_{0.11}Mn_{0.89}O_2$ and $Na_{0.20}Fe_{0.11}Mn_{0.89}O_2$.

Sample	C (Kerg/G^{2}mol)	θ (K)	T_N/T_C (K)	μ_{eff} (μ_B)	μ_{calc} (μ_B)
$Na_{0.44}MnO_2$	2.122(1)	-208(2)	16	4.11	4.23
$Na_{0.44}Fe_{0.11}Mn_{0.89}O_2$	2.38(1)	-217(9)	20	4.37	4.98
$Na_{0.20}Fe_{0.11}Mn_{0.89}O_2$	2.83(6)	-213(9)	50	4.76	4.88

Both materials show maxima at low temperature at a similar temperature to a divergence between the ZFC and FC measurements, indicative of spin glass behaviour, commensurate with the variation of exchange energies caused through the different transition metal ions (Mn^{3+}, Mn^{4+} and Fe^{3+}) as well as the disorder caused through the Na ions intercalated.

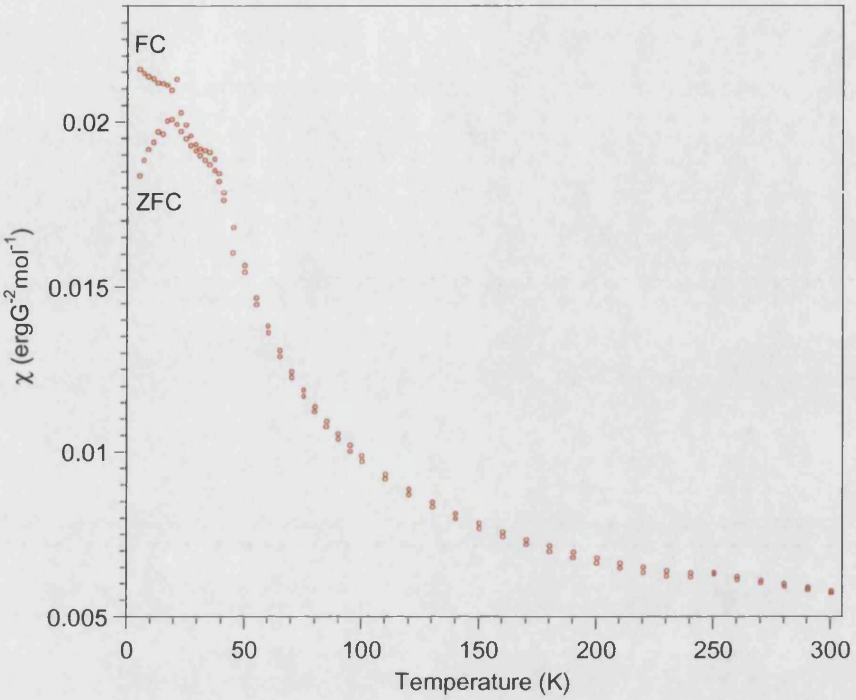

Figure 5.22. Magnetic susceptibility showing low temperature maxima and divergence between zero field cooled (ZFC) and field cooled (FC) measurements indicative of a spin glass and Curie-Weiss behaviour of $Na_{0.20}Fe_{0.11}Mn_{0.89}O_2$.

5.6. Conclusions.

The framework structure of $Na_{0.44}MnO_2$ is complex, containing two crystallographic distinct manganese sites. This material has attracted the most attention as a possible cathode material for lithium batteries, primarily because not only does it exhibit excellent capacities and retention on cycling but it also does not decompose to spinel type materials on charging and discharging. Little work has been reported on the magnetism and the effects of doping and average manganese oxidation state on the ordering in this material. We have shown that it is possible to remove the template ion and to intercalate different species into the larger 's' shaped tunnels and that selectivity decreases as a function of increasing ionic radii of the intercalated species. However it can also be shown that retention of the intercalated species increases with increasing ionic radii.

Changes in the average manganese oxidation state of this material have a significant effect on the observed magnetism due to increased disorder. In contrast, doping the framework with another transition metal has little effect on the observed magnetism, though upon removal of some of the template ion the magnetism changes significantly. The possibility of intercalation of these framework doped materials exists which, would further change the observed magnetism and electronic structure.

5.5. References.

(1) W. G. Mumme, *Acta Crystallographica B*, **1967**, *24*, 1114.

(2)\J. P. Parant, R. Olazcuaga, M. Devalette, C. Fouassier, P. Hagenmuller, *Journal of Solid State Chemistry*, **1971**, *3*, 1.

(3) A. R. Armstrong, H. Huang, R. A. Jennings, P. G. Bruce, *Journal of Materials Chemistry*, **1998**, *8(1)*, 255.

(4) M. M. Doeff, T. J. Richardson, L. Kepley, *Journal of the Electrochemical Society*, **1996**, *143(8)*, 2507.

(5) A. Mendiboure, C. Delmas, P. Hagenmuller, *Journal of Solid State Chemistry* **1985**, *57*, 323.

(6) M. M. Thackeray, *Progress in Solid State Chemistry*, **1997**, *25*, 1.

(7) Y. U. Jeong, A. Manthiram, *Journal of Solid State Chemistry*, **2001**, *156(2)*, 331.

(8) M. M. Doeff, M. Y. Peng, Y. P. Ma, L. C. De Jonghe, *Journal of the Electrochemical Society*, **1994**, *141(11)*, L145.

(9) Y. U. Jeong, A. Manthiram, *Electrochemical and Solid State Letters*, **1999**, *2(9)*, 421.

(10) Q. Feng, T. Horiuchi, L. H. Lui, K. Yanagisawa, T. Mitsushio, *Chemistry letters* **2000**, *3*, 284.

(11) N. Floros, C. Michel, M. Hervieu, B. Raveau, *Journal of Solid State Chemistry*, **2001**, *162*, 34.

(12) M. M. Doeff, T. J. Richardson, J. Hollingsworth, C. W. Yuan, M. Gonzales, *Journal of Power Sources*, **2002**, *112*, 294.

(13) S. Ching, J. L. Roark, N. Duan, S. L. Suib, *Chemistry of Materials*, **1997**, *9(3)*, 750.

(14) D. R. Lide, *CRC Handbook of Chemistry and Physics, 76th edition*, New York, **1995**, section 12.

CHAPTER 6: Layered Systems.

6.1. Introduction.

Many layered manganese oxides have been reported to date with interlayer gaps ranging from 4Å up to 10Å in burserite.[1] All these materials have layers built up of MnO_2 sheets, and the size of the interlayer gap is a result of the method employed and the size of the template ion used in their preparation. Materials with the α-$NaMnO_2$ and β-$NaMnO_2$ structures were first reported by Parant *et al* in 1971,[2] with further details described by Mendiboure *et al.*[3] More recently, the applicability of α-$LiMnO_2$ for lithium batteries was investigated. Preparations of this material have been achieved in two ways, firstly by solid state reaction of alkali metal carbonate with manganese oxide and secondly by ion exchange of α-$NaMnO_2$ with LiCl.[4-7] It has been reported that the Jahn-Teller effect of the Mn^{3+} ion affects the stability of the cell on electrochemical intercalation/deintercalation and original layered structure is converted to Li spinel, giving poor cycling properties.[8]

Conducting polymers, such as polyaniline have attracted a great deal of attention recently due to their promising electrical properties and their potential applications in a variety of devices, such as electrochromic displays and sensor devices.[9] This has led to the design and synthesis of nanocomposite materials that exhibit desired properties by achieving complementary behaviour between the polymer and the inorganic host lattice.[10] This 'encapsulation' of the polymer can offer many advantages, for example by inhibiting interchain defects which affect conjugation and hence the conduction properties.[11] Additionally, the inorganic host can offer enhanced mechanical, thermal and chemical stabilities.

Many authors have studied the intercalation of conducting polymers into the channels of zeolites in particular zeolite Y and mordenite.[12-21] Monomers are initially intercalated into the framework and then polymerisation is achieved by treatment with an oxidant. The degree of chain oxidation and chain lengths are therefore influenced by the dimensionality of the zeolite channels.[16] Polyacrylonitrile when encapsulated in zeolite shows good conduction and the resulting material exhibits a semiconductor to metal transition in the temperature range of 70-150K.[14] Polymerisation of simple alkynes within modified MCM-41 shows complete filling of the mesopores for polyethyne and polypropyne, producing a material with a high content of low defect polymer.[22] It is also possible to recover polymer from the zeolite channel by dissolution of the zeolite.[17,18]

The intercalation of polymers into layered frameworks such as FeOCl has also been studied extensively, using pyrrole, aniline and thiophene to incorporate into the interlayer gap.[9,23-26] The polymers can be removed by dissolving the FeOCl in acid and it has been shown that whilst the resulting polymer has a much smaller molecular weight than the bulk prepared polymer, they show a narrower length distribution. Conduction and magnetic studies show that the FeOCl host lattice dominates these properties. Water soluble polymers have been intercalated into V_2O_5.[27] Other systems studied include LnOCl, where Ln is Ho, Er, Tm, Yb, MoS_2 and $RuCl_3$.[28-31]

6.2. Synthesis.

Stoichiometric ratios of Na_2CO_3 and Mn_2O_3 were ground together using an agate pestle and mortar. The mixture was then pressed into pellets, transferred to a furnace and heated under flowing oxygen at 850°C and 780°C to obtain the beta and the alpha phase respectively.[2] The samples were confirmed to be single phase using a Siemens D500 X-ray diffractometer. An insertion study was conducted by treating the as-prepared α-$NaMnO_2$ and β-$NaMnO_2$ samples with LiI, KOH, NH_4I, CsI and CuI_2, based on the equation given in 6.1. All samples were stirred overnight at room temperature in acetonitrile.[32]

$$xLiI + NaMnO_2 \rightarrow \tfrac{1}{2}\,xI_2 + Li_xNa_{1.0\text{-}y}MnO_2 \qquad \text{-(6.1)}$$

All reactions were done with an excess of metal iodide and iodine was liberated instantaneously in the reactions with the α-$NaMnO_2$, with the exception of KOH. Treatment of the β-$NaMnO_2$ phase with these iodides showed no iodine liberation except with NH_4I, suggesting that intercalation did not take place.

Todorokite was prepared as reported by Suib et al, from the layered compound birnessite.[33,34] A 200ml solution, labelled solution A, was prepared as 20mmol of $KMnO_4$ in a NaOH solution with a final concentration of 4M. A second solution labelled B was prepared from 57 mmol of $MnCl_2{\cdot}4H_2O$ and 20mmol of $MgSO_4{\cdot}7H_2O$ in 300ml of distilled water. Mg^{2+} is required for thermal stability. Solution B was then added to solution A dropwise over a period of approximately 10 minutes The solution was then left vigorously stirring for 1 hour. The resulting suspension is then aged for 4 days at room temperature. The sample was then filtered and washed until the pH was about 7. The birnessite product was then autoclaved at 160°C for 48 hours to convert the layered species to the tunnel material, todorokite.

Intercalation of pyrrole and aniline into the interlayer space was done by stirring at room temperature overnight and by refluxing with pyrrole/aniline at 60°C for 24 hours.[23] The water was removed from the todorokite by heating the sample in an inert atmosphere of nitrogen prior to reaction with the polymer.

Intercalation of α-$NaMnO_2$ was achieved by stirring the material with an excess of aniline or pyrrole at room temperature, in air for 2-3 days. The subsequent solution was filtered and washed with distilled water before being dried at room temperature overnight.

6.3. Results and discussion

6.3.1. α-$NaMnO_2$/β-$NaMnO_2$

6.3.1.1. Structure

Both alpha and beta have layered structures but whereas α-$NaMnO_2$ is made up of MnO_2 sheets built up of edge sharing MnO_6 octahedra, in β-$NaMnO_2$ the MnO_2 sheets are constituted of a double stack of edge-sharing MnO_6 octahedra. In both structures the Na ions occupy octahedral sites within the interlayer space. (Figure 6.1) [3]

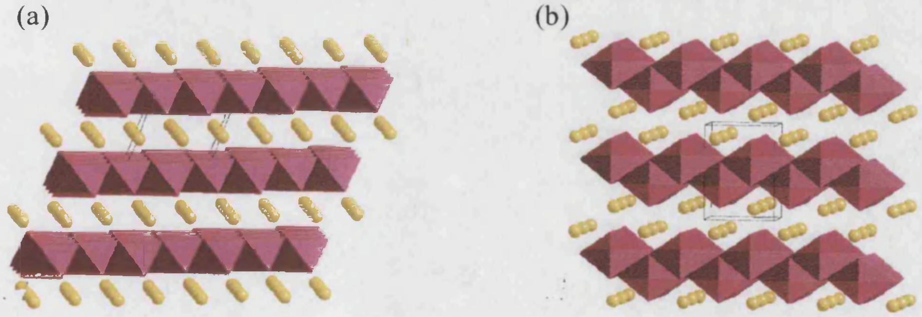

Figure 6.1. Schematic representation of (a)α-$NaMnO_2$ and (b) β-$NaMnO_2$, where the pink squares represent the MnO_6 octahedra and the yellow spheres are the sodium cations.

On initial synthesis a pure single phase of both α-$NaMnO_2$ and β-$NaMnO_2$ is produced. However, α-$NaMnO_2$ was found not to be stable with time and exposure to air over a timescale of several weeks. The α-$NaMnO_2$ was found to decompose to α-$Na_{0.70}MnO_{2.05}$, a similar layered structure, though no further evidence of the hydration of this phase to layered birnessite was observed.[35] These two structures differ such that α-$Na_{0.70}MnO_{2.05}$ exhibits ABBA oxygen stacking with the sodium occupying a prismatic site within the layers, whilst the α-$NaMnO_2$ has ABCABC oxygen stacking with the sodium occupying octahedral sites between the layers.[3] Figure 6.2 shows the complete conversion of α-$NaMnO_2$ to α-$Na_{0.70}MnO_{2.05}$.

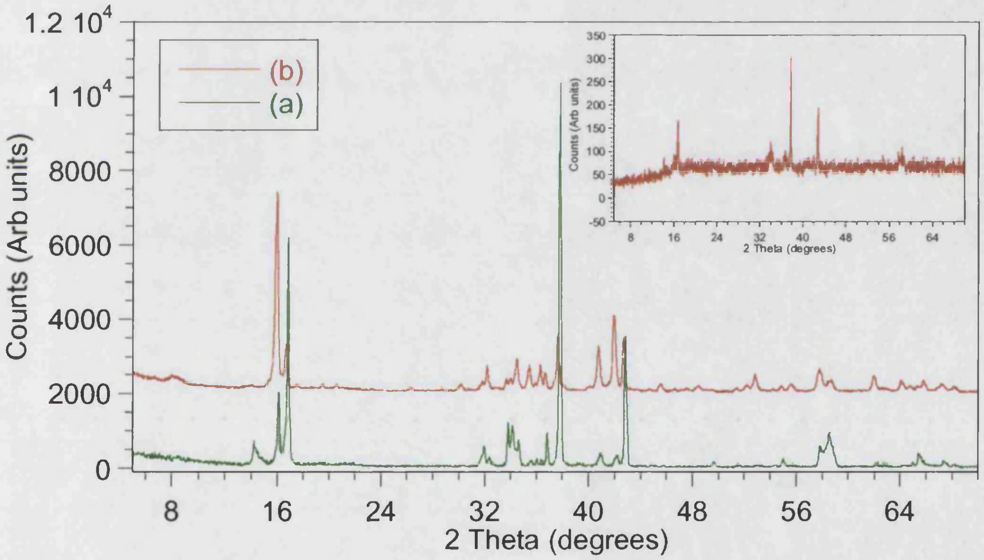

Figure 6.2. X-ray traces showing growth of the α-$Na_{0.70}MnO_{2.05}$ *phase. (a) X-ray taken after a few months, showing increase in peak at ~16°. (b) Shows almost complete conversion of* α-$NaMnO_2$ *phase into* α-$Na_{0.70}MnO_{2.05}$*; inset shows the pure* α-$NaMnO_2$ *phase.*

The refinement of both X-ray and neutron diffraction proved difficult due to the presence of stacking faults and intergrowths. This is especially true for α-$NaMnO_2$ where the presence of α$Na_{0.7}MnO_2$ not only results in extra peaks but also affects the peak intensities. Furthermore, as has been observed with other tunnel and layered structures the X-ray data for both phases shows preferred orientation along the [111] axis for α-$NaMnO_2$, and the [200] axis for β-$NaMnO_2$. Refinement fit data are given in tables 6.1 and 6.2; the refinement patterns are given in figure 6.3 through 6.6 for α-$NaMnO_2$ and β-$NaMnO_2$, respectively.

Table 6.1. Goodness of fit data for the Rietveld refinement of neutron data at 50K and room temperature X-ray diffraction measurements of α-$NaMnO_2$ and β-$NaMnO_2$.

	χ^2	wRp (%)	Rp (%)
Alpha (Neutron)	14.85	5.72	4.52
Alpha (X-ray)	2.150	27.05	20.12
Beta (Neutron)	17.74	8.35	5.35
Beta (X-ray)	13.14	17.86	12.61

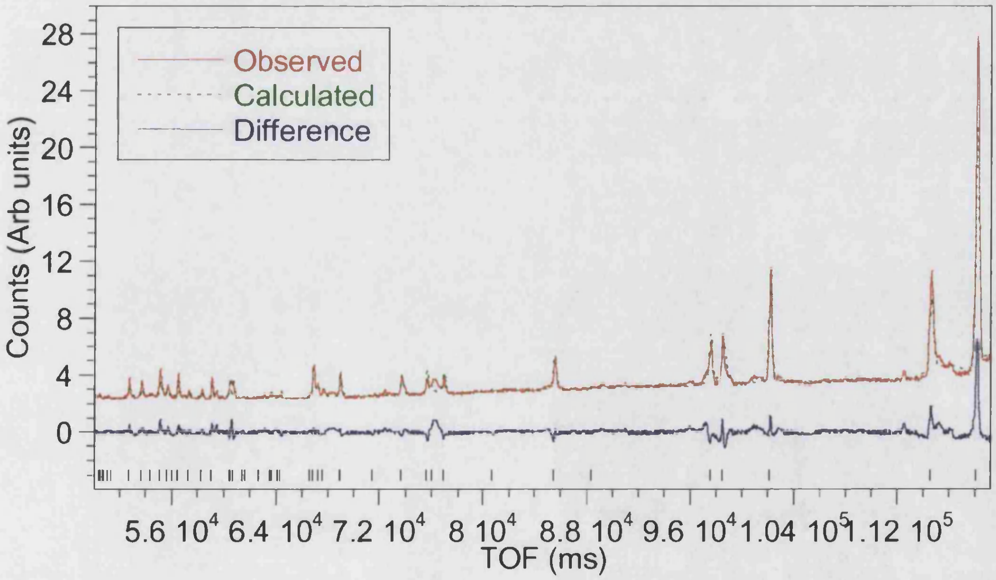

Figure 6.3. Observed, calculated and difference for the Rietveld refinement of 50K neutron data for α-$NaMnO_2$ refined in the C 2/m space group.

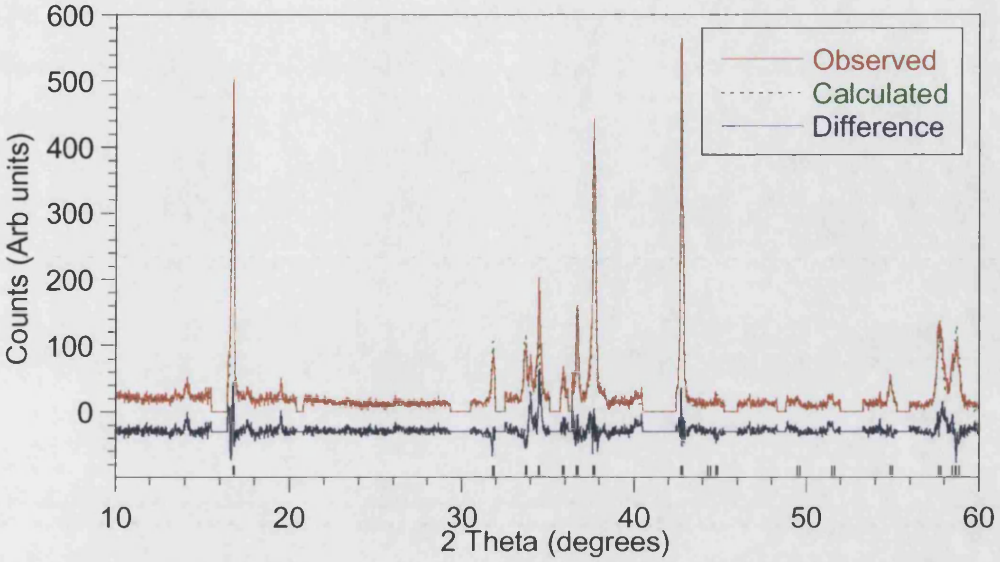

Figure 6.4. Observed, calculated and difference for the Rietveld refinement of room temperature X-ray diffraction data for α-NaMnO$_2$ refined in the C 2/m space group.

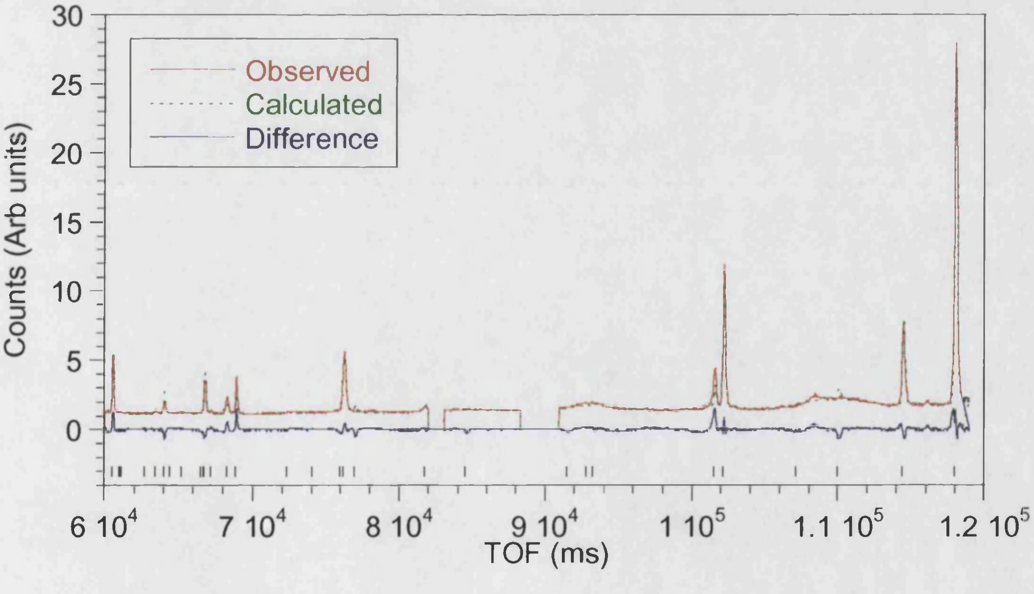

Figure 6.5. Observed, calculated and difference for the Rietveld refinement of 50K neutron diffraction data for β-NaMnO$_2$ refined in the Pmmn space group.

Table 6.2. Final parameters derived from the Rietveld refinement of 50K neutron diffraction and room temperature X-ray diffraction measurements for α*-NaMnO*$_2$ *and* β*-NaMnO*$_2$*.*

	Alpha (Neutron)	Alpha (X-ray)	Beta (Neutron)	Beta (X-ray)
a (Å)	5.63888(29)	5.6739(7)	4.74554(11)	4.7835(4)
b (Å)	2.85747(9)	2.85981(33)	2.85538(5)	2.85619(26)
c (Å)	5.77076(27)	5.7991(10)	6.31945(19)	6.3274(6)
β	112.8540(29)	113.138(7)	90	90
Cell Vol (Å^3)	85.684(7)	86.529(21)	85.631(4)	86.449(14)
Mn x	0	0	0.25	0.25
y	0	0	0.25	0.25
z	0	0	0.704(4)	0.6133(13)
Uiso x 100	5.27(27)	0.1	19.1(9)	0.1
O1 x	0.2924(7)	0.3109(28)	0.25	0.25
y	0	0	0.75	0.75
z	0.7912(7)	0.7947(34)	0.8691(2)	0.9065(35)
Uiso x 100	2.87(14)	0.1	2.81(20)	0.1
O2 x			0.25	0.25
y			0.75	0.75
z			0.4153(7)	0.3489(34)
Uiso x 100			1.79(20)	0.1
Na x	0	0	0.25	0.25
y	0.5	0.5	0.25	0.25
z	0.5	0.5	0.179(29)	0.1270(17)
Uiso x 100	9.5(4)	0.1	5.1(4)	0.1

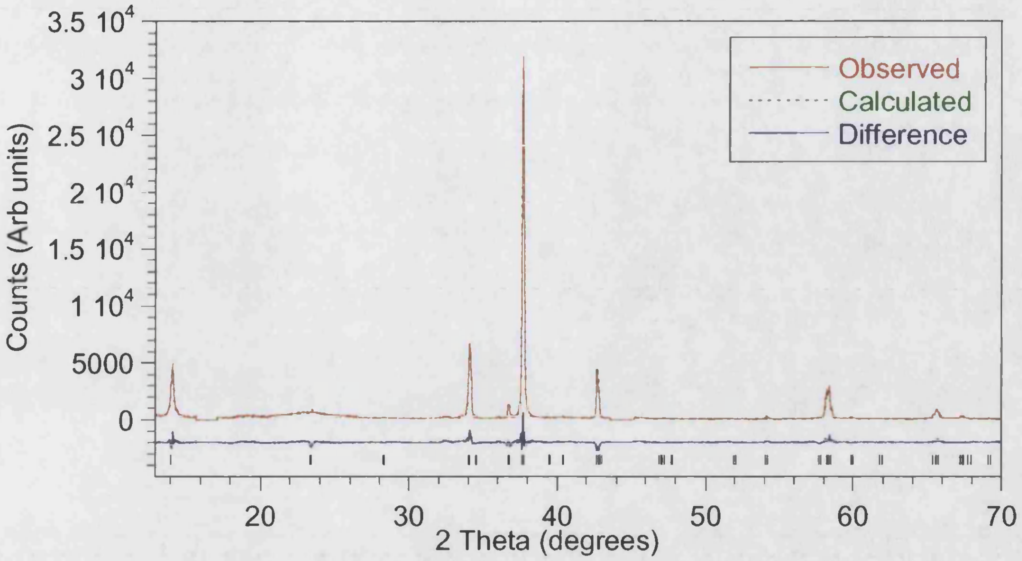

Figure 6.6. Observed, calculated and difference for the Rietveld refinement of room temperature X-ray diffraction data for β-NaMnO$_2$ refined in the Pmmn space group.

EDX data were collected for both these materials, and confirmed the Na:Mn ratio of approximately 1:1 for the beta phase giving a formulae of $Na_{1.07(1)}MnO_2$. However a slightly higher Na:Mn ratio was observed for the alpha phase, giving a formula of $Na_{1.22(2)}MnO_2$, which can be attributed to additional Na in the layers. The thermal analysis of α-NaMnO$_2$ material showed a three step decomposition in an inert atmosphere of nitrogen, whilst β-NaMnO$_2$ exhibited a two step route. X-ray analysis of the residues could be identified as the thermodynamically stable $Na_{0.44}MnO_2$. Table 6.3 gives the decomposition temperatures and percentage weight loss for both α-NaMnO$_2$ and β-NaMnO$_2$. In both structures the first weight loss is attributable to loss of surface water (Equation 6.2). The second weight loss can be explained by loss of O_2 as the layered phase breaks down to $Na_{0.44}MnO_2$ and Mn_2O_3 as given by equation 6.3. The TGA traces are given in figures 6.7 and 6.8 for α-NaMnO$_2$ and β-NaMnO$_2$ respectively.

$$NaMnO_2 \bullet xH_2O \rightarrow NaMnO_2 + xH_2O\uparrow \qquad -(6.2)$$

$$NaMnO_2 \rightarrow xNa_{0.44}MnO_2 + yMn_2O_3 + zO_2\uparrow \qquad -(6.3)$$

Table 6.3. Decomposition routes and percentage weight losses for α-$NaMnO_2$ and β-$NaMnO_2$.

	1st decomposition			2nd Decomposition			3rd Decomposition		
	onset (°C)	endset (°C)	%Wt loss	onset (°C)	endset (°C)	%Wt loss	onset (°C)	endset (°C)	%Wt loss
Alpha	32.50	124.60	1.675	456.06	599.26	1.924	663.53	759.17	0.572
Beta	41.41	81.89	0.571	416.33	621.25	1.787			

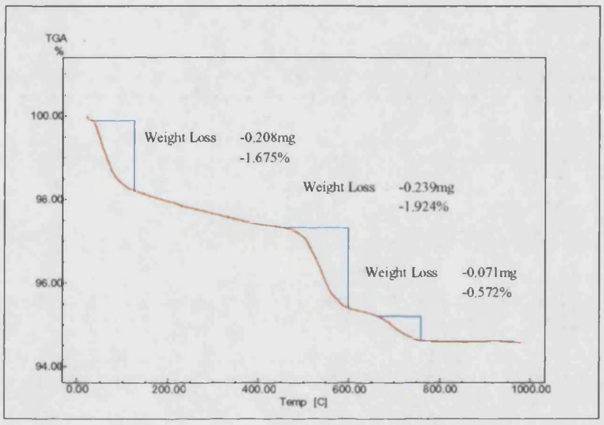

Figure 6.7. TGA trace showing a three step decomposition route and percentage weight losses for α-$NaMnO_2$ in an inert atmosphere of nitrogen.

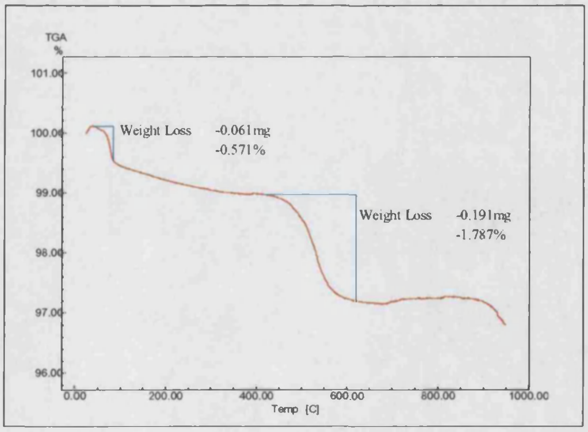

Figure 6.8. TGA trace showing a two step decomposition route and percentage weight losses for β-$NaMnO_2$ in an inert atmosphere of nitrogen.

The intercalation chemistry of these layered systems has been considered by many authors particularly battery technology.[5,7,8,36-37] Contrary to the data reported by Omomo *et al* and the phenomena seen in the tunnel type structures, it proved not possible to leach the Na from the interlayer space.[38,39] X-ray analysis of such experiments showed that the crystalline structure had collapsed to an amorphous phase. It can be seen from figure 6.9 that the Na environment in β-$NaMnO_2$, is more restrictive than that in the α-$NaMnO_2$ form suggesting that intercalation of the alpha form should be possible whilst intercalation of the beta form will be difficult if not impossible. The α-$NaMnO_2$ contains a layer of Na^+ in contrast to the two Na/O layers in β-$NaMnO_2$. This repulsive Na^+-Na^+ interaction will promote the separation of layers and allow guest ions or molecules to intercalate.

The intercalation of cations into the alpha phase results in an increased separation of the layers. X-ray diffraction showed that this reaction causes a transformation from α$NaMnO_2$ to the monoclinic layered birnessite structure, as shown in figure 6.10. Table 6.4 gives the refined lattice parameters for the intercalated species (Figures 6.11 to 6.15).

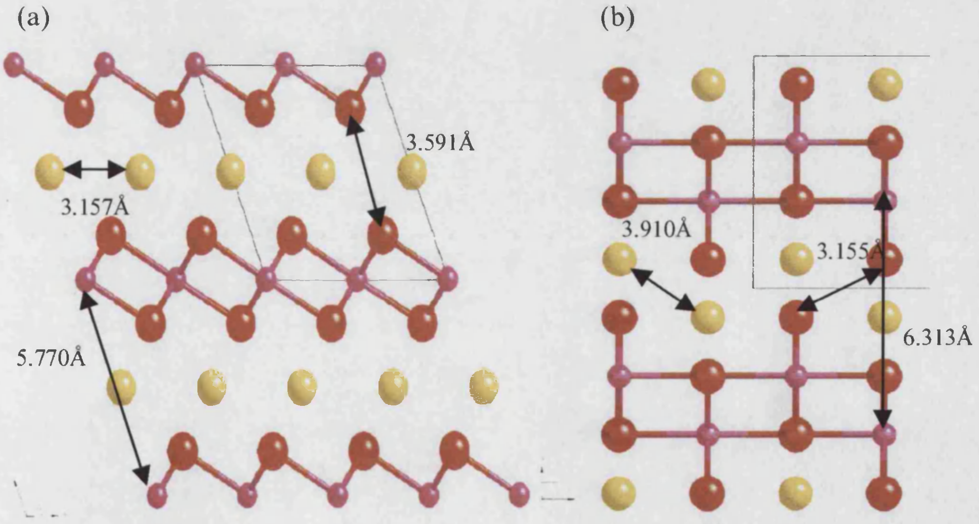

Figure 6.9. Ball and stick representation of (a)α-$NaMnO_2$ and (b)β-$NaMnO_2$ showing sodium packing, where the pink atoms are the manganese ions, red are the oxygen and yellow are the Na cations.

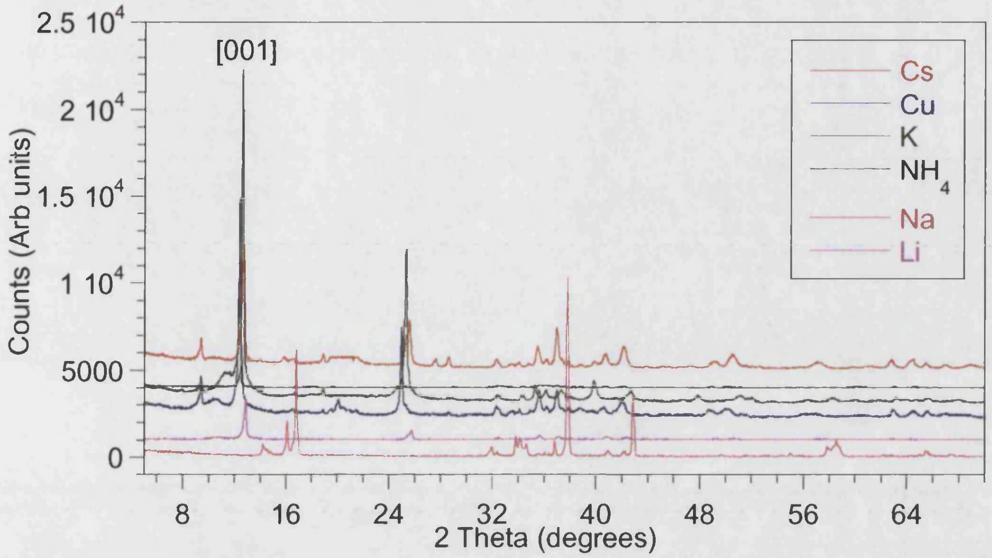

Figure 6.10. Room temperature X-ray diffraction traces for α-$NaMnO_2$ and intercalated species showing the increased layer separation as indicated by the [001] peak at ~16° two theta belonging to the birnessite phase.

Table 6.4. Final lattice parameters for the Lebail extractions of the X-ray diffraction data for the Intercalated α-$NaMnO_2$ species refined in the C 2/m space group.

	a (Å)	b (Å)	c (Å)	β	Cell Vol (Å^3)	χ^2
Li	5.2202(8)	2.8478(5)	7.2422(8)	103.780(15)	104.563(28)	3.602
K	5.1668(7)	2.8465(5)	7.1705(11)	100.634(21)	103.646(30)	10.56
Cu	5.1829(10)	2.8446(6)	7.3297(10)	103.502(13)	105.15(4)	13.12
Cs	5.2019(6)	2.85264(32)	7.1962(13)	103.502(13)	103.8314(26)	10.54
NH_4	5.170(5)	2.8616(23)	7.3367(33)	103.16(7)	105.70(14)	4.686

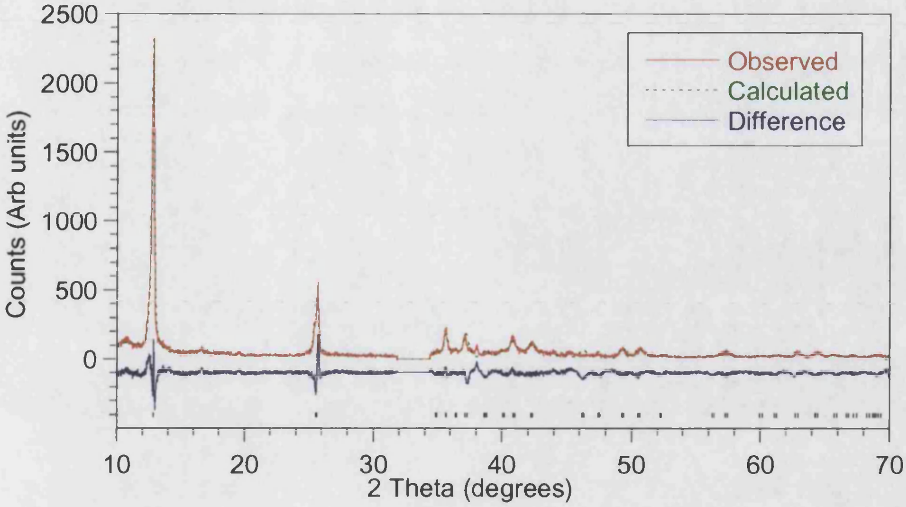

Figure 6.11. Observed, calculated and difference of the Lebail fit of the room temperature X-ray for α-NaMnO$_2$ after intercalation with lithium in the C2/m space group.

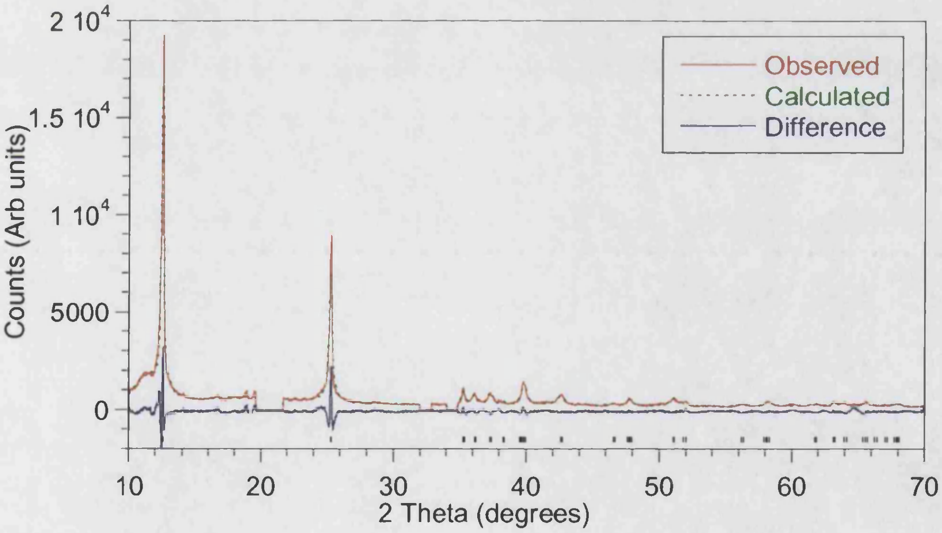

Figure 6.12. Observed, calculated and difference of the Lebail fit of the room temperature X-ray for α-NaMnO$_2$ after intercalation with potassium in the C2/m space group.

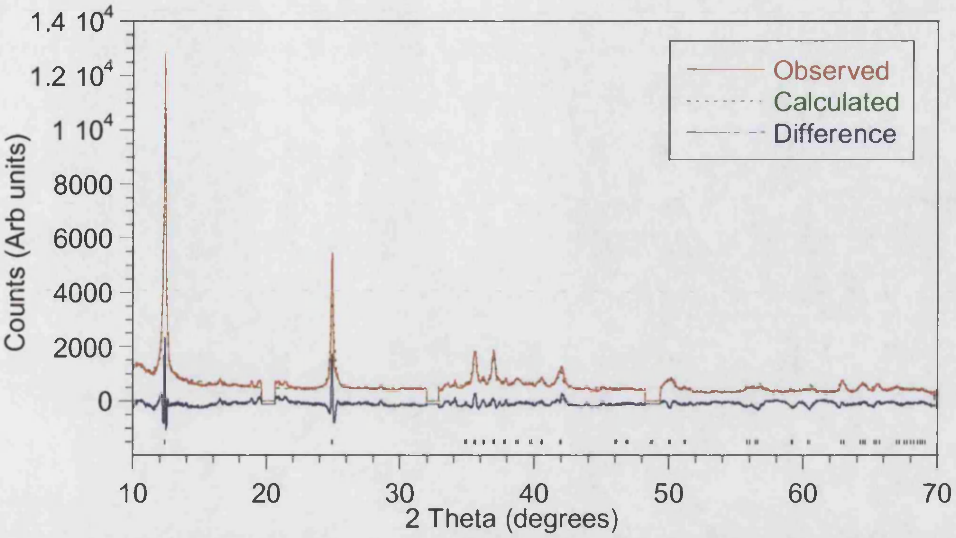

Figure 6.13. Observed, calculated and difference of the Lebail fit of the room temperature X-ray for α-NaMnO$_2$ after intercalation with copper in the C2/m space group.

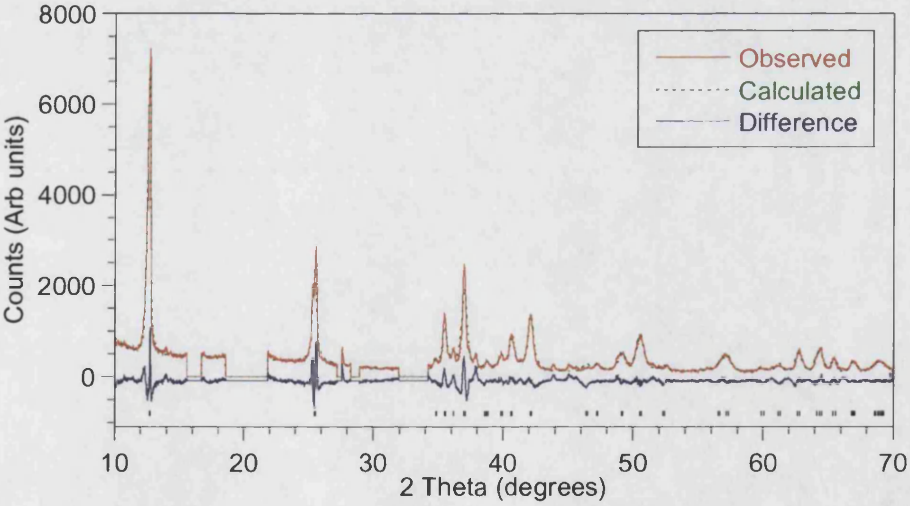

Figure 6.14. Observed, calculated and difference of the Lebail fit of the room temperature X-ray for α-NaMnO$_2$ after intercalation with caesium in the C2/m space group.

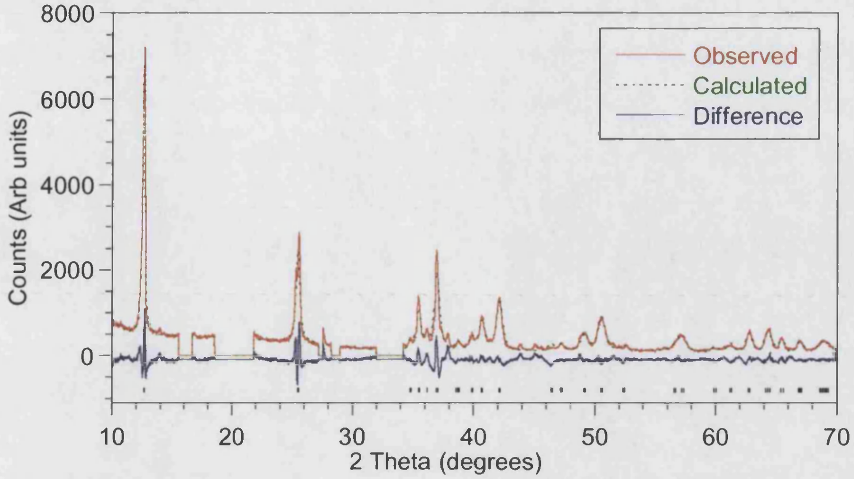

Figure 6.15. Observed, calculated and difference of the Lebail fit of the room temperature X-ray for α-NaMnO$_2$ after intercalation with NH$_4$ in the C2/m space group.

On intercalation there is a large increase in cell volume as the interlayer space is increased to approximately 7Å giving similar cell dimensions to birnessite.[33,40] EDX results are given in table 6.5. It is interesting to note that, as with the intercalation of other tunnel/layered species the amount intercalated is dependent upon the ionic radii of the intercalated species, despite the guest species having more available space as the layers can widen to accommodate, unlike the tunnel structures (Figure 6.16).

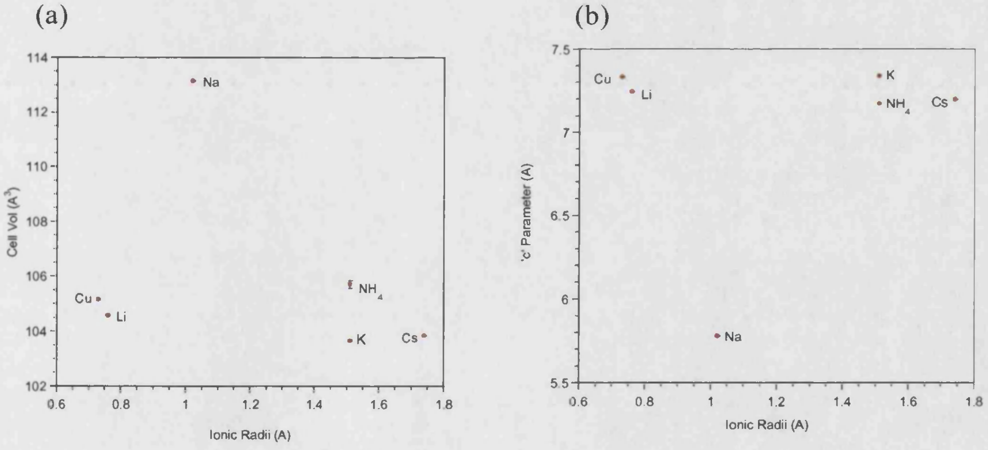

Figure 6.16. (a) Cell Volume and (b) lattice parameter c (interlayer gap) as a function of ionic radii.

Table 6.5. Results obtained by EDX for the chemical composition of intercalated α-NaMnO₂.

Sample	EDX data
Li into α-$NaMnO_2$	No data
K into α-$NaMnO_2$	$K_{0.140(1)}Na_{0.0200(1)}MnO_2$
NH_4 into α-$NaMnO_2$	No data
Cu into α-$NaMnO_2$	$Cu_{0.240(2)}Na_{0.400(4)}MnO_2$
Cs into α-$NaMnO_2$	$Cs_{0.0600(6)}Na_{0.350(4)}MnO_2$

The intercalation of β-$NaMnO_2$ with Li, Cu and Cs yielded no reaction as expected. However treatment of the beta phase with KOH and NH_4I resulted in the observation of an alternative phase whereby the layers appear to be separated by a larger gap than in birnessite phase seen in the intercalation of the alpha phase with the X-ray traces similar to those observed for burserite. It can be suggested that the larger gap observed is as a result of the double stack of MnO_2 sheets remaining intact (Figure 6.17). The lattice parameters of the new phases were refined using the burserite model in orthorhombic symmetry using the Celref program and are given in table 6.6. EDX data were collected for the potassium intercalated species, and whilst the results show only a negligible intercalation of K they do show a marked decrease in the amount of intercalated Na, implying an ion exchange reaction has taken place rather than redox type intercalation. Since the intercalation of either smaller cations such as Li or larger cations such as Cs proved difficult it can be suggested that intercalation is as a function of size and that the similar sizes of K and NH_4 are just right to allow the prizing apart of the layers in β-$NaMnO_2$.

Table 6.6. Final lattice parameters derived by the refinement of the β-NaMnO₂ Intercalated species using the Cellref program.

	a (Å)	b (Å)	c (Å)	Cell Vol (Å^3)
K	6.2787(27)	2.8829(3)	9.8420(30)	178.15(3)
NH_4	6.2923(55)	2.8841(20)	9.8070(1)	177.97(4)

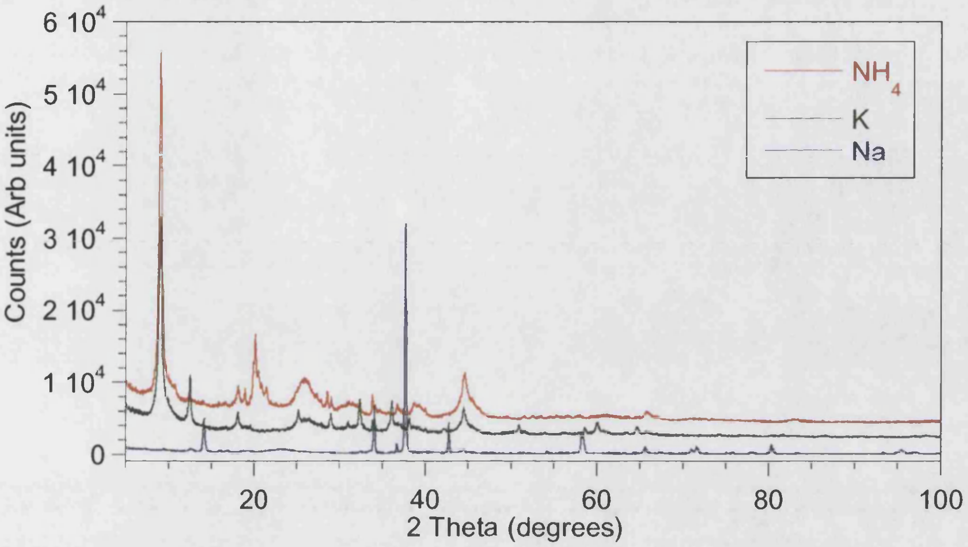

Figure 6.17. Room temperature X-ray diffraction traces for β-NaMnO₂ and intercalated species showing the increased layer separation as indicated by the peak at ~9Å.

6.4. Magnetic properties.

α-NaMnO$_2$ and β-NaMnO$_2$ show metamagnetic properties with a broad antiferromagnetic hump at high temperature followed by a Curie tail at low temperature and a divergence between ZFC and FC data (Figure 6.18 and 6.19 respectively). Since the magnetic transitions appear to start at room temperature, a Curie-Weiss plot to determine the observed magnetic moment could not be calculated. Since all the manganese in these materials is in the Mn^{3+} oxidation state, these materials could be expected to have an observed magnetic moment of approximately 4.89μ_B. The interpretation of the magnetic information for α-NaMnO$_2$ is further complicated by the loss of Na and subsequent growth of α-Na$_{0.70}$MnO$_{2.05}$ which itself exhibits similar magnetic ordering. The metamagnetism is due to the strong exchange with the MnO$_2$ sheets and weak coupling in the third direction as a result of the of the layered nature of the structure.

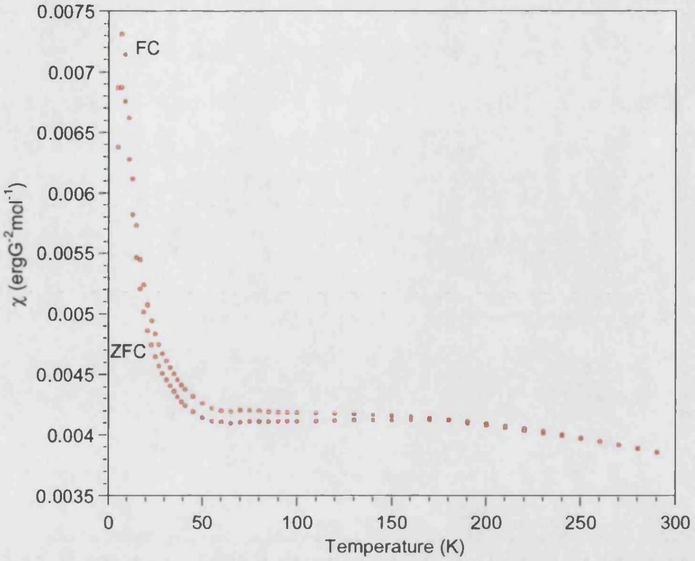

Figure 6.18. Zero field cooled (ZFC) and field cooled (FC) magnetic susceptibilities of α*-NaMnO*$_2$ *showing the metamagnetic character.*

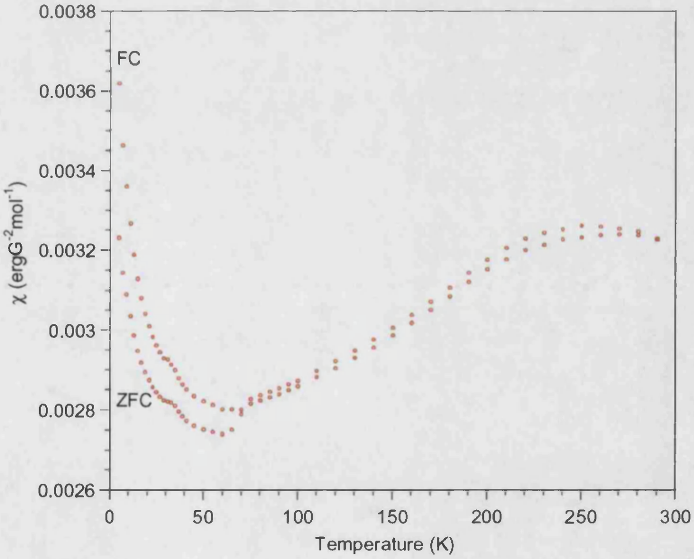

Figure 6.19. Zero field cooled (ZFC) and field cooled (FC) magnetic susceptibilities of β*-NaMnO*$_2$ *showing the metamagnetic character.*

The intercalation of foreign species into α-NaMnO$_2$ results in a large change in the magnetic properties, the metamagnetic ordering is destroyed and for Li and Cs the materials show maxima at ~20K with no difference between ZFC and FC indicative of antiferromagnetic order (figures 6.20 to 6.21). Intercalation of NH$_4$, Cu and K results in materials that appear to exhibit glassy type behaviour from the difference between the ZFC and FC. Curie-Weiss plots of the paramagnetic region 150-300K showed linear characteristics from which the observed magnetic moment was determined. These results are given in table 6.7.

Table 6.7. Curie constant, Weiss constant and observed magnetic moment for intercalated α-$NaMnO_2$ materials.

	$T_N/T_C/T_F$ (K)	C (Kerg/G^2mol)	θ (K)	μ_{obs} (μ_B)
Li	35	1.38(1)	-110(2)	3.32
K	40	2.04(2)	-121.(3)	4.05
NH_4	40	1.526(4)	-86.6(1)	3.49
Cu	40	1.205(1)	-72.9(3)	3.10
Cs	30	1.28(1)	-99(3)	3.20

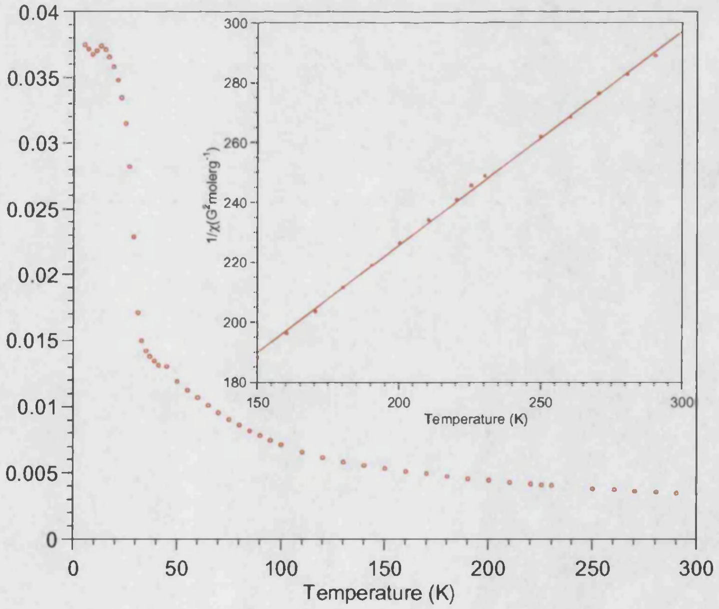

Figure 6.20. Magnetic susceptibility showing a maximum at 20K indicative of antiferromagnetic ordering for lithium intercalated α-$NaMnO_2$; inset shows Curie-Weiss behaviour.

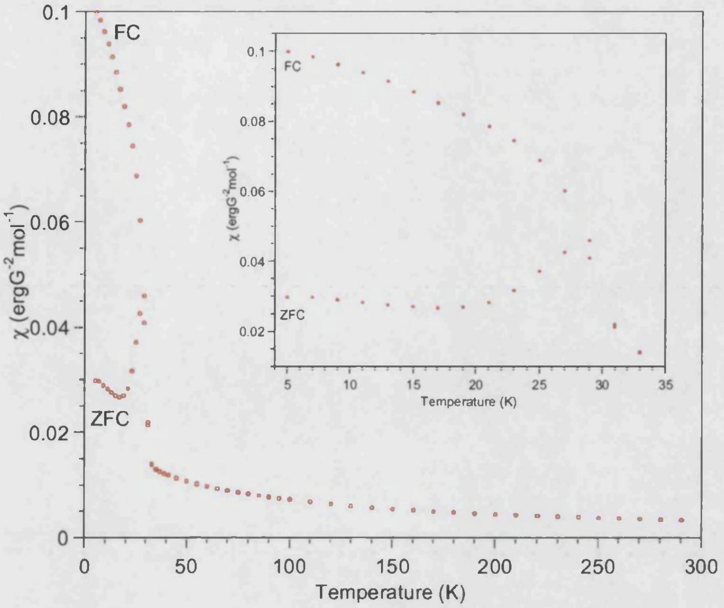

Figure 6.21. Magnetic susceptibilities of copper intercalated α-NaMnO$_2$ showing a divergence between zero field cooled (ZFC) and field cooled (FC) measurements indicative of spin glass behaviour; inset shows region below T_F.

The intercalation of both potassium and NH$_4$ into β-NaMnO$_2$ results in these materials showing a transition at ~30K (see figures 6.22 and 6.23) where there is a large spontaneous moment and a difference between the ZFC/FC susceptibilities. This is indicative of a weak ferromagnetic component, though the Curie-Weiss fits give a negative Weiss constant therefore implying competing interactions and the presence of a spin glass state. Table 6.8 gives the SQUID results for the intercalated beta phases.

Table 6.8. Curie constant, Weiss constant and observed magnetic moments for intercalated βNaMnO$_2$.

	$T_N/T_C/T_F$ (K)	C (Kerg/G^{2}mol)	θ (K)	μ_{obs} (μ_B)
K	40	1.97(1)	-154(3)	3.97
NH$_4$	40	2.913(4)	-226.4(6)	4.83

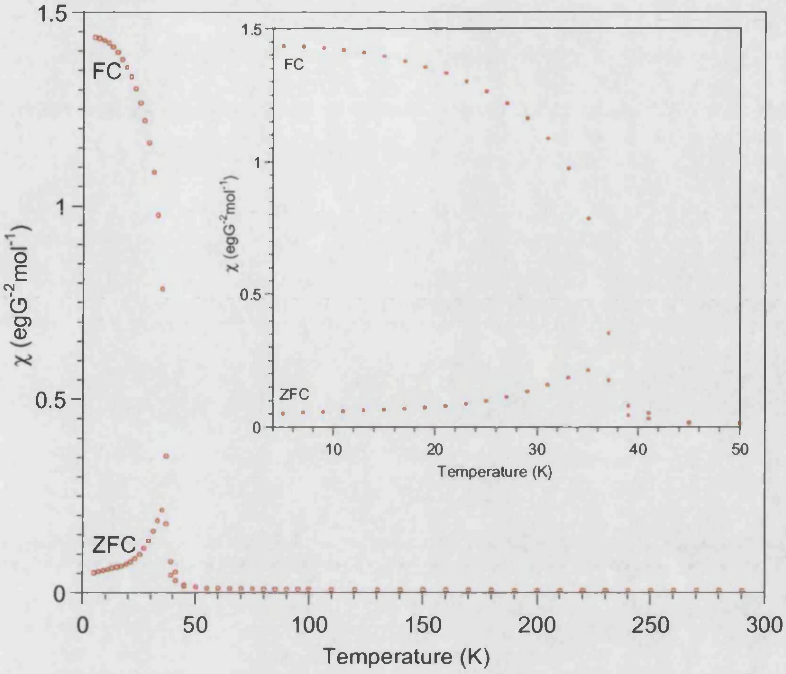

Figure 6.221. Magnetic susceptibilities of potassium intercalated β-NaMnO$_2$ showing the divergence between zero field cooled (ZFC) and field cooled (FC) measurements indicative of spin glass behaviour; inset shows region below T_F

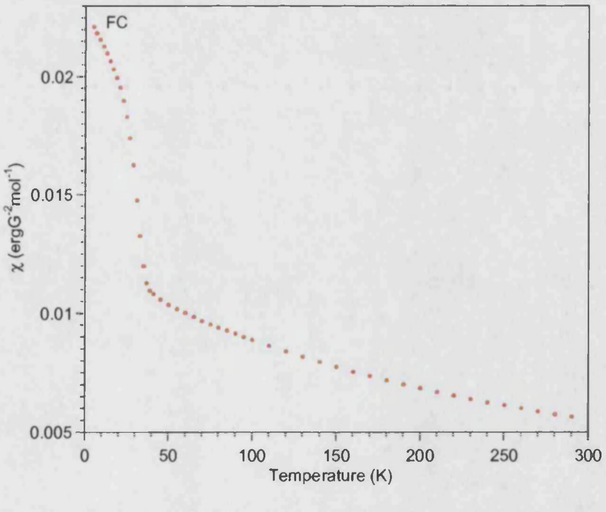

Figure 6.23. Field cooled (FC) magnetic susceptibility showing spin glass behaviour for NH$_4$ intercalated β-NaMnO$_2$.

6.3.2. Pyrrole intercalation into Todorokite/Birnessite.

The Cerius^2 computer program was employed to investigate the potential size constraints on intercalating polymer/monomer units of pyrrole into the tunnel site of todorokite. The derived structure, shown in Figure 6.24, was predicted to be stable and therefore synthetic procedures were attempted.

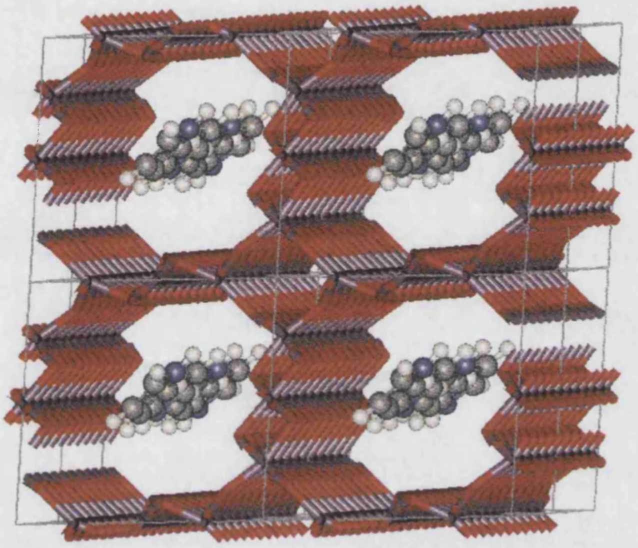

Figure 6.24. Computer generated representation of the intercalation of pyrrole into the tunnel sites of todorokite.

On X-ray diffraction of the synthetic todorokite phase it was evident that a second phase was present that can be identified as the birnessite precursor. However differences can be obseved between the X-ray diffraction patterns of the two phase parent material and the material obtained after intercalation with pyrrole. It is the peaks attributable to the birnessite phase that show these differences upon intercalation with pyrrole whilst the todorokite peak remain unchanged suggesting that it is the birnessite material which takes up the organic rather than the todorokite (Figure 6.25). Reactions of pyrrole with a pure todorokite material produced after these initial findings, showed no change in X-ray diffraction patterns, suggesting that the framework of the todorokite is resistant to the intercalation of polymeric materials.

Raman data collected for the mixed todorokite/birnessite material after intercalation with the polymer confirmed the presence of the organic, exhibiting two broad features in the data collected at 0.4mV at approximately 1325 cm^{-1} and 1575 cm^{-1}

attributable to C-H bend and C=C stretching vibrations of the pyrrole respectively (figure 6.26). Vibrations below 800 cm $^{-1}$ are likely attributable to Mn-O vibrations of the todorokite framework and birnessite layers.

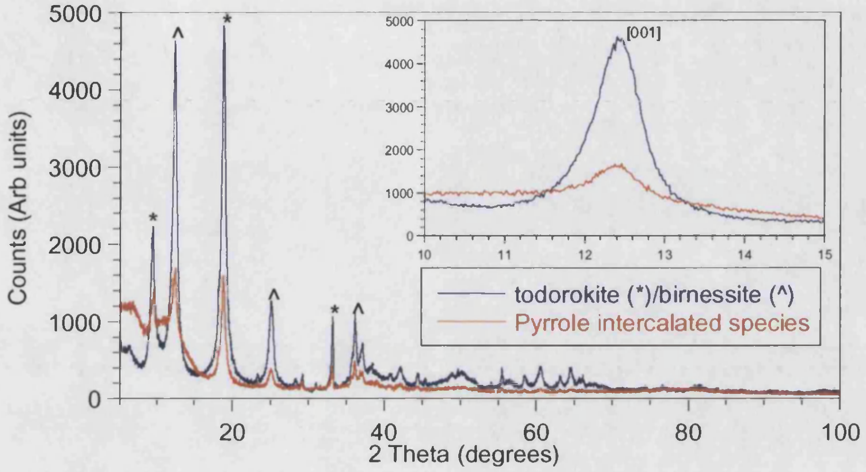

Figure 6.25. X-ray diffraction traces for the parent two phase todorokite/birnessite material and the pyrrole intercalated material showing changes in the lattice parameters and changes in intensity of the birnessite (peaks marked by ^) phase as a result of disorder induced by pyrrole intercalation; inset shows the birnessite [001] peak before and after pyrrole intercalation.

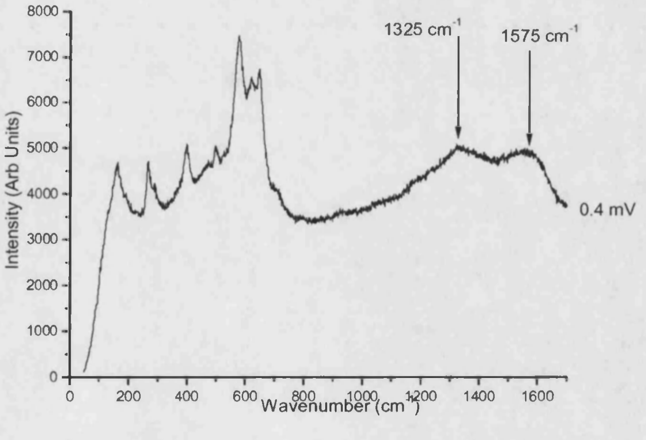

Figure 6.26. Raman Spectra for the pyrrole intercalated todorokite/birnessite mixed phase material collected using 632.8nm excitation showing the C=C and C-H vibrations of the pyrrole at 1575 cm^{-1} and 1325 cm^{-1} respectively .

Following the observation that the birnessite precursor is susceptible to polymer intercalation, pure samples were prepared and subsequently intercalated with pyrrole. Birnessite crystallises in the monoclinic space group, C 2/m. The material shows poor crystallinity due to the large interlayer gap and the presence of water in the layers. A Lebail extraction plot is shown in figure 6.27, the region cut between 17 and 20 two theta is due to a broad hump, possibly due to intergrowths or stacking faults within the material. Table 6.9 give the refined lattice parameters and the goodness of fit parameters for the refinement.

Table 6.9. Final Lattice Parameter and Goodness of fit factors for the Rietveld refinement of birnessite refined in the c 2/m space group.

a (Å)	b (Å)	c (Å)	β	Cell volume (Å^3)	χ^2	wRp (%)	Rp (%)
4.774(5)	2.8561(17)	7.404(4)	105.77(5)	97.15(13)	2.640	25.57	18.16

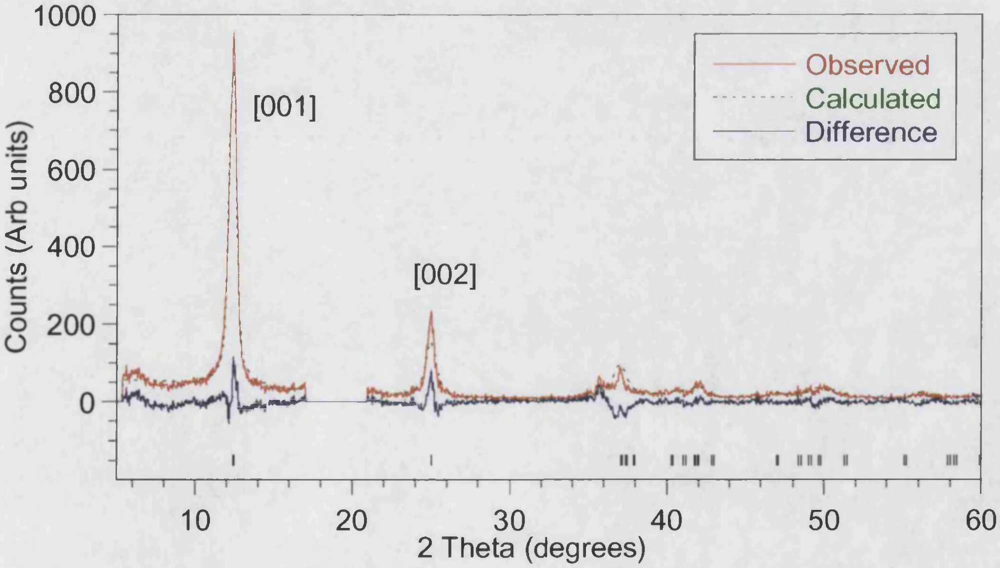

Figure 6.27. Observed, calculated and difference for the Lebail extraction of Na birnessite.

Intercalation of pyrrole results in a gradual decrease in peak intensity as shown in figure 6.28 accompanied by a shift in the [001] peak suggesting an increase in the interlayer space. Refinement of the lattice parameters using GSAS was not possible due to the poor quality of the data. These changes eventually lead to the production of a material amorphous to X-ray diffraction.

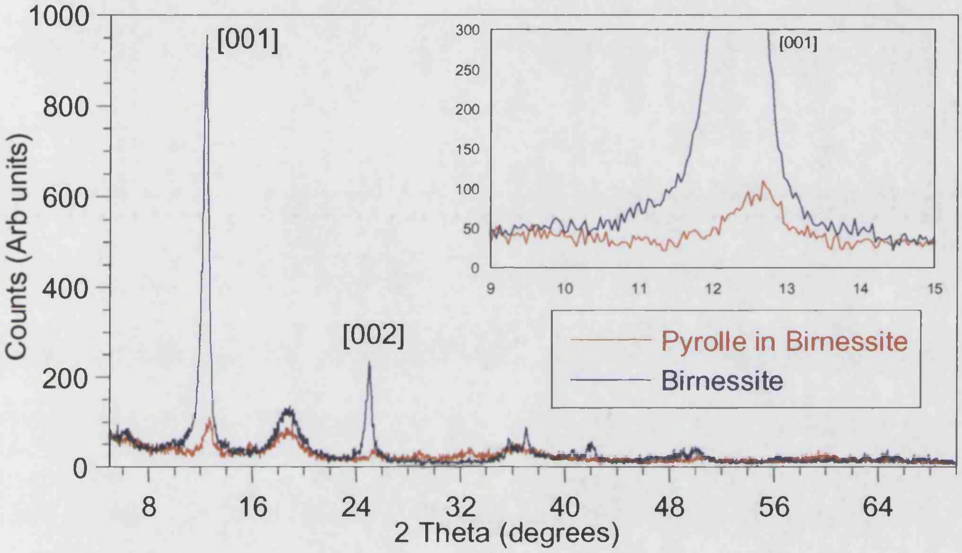

Figure 6.28. X-ray diffraction traces for birnessite and Pyrrole intercalated birnessite; Inset shows the shift of the [001] peak.

Infrared spectra collected for both the birnessite and the pyrrole intercalated birnessite are shown in figure 6.29. The intercalated species clearly show absorptions at approximately 1500, 600 and 200cm^{-1}, which, correspond to N-H stretching and bending motions confirming the presence of the organic. These absorptions are not present in the parent Birnessite material confirming that intercalation has occurred.[21]

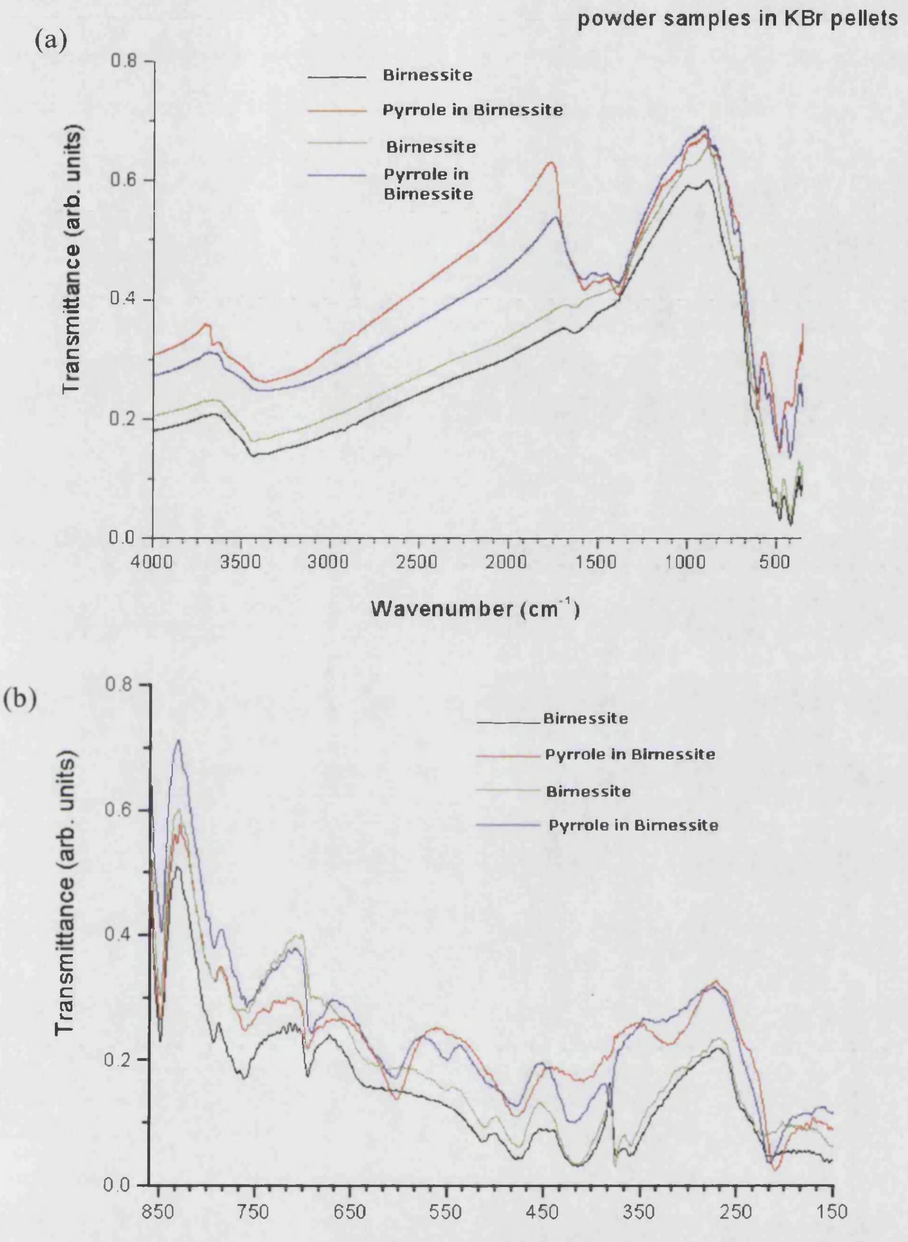

Figure 6.29. (a) FT-IR spectra and (b) Far Infra Red spectra for birnessite and pyrrole in birnessite.

Thermal analysis data collected for the mixed todorokite/birnessite phase showed an increased weight loss from 5.8% to 13.921% also consistent with pyrrole uptake (Figure 6.30). The first decomposition begins at 45.32°C and ends at 113.70°C and is accompanied by a weight loss of 3.654%, this weight loss is mirrored in the parent material and likely due to loss of water. The second step begins at 162.54°C and ends at 358.40°C, accompanied by a 13.921% weight loss, due to loss of the organic species. Further heating results in the decomposition of the material to an amorphous phase. It should be noted that this material contains a mixture of todorokite and birnessite phases and therefore, an accurate value for the amount of polymer intercalated into the birnessite material can not be determined.

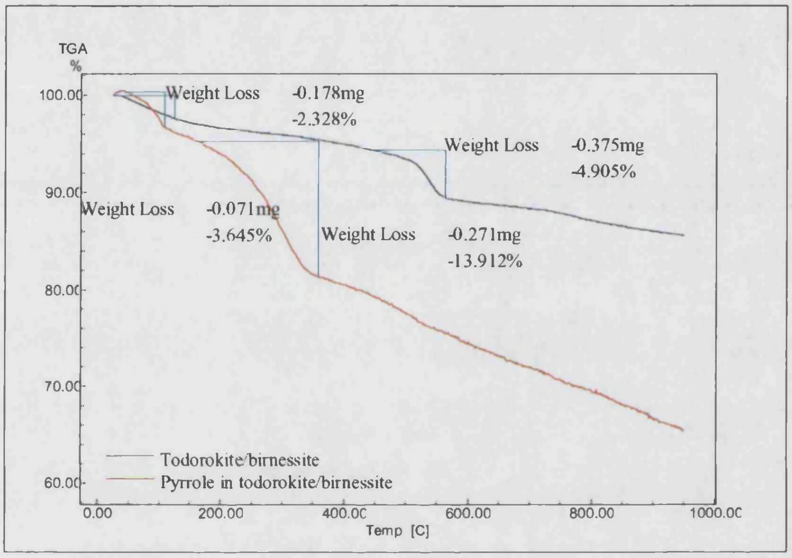

Figure 6.30 TGA traces showing decomposition routes and the increase in percentage weight loss for pyrrole treated and the todorokite/birnessite mixed phase.

As expected the magnetic data collected using the SQUID magnetometer showed marked differences. Both materials exhibited glassy type behaviour with divergence of the susceptibility below T_F.[33] However, a 10-fold increase in the magnitude of the susceptibility was observed on the intercalation of the pyrrole. This increase was also seen in the magnetic data collected for the mixed todorokite/birnessite phase. The Curie-Weiss data is given in table 6.10 and it can be clearly seen from the observed magnetic moments that the average manganese oxidation state changes as a result of intercalation. Magnetic behaviour is plotted in figures 6.31 to 6.33.

Table 6.10. Curie constant, Weiss constant and magnetic moments for both birnessite and pyrrole in birnessite.

	C	θ (K)	μ_{eff} (μ_B)	μ_{calc} (μ_B)
Birnessite	1.86(5)	-40.1(5)	3.86	4.37
Pyrrole in Birnessite	2.45(2)	-176(2)	4.43	-

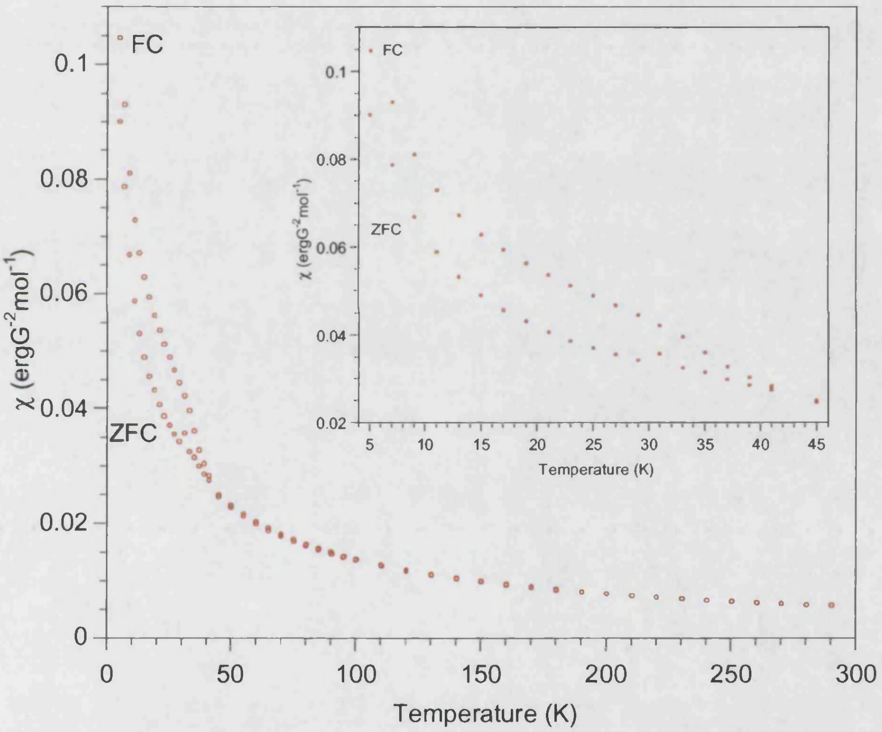

Figure 6.31. Magnetic susceptibilities showing divergence between zero field cooled (ZFC) and field cooled (FC) measurements for birnessite indicative of spin glass behaviour; inset shows the region below T_F.

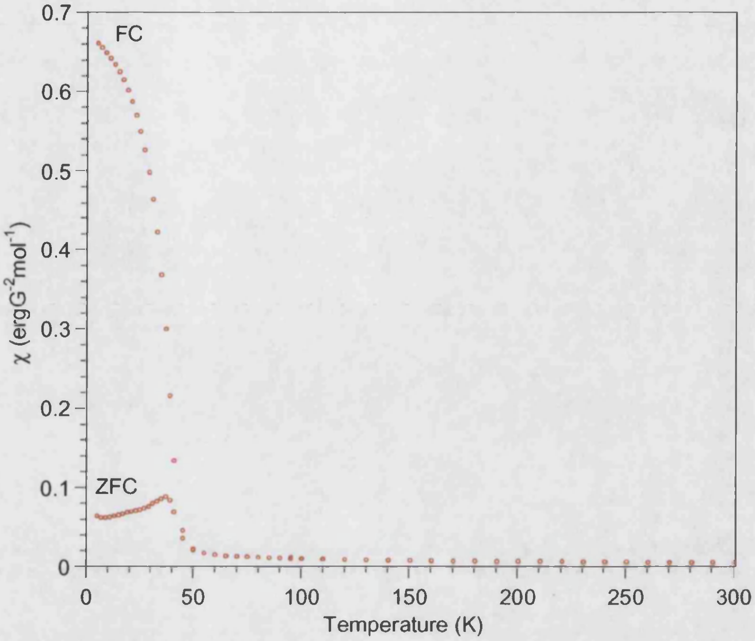

Figure 6.32. Magnetic susceptibilities showing divergence between zero field cooled (ZFC) and field cooled (FC) measurements for pyrrole intercalated birnessite indicative of spin glass behaviour; inset shows region below T_F.

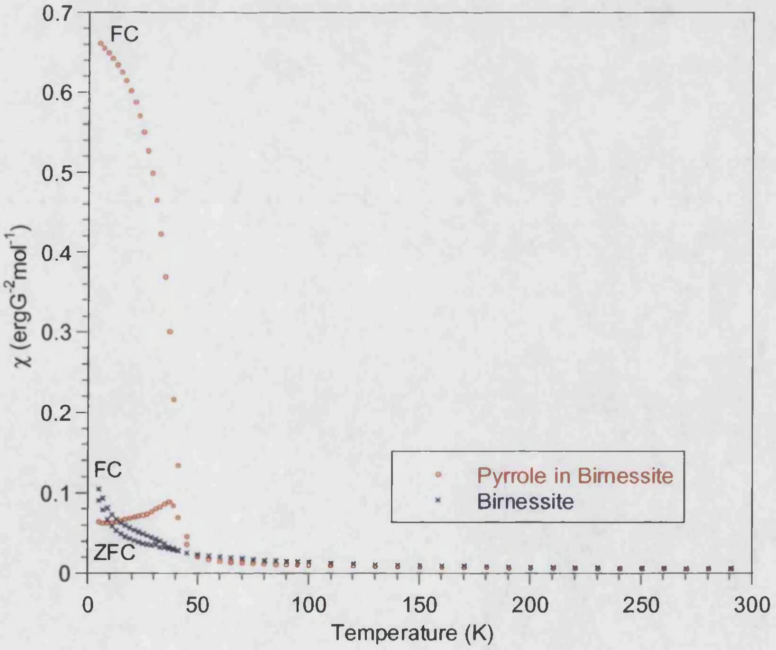

Figure 6.33. Magnetic susceptibility measurements of both birnessite and pyrrole intercalated birnessite showing increased magnitude of the susceptibility.

6.3.3. Polymer intercalation into α-$NaMnO_2$.

The structure of α-$NaMnO_2$ is discussed above. When treated with aniline and pyrrole while stirring at room temperature no loss in peak intensity is observed as with birnessite. In contrast on intercalation a large increase in peak intensity is observed suggesting increased crystallinity due to increased ordering. An additional peak is also observed at a high d-spacing of approximately 16.5Å for the aniline intercalated species and 7.8Å for the pyrrole intercalated species, which indicates that the interlayer space has been increased to accommodate the organic species and is consistent with the sizes required to accommodate the polymeric species. Figure 6.34 And 6.35 show the differences in the α-$NaMnO_2$ and the species intercalated with aniline and pyrrole respectively. The insertion of aniline into the framework appears more complete than that with pyrrole, since the framework is completely oxidised to α-$Na_{0.70}MnO_{2.05}$ with aniline but with pyrrole some of the α-$NaMnO_2$ remains.

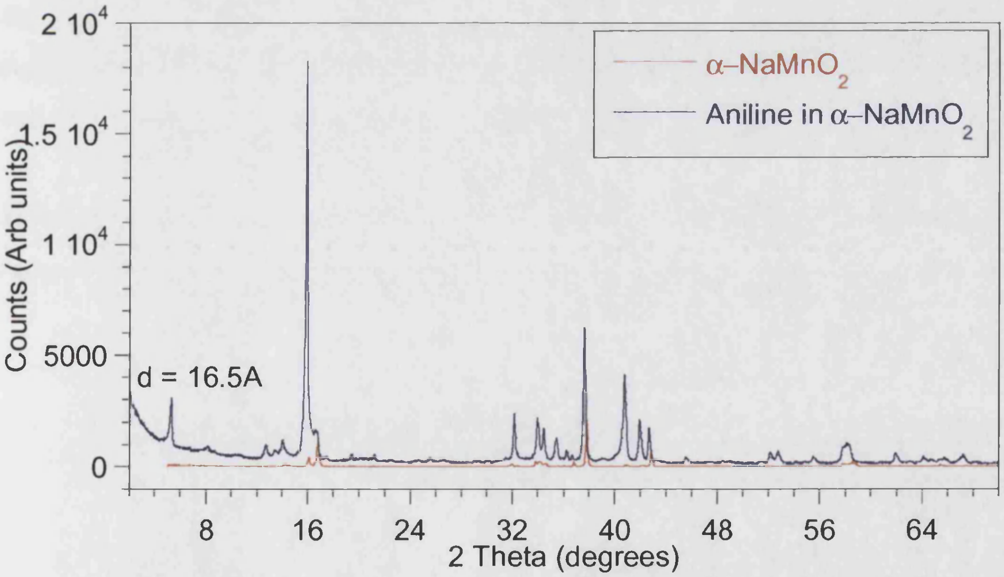

Figure 6.34. X-ray diffraction data for α-$NaMnO_2$ and aniline intercalated α-$NaMnO_2$ showing the additional peak at a d-spacing of 16.5Å.

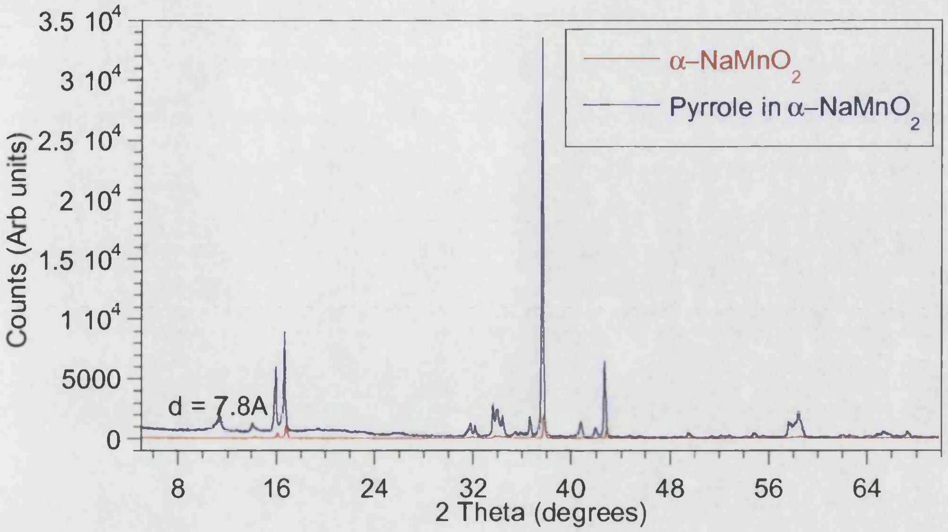

Figure 6.35. X-ray diffraction data for α-NaMnO₂ and pyrrole intercalated α-NaMnO₂ showing the additional peak at a d-spacing of 7.8Å

The peaks were indexed using the Crysfire and Celref programs to obtain an approximate cell.[41] The data was then refined using the Lebail function in the monoclinic space group, Pm. The refinement data is given in table 6.11 along with a summary of the refinement data for α-$NaMnO_2$. Figure 6.36 shows the observed, calculated and difference plots obtained from the Lebail fits.

Table 6.11. Final lattice parameters and goodness of fit factors for the Rietveld refinements of α-NaMnO₂ and analine intercalated species.

	Alpha (Neutron)	Alpha (X-ray)	Aniline
a (Å)	5.63888(29)	5.6739(7)	16.7981(10)
b (Å)	2.85747(9)	2.85981(33)	5.8879(5)
c (Å)	5.77076(27)	5.7991(10)	14.0479(16)
β	112.8540(29)	113.138(7)	93.817(7)
Cell Vol (Å^3)	85.684(7)	86.529(21)	1386.34(21)
χ^2	14.85	2.150	5.931
wRp (%)	5.72	27.05	10.87
Rp (%)	4.52	20.12	7.69

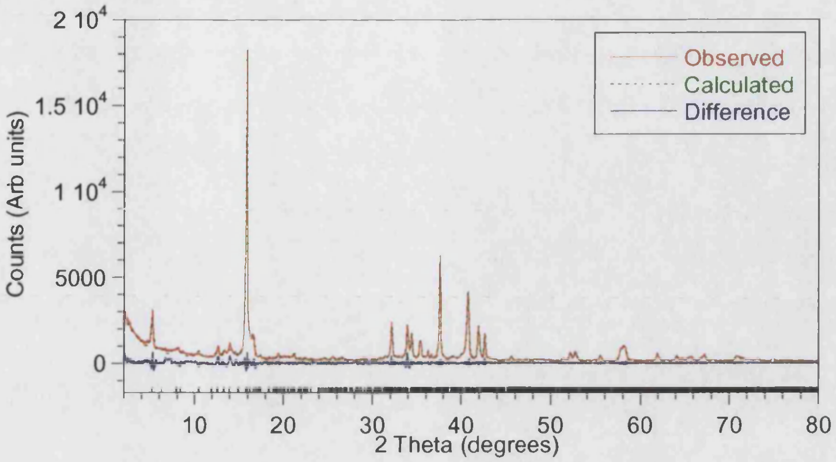

Figure 6.36. Observed, calculated and difference for the Lebail extraction of the X-ray diffraction data for aniline intercalated α-$NaMnO_2$.

Thermal analysis of both the pyrrole and the aniline intercalated species showed much larger total weight losses of 4.6% and 14.8% respectively compared to the 2.5% weight loss seen in the decomposition of pure α-$NaMnO_2$. The smaller weight loss seen in the pyrrole intercalated species and the low temperature first decomposition step are consistent with the suggestion that the intercalation of pyrrole is incomplete. Since the thermal stability of the polymer is higher with respect to monomer or dimer units and increases with unit length, the high first decomposition step for the aniline intercalated species supports the suggestion that polymerisation has occurred in α$NaMnO_2$ when compared to the lower stabilities observed for birnessite.[42] Table 6.12 gives the decomposition temperature compared to those of α$NaMnO_2$ and TGA plots are given in figure 6.37 and 6.38 for aniline and pyrrole respectively.

Table 6.12. Thermal analysis decomposition data for α-$NaMnO_2$ and the aniline and pyrrole intercalated species.

	1st decomposition			2nd Decomposition			3rd Decomposition		
	Onset (°C)	Endset (°C)	% Wt loss	Onset (°C)	Endset (°C)	%Wt loss	Onset (°C)	Endset (°C)	% Wt loss
Alpha	75.08	100.02	1.417	475.53	600.47	1.114			
Aniline	228.34	274.90	8.457	347.26	398.37	2.518	469.21	610.90	3.844
Pyrrole	42.38	140.42	0.106	213.30	345.94	1.494	395.75	563.52	2.996

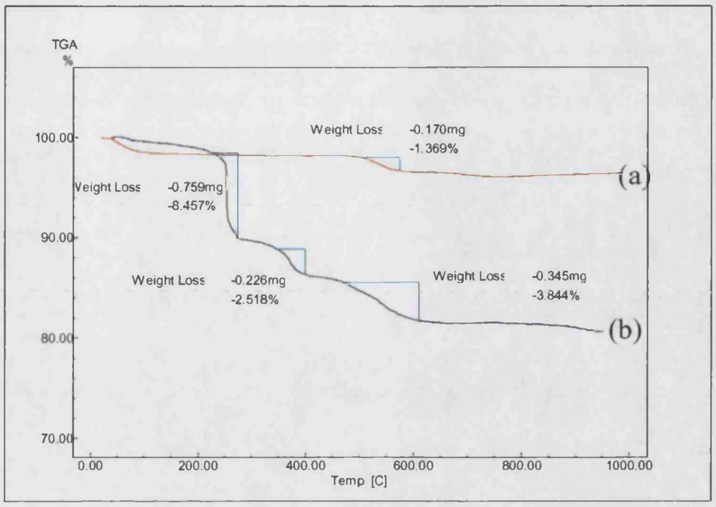

Figure 6.37. TGA traces showing decomposition routes and increased weight loss for (a) α-$NaMnO_2$ and (b) the aniline intercalated species.

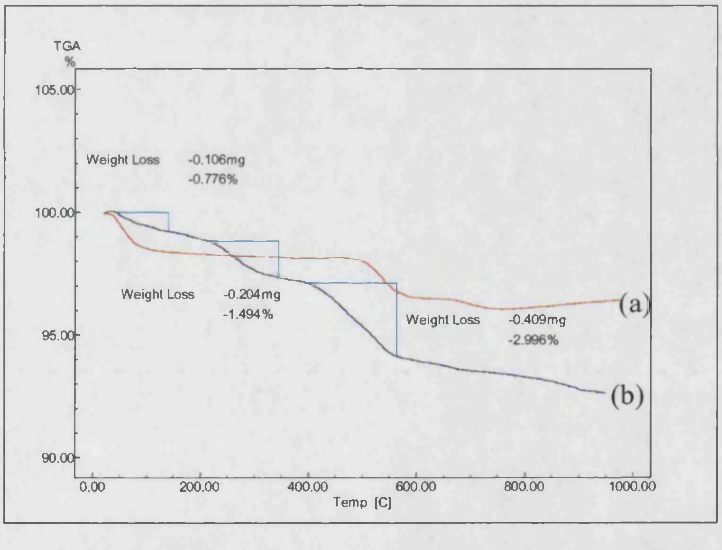

Figure 6.38. TGA traces showing decomposition routes and increased weight loss for (a) α-$NaMnO_2$ and (b) the pyrrole intercalated species.

α-$NaMnO_2$ is metamagnetic as described above. As with the birnessite materials, intercalation of the aniline results in a huge increase in the magnitude of the magnetisation. However, after intercalation with pyrrole this increase is not evident again supporting the suggestion that the intercalation of pyrrole is incomplete and does not greatly affect the Mn oxidation state. Both intercalated species exhibit glassy behaviour suggesting that the increased interlayer space destroys the metamagnetic ordering between the layers. Figures 6.39 through 6.40 show the magnetic behaviour of the intercalated species. Curie-Weiss data for the intercalated species is given in table 6.13. Due to the high ordering temperature of α-$NaMnO_2$ the Curie-Weiss law could not be fitted. As with birnessite a clear change in the framework oxidation state is observed. Figure 6.41 shows the differences in magnetic susceptibities of the α-$NaMnO_2$ and the polymer intercalated species.

Table 6.13. Curie constant, Weiss constant and magnetic moments for both aniline and Pyrrole intercalated α-$NaMnO_2$.

	C	θ (K)	μ_{eff} (μ_B)
Aniline	2.501(7)	-301(1)	4.47
Pyrrole	2.72(3)	-869(9)	4.67

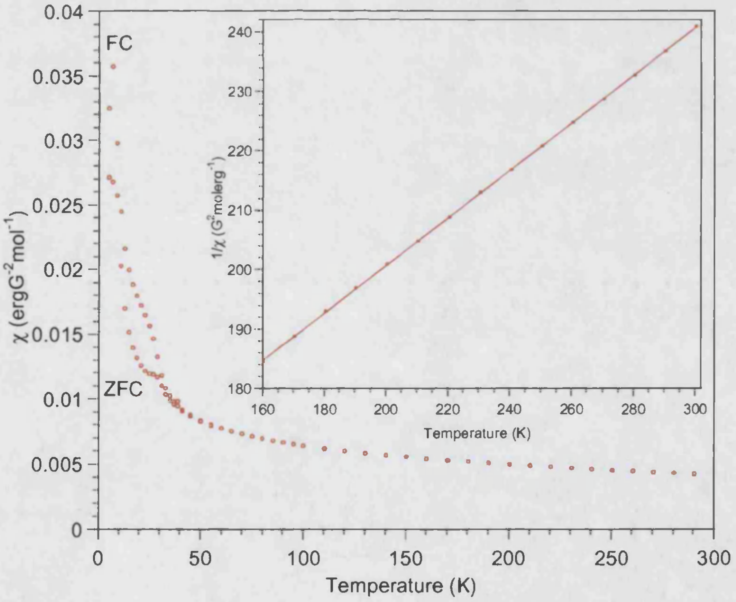

Figure 6.39. Magnetic susceptibilities showing the divergence between zero field cooled (ZFC) and field cooled (FC) measurements for aniline in α-$NaMnO_2$; *inset shows Curie-Weiss behaviour of the paramagnetic region.*

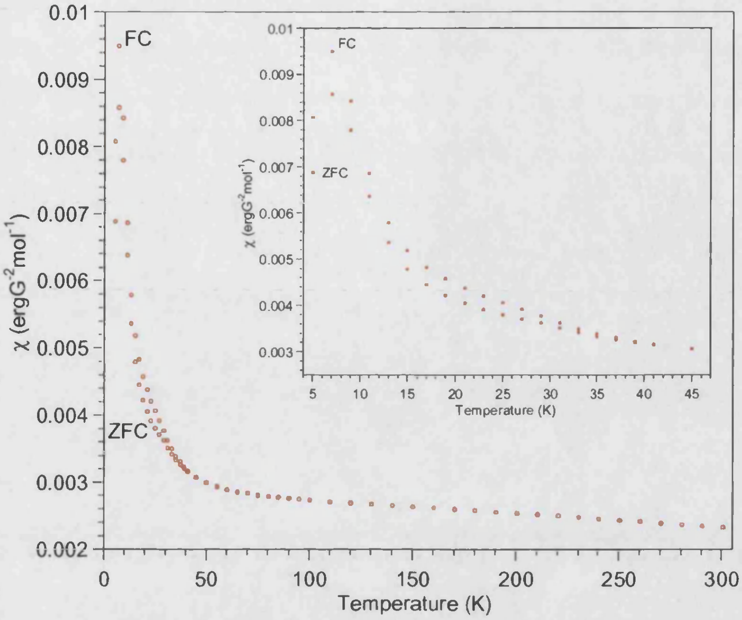

Figure 6.40. Magnetic susceptibilities showing the divergence between zero field cooled (ZFC) and field cooled (FC) measurements for pyrrole in α-NaMnO$_2$; inset shows the region below T_F.

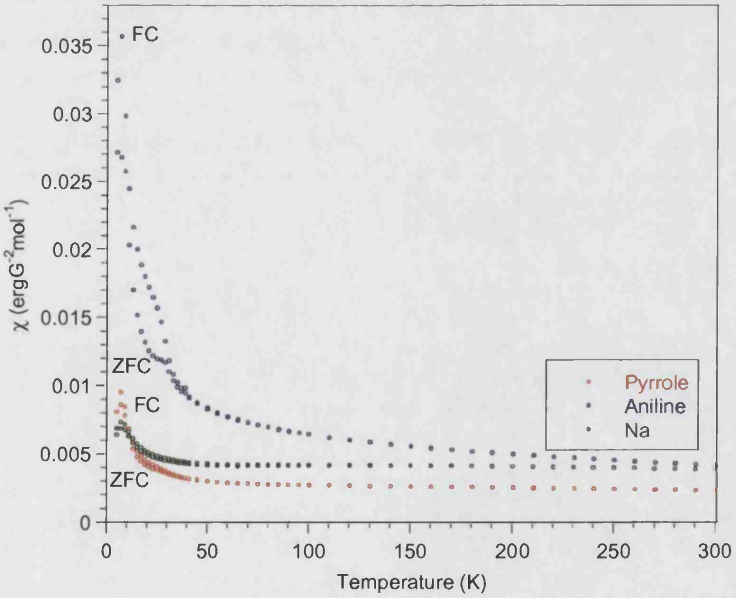

Figure 6.41. Magnetic susceptibilities for α-NaMnO$_2$ and both the aniline and pyrrole intercalated materials showing the increased magnetisation of the polymer intercalated species.

6.4. Conclusions.

We have shown that whilst it is not possible to remove the Na counter ion from the interlayer space it is possible to conduct intercalation experiments resulting in an increased interlayer gap. The presence of single MnO_2 sheets in α-$NaMnO_2$ does not appear to inhibit intercalation, with the insertion of large cations such as Cs possible. Intercalation of the β-$NaMnO_2$ phase is more difficult due to the presence of the double layers of MnO_2 sheets, which effectively lock the template ion into the layer space. However, intercalation of K and NH_4 appeared to be possible, with a much larger interlayer gap being observed than in the K or NH_4 alpha intercalated materials suggesting that the MnO_2 layers remain intact.

Both α-$NaMnO_2$ and β-$NaMnO_2$ exhibit complex magnetic properties, due to weak interactions and dimensionality of the system. The different magnetic properties seen show how sensitive these systems are to guest molecules as well as illustrating the flexible nature of the manganese to adopt varying oxidation states to maintain charge balance.

The results discussed here suggest that it is also possible to intercalate large organic molecules into the interlayer spaces of these materials. The use of X-ray diffraction, FTIR and SQUID magnetic measurements confirm the presence of the aniline or pyrrole in the samples. In birnessite and α-$Na_{0.70}MnO_2$ a loss of peak intensity is observed suggesting a loss in crystallinity on intercalation of the organic, this would suggest that the system has an increased degree of disorder, which is not consistent with the polymerisation of the organic which should result in an increased layer spacing and increased order due the conjugate nature of the polymer. However on intercalation α-$NaMnO_2$ shows an increased peak intensity and hence crystalllinity, it is also evident from the X-ray data that the interlayer space has been increased. Since it can be seen from the IR, TGA and SQUID data that the organic is present it can be suggested that the aniline and pyrrole in this case are polymerised on reaction with the framework. This can be confirmed from the TGA data which shows a lower temperature of decomposition in the birnessite as the monomer unit is lost, $45^{O}C$, since the polymer is more thermally stable a higher temperature of decomposition is observed. The mechanism for the polymerisation is not well defined, but is driven by the framework and hence the average manganese oxidation state. In birnessite and α-$Na_{0.70}MnO_{2.05}$ is between 3.4 and 3.55, which leads to a stable framework. In αNaMnO$_2$, however the average manganese oxidation state is close to +3 as seen in Chapter 6 this material has lost Na over time and hence the framework is already susceptible to oxidation leading to a mixed valence state. It may be this susceptibility to oxidation that drives the polymerisation reaction. This contrasts with data published for other framework systems, where the framework acts only as a physical constraint in the dimension of growth and does not contribute to the polymerisation reaction.

6.5. References.

(1) Q. Feng, H. Kanoh, K. Ooi, *Journal of Materials Chemistry*, **1999**, *9(2)*, 319.

(2) J. P. Parant, R. Olazcuaga, M. Devalette, C. Fouassier, P. Hagenmuller, *Journal of Solid State Chemistry*, **1971**, *3*, 1.

(3) A. Mendiboure, C. Delmas, P. Hagenmuller, *Journal of Solid State Chemistry*, **1985**, *57(3)*, 323.

(4) A. Caballero, L. Hernan., J. Morales, L. Sanchez, J. S. Pena, M. A. G. Aranda, *Journal of Materials Chemistry*, **2002**, *12(4)*, 1142.

(5)P. G. Bruce, A. R. Armstrong, R. L. Gitzendanner, *Journal of Materials Chemistry*, **1999**, *9(1)*, 193.

(6) J. M. Paulsen, S. L. Thomas, J. R. Dahn, *Journal of the Electrochemical Society*, **1999**, *146(10)*, 3560.

(7) J. M. Paulsen, J. R. Dahn, *Solid State Ionics*, **1999**, *126*, 3.

(8) G. Vitins, K. West, *Journal of the Electrochemical Society*, **1997**, *144(8)*, 2587.

(9) C. G. Wu, D. C. Degroot, H. O. Marcy, J. L. Schindler, C. R. Kannewurf, T. Bakas, V. Papaefthymiou, W. Hirpo, J. P. Yesinowski, Y. J. Liu, M. G. Kanatzidis, *Journal of the American Chemical Society*, **1995**, *117(36)*, 9229.

(10) E. Ruiz-Hitzky, *Advanced Materials*, **1993**, *5*, 334.

CHAPTER 6: Layered Systems.

(11) D. J. Cardin, *Advanced Materials*, **2002**, *14*, 553.

(12) C. R. Martin, *Accounts of Chemical Research*, **1995**,*28(2)*, 61.

(13) K. Moller, T. Bein, R. X. Fischer, *Chemistry of Materials*, **1998**, *10(7)*, 1841.

(14) S. Esnouf, F. Beuneu, P. Enzel, T. Bein, *Physical Review B*, **1997**, *56(20)*, 12899.

(15) P. Enzel, T. Bein, *Journal of Physical Chemistry*, **1989**, *93(17)*, 6270.

(16) P. Enzel, T. Bein, *Journal of the Chemical Society. Chemical Communications*, **1989**, *18*, 1326.

(17) P. Enzel, T. Bein, *Chemistry of Materials*, **1992**, *4(4)*, 819.

(18) J. Jang, B. Lim, J. Lee, T. Hyeon, *Chemical Communications*, **2001**, *1*, 83.

(19) V. M. Cepak, C. R. Martin, *Chemistry of Materials*, **1999**, *11(5)*, 1363.

(20) Z. Zhang, S. Dai, D. A. Blom, J. Shen, *Chemistry of Materials*, **2002**, *14(3)*, 965.

(21) T. Bein, P. Enzel, *Angewandte Chemie. International Edition*, **1989**, *28(12)*, 1692.

(22) D. J. Cardin, S. P. Constantine, A. Gilbert, A. K. Lay, M. Alvaro, M. S. Galletero, H. Garcia, F. Marquez, *Journal of the American Chemical Society*, **2001**, *123(13)*, 3141.

(23) M. G. Kanatzidis, L. M. Tonge, T. J. Marks, H. O. Marcy, C. R. Kannewurf, *Journal of the American Chemical society*, **1987**, *109(12)*, 3767.

(24) S. M. Kauzlarich, J. F. Ellena, P. D. Stupik, W. M. Reiff, B. A. Averill, *Journal of the American Chemical Society*, **1987**, *109(15)*, 4561.

(25) H. Sakaebe, S. Higuchi, K. Kanamura, H. Fujimoto, Z. Takehara, *Solid State Ionics*, **1995**, *79*, 234.

(26) M. G. Kanatzidis, C. G. Wu, H. O. Marcy, D. C. DeGroot, C. R. Kannewurf, A. Kostikas, *Adanced Materials*, **1990**, *2(8)*, 364.

(27) Y. J. Liu, D. C. DeGroot, J. L. Schindler, C. R. Kannewurf, M. G. Kanatzidis, *Advanced Materials*, **1993**, *5(5)*, 369.

(28) K. Song, S. Kauzlarich, *Chemistry of Materials*, **1994**, *6(4)*, 386.

(29) M. G. Kanatzidis, R. Bissessur, D. C. DeGroot, J. L. Schindler, C. R. Kannewurf, *Chemistry of Materials*, **1993**, *5(5)*, 595.

(30) L. Wang, P. Brazis, M. Rocci, C. R. Kannewurf, M. G. Kanatzidis, *Chemistry of Materials*, **1998**, *10(11)*, 3298.

(31) L. Wang, J. L. Schindler, J. A. Thomas, C. R. Kannewurf, M. G. Kanatzidis, *Chemistry of Materials*, **1995**, *7(10)*, 1753.

(32) Q. Feng, H. Kanoh, K. Ooi, M. Tani, Y. Nakacho, *Journal of the Electrochemical Society*, **1994**, *141*, L135.

(33) S. L. Suib, L. E. Iton, *Chemistry of Materials*, **1994**, *6(4)*, 429.

(34) E. Nicolas-Tolentino, Z. R. Tian, H. Zhou, G. G. Xia, S. L. Suib, *Chemistry of Materials*, **1999**, *11(7)*, 1773.

(35) K. S. Abou-El-Sherbini, M. H. Askar, R. Schollhorn, *Solid State Ionics*, **2002**, *150*, 407.

(36) W. Tang, H. Kanoh, K. Ooi, *Journal of Solid State Chemistry*, **1999**, *142*, 19.

(37) A. R. Armstrong, P. G. Bruce, *Nature*, **1996**, *381*, 499.

(38) Y. U. Jeong, A. Manthiram, *Journal of Solid State Chemistry*, **2001**, *156*, 331.

(39) Y. Omomo, T. Sasaki, M. Watanabe, *Solid State Ionics*, **2002**, *151*, 243.

(40) Q. Feng, T. Horiuchi, T. Mitsusio, K. Yanagisawa, N. Yamasaki, *Journal of Materials science Letters*, **1999**, *18(17)*, 1375.

(41) R. Shirley, *The CRYSFIRE System for Automatic Powder Indexing*, **2000**, *v 3.25*.

(42) V. T. Truong, B. Ennis, T. G. Turner, C. M. Jenden, *Polymer International*, **1992**, *27(2)*, 187.

CHAPTER 7: $Pr_{1-x}Ca_{1+x}MnO_4$ System.

7.1. Introduction.

Recent interest in the perovskites with the general formula, $Ln^{3+}_{2-x}A^{2+}_{x}MnO_3$, where Ln^{3+} = Lanthanide and A^{2+} is typically Sr or Ca, has been generated through their strong correlations between charge and spin ordering with electrical resistivity.[1-12] For specific composition ranges in the solid solutions the materials show ferromagnetism, which is also associated with a transition from an insulator to a metal on cooling. At temperatures around this critical point the application of a magnetic field can drive the system from a paramagnetic insulator to a ferromagnetic metal, effectively generating a near 100 % change in the resistivity, known as colossal magnetoresistance. Materials with such magnetoresistance are of great potential value in many magnetic storage and sensing device applications. However, for a material to be usefully employed in such areas, the effect would need to be observed at room temperature and in low magnetic fields. Although many systems have been investigated, these combinations of properties have been difficult to produce in the perovskite structures. To address this issue, manipulation of the electronic properties of perovskite manganates has been investigated through the formation of analogous layered systems, such as the Ruddlesden-Popper series. These structures, forming with the general formula $Ln^{3+}A^{2+}_{n+1}Mn_nO_{3n-1}$ are composed of n layers of connected Mn-O planes with an A-O rock salt layer separating them. One goal of this research is to produce strong ferromagnetic exchange within the planes, with weaker interactions in the third direction, possibly leading to transitions to ferromagnetism to be induced in lower fields.

In the Ruddlesden-Popper series, the n = 1 member, has the pseudo two dimensional K_2NiF_4 structure with no Mn-O-Mn linkage in the *c* direction and consequently has a particularly narrow bandwidth compared with the three dimensional perovskite structures. The $La_{1-x}Sr_xMnO_4$ phase within the n = 1 series has been most extensively studied. These phases have a pseudo two dimensional K_2NiF_4 type structure with two distinct A sites, one is a relatively large 12 co-ordinate site (P) situated within the Perovskite like blocks and a smaller 9 co-ordinate site (R) situated on the edge of the Perovskite blocks in the rock salt layers (AO). Unless the A cations are sufficiently distinct from each other they are able to order and inevitably distribute between the two sites (figure 7.1).[8,13,14] $LaSrMnO_4$ phases, in general, show antiferromagnetic ordering at low temperature with no evidence of ferromagnetic ordering in contrast to the corresponding perovskites instead there is a tendency towards antiferromagnetic ordering with increasing x. Specific composition with the series, such as $Ln_{0.5}Sr_{1.5}MnO_4$, show charge ordering transitions, where the Mn^{3+} and Mn^{4+} order onto crystallographically distinct sites. All compositions across the series display relatively high electrical resistance via a thermally activated mechanism.[15] Doping of the Mn sites with Rh^{3+} leads to the first K_2NiF_4 oxide with strong ferromagnetic interactions, where bulk magnetisation stems from the alignment of the magnetic field of ferromagnetic $(Mn/Rh)O_2$ sheets, which are not magnetically ordered along [001] in zero applied field.[16]

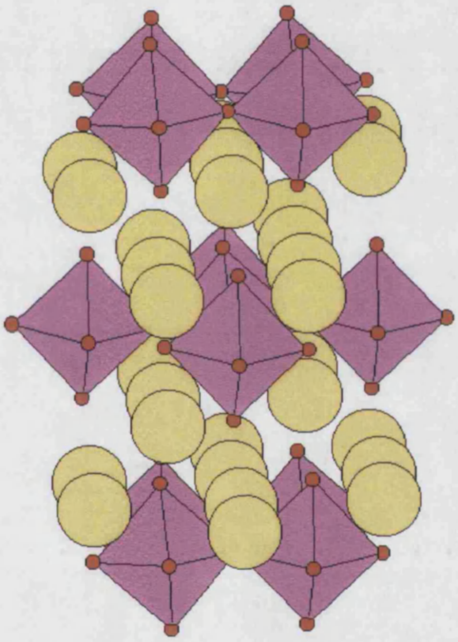

Figure 7.1. Schematic representation of the Ruddlesden-Popper K_2NiF_4 structure, where the B site octahedra are pink and the yellow spheres represent the cations on the A site.

Less attention has been paid to the $Ln_{2-x}Ca_xMnO_4$ series, which has been reported to crystallise with orthorhombic symmetry with the exception of Ln = Pr, which is tetragonal.[17-19] Structural phase transition occurring between 290 K and 340 K, are observed on heating the orthorhombic compositions producing tetragonal structures, which was reported to be a result of liberation of the Jahn Teller constraint by thermal energy. Maignan suggested that the small size of Ca^{2+} cations should promote ferromagnetism due to the increased bandwidth that correspondingly enhances the double exchange, though they reported only an anomalously low ferromagnetic moment on the Mn. They further suggested the structures adopt a *Aba2* space group, however, they were not able to accurately refine of the positions of the oxygen atoms located in the [MnO_2] planes.[20] The work discussed here focuses on the correlations between structure and magnetic behaviour of a series of materials with the formulae $Ln_{0.5}Ca_{1.5}MnO_4$, where Ln is Pr, Nd, Dy, Er, Ho, Sm and Tb.

7.2. Synthesis.

The $Ln_{0.5}Ca_{1.5}MnO_4$ (Ln = Lanthanide) series were synthesised from stoichiometric mixtures of MnO_2, $CaCO_3$ and the rare earth oxide Pr_6O_{11}, Nd_2O_3, Dy_2O_3, Er_2O_3, Ho_2O_3, Sm_2O_3 and Tb_2O_3. The starting materials were initially heated to 1000°C to allow decomposition of the carbonates, pressed into pellets and fired at 1200°C for 2 days. Further heating were performed at 1350°C in 25 hour cycles, followed by an intermittent regrinding and measurement of the X-ray diffraction pattern to follow the progress of the reaction. Magnetic data was collected using a Quantum Design MPMS7 SQUID magnetometer and electrical measurements were made using the Oxford Instruments MAGLAB. X-ray diffraction patterns were collected on a Siemens D500 diffractometer fitted with a primary monochromator emitting $CuK_{\alpha 1}$ radiation at λ = 1.54056. Measurements during the synthesis process were recorded over an angular range of 10° to 70° with a step size of 0.04° and count time of 2 seconds per step. Extended scans were performed on single-phase material over an angular range of 10° to 100° with a step size of 0.02° and count time of 15 seconds per step. Powder Neutron diffraction measurements were performed at the National Institute of Standards and Technology (NIST), Gaithersburg, Maryland, USA using a Cu (311) monochromator (λ = 1.5401) and 14' final collimation. Scans were taken from 3° to 165° with a step size of 0.05°. Reitveld profile refinements were carried out with the GSAS suite of programs using a pseudo-Voigt peak shape function. Cooling for low temperature measurements was performed with a closed cycle refrigerator.

7.3. Results and Discussion.

7.3.1. Structure.

Initial reaction of the starting materials showed that the perovskite phase was first to form and that the crystallisation of the K_2NiF_4 type structure formed after several firings at high temperatures (1350°). This was evident from the powder X-ray diffraction patterns, in particular the region between the main reflections around 33° and 34° two-theta. As the reaction proceeds the central feature in this region is reduced in intensity, and was indexed as the intense [002] and [121] reflections for the perovskite structure (within the Pnma space group). The initial poor crystallinity and unresolved reflections around 33° and 34° is probably due to intergrowth between the perovskite phase and the K_2NiF_4-type structure as well as other members of the Ruddlesden-Popper series, which form during the synthesis procedure.

The cell parameters for the $Ln_{0.5}Ca_{1.5}MnO_4$ series were obtained by performing the Lebail intensity extraction procedure within the GSAS program, using a space group without any systematic absences.[21] The values obtained are given in table 7.1 and the volume as a function of cation size is plotted in figure 7.2, note the long axis through the layers has been defined as the b-axis.

Table 7.1. Final lattice parameters/cell volume from lebail extraction of X-ray diffraction data refined in the C 2/m space group.

	Lattice Parameters			
Sample	a (Å)	b (Å)	c (Å)	Cell volume ($Å^3$)
$Pr_{0.5}Ca_{1.5}MnO_4$	5.3901(9)	11.8267(23)	5.3687(9)	342.24(11)
$Nd_{0.5}Ca_{1.5}MnO_4$	5.3767(7)	11.8195(12)	5.3638(6)	340.87(7)
$Sm_{0.5}Ca_{1.5}MnO_4$	5.3661(8)	11.7756(15)	5.3594(8)	338.66(8)
$Gd_{0.5}Ca_{1.5}MnO_4$	5.3909(6)	11.6868(19)	5.3338(7)	336.04(8)
$Tb_{0.5}Ca_{1.5}MnO_4$	5.3837(11)	11.6822(23)	5.3478(12)	336.34(12)
$Dy_{0.5}Ca_{1.5}MnO_4$	5.4021(6)	11.7032(14)	5.3396(5)	337.58(6)
$Ho_{0.5}Ca_{1.5}MnO_4$	5.3395(5)	11.6657(11)	5.3698(5)	334.48(6)
$Er_{0.5}Ca_{1.5}MnO_4$	5.3879(12)	11.6678(29)	5.3410(12)	335.76(13)

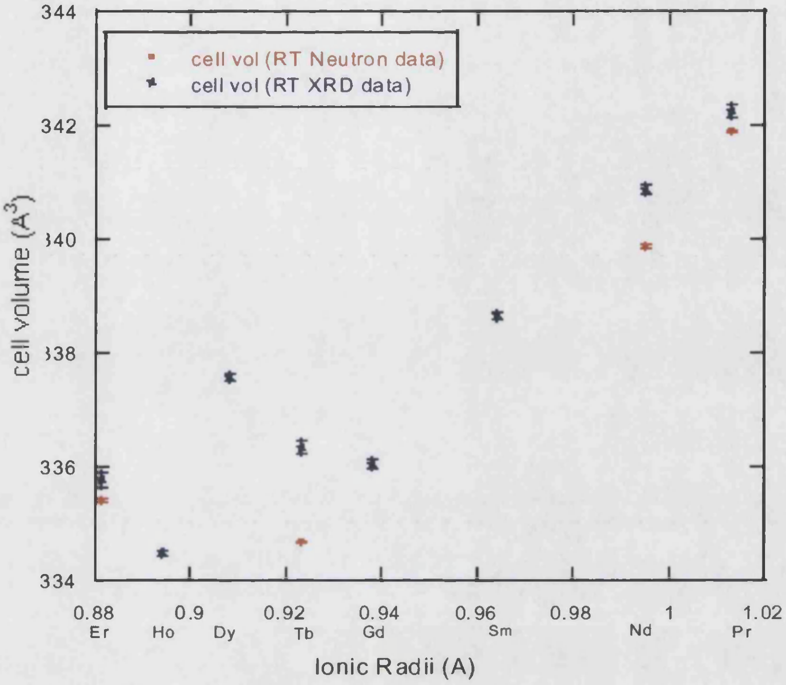

Figure 7.2. Cell volume as a function of ionic radii for lanthanide series.

It is evident that there is a reduction in the volume of the cell with decreasing lanthanide ionic radii. A plateau is observed for the smaller ions from Dy to Er and represents the minimum Mn-O bond distance that can be obtained.

Powder neutron diffraction was initially performed on four materials, namely $Pr_{0.5}Ca_{1.5}MnO_4$ $Nd_{0.5}Ca_{1.5}MnO_4$, $Tb_{0.5}Ca_{1.5}MnO_4$ and $Er_{0.5}Ca_{1.5}MnO_4$ at both room temperature and 15K. This was done to investigate the distortion as a function of increasing lanthanide size. All patterns obtained showed the same systematic absences, implying identical space groups. Two space groups were suggested by Maignan *et al*, namely Abm2 and Abma, Our comparison through Rietveld analysis confirmed the Abma (or Cmca in its ABC setting) space group, with the lowering to Abm2 unjustified with no significant improvement to the fits apparent.[1,20,21] Trace amounts of $Ca_xPr_{1-x}MnO_3$ (~6%) have been taken into account in the refinement. The observed cell volume from the refinements is plotted in figure 7.2 as a function of lanthanide ionic radii and exhibits the same trends observed by X-ray analysis. Refined powder neutron diffraction patterns for $Pr_{0.5}Ca_{1.5}MnO_4$, $Nd_{0.5}Ca_{1.5}MnO_4$, $Er_{0.5}Ca_{1.5}MnO_4$ and $Tb_{0.5}Ca_{1.5}MnO_4$ are given in figures 7.3 through 7.9. Atom positions and neutron fit data are given in tables 7.2 and 7.3. In each case the manganese has four long Mn-O bonds and two shorter ones given in tables 7.4 through 7.7.[22] All $Ln_{0.5}Ca_{1.5}MnO_4$ manganates have been refined in the orthorhombic system with no evident change in symmetry for praseodymium as reported by Daoudi *et al.*[17] There is also no indication of an orthorhombic to tetragonal phase change at low temperatures as suggested by some authors, with the symmetry and space group remaining unchanged for the low temperature data.[17,23,24]

Table 7.2. Atomic positions obtained from Rietveld profile refinements of powder neutron diffraction data of $Pr_{0.5}Ca_{1.5}MnO_4$ at 15 K (Pr 15 K) and room temperature (Pr RT) and $Nd_{0.5}Ca_{1.5}MnO_4$ at 15 K (Nd 15 K) and room temperature (Nd RT), in the space group Cmca.

	Pr 15 K	Pr RT	Nd 15 K	Nd rt
a (Å)	5.3581 (1)	5.3638 (1)	5.3450 (3)	5.3528 (3)
b (Å)	11.7822 (2)	11.8164 (2)	11.7755 (5)	11.8145 (5)
c (Å)	5.3883 (1)	5.3941 (1)	5.3693 (3)	5.3756 (3)
Cell Volume (Å^3)	340.16 (1)	341.88 (1)	337.95 (3)	339.96 (3)
Pr / Nd /Ca (0, y, z)				
y	0.3564 (1)	0.3568 (1)	0.3566 (2)	0.3570 (2)
z	-0.0079 (1)	-0.0075 (1)	-0.0078 (2)	-0.0073 (2)
U_i (x 100)	0.88 (4)	1.19 (5)	1.10 (6)	1.52 (7)
Mn (0, 0, 0)				
U_i (x 100)	0.70 (6)	0.73 (7)	1.3 (1)	1.4 (1)
O (1) (0.25, y, 0.25)				
y	-0.0103 (1)	-0.0085 (2)	-0.0093 (3)	-0.0059 (5)
U_{11} (x 100)	0.82 (9)	0.83 (9)	1.9 (2)	2.4 (2)
U_{22} (x 100)	1.29 (8)	1.78 (9)	1.6 (1)	2.0 (2)
U_{33} (x 100)	1.6 (1)	1.9 (1)	0.7 (2)	1.0 (2)
U_{13} (x100)	-0.09 (6)	-0.36 (7)	0.0 (1)	-0.1 (1)
O (2) (0, y, z)				
y	0.1654 (1)	0.1649 (1)	0.1647 (2)	0.1648 (2)
z	0.0315 (3)	0.0261 (4)	0.0346 (7)	0.026 (1)
U_{11} (x 100)	1.83 (11)	1.89 (1)	1.8 (2)	1.8 (2)
U_{22} (x 100)	0.26 (7)	0.53 (7)	0.2 (1)	0.6 (1)
U_{33} (x 100)	1.28 (9)	1.9 (1)	2.3 (2)	3.7 (3)
U_{23} (x 100)	0.14 (7)	0.1 (1)	0.6 (1)	0.6 (2)
wRp (%)	7.43	7.26	8.21	8.75
Rp (%)	5.31	5.45	6.29	6.86
χ^2	3.663	1.405	3.082	2.185

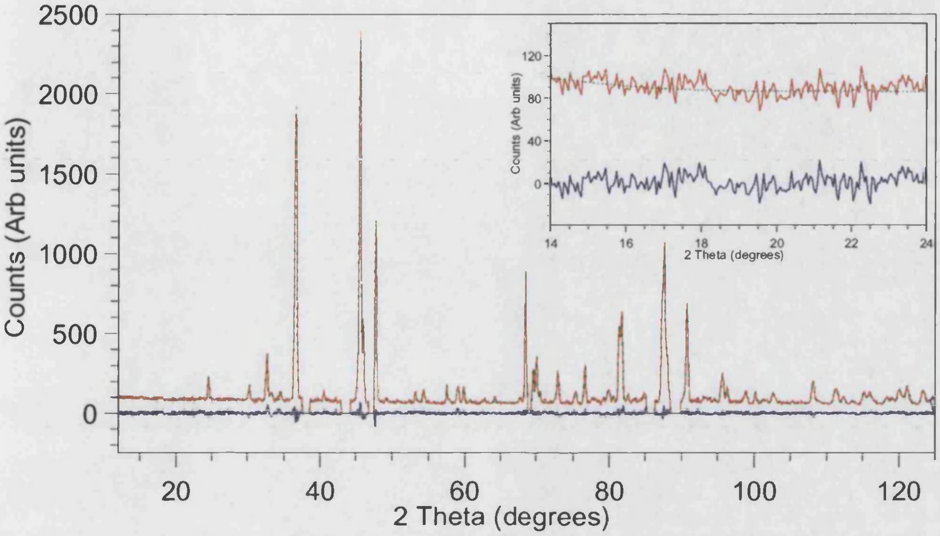

Figure 7.3. Observed, calculated and difference from the Rietveld refinement of $Pr_{0.5}Ca_{1.5}MnO_4$ *at room temperature. Insert shows the absence of magnetic peaks between 12 and 24° 2 theta. Refined in the C2/m space group.*

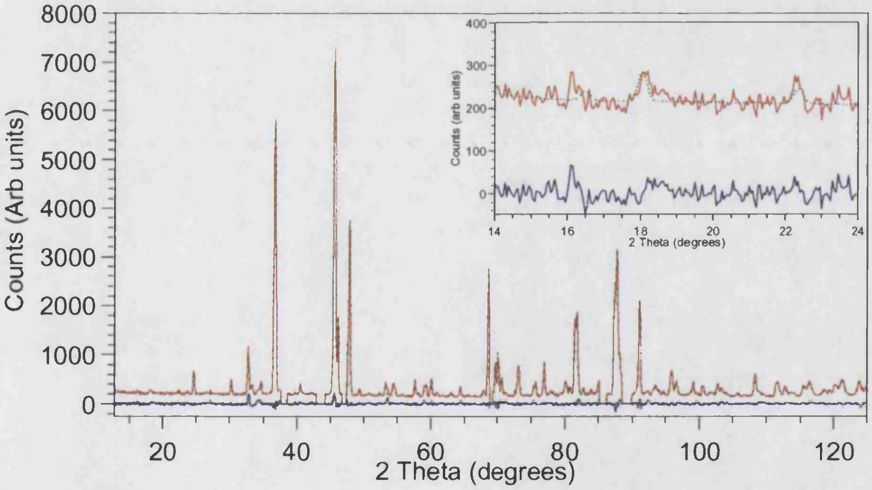

Figure 7.4. Observed, calculated and difference from the Rietveld refinement of $Pr_{0.5}Ca_{1.5}MnO_4$ *at 15K. Insert shows the presence of magnetic peaks between 12 and 24° 2 theta. Refined in the C 2/m space group.*

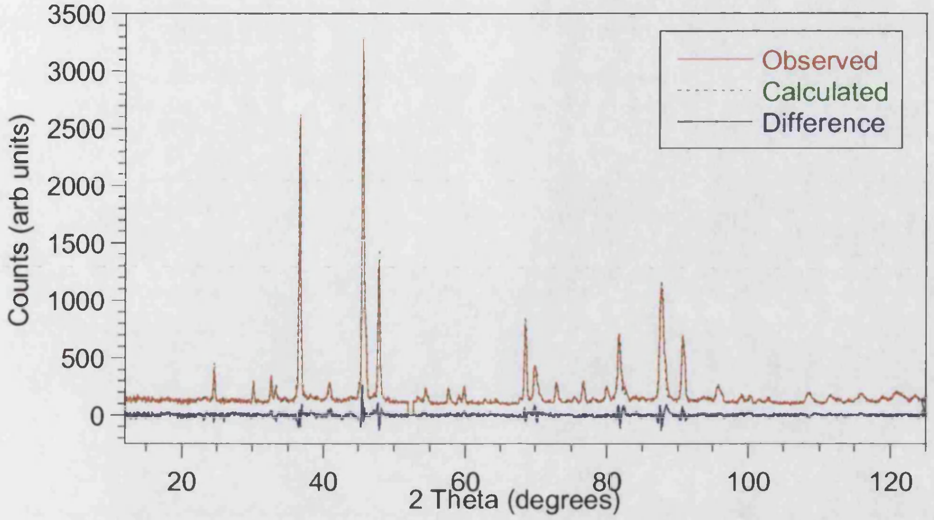

Figure 7.5. Observed, calculated and difference for the Rietveld refinement of $Nd_{0.5}Ca_{1.5}MnO_4$ *at room temperature refined in the C2/m space group.*

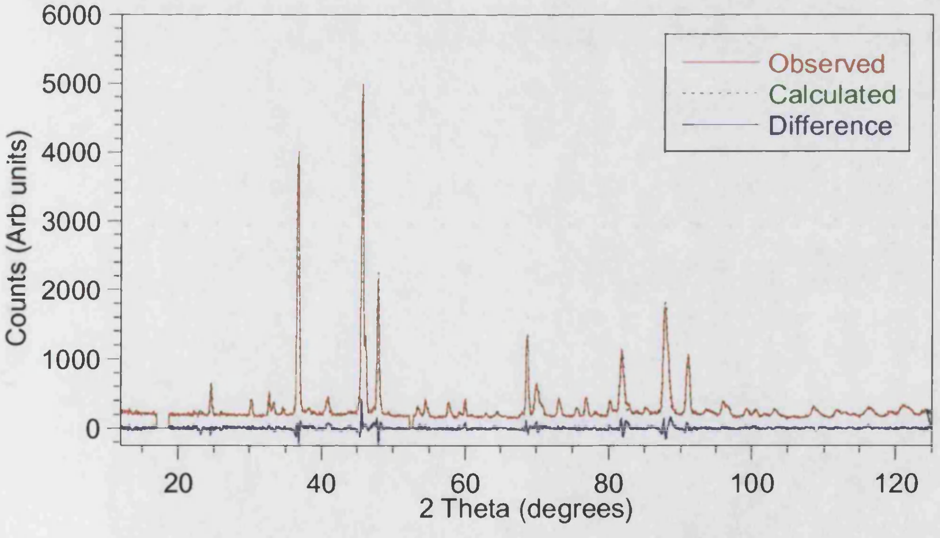

Figure 7.6. Observed, calculated and difference for the Rietveld refinement of $Nd_{0.5}Ca_{1.5}MnO_4$ *at 15K refined in the C2/m space group.*

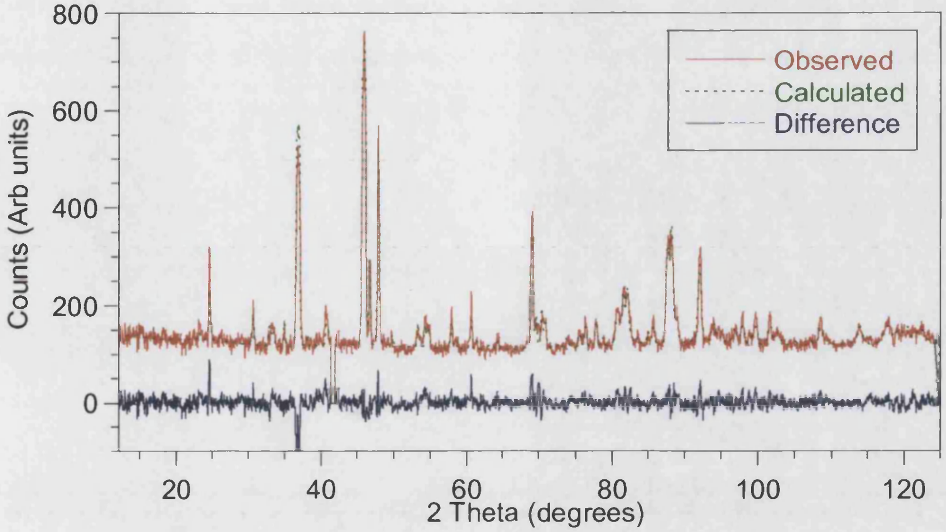

Figure 7.7. Observed, calculated and difference for the Rietveld refinement of $Er_{0.5}Ca_{1.5}MnO_4$ *at room temperature refined in the C2/m space group.*

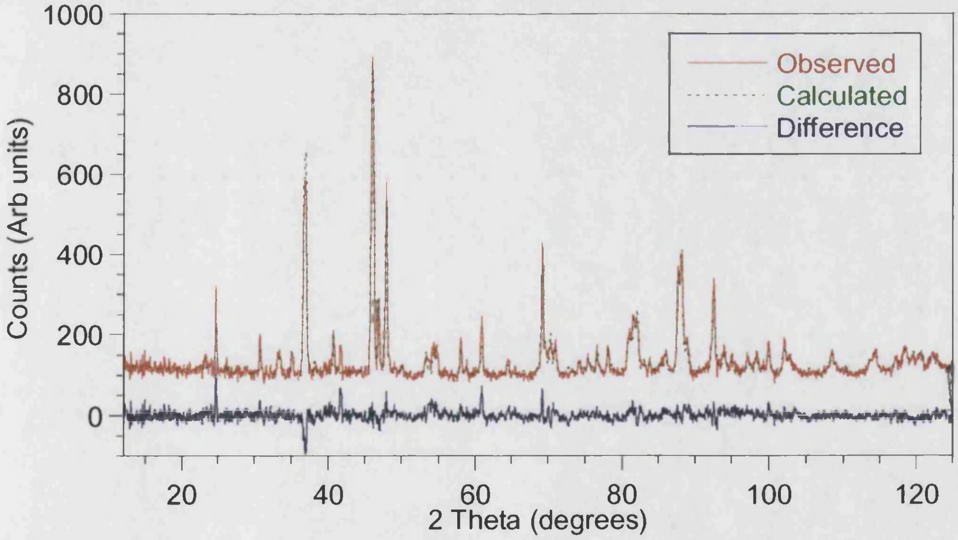

Figure 7.8. Observed, calculated and difference for the Rietveld refinement of $Er_{0.5}Ca_{1.5}MnO_4$ *at 15K refined in the C2/m space group.*

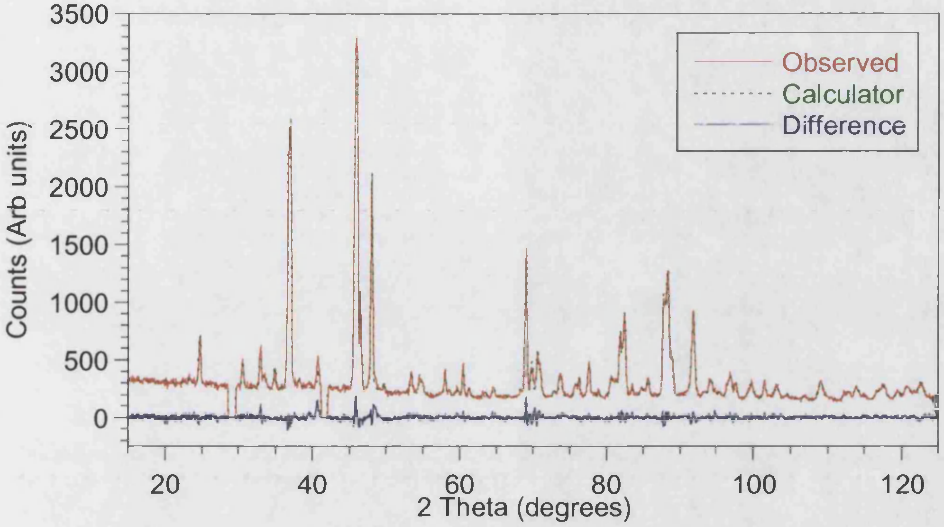

Figure 7.9. Observed, calculated and difference for the Rietveld refinement of $Tb_{0.5}Ca_{1.5}MnO_4$ *at room temperature refined in the C2/m space group.*

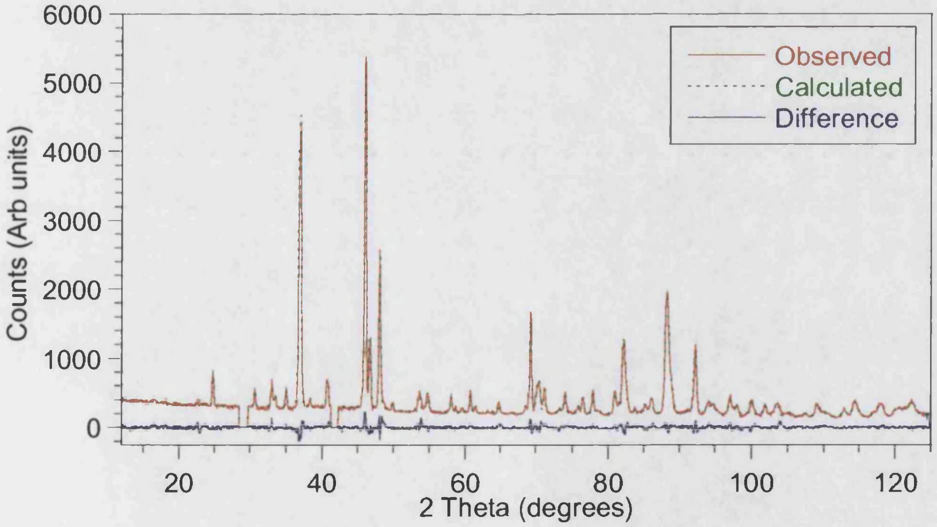

Figure 7.10. Observed, calculated and difference for the Rietveld refinement of $Tb_{0.5}Ca_{1.5}MnO_4$ *at 15K refined in the C2/m space group.*

Table 7.3. Atomic positions obtained from Rietveld profile refinements of powder neutron diffraction data of $Er_{0.5}Ca_{1.5}MnO_4$ *at 15 K (Pr 15 K) and room temperature (Pr RT) and* $Tb_{0.5}Ca_{1.5}MnO_4$ *at 15 K (Nd 15 K) and room temperature (Nd RT), in the space group Cmca.*

	Er 15K	Er RT	Tb 15 K	Tb RT
a (Å)	5.3438 (4)	5.3381 (4)	5.3378 (2)	5.3253 (2)
b (Å)	11.6103 (7)	11.6585 (9)	11.6530 (4)	11.6920 (4)
c (Å)	5.3872 (4)	5.3887 (4)	5.3598 (2)	5.3748 (2)
Cell Volume ($Å^3$)	334.24 (4)	335.36 (5)	333.39 (2)	334.65 (2)
Pr / Nd / Ca (0, y, z)				
y	0.3559 (3)	0.3566 (3)	0.3554 (2)	0.3563 (2)
z	-0.0085 (3)	-0.0077 (3)	-0.0089 (2)	-0.0080 (2)
U_i (x 100)	0.00	0.00	0.93 (5)	1.30 (5)
Mn (0, 0, 0)				
U_i (x 100)	0.4 (2)	0.7 (2)	0.73 (9)	0.80 (9)
O (1) (0.25, y, 0.25)				
y	-0.0159 (4)	-0.0155 (5)	-0.0148 (2)	-0.0131 (2)
U_{11} (x 100)	1.7 (3)	2.2 (3)	1.6 (2)	1.0 (1)
U_{22} (x 100)	1.5 (3)	1.4 (3)	0.9 (1)	1.7 (1)
U_{33} (x 100)	1.4 (3)	0.8 (3)	0.9 (1)	1.8 (1)
U_{13} (x100)	-0.6 (2)	-0.5 (2)	-0.15 (9)	-0.33 (9)
O (2) (0, y, z)				
y	0.1645 (4)	0.1649 (4)	0.1658 (1)	0.1654 (1)
z	0.048 (1)	0.045 (1)	0.0421 (5)	0.0387 (5)
U_{11} (x 100)	3.9 (4)	3.4 (5)	3.2 (2)	2.9 (2)
U_{22} (x 100)	0.6 (2)	0.2 (3)	0.1 (1)	0.5 (1)
U_{33} (x 100)	2.3 (3)	3.0 (4)	0.6 (1)	2.0 (1)
U_{23} (x 100)	0.7 (2)	-0.1 (3)	0.05 (9)	0.0 (1)
wRp (%)	8.47	7.94	7.15	6.30
Rp (%)	6.93	6.46	5.38	4.72
χ^2	1.524	1.424	2.770	1.874

Table 7.4. Bond Lengths and Bond angles from Rietveld refinement of $Pr_{0.5}Ca_{1.5}MnO_4$.

	15K		Room Temperature	
		Valence		Valence
Mn-O (Å)	1.90351(11)	0.666	1.90441(12)	0.664
Mn-O (Å)	1.90351(11)	0.666	1.90441(12)	0.664
Mn-O (Å)	1.90351(11)	0.666	1.90441(12)	0.664
Mn-O (Å)	1.90351(11)	0.666	1.90441(12)	0.664
Mn-O (Å)	1.9559(11)	0.578	1.9541(13)	0.581
Mn-O (Å)	1.9559(11)	0.578	1.9541(13)	0.581
Total Valence		3.82		3.82

Table 7.5. Bond Lengths and Bond angles from Rietveld refinement of $Nd_{0.5}Ca_{1.5}MnO_4$.

	15K		Room Temperature	
		Valence		Valence
Mn-O (Å)	1.89721(22)	0.667	1.89782(23)	0.676
Mn-O (Å)	1.89721(22)	0.667	1.89782(23)	0.676
Mn-O (Å)	1.89721(22)	0.667	1.89782(23)	0.676
Mn-O (Å)	1.89721(22)	0.667	1.89782(23)	0.676
Mn-O (Å)	1.9482(20)	0.590	1.9517(24)	0.584
Mn-O (Å)	1.9482(20)	0.590	1.9517(24)	0.584
Total Valence		3.85		3.87

Table 7.6. Bond Lengths and Bond angles from Rietveld refinement of $Er_{0.5}Ca_{1.5}MnO_4$.

	15K		Room Temperature	
		Valence		Valence
Mn-O (Å)	1.9059(5)	0.662	1.9048(5)	0.663
Mn-O (Å)	1.9059(5)	0.662	1.9048(5)	0.663
Mn-O (Å)	1.9059(5)	0.662	1.9048(5)	0.663
Mn-O (Å)	1.9059(5)	0.662	1.9048(5)	0.663
Mn-O (Å)	1.925(4)	0.628	1.938(5)	0.607
Mn-O (Å)	1.924(4)	0.628	1.938(5)	0.607
Total Valence		3.90		3.87

Table 7.7. Bond Lengths and Bond angles from Rietveld refinement of $Tb_{0.5}Ca_{1.5}MnO_4$.

	15K		Room Temperature	
		Valence		Valence
Mn-O (Å)	1.89894(18)	0.674	1.89771(17)	0.676
Mn-O (Å)	1.89894(18)	0.674	1.89771(17)	0.676
Mn-O (Å)	1.89894(18)	0.674	1.89771(17)	0.676
Mn-O (Å)	1.89894(18)	0.674	1.89771(17)	0.676
Mn-O (Å)	1.9454(17)	0.595	1.9447(17)	0.596
Mn-O (Å)	1.9454(17)	0.595	1.9447(17)	0.596
Total Valence		3.89		3.90
Mn-O-Mn	169.57(11)		170.76(12)	

7.3.2. Magnetisation and Transport Properties.

Rare earths with small ionic radii exhibit paramagnetic character, as the ionic radii increase a glassy transition is observed in Nd and Sm. $Pr_{0.5}Ca_{1.5}MnO_4$ orders antiferromagnetically with a T_N of approximately room temperature. Figure 7.11 shows the obtained SQUID data illustrating the antifrromagnetic, spin glass and paramagenetic behaviour observed for Ln = Pr, Nd, Sm and Tb respectively. Change in magnetic properties as a function of increasing ionic radii is given in figure 7.12. Previous authors have reported the $Pr_{0.5}Ca_{1.5}MnO_4$ phase as paramagnetic/ferromagnetic this is possibly due to the presence of small amounts of perovskite second phase which leads to a weak ferromagnetic component or intergrowths corresponding to $(Ln,A)_{n+1}Mn_nO_{3n+1}$, where n = 3 or 4.[20] It was not possible to fit the paramagnetic regions to the Curie-Weiss law due to the high magnetic transition temperatures and short range correlations, which are not Curie-Weiss in behaviour.

Since susceptibility is dependent upon the bandwidth, loss of overlap due to distortion, and strength of coupling is therefore dependent upon the bond angle. In the Pr phase the bond angle is around 180°, therefore there is strong superexchange and the phase is antiferromagnetic. However in the Nd phase the bond angle is less than 180°, and is therefore Paramagnetic. A Jahn-Teller distortion is also observed in the Ln_2CrO_4 phases reported by Romero de Paz *et al*, whereby when Ln is Praseodymium the distortion is small but as Pr is replaced by smaller lanthanide elements this distortion increases.[18,25] Only the two layer Ruddlesden-Popper phases containing La and Sr show true ferromagnetic character, which comes from a reduced bandwidth in the xy plane making Double exchange possible.

In $Pr_{0.5}Ca_{1.5}MnO_4$ the manganese spins align antiferromagnetically with a Néel temperature (T_N) of about room temperature and a saturated sublattice moment of $0.83\mu_B$ and is orientated in the xy direction perpendicular to the c-axis. Neutron diffraction data collected for the phase $Pr_{0.5}Ca_{1.5}MnO_4$ confirms the presence of antiferromagnetic ordering with additional 'magnetic' peaks being observed in the low temperature (15K) pattern. The magnetic peaks in the 15K data and the absence of magnetic peaks at room temperature are shown in the inserts of figure 7.4 and 7.3 respectively. The magnetic model shown in figure 7.13 was derived using GSAS and the SARAh refinement programs.[21,26] The proposed magnetic model is similar to those reported for Fe, Cu, Ni and Cr and identical to the model proposed by Yamada et al for La_2CoO_4.[25,27-30] The highest intensity magnetic peaks correspond to the reflections [100] or [1-10] and [120] or [1-20] using Bertraut's notation the model can be assigned the mode C_yG_x or $C_y + G_x$; where the components are coupled so that $|S_{ix}| = |S_{iy}|$.[25,30,31] It is worth noting that above room temperature the Pr remains disordered due to the random distribution of the Ca^{2+} and Pr^{3+} in the R and P sites.

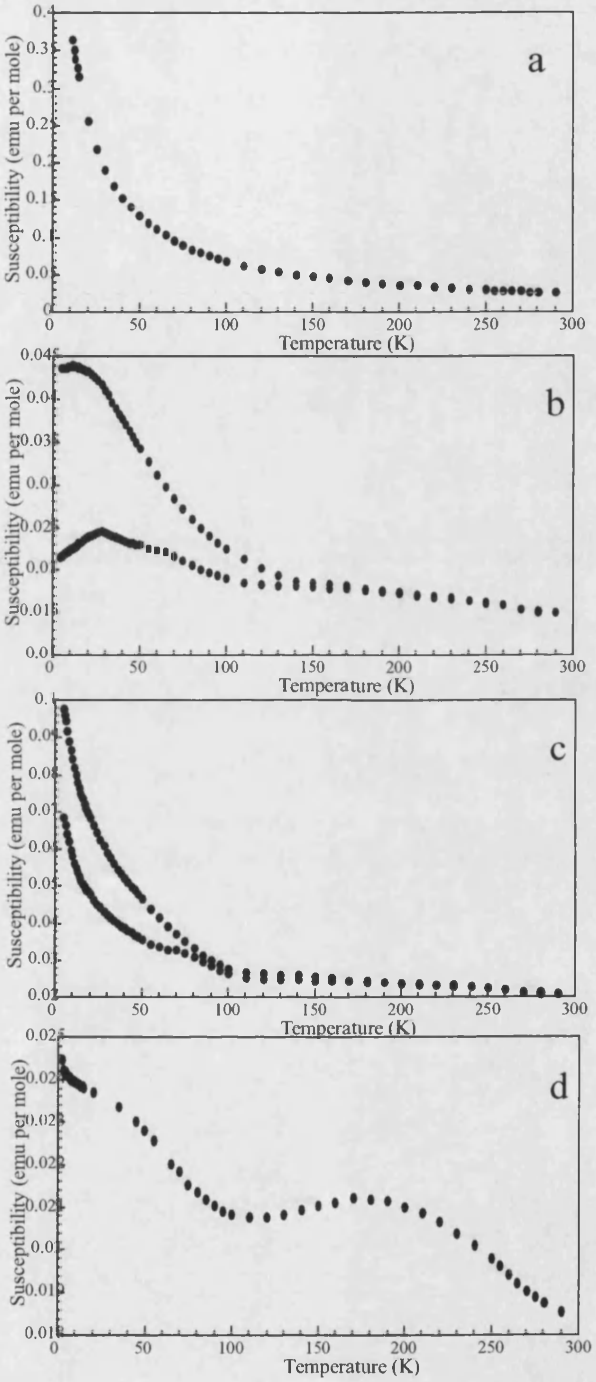

Figure 7.11. Magnetic susceptibility of (a) $Tb_{0.5}Ca_{1.5}MnO_4$ showing paramagnetic character, (b) $Sm_{0.5}Ca_{1.5}MnO_4$ showing spin glass behaviour, (c) $Nd_{0.5}Ca_{1.5}MnO_4$ also showing spin glass behaviour and (d) $Pr_{0.5}Ca_{1.5}MnO_4$ exhibiting antiferromagnetic ordering.

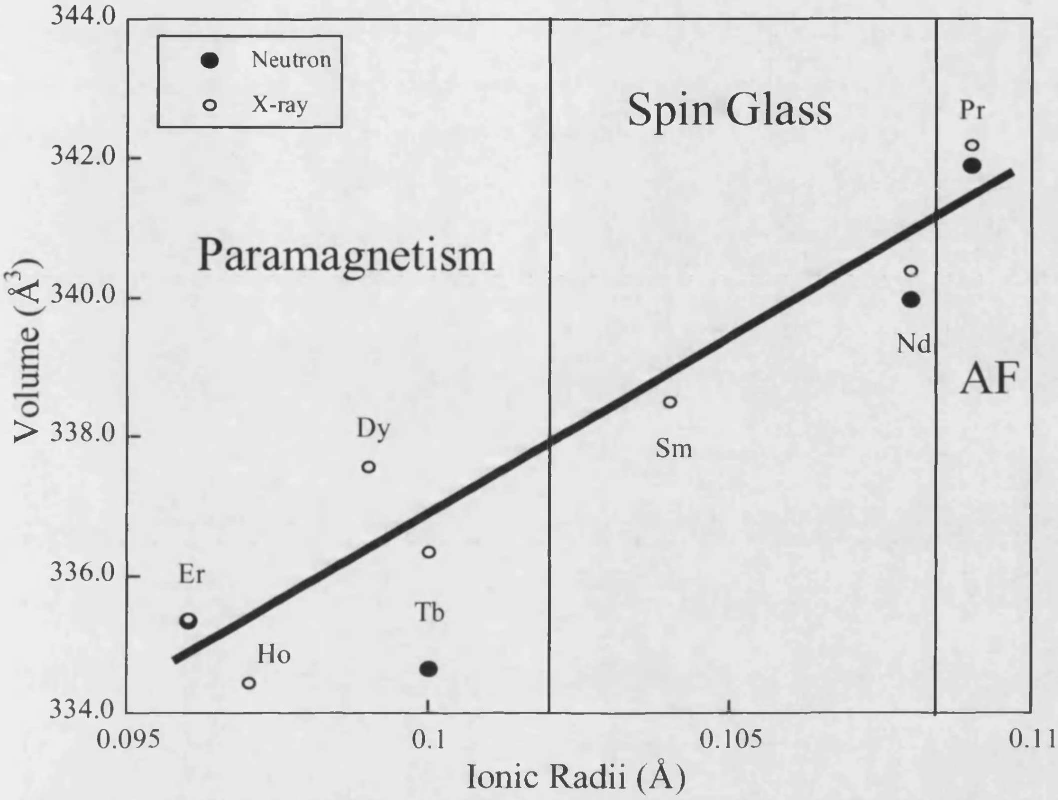

Figure 7.12. Magnetic behaviour as a function of increasing ionic radii and volume.

Figure 7.13. Antiferromagnetic structure of $Pr_{0.5}Ca_{1.5}MnO_4$ derived by Reitveld refinement of low temperature neutron data, where the blue spheres represent the manganese ions and the arrows show the direction of the magnetic spins.

The resistance of $Pr_{0.5}Ca_{1.5}MnO_4$ was measured over a temperature range of 170-400K in zero field and an applied field of 5T, an exponential decrease in resistance with increasing temperature is observed in both zero and applied field. When plotted (figure 7.14) together both sets of data are superimposable indicating that no CMR is present in these samples as previously reported.[20] These phases are semiconductors with band gaps of approximately 0.13eV for $Pr_{0.5}Ca_{1.5}MnO_4$.

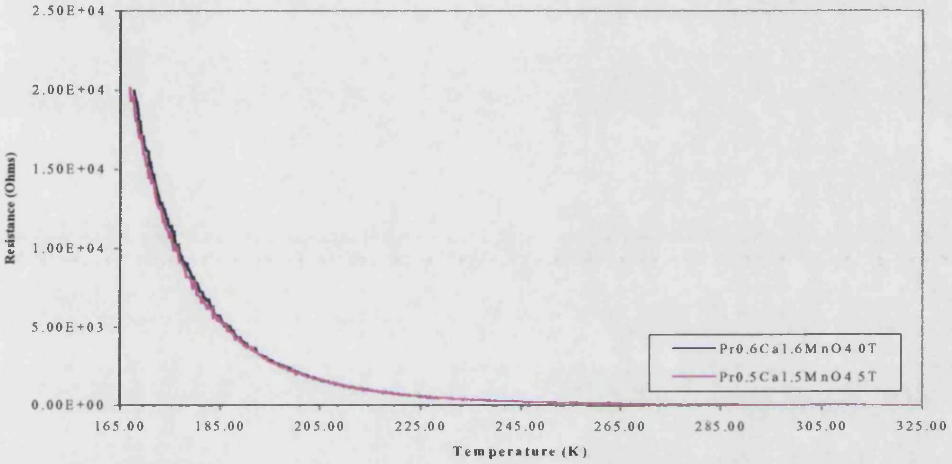

Figure 7.14 Plot of resistance against temperature showing semiconducting behaviour.

7.4. Conclusions.

Our results show that members of the $Ln_{0.5}Ca_{1.5}MnO_4$ family are paramagnetic with the exception of $Nd_{0.5}Ca_{1.5}MnO_4$ and $Sm_{0.5}Ca_{1.5}MnO_4$, which are spin glass in character, and $Pr_{0.5}Ca_{1.5}MnO_4$, which exhibits antiferromagnetic ordering. This is primarily due to loss of overlap due to distortion away from the ideal bond angle of 180^{o} leading to paramagnetism. In $Pr_{0.5}Ca_{1.5}MnO_4$ the bond angle is around 180^{o} making possible superexchange and hence the observation of antiferromagnetism. Despite previous suggestions no CMR is observed in these phases.

7.5. References.

(1) A. Maignan, C. Martin, F. Damay, B. Raveau, *Chemistry of Materials*, **1998**, *10(4)*, 950.

(2) E. Pollert, Z. Jirak, *Journal of Solid State Chemistry*, **1980**, *35*, 262.

(3) F. Damay, C. Martin, A. Maignan, M. Hervieu, B. Raveau, Z. Jirak, G. Andre, F. Bouree, *Chemistry of Materials*, **1999**, *11(3)*, 536.

(4) H. R. Rim, S. K. Jeung, E. Jung, J. S. Lee, *Materials Chemistry and Physics*, **1998**, *52(1)*, 54.

(5) I. O. Troyanchuk, N. Y. Samsonenko, H. Szymczak, A. Nabialek, *Journal of Solid State Chemistry*, **1997**, *131*, 144.

(6) M. Hervieu, C. Martin, A. Maignan, G. Van Tendeloo, Z. Jirak, J. Hejtmanek, A. Barnebe, D. Thopart, B. Raveau, *Chemistry of Materials*, **2000**, *12(15)*, 1456.

(7) N. Kamegashira, Y. Hiyoshi, N. Wajima, *Journal of Materials Science Letters*, **1985**, *4(1)*, 103.

(8) S. Mori, C. H. Chen, S. W. Cheong, *Nature*, **1998**, *392*, 473.

(9) Y. Moritomo, A. Asamtsu, H. Kuwahara, Y. Tokura, *Nature*, **1996**, *380*, 141.

(10) Z. Jirak, F. Damay, M. Hervieu, C. Martin, B. Raveau, G. Andre, F. Bouree, *Physical Review B*, **2000**, *61(2)*, 1181.

(11) M. Hervieu, B. Barnabe, C. Martin, A. Maignan, B. Raveau, *Physical Review B - Condensed Matter*, **1999**, *60(2)*, R726.

(12) M. Dlouha, S. Vratislav, Z. Jirak, *Physica B*, **1998**, *241*, 424.

(13) Y. Moritomo, Y. Tomioka, A. Asamtsu, Y. Tokura, Y. Matsui, *Physical Review B*, **1995**, *51(5)*, 3297.

(14) C. N. R. Rao, P. Ganguly, K. K. Singh, R. A. Mohan Ram, *Journal of Solid State Chemistry*, **1988**, *72*, 14.

(15) B. J. Sternlieb, J. P. Hill, U. C. Wildgruber, G. M. Luke, B. Nachumi, Y. Moritomo, Y. Tokura, *Physical Review Letters*, **1996**, *76(12)*, 2169.

(16) P. D. Battle, J. C. Burley, E. J. Cussen, G. C. Hardy, M. A. Hayward, L. D. Noailles, M. J. Rosseinsky, *Chemical Communications,* **1999**, *19*, 1977.

(17) A. Daoudi, G. Le Flem, *Journal of Solid State Chemistry*, **1972**, *5*, 57.

(18) A. Daoudi, G. Le Flem, *Materials Research Bulletin*, **1973**, *8*, 1103.

(19) N. Kamegashira, A. Shimono, H. W. Xu, H. Satoh, K. Hayashi, T. Kikuchi, *Materials Chemistry and Physics*, **1990**, *26(5)*, 483.

(20) A. Maignan, C. Martin, G. Van Tendeloo, M. Hervieu, B. Raveau, *Journal of Materials Chemistry*, **1998**, *8(11)*, 2411.

(21) R. B. Von Dreele, A. C. Larson. *General Structure Analysis System (GSAS)*, University of Califonia, **2001**.

(22) C. Hormillosa, S. Healey, T. Stephen, *Bond Valence Calculator*, 2.00 ed.; I. D. Brown: Ontario, **1993**.

(23) G. H. Lander, P. J. Brown, J. Spalek, J. M. Honig, *Physical Review B*, **1989**, *40(7)*, 4463.

(24) J. Rodriguez-Carvajal, J. L. Martinez, J. Pannetier, R. Saez-Puche, *Physical Review B*, **1988**, *38(10)*, 7148.

(25) J. Romero de Paz, M. T. Fernandez-Diaz, J. Hernandez Velasco, R. Saez-Puche, J. L. Martinez, *Journal of Solid State Chemistry*, **1999**, *142*, 29.

(26) A. S. Wills, *Physica B*, **2000**, *276*, 680.

(27) K. Yamada, Y. Kakurai, T. R. Thurston, M. A. Kastner, R. J. Birgeneau, G. Shirane, Y. Hidaka, T. Murakami, *Physical Review B*, **1989**, *40(7)*, 4557.

(28) M. A. Shamsutdinov, V. N. Nazarov, A. A. Khalfina, *Journal of Magnetism and Magnetic Materials*, **2000**, *214*, 139.

(29) M. M. Nguyen-Trut-Dinh, M Vlasse, M. Perrin, G. Le. Flem, *Journal of Solid State Chemistry*, **1980**, *32*, 1.

(30) J. Rodriguez-Carvajal, M. T. Fernadez-Diaz, J. L. Martinez, F. Fernandez, R. Saez-Puche, *Europhysics Letters*, **1990**, *11(3)*, 261.

(31) E. F. Bertaut, *Acta Crystallographica A*, **1968**, *24*, 217.

CHAPTER 8: Conclusions.

8.1. Conclusions.

The work contained in this thesis clearly illustrates the effects of intercalation on the structure and properties of a series of porous manganese oxides. In all the porous materials discussed here intercalation/deintercalation typically occurs by a combination of ion exchange and redox-type mechanisms, with selectivity decreasing with increasing ionic radii of the guest species, such that a larger amount of lithium can be intercalated into the tunnel site when compared to a larger cation such as potassium.

Whilst much of the existing work done concentrates on the possibility of using these materials as cathode materials in lithium batteries and hence centre on the electrochemical intercalation/deintercalation of lithium, little attention has been focused on the role intercalation on the properties of these materials as discussed here. It can be seen that the observed properties are dictated by the total intercalated and the identity of the intercalated species, for example in the hollandite system thermal stability decreases with increasing amount intercalated. This is also seen in both the $Na_{0.40}MnO_2$ and $Na_{0.44}MnO_2$ systems. Magnetic behaviour is also affected by intercalation for example in the $Na_{0.44}MnO_2$ system increasing ionic radii of the intercalated species results in increasing paramagnetic character and in the hollandite system the maximum magnetic moment at 5K decreases with intercalation. This work contributes to a greater understanding of the correlations between structure and properties allowing for the design of materials exhibiting certain physical phenomena.

Contrary to reports in the literature, $Na_{0.40}MnO_2$ does not appear to exhibit the romanechite structure as seen by the poor fits obtained by Rietveld refinement of both neutron and X-ray data. Intercalation and deintercalation of this material suggests that the material is indeed porous. However, comparison to emerging trends within these materials indicates a smaller pore dimension than tunnels formed in romanechite supporting the idea that the reported structure is incorrect. Whilst two plausible cells are discussed here the quality of the data collected did not allow for a full structural solution.

This thesis also reports the synthesis of novel host:polymer nanocomposite materials based on the intercalation of conducting polymers, pyrrole and aniline, into the interlayer gap of the layered manganese oxides birnessite and α-$NaMnO_2$. The intercalation of aniline into α-$NaMnO_2$ results in the first ordered polymer in an inorganic framework as evidenced by X-ray diffraction studies. However intercalation of polymer into the similarly layered birnessite material results in disordered material which is amorphous to X-ray diffraction. In both cases the intercalation of the polymer is evidenced by infrared spectroscopy and larger percentage weight losses observed by thermal analysis. Intercalation of the polymer also results in huge increases in the magnitude of the observed magnetisation.

The possibility of doping the manganese framework with other first row transition metals is briefly considered here. An enhanced understanding of the role of the manganese oxidation state on the properties could be investigated through framework doping and may lead to the synthesis of novel materials exhibiting alternative properties to those of the pure manganese derivatives.

Further good quality diffraction data needs to be collected for the $Na_{0.40}MnO_2$ phase and its intercalated analogues, preferably using central facilities such as the Synchrotron radiation source at Daresbury laboratory, UK to fully elucidate the structure and thus allow the properties to be fully characterised.

The understanding of the behaviour of novel polymer:manganese oxide nanocomposite materials can be investigated by in-depth structural studies including in-situ experiments to gain an enhanced understanding of the complex polymerisation mechanisms. The possibility also exists for the synthesis of further novel materials using alternative porous manganese oxides as host materials and a range of conducting polymers.